Mid-infrared Laser Spectroscopy for Trace Gas Detection

Katherine Marya Manfred

Magdalen College

University of Oxford

A thesis submitted for the degree of

Doctor of Philosophy

Michaelmas 2015

Declaration of Authorship

I declare that this thesis titled *Mid-infrared Laser Spectroscopy for Trace Gas Detection* and the work presented in it are my own. I confirm that the following statements are true:

- This work was done wholly while in candidature for a research degree at the University of Oxford.
- Where I have consulted or paraphrased the published work of others, this is always clearly attributed.
- Where I have quoted from the work of others, the source is always given. With the exception of such quotations, this thesis is entirely my own work.
- I have acknowledged all main sources of help and assistance I have received in addition to that of my supervisor.
- Where the thesis is based on work done by myself jointly with others, I have made clear exactly what was done by others and what I have contributed myself.
- I have not used the services of any agency providing specimen, model, or ghost-written work in the preparation of this thesis.
- I agree to retain an electronic copy of this work until the publication of my final examination result.
- I agree to make any such electronic copy available to the examiners should it be necessary.

Signature	Date

Mid-infrared Laser Spectroscopy for Trace Gas Detection

Katherine Marya Manfred

Magdalen College
University of Oxford

A thesis submitted for the degree of

Doctor of Philosophy

Michaelmas 2015

Laser spectroscopy offers a powerful and adaptable toolkit of techniques for sensitive and selective gas detection. New semiconductor laser sources that can emit high power mid-infrared radiation at room temperature have reawakened interest in exploiting the spectrally separated, strongly absorbing ro-vibrational transitions in this region. The aim of this thesis is the demonstration of absorption spectroscopy methods with interband cascade lasers (ICLs) and quantum cascade lasers (QCLs) to detect gases relevant to physiology and atmospheric science.

Modulation of laser frequency *via* the injection current can increase instrument performance and prevent long-term drifts in laser output. An 8.2 μm QCL was locked to a CH_4 ro-vibrational line using a $3f$ signal, limiting the laser frequency deviation to 3 MHz over 120 s. Frequency modulation spectroscopy (FMS) at 20 MHz demonstrated a twofold improvement for NO measured with a 5.3 μm QCL despite residual amplitude modulation. Broadband RF current perturbation of a 5.3 μm QCL was shown to broaden the laser linewidth and enhance the sensitivity of off-axis cavity-enhanced absorption spectroscopy (CEAS) tenfold.

Optical-feedback CEAS (OF-CEAS), which achieves high intracavity power and elongated periods of resonant cavity excitation, was performed using V-shaped and linear optical cavities. ICL and EC-QCL sources were utilized for the first time for sensitive OF-CEAS detection of VOCs and N_2O. OF-CEAS using a V-shaped cavity and 3.2 μm ICL achieved an α_{min} of 2.5×10^{-8} cm^{-1} for N_2O measurements. While the 5 μm EC-QCL achieved similar single-scan precision, mode-hopping prevented consistent measurements. The novel use of a linear optical cavity for OF-CEAS was demonstrated theoretically and experimentally with a 5.3 μm QCL to achieve excellent sensitivities (4×10^{-9} cm^{-1} Hz$^{-1/2}$). The successful demonstration of these techniques paves the way for new QCL and ICL technology to be incorporated in future laser absorption spectrometers for the laboratory, field, and clinic.

Acknowledgements

First and foremost, this work would not have been possible without Grant's constant support – I have been very fortunate to have exciting challenges to stretch my mind and freedom to do things my way. Anche ho bisogno di ringraziare Luca, un mentore ed amico (e maestro di lingua italiana) meraviglioso. I have looked forward to coming to the lab every day for the past few years because of all the wonderful people I work with, and so I extend a big thanks to Gus and Rob for their honest wisdom, Graham and Michele for always knowing the answer, James for being the best desk buddy, Kim for being a model of organization and reliability, Katie and Nick for being such patient and brilliant apprentices, and everyone else who put up with me in the office, lab, and tea room. And, of course, I am incredibly grateful for the heroes of the PTCL workshops who unfailingly made sure all the bits and bobs of my experiments worked.

My amazing family has managed to show their support from across the ocean, and forgiven me for all the missed birthdays and Christmases. I will always be thankful to Claire and Chris who were the best role models, helped me adjust to life changes, and lovingly picked me back up and gave me a dog to cuddle when I stumbled. I have been honoured to have some wonderful friends who have helped me along the way, but I was particularly lucky to share a kitchen with Caroline my first year – a few years and many cakes later, she is still a constant support and as close as family. And lastly to my favourite sister - you started teaching me the alphabet when I was a few years old and I have been learning by your example ever since.

List of Publications

- **Enhancing the sensitivity of mid-IR quantum cascade laser-based cavity-enhanced absorption spectroscopy using RF current perturbation**
  Katherine M. Manfred, James M. R. Kirkbride, Luca Ciaffoni, Robert Peverall, Grant A. D. Ritchie
  Opt. Lett. **39**, 6811–6814 (2014).

- **Optical-feedback cavity-enhanced absorption spectroscopy in a linear cavity: model and experiments**
  Katherine M. Manfred, Luca Ciaffoni, Grant A. D. Ritchie
  Appl. Phys. B **120**, 329–339 (2015).

- **Optical-feedback cavity-enhanced absorption spectroscopy with a 3.24 μm interband cascade laser**
  Katherine M. Manfred, Grant A. D. Ritchie, Norbert Lang, Jürgen Röpcke, Jean-Pierre H. van Helden
  Appl. Phys. Lett. **106**, 221106 (2015).

Contents

List of Figures

Variables

α	absorption coefficient
α^o	saturation-corrected absorption coefficient
α_{min}	minimum detectable absorption coefficient
$\delta\alpha_{min}^{SN}$	shot noise-limited α_{min}
α_H	Henry laser broadening coefficient
α_{JC}	quantum state index
β	feedback coefficient
Γ_o	laser cavity loss
γ_{air}	air-broadening coefficient
γ_{fb}	OF-CEAS correction factor
γ_{self}	self-broadening coefficient
δ	attenuation factor
ε	dielectric constant
ε^2	field overlap term
η	quantum efficiency
κ	feedback rate
λ	wavelength
μ	transition dipole moment
ν_i	vibrational mode
ν	frequency (Hz)
$\bar{\nu}$	average frequency
$\tilde{\nu}$	frequency (cm^{-1})
ν_{fb}	coupled laser frequency
ν_I	idler frequency
ν_o	free-running frequency
ν_P	pump frequency
ν_S	signal frequency
ν_{sb}	sideband frequency
$\Delta\nu$	FWHM
$\Delta\nu_i$	linewidth from component i
$\Delta\nu_{\text{locked}}$	locked laser linewidth
ρ	spectral radiation density
σ	integrated molecular absorption cross-section
σ^2	variance
σ_{AW}	Allan-Werle standard deviation
σ_{res}	standard deviation of residual
τ	averaging time
τ_{ji}	relaxation time constant for transition $j \leftarrow i$

τ_p	pressure-dependent collisional time constant
τ_{RD}	ring-down time
Φ	phase offset
ϕ_i	phase term for lock-in inputs
ψ	frequency and amplitude modulation phase offset
A	absorption
A_{fm}	FMS absorption
A_{21}	Einstein coefficient for spontaneous emission
B_{12}	Einstein coefficient for stimulated absorption
B_{21}	Einstein coefficient for stimulated emission
C	molecular spin symmetry
C_i	feedback scaling factor
c	speed of light
$c_{\min}$	minimum detectable concentration
D^*	detectivity
D_{fm}	FMS dispersion
E	radiation field
E_{ji}	energy separation of states j and i
$\mathcal{F}$	finesse
f	focal length
Δf	detector bandwidth
FSR	free spectral range
G	gain factor
H_i	intensity transfer function
h	Planck constant
h_i	field transfer function
I	radiation intensity
I_{sat}	saturation intensity
J	angular momentum quantum number
J_n	Bessel functions of the first kind
k	phase factor
k_B	Boltzmann constant
L	cavity length or path length
L'	laser–cavity distance
L_i	length of cavity arm
l_i	dielectric layer thickness
ℓ	laser cavity size
$\mathbf{M}$	ray trace matrix
M_a	amplitude modulation index
M_ν	frequency modulation index
M_i	cavity mirror label
m	molecular mass
m, n	transverse mode order
m_p	ratio of absorption to pressure
MDA	minimum detectable absorption
N	integer
N_i	number density of molecules in state i
N^o	number density of molecules at 760 Torr

n_i	refractive index
n_o	refractive index laser gain medium
n_{fit}	number of fitting parameters
NEAS	noise equivalent absorption sensitivity
P	pressure
P_{circ}	intracavity circulating optical power
P_{inc}	incident optical power
q	complex parameter of Gaussian beam
$\mathcal{R}$	radius of curvature of Gaussian beam wavefront
$\mathcal{R}^*$	responsivity
R	effective (total) reflectivity
R_i	reflectivity of component i
R_o	reflectivity of laser facet
r_i	reflection coefficient
T	temperature
T_i	transmittivity of mirror i
t	time
t^o	start time of scan
t_i	transmission coefficient
V_{LIi}	output of lock-in i
V_n	noise voltage
V_s	signal voltage
Δv	vibrational quantum number
w	Gaussian beam spot size
w_o	Gaussian beam waist size
X	representation of arbitrary molecule
$[X]$	concentration of species X
x, y	position in Cartesian coordinates of plane transverse to optical axis
z	position along optical axis
z_o	position of beam waist

Abbreviations

AM	**a**mplitude **m**odulation
AOM	**a**cousto-**o**ptic **m**odulator
BB	**b**road**b**and perturbation
CARS	**c**oherent **a**nti-Stokes **R**aman **s**pectroscopy
CEAS	**c**avity-**e**nhanced **a**bsorption **s**pectroscopy
cw	**c**ontinuous **w**ave
DAQ	**d**ata **aq**uisition card
DFB	**d**istributed **f**eed**b**ack
DFG	**d**ifference **f**requency **g**eneration
EC	**e**xternal **c**avity
FAMOS	**Fa**raday **mo**dulation **s**pectroscopy
FFT	**f**ast **F**ourier **t**ransform
FM	**f**requency **m**odulation
FMS	**f**requency **m**odulation **s**pectroscopy
FSR	**f**ree **s**pectral **r**ange
FWHM	**f**ull-**w**idth at **h**alf-**m**aximum
GHG	**g**reen**h**ouse **g**as
HILIC	**h**ydrophilic **i**nteraction **li**quid **c**hromatography
HITRAN	**Hi**gh Resolution **Tran**smission database
HPLC	**h**igh **p**erformance **l**iquid **c**hromatography
ICL	**i**nterband **c**ascade **l**aser
ICOS	**i**ntegrated **c**avity **o**utput **s**pectroscopy
INFAMS	**in**tracavity **Fa**raday **m**odulation **s**pectroscopy
IR	**i**nfra**r**ed
laser	**l**ight **a**mplification by **s**timulated **e**mission of **r**adiation
LED	**l**ight **e**mitting **d**iode
LI	**l**ock-**i**n amplifier
LIDAR	**li**ght **d**etection **a**nd **r**anging
MBE	**m**olecular **b**eam **e**pitaxy
MCT	**m**ercury **c**admium **t**elluride detector
MDA	**m**inimum **d**etectable **a**bsorption
MS	**m**ass **s**pectrometry
NEAS	**n**oise **e**quivalent **a**bsorption **s**ensitivity
NICE-OHMS	**n**oise-**i**mmune **c**avity-**e**nhanced **o**ptical **h**eterodyne **m**olecular **s**pectroscopy
NO_x	NO + NO_2
NP	**n**o **p**erturbation
OAPM	**o**ff-**a**xis **p**arabolic **m**irror
OF-CEAS	**o**ptical **f**eedback **c**avity-**e**nhanced **a**bsorption **s**pectroscopy

OPO	**o**ptical **p**arametric **o**scillator
PAS	**p**hoto**a**coustic **s**pectroscopy
PD	**p**hotodiode **d**etector
ppb	**p**arts **p**er **b**illion (10^{-9}) by volume
PPLN	**p**eriodically **p**oled **l**ithium **n**iobate
ppm	**p**arts **p**er **m**illion (10^{-6}) by volume
ppt	**p**arts **p**er **t**rillion (10^{-12}) by volume
PTR-MS	**p**roton **t**ransfer **r**eaction **m**ass **s**pectrometry
PVD	**p**hoto**v**oltaic **d**etector
PZT	**p**ie**z**oelectric **t**ransducer
QCL	**q**uantum **c**ascade **l**aser
QEPAS	**q**uartz-**e**nhanced **p**hoto**a**coustic **s**pectroscopy
RAM	**r**esidual **a**mplitude **m**odulation
RF	**r**adio **f**requency
SIFT-MS	**s**elected **i**on **f**low **t**ube **m**ass **s**pectrometry
SM	**s**ingle frequency **m**odulation
SNR	**s**ignal-to-**n**oise **r**atio
TDL	**t**unable **d**iode **l**aser
TEM	**t**ransverse **e**lectro**m**agnetic
VCSEL	**v**ertical-**c**avity **s**urface-**e**mitting **l**aser
VOC	**v**olatile **o**rganic **c**ompound
WMS	**w**avelength **m**odulation **s**pectroscopy

Chapter 1

Laser Absorption Spectroscopy: Principles and Motivations

1.1 Introduction

Air is a magical substance. It is an invisible, virtually unnoticeable sea containing a vast array of reactants and products that make life possible on this planet. In 1674, Sir Robert Boyle aptly described its importance and complexity:[1]

> *[Air] is not, as many imagine, a Simple and Elementary Body, but a confus'd Aggregate of Effluviums from such differing Bodies, that, though they all agree in constituting, by their minuteness and various motions, one great mass of Fluid matter, yet perhaps there is scarce a more heterogeneous Body in the world.*

Science has come a long way in understanding the constituents and properties of air and other complex gas mixtures. Gases pose unique challenges for detection and measurement: gases are well-mixed, largely transparent, and have variable densities according to pressure, volume, and temperature conditions. Despite these challenges, quantifying the concentration of a particular species can be vitally important for scientific endeavour, as well as human health and safety.

The canary is, perhaps, one of the earliest gas sensors used for human safety, while the olfactory prowess of canines has long been exploited for bomb detection and earthquake rescue operations, with continuing progress in early cancer detection.[2] Today, the military has even recruited honeybees to sniff out landmines.[3] But what if we could achieve all these

objectives with small, customizable, affordable devices sans fur and stingers? The ability to detect and quantify specific molecules in air is of great importance for environmental monitoring, medical diagnostics, and security. Increasingly, regulations require monitoring of workplace air quality, and of industrial and automotive emissions, driving commercial interest in gas sensing development. The gas sensing market is projected to be worth £1.5 billion per annum by 2018.[4] Laser absorption spectroscopy is widely-accepted to be one of the best ways to achieve the necessary sensitivity, selectivity, and accuracy required for trace gas detection applications.

For nearly two centuries, scientists have known that each type of gas attenuates the transmission of a characteristic collection of wavelengths of light. While this allowed the identification of different gases, it was not until the development of quantum mechanics in the early 20^{th} century that this behaviour could be justified. The quantized energy levels of electrons and nuclei in atomic or molecular systems means that only discrete quanta of energy, such as photons, will induce a change in the system. A molecule can absorb the energy of a photon and thereby induce a change from an electronic, vibrational, or rotational state into a state that is higher in energy. Electronic excitations usually require high energy UV or visible radiation, which often causes dissociation making them unsuitable for non-invasive sensing. Pure rotational excitations, on the other hand, correspond to low-energy microwave wavelengths. These transitions are very close in energy and therefore more difficult to distinguish. Vibrational excitations are ideal for gas detection being well-separated, non-destructive, and within the visible and infrared bands of the spectrum where lasers and other light sources are readily available.

As seen in Figure 1.1, an excitation from one vibrational state to another is actually a transition from one series of rotational states to another series.[5] Rotational-vibrational (or ro-vibrational) transitions that can be excited with infrared radiation are, however, limited by selection rules. For most molecules, the transition must satisfy the selection rules:

$$\Delta v_{ij} = \pm 1 \quad \Delta J_{ij} = \pm 1 \tag{1.1}$$

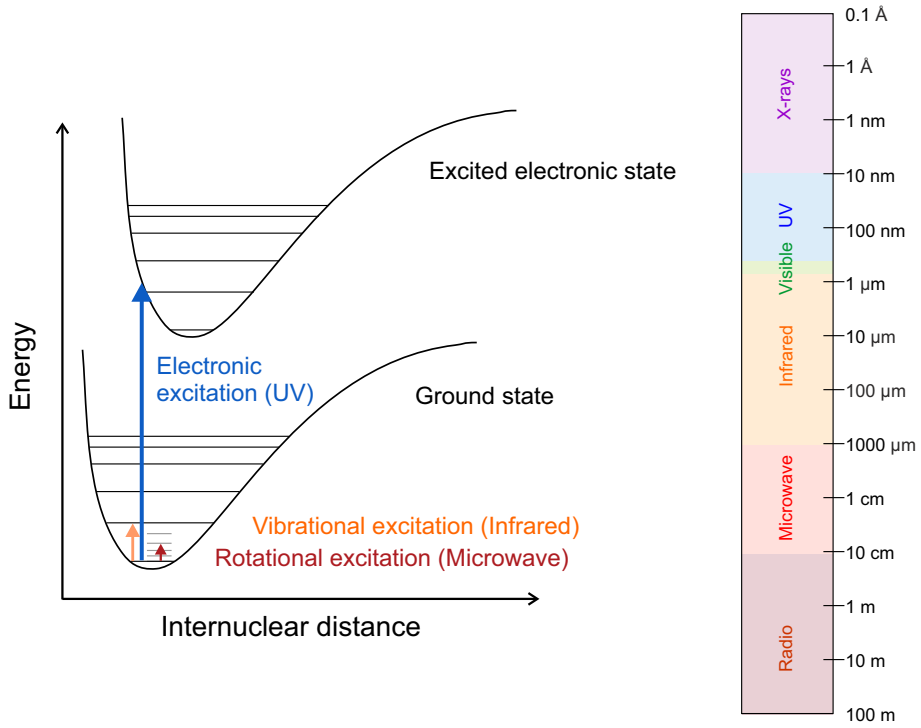

Figure 1.1: Simplistic model of molecular energy levels for two different electronic states. Arrows indicate electronic (blue), vibrational (orange), and rotational (red) transitions, which correspond to UV, infrared, and microwave photon energies, respectively. The electromagnetic spectrum is shown on the right labelled by wavelength (λ) for reference.

where Δv_{ij} and ΔJ_{ij} represent the changes in the vibrational and rotational state quantum numbers respectively. The second rule gives rise to two branches, one on either side of the energy for the pure vibrational transition; the lower energy ($\Delta J_{ij} = -1$) is termed the P branch, while the higher energy ($\Delta J_{ij} = +1$) is labelled the R branch. Molecules with non-zero electronic angular momentum in the ground electronic state can also undergo $\Delta J_{ij} = 0$ transitions; these appear as a central Q branch. The result is an infrared spectrum formed of a series of ro-vibrational transitions across a range of frequencies. For relevant small molecules, the energy and temperature-dependent probability of these ro-vibrational states have been calculated, and thus can serve as a quantifiable signature of the gas.

1.2 Physical basis of absorption spectroscopy

In order to use ro-vibrational transitions for detection, their fundamental characteristics must be defined. A molecular ro-vibrational spectral line is defined by three parameters: centre frequency, lineshape, and absorption strength.

1.2.1 Frequency

The frequency of a transition is fundamentally determined by the energy difference between the upper and lower states of the ro-vibrational transition. Bonding force constants, which are related to the energy levels of different states, vary depending on electronic structure and environment, and so differentiation of species – including isotopic analogues – is possible. The centre frequency of a given transition can shift slightly when pressure-induced distortions in the potential energy surface arise due to interactions with neighbouring molecules. The HITRAN (**hi**gh-resolution **tran**smission) international database for gas-phase molecular absorption constants provides pressure-shift estimates for transitions included in the database, however in practice these will depend on the buffer gas and are generally not precisely known.[6] Pressure-shifts only become important at very high pressures, and thus no significant shifts are expected for most trace gas sensing applications which require atmospheric pressure. A typical pressure shift at 1 atm in the relevant wavelength region is ~ 0.005 cm^{-1}, much less than the absorption linewidth under the same conditions.

Throughout this thesis, the frequency units follow the following convention: ν refers to frequency in Hz and $\tilde{\nu}$ is the equivalent value in units of wavenumber (cm^{-1}).

1.2.2 Lineshape

The shape of the measured absorption line is the convolution of the frequency distribution of the laser and the frequency-dependent molecular absorption cross-section. There are four potential types of molecular linewidth broadening to be considered: natural (uncertainty), Doppler, pressure (collisional), and saturation. The first, natural broadening, is simply a result of the Heisenberg uncertainty principle, which states that:

$$\Delta E \geq \frac{h}{2\pi\tau_{ji}} \tag{1.2}$$

where τ_{ji} is the lifetime of the transition $j \leftarrow i$, ΔE is the energy of the transition ($\Delta E = hc\Delta\tilde{\nu}$), and h is Planck's constant. Transitions with short lifetimes will have a broader distribution of measured frequencies. At room temperature and within the mid-

infrared spectral region natural broadening is orders of magnitude smaller than pressure and temperature-dependent broadening mechanisms and can be neglected.

Doppler broadening is related to the distribution of molecular velocities. The Doppler effect describes the frequency shift of electromagnetic oscillations due to movement towards or away from a reference point (or absorbing species). The Maxwellian distribution of molecular velocities within the sample results in a Gaussian lineshape that has a frequency full-width at half-maximum (FWHM) of:

$$\Delta\nu_D = \nu\sqrt{\frac{8k_BT\ln 2}{mc^2}}. \tag{1.3}$$

The ratio of the Doppler linewidth ($\Delta\nu_D$) to the centre frequency (ν) is therefore related to the Boltzmann constant (k_B), temperature (T), speed of light (c), and molecular mass (m). This effect is inhomogeneous, meaning not all molecules are affected in the same way. At room temperature, gas molecules will have Doppler linewidths on the order of a few hundred MHz in the mid and near-infrared and this broadening mechanism does contribute substantially to the absorption lineshape.

Pressure broadening is another significant contributor to the lineshape and is caused by the exchange of energy between colliding molecules. This is similar to natural broadening, however the time constant in this case is the mean time between collisions (τ_p):

$$\Delta\nu_p = \frac{1}{2\pi\tau_p}. \tag{1.4}$$

Collisional broadening affects all molecules in the system in the same way, therefore it can be modelled as a homogeneous, Lorentzian distribution. The magnitude of the effect depends on the collisional behaviour of the two gas molecules involved, and therefore the total broadening is a sum of species-dependent broadening effects, scaled by the partial pressure of each gas in the sample. Pressure broadening coefficients are given in the HITRAN database for collisions between two molecules of the same gas (γ_{self}), as well as for a standard air mixture (γ_{air}), in units of cm^{-1} atm^{-1}, the half-width at half-maximum per atmosphere of pressure. Typical values of γ_{air} are ~ 0.05 cm^{-1} atm^{-1}, though γ_{self} is several times larger

for polar molecules.

Distortion of the lineshape can occur if an intense light source increases the fraction of molecules in the upper energy state (or energy gap close to thermal energy in the case of microwave spectroscopy). In the limit where the ratio of the number of molecules in the upper state to the lower state approaches unity, the gas becomes "transparent" – for each photon absorbed by a molecule in the lower state, another will be emitted from a different molecule in the excited state. As the system approaches this limit, the measured absorption becomes dependent on the intensity of light in addition to the characteristics of the sample.

Many gas sensing applications use sample pressures ranging from a few Torr to atmospheric pressure at room temperature. Under these conditions, both the pressure and Doppler broadening contributions will influence the molecular lineshape. Since the linewidths of the laser sources used here (< 10 MHz) are much narrower than the linewidths of the transitions (typically > 100 MHz), in practice the measured lineshape is solely determined by the properties of the gas sample. Generally a Voigt profile, the convolution of Lorentzian and Gaussian broadening mechanisms, accurately describes the measured spectral line. A comparison of these three lineshapes is shown in Figure 1.2. Other lineshape models have been used in the past to describe molecular absorption profiles, for example the Galatry model that accounts for the secondary effect of Dicke narrowing of the Doppler contribution

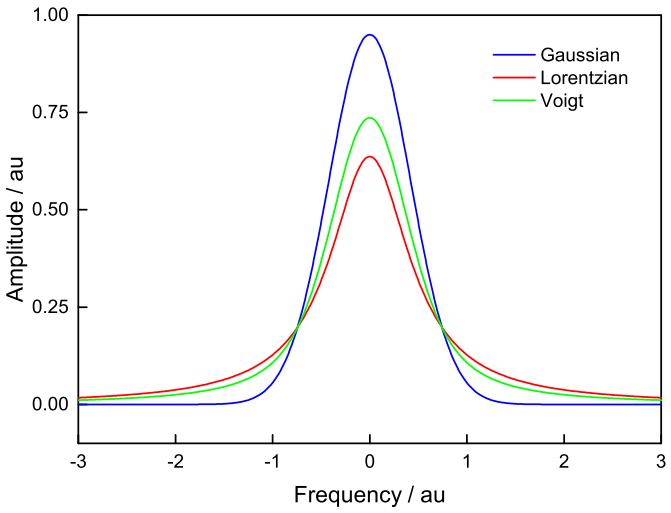

Figure 1.2: Gaussian (blue), Lorentzian (red), and Voigt (green) profiles. All lineshapes have equal integrated areas (1 a.u.^{2}) and FWHM (1 a.u.), and the Voigt profile was set so that the Gaussian and Lorentzian contributions are equal.

due to collisions.[7] For the studies conducted in this work, the Voigt model was sufficient in all cases.

1.2.3 Linestrength

The magnitude of an absorption feature – the total attenuation of light over the frequency range associated with the transition – is related to the concentration of the target gas molecule and absorption cross-section of the transition probed. The integrated absorption cross-section (σ) is an effective area over which an incident photon will be absorbed, which is related to the likelihood of extinction.

When molecules are irradiated by electromagnetic radiation with an energy corresponding to the energy difference between two stationary states, the photon may interact with the molecule in three ways: induced absorption, spontaneous emission, or stimulated emission.[5] Absorption spectroscopy is primarily concerned with the first process, which can be described for a given species X by:

$$X + h\nu \rightarrow X^* \tag{1.5}$$

with ν denoting the frequency of the radiation and X^* indicating the species in an excited state. Labelling population densities of the lower and upper energy states as N_1 and N_2, respectively, the rate of excitation by induced absorption can be described by:

$$\frac{dN_2}{dt} = N_1 B_{12} \rho(\nu). \tag{1.6}$$

B_{12} is the Einstein coefficient for stimulated absorption and is equal in magnitude to the stimulated emission coefficient (B_{21}) provided that each state has the same degeneracy. The value of B_{12} is determined by the overlap of the wave functions of the two states and the electric dipole operator.[5] In order for a transition to be strongly infrared-active, *i.e.* $B_{12} \neq 0$, it must induce a change in dipole moment. The frequency-dependent spectral

radiation density ($\rho(\nu)$) is related to the incident radiation field amplitude (E_{inc}) by:[8]

$$\rho(\nu) = \left(\frac{\varepsilon}{4\pi}\right) |E_{\text{inc}}(\nu)|^2 \tag{1.7}$$

with ε denoting the dielectric constant. The rate of excitation is therefore linearly related to the intensity of the incident light ($I_{\text{inc}} \propto |E_{\text{inc}}|^2$).

The other two processes are the main mechanisms for depletion of the upper state population to the lower state. Stimulated emission is very similar to absorption and can be described by: $dN_2/dt = -N_2 B_{21} \rho(\nu)$. Spontaneous emission is described by another Einstein coefficient (A_{21}) which is the inverse of the natural lifetime of the transition. Therefore, the total rate of population transfer is given by:[5,8]

$$\frac{dN_2}{dt} = (N_1 - N_2)\, B_{12} \rho(\nu) - N_2 A_{21}. \tag{1.8}$$

In most circumstances, the excited state population will be quite small compared to the ground state ($N_2 \ll N_1$), which means that the excitation rate is determined primarily by B_{12}. This can be converted to the integrated absorption cross-section:

$$\sigma = \int h N_1 B_{12} \mathrm{d}\nu. \tag{1.9}$$

The population density term takes into account temperature-dependent changes in population, particularly important for hot band transitions. The population of states with energy E at temperature T follows a Boltzmann distribution ($\propto \exp\left(\frac{-E}{k_B T}\right)$). Values of σ as given in HITRAN have units of $\text{cm}^{-1}\text{cm}^2$. To convert to $\sigma_{\max}$, the maximum amplitude of the absorption transition (typically at line centre, ν_o), one must take into account the linewidth in units of cm^{-1} ($\Delta\tilde{\nu}$). For a transition dominated by pressure broadening, this can be estimated by:

$$\sigma_{\max} = \sigma(\nu_o) = \frac{2\sigma}{\pi \Delta\tilde{\nu}} \tag{1.10}$$

where $\Delta\tilde{\nu}$ is the FWHM of the absorption profile.

1.2.4 Beer-Lambert Law

The photon density of a beam of light travelling through an absorbing medium will increase due to emission and decrease due to induced absorption. The attenuation is therefore related to the product of the photon energy and sum of the rates of these two processes. Considering light with a linewidth of $\mathrm{d}\nu$ travelling a distance L, this results in:

$$\frac{\mathrm{d}\left(I(\nu)\mathrm{d}\nu\right)}{\mathrm{d}L} = h\nu I(\nu)\left[-N_1 B_{12} + N_2 B_{21}\right]. \tag{1.11}$$

As the radiation passes through the sample, most of the molecules will generally be in the lower state, and correspondingly N_2 negligibly small. The Beer-Lambert law states that the incremental change in intensity travelling a short distance ($\mathrm{d}L$) will follow the relationship $\mathrm{d}I = -I\alpha\mathrm{d}L$. The absorption coefficient (α) is a frequency-dependent quantity with units of cm^{-1} which can be related to the properties of the gas sample:

$$\int_{\nu_1}^{\nu_2} \alpha \mathrm{d}\nu = B_{12} N_1 h c_x \bar{\nu} = \sigma[X] \tag{1.12}$$

with $\bar{\nu}$ the average frequency. The value of α is therefore dependent on radiation frequency, the molecular transition being excited, and the concentration of the target species ([X]). As the laser frequency can be selected and transition constants are known for these gases, the only variable to measure is the concentration of the gas. The ratio of the laser intensity over a given path length (L) with the sample (I) compared to without (I_o) can therefore be used to determine the concentration of the gas species X:

$$\frac{I}{I_o} = \exp\left(-[X]\sigma L\right). \tag{1.13}$$

This important relationship is the fundamental basis of absorption spectrometers. Two important components of absorption spectrometers – light sources and detectors – are discussed next, followed by an introduction to variations in technique.

1.3 Laser sources

The fundamental characteristics of lasers make them ideal light sources for precise spectroscopic measurements. The stimulated emission is directional and nearly monochromatic, and commercial sources often output high powers with efficient conversion of wall-plug energy. The emitted frequency and linewidth can often be tuned by the user, providing flexibility for a range of measurement methods that may be used for varied applications. It is also desirable to have cheap, compact, room temperature-operated, and stable sources.

Much of the vast collection of previous work on laser spectroscopy-based gas measurements has relied on laser sources emitting in the visible (400 – 750 nm) or near-infrared (750 – 2000 nm). Lasers emitting in the 1310 – 1550 nm region, in particular, are prevalent in telecommunications and consumer electronics, as well as industrial and domestic sensors, so their development has been of great commercial interest. Cheap, robust, compact systems are readily available for these wavelengths, and the optics and detectors are correspondingly well-developed. For absorption spectroscopy, however, the mid-infrared region (2 – 10 μm) has great potential for trace gas sensing. Absorption cross-sections are larger in this region, making it easier to sensitively detect very small concentrations of a target molecule. As Figure 1.4 shows in Section 1.3.4, this region covers many fundamental stretch and bend vibrational modes; at room temperature, gases are typically in their ground vibrational state making N_1 in Equation 1.11 large and the likelihood of absorption high. Excellent selectivity can be achieved due to the greater separation of transitions and narrower Doppler linewidths. From a more pragmatic perspective, detectors in this region are not affected by stray light, and long-wave radiation is less harmful to human eyes due to absorption at the cornea (whereas near-infrared and visible can penetrate to the retina).[9]

There are some drawbacks, mainly due to the lower energy of the radiation. Detectivity is intrinsically limited by the low photon energy, and detectors often require active cooling to counteract thermal variations. Optics are harder to source as typical materials (*e.g.* quartz) absorb infrared light. However, with the increasing use of mid-infrared sources, the optics and detector technology are expected to continue to progress as new materials

are developed. Despite these challenges, mid-infrared absorption spectroscopy is still very attractive for trace gas detection. The introduction of new laser sources in this region makes it an exciting area of research, both in building application-based spectrometers and for studying the fundamental physics of the sources.

1.3.1 Gas, chemical, & free electron lasers

In past decades, a variety of light sources have been used to generate mid-infrared radiation. A summary of the main sources available in this spectral region is given here, though the use of many of these systems has declined in recent years and become obsolete due to continued technological progress.

The earliest infrared lasers were gas and chemical lasers. These are only tunable within the vibrational bands of the excited molecule, making them useful over small, fixed regions of the mid-infrared region. CO_2 lasers, still commonly used in surgery and industrial etching, emit around 10.6 or 9.6 μm depending on the transition used.[10] The former is more commonly used, as this is based on the relaxation from the first excited state ν_3 (asymmetric stretch) to the first excited state of ν_1 (symmetric stretch).[10] The lower wavenumber transition is based on a different transition involving excitation of the ν_2 bending vibrational mode. All rotational states are involved in the light amplification. The laser properties can be changed by adjusting the pressure of the gas in the laser cavity and the buffer gas mixture used. For example, adding N_2 increases the number density of molecules in the upper state (of the 10.6 μm transition) while He atoms aid depletion of the population in the lower state, both of which increase the population inversion required for laser action.[11] Due to the high quantum efficiency of excitation and high pumping efficiency, CO_2 lasers are some of the most powerful commercially available and many achieve continuous wave (cw) powers of 10s of kW. This makes them very useful for applications requiring a high intensity – such as surgeries – however use in high resolution spectroscopy is limited by the relatively broad linewidth and discrete wavelength selection. Even at low pressures, the emitted linewidth is limited by the Doppler broadening of the molecules, which is about 50 MHz at room temperature.[10] CO gas lasers are very similar to their sister CO_2 gas laser,

however these emit around 5 μm and require cryogenic cooling.[10,11]

Fluoride-based chemical lasers can produce extremely high infrared powers but have limited utility. HF lasers emit in the 2.7 – 2.9 μm window where strong CO_2 absorption limits any open-path applications. DF lasers, on the other hand, emit at 3.8 μm and can be used for applications requiring long-range, open-path transmission.[11] Since the reactions involved in the lasing mechanism require highly corrosive F_2, DF lasers have been developed primarily for military purposes. Notably, the US Navy developed a DF laser-based weapon that can emit over 2 MW of power for several seconds.[12]

Free electron lasers are powerful sources for electromagnetic radiation from the vacuum UV to far-infrared but require large facilities and are costly to operate. These lasers, similar to particle accelerators, use strong magnets to accelerate an electron beam. A periodic variation of the magnetic poles – an arrangement termed the "wiggler" – causes the electrons to accelerate in the transverse direction, which results in emitted photons.[10,11] Despite the high cost and poor efficiency, they do fulfil the need for high power, far-infrared light (10^2 μm region) where many polar molecules have unique spectral signatures.

1.3.2 Diode lasers

Semiconductor materials can be used as laser gain media. In semiconductors, the highest occupied electronic level (valence band) and lowest unoccupied electronic level (conduction band) are separated by a characteristic energy band gap (ΔE). When a semiconductor lattice is doped with elements from nearby groups, the properties of the material can be altered quantitatively. Doping changes the Fermi level of the semiconductor, a thermodynamic property defined as the highest occupied energy level at absolute zero temperature that describes the ease by which electrons can thermally populate the conduction band. Essentially, doping introduces impurities that increase the electronic energy levels near the conduction band (n-type) or increase the availability of holes in the valence band (p-type). When a forward-biased voltage is applied across a p–n junction, the electrons and holes continuously recombine at the junction and a current flows from the p-type towards the n-type material. By tuning the band gap at the interface and the voltage applied, energy can

be released from the electron-hole recombination in the form of photons with the desired wavelength. Light-emitting diodes (LEDs), based on this simple mechanism, are ubiquitous in products ranging from consumer electronics to household appliances.

1962 was a landmark year for laser science with the demonstration of the first diode laser at GE.[13] In order to turn the diode into a laser, the p–n junction is placed inside a Fabry-Pérot optical resonator so that photons emitted will bounce back-and-forth, stimulating coherent emission as the recombination across the band gap continues. Within only a few years, many laboratories across the globe were working on diode laser technology. The next notable step in innovation occurred in 1968 when the first successful double heterostructure laser was demonstrated.[14] Unlike the earlier homostructure devices, the double heterostructure includes a thin active region layer of a different semiconductor material in between the p- and n-type layers that forms a wave guide to contain the free electrons and holes and enhance stimulated amplification. These devices are characterized by low threshold currents due to effective wave guiding by the cladding material and small band gap in the active region compared to the cladding, leading to fewer losses in the wings.[14,15] The initial work was based on GaAs; as with other III-V semiconductors, these band gaps were limited to photon energies in the visible and near-infrared. Commercial interests in the telecommunications sector pushed the development of diode lasers in the 1310 – 1550 nm region. Quite quickly, however, a new branch of the field emerged focussing on lead-based IV-VI semiconductors emitting in the 4 – 10 μm region.[11,16] Lead-salt lasers were the established mid-infrared laser source for many decades, however the cryogenic cooling requirement for cw operation was never overcome and they have since become very nearly obsolete. Effective cooling becomes increasingly vital for longer wavelengths where the energy band gap decreases and becomes comparable to the thermal energy.

1.3.3 Optical parametric sources

Ultimately, diode lasers have not become an ideal source of mid-infrared light for spectroscopy due to limitations on the material and operating temperature: increasing doping to extend the wavelength range increases Auger (non-radiative) recombination; and the

small band gaps required for longer wavelengths imposes limits on the maximum operating temperature, well below room temperature for cw lasers. For several decades, tunable mid-infrared radiation was produced instead by shifting the wavelength of near-infrared or visible sources using non-linear optical methods. Optical parametric oscillators (OPOs) and difference frequency generation (DFG) – a type of optical parametric amplification – have been the most common non-linear techniques for this region. Optical parametric processes, in general, involve amplification of a signal beam (ν_S) from a strong pump beam (ν_P) with momentum conserved by the simultaneous generation of an idler beam (ν_I). The frequencies must obey $\nu_I < \nu_S < \nu_P$. DFG is, as the name suggests, the generation of an idler beam at a frequency that is the difference of input signal and pump beams.[17,18] The power of the output beam, proportional to the powers of each of the inputs, can reach up to 100s of μW in a well-aligned system with 100s of mW of input power.[19,20] The wave mixing occurs in a non-linear crystal, usually made of periodically poled lithium niobate (PPLN) crystal, where the pump and signal fields must be phase-matched. The PPLN crystal is only transparent to wavelengths up to 4.6 μm and therefore does impose some spectral limitation, although other non-linear crystals can be used to produce light at higher wavelengths.[21]

OPOs use a non-linear dielectric material to split the pump energy into photon pairs. Theoretically, an infinite combination of frequencies can be produced from a given pump input, however tuning the phase-matching conditions allows the selection of a single pair of frequencies. OPOs use a resonator to pass the pump beam through the crystal many times in order to maximize the output signal power. The resonator can be used to selectively output only the signal beam if the path length is resonant with the signal frequency but non-resonant with the pump and idler. Fibre-based OPOs have been demonstrated to output powers of up to a few Ws in pulsed or cw mode.[22–24] Although both techniques allow the flexibility of producing high quality beams within a large spectral region using readily available near-infrared and visible sources, the systems are complex and difficult to incorporate into field-ready instruments.

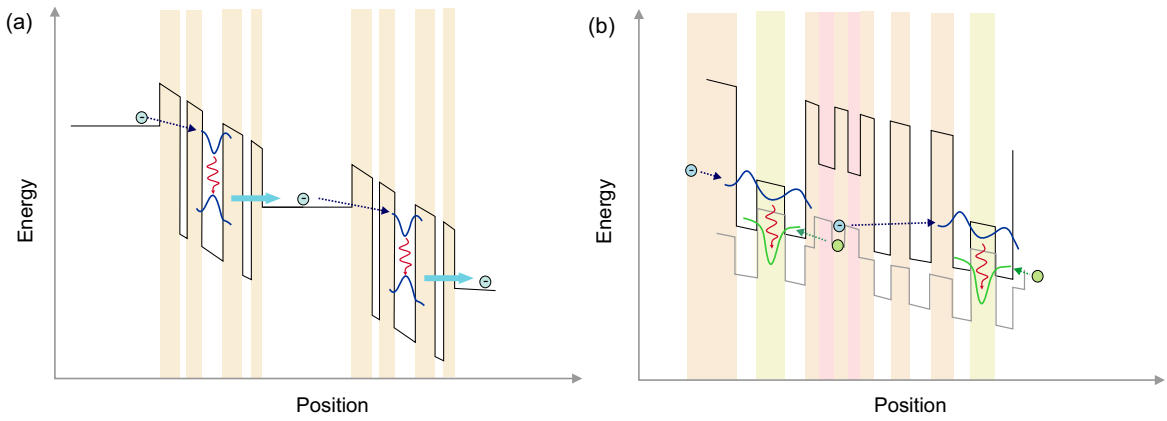

Figure 1.3: (a) Schematic showing two active regions in an intersubband QCL. A voltage is applied across the semiconductor layers (indicated by different-coloured shading), causing electrons (blue circles) to relax radiatively (red arrow) in the active region from an upper to lower state within the same band. Usually there is a third energy level below the lower one to encourage depletion and thereby maintain population inversion. The electrons then tunnel through the injector region (dashed arrow) before coming to the next active region. (b) A similar schematic for ICLs showing the radiative recombination of electrons (blue) and holes (green) in the W-shaped potential well of the active region. The electrons then tunnel through the injector region. The ICL generally includes more variations of doped semiconductor material to achieve the required potential surfaces, as shown by the multiple shaded regions.

1.3.4 QCLs

Fortunately, a different semiconductor laser was developed to meet the mid-infrared challenge. Kazarinov and Suris first proposed the idea of intersubband semiconductor transitions in 1971.[25] Intersubband lasers generate photons *via* an electronic relaxation within the conduction band rather than electron-hole recombination across the energy band gap. In order for this mechanism to produce the required photon densities, many of these intersubband transitions occur in series across the semiconductor chip, causing the electrons to "cascade" down a stairway of potentials when a voltage is applied. The actual realization of the device, however could not be achieved until molecular beam epitaxy methods for precise semiconductor layering had improved. Jérôme Faist and co-workers at Bell Laboratories demonstrated the first mid-infrared quantum cascade laser (QCL) emitting at 4.2 μm in 1994.[26] Progress was rapid with the first cw QCL operational the following year, room temperature pulsed lasers introduced in 1996, and cw, room temperature lasers produced from 2001.[27–29]

Figure 1.3 (a) shows a schematic of the QCL chip, a repeated pattern of semiconductor

layers broadly classified as active and injector regions. In the active region, which can be described using a simple three-level system, electrons first radiatively relax between subbands with the photon wavelength dependent on the energy separation E_{32}, followed by a non-radiative relaxation to a lower state. The E_{21} energy is similar to the phonon resonance, making the time constant of this relaxation (τ_{21}) on the order of only 300 fs. This ensures that the lower state of the radiative transition remains depopulated in order to maintain a population inversion. The electrons then proceed into the injector region where they tunnel through a series of minibands and are injected into the upper state of the next transition. Typically this process is repeated 20 – 30 times in a single chip, which requires up to 1000 separate layers to be fabricated with thicknesses ranging from 0.5 – 10 nm. The minibands of the injector region allow greater current flow in order to enhance the potential output power of the device. The wavelength emitted can be tuned somewhat by changing the current applied across the chip, but the main determinants are the thickness and composition of the semiconductor layers. Typically mid-infrared QCLs contain InGaAs/AlInAs or GaAs/AlGaAs combinations.[30] Continued progress in QCL technology has extended the coverage from 3 to about 15 μm, which covers many important vibrational bands where other semiconductor lasers are unavailable as shown in Figure 1.4, though losses increase at longer wavelengths.

Quantum cascade laser devices can broadly be grouped into three types based on the wavelength selection mechanism: Fabry-Pérot, distributed feedback (DFB), and external cavity (EC). For Fabry-Pérot lasers, the simplest type, a resonator is formed in the wave guide material by cleaving and polishing the chip faces. While these lasers can produce high powers and have been successfully used for gas sensing, multimode emission makes them unattractive for high resolution trace gas spectroscopy.[32] DFB-QCLs are fabricated with a distributed Bragg reflector on the top surface of the chip formed by alternating the thickness of the top layer material. Due to the interference of reflections off the reflector, only one wavelength within the gain spectrum of the chip experiences constructive interference and is emitted. The emission linewidth from DFB lasers is typically quite narrow and becomes limited in practice by the stability of the applied current to $\leq$ few MHz. The Bragg grating

and gain medium have different temperature dependencies, limiting the range of frequencies that can be produced by a single DFB-QCL chip to typically 10 cm^{-1}. This means multiple lasers may be required for multiple gas measurements. Conversely, broad tunability is an advantage of EC-QCLs, which use an external grating system for wavelength selection, and can cover > 100 cm^{-1}. Mechanical tuning of the grating is limited to rates ≤ 1 kHz; rapid modulation with small (up to a few cm^{-1}) frequency excursions can only be applied *via* the driving current. The laser chips are capable of emitting a broad range of wavelengths since active regions within the same chip can have different structures without interrupting the electron cascade. Due to the added complexity of the external piezo-mounted grating and mirrors these lasers tend to be quite costly, and their linewidths (≤ 20 MHz) are typically broader than DFB systems. All types can be used for cw or pulsed emission, though the trace gas sensing applications explored in this work utilized only cw systems.

Single mode, cw DFB and EC-QCLs have many characteristics that make them ideal

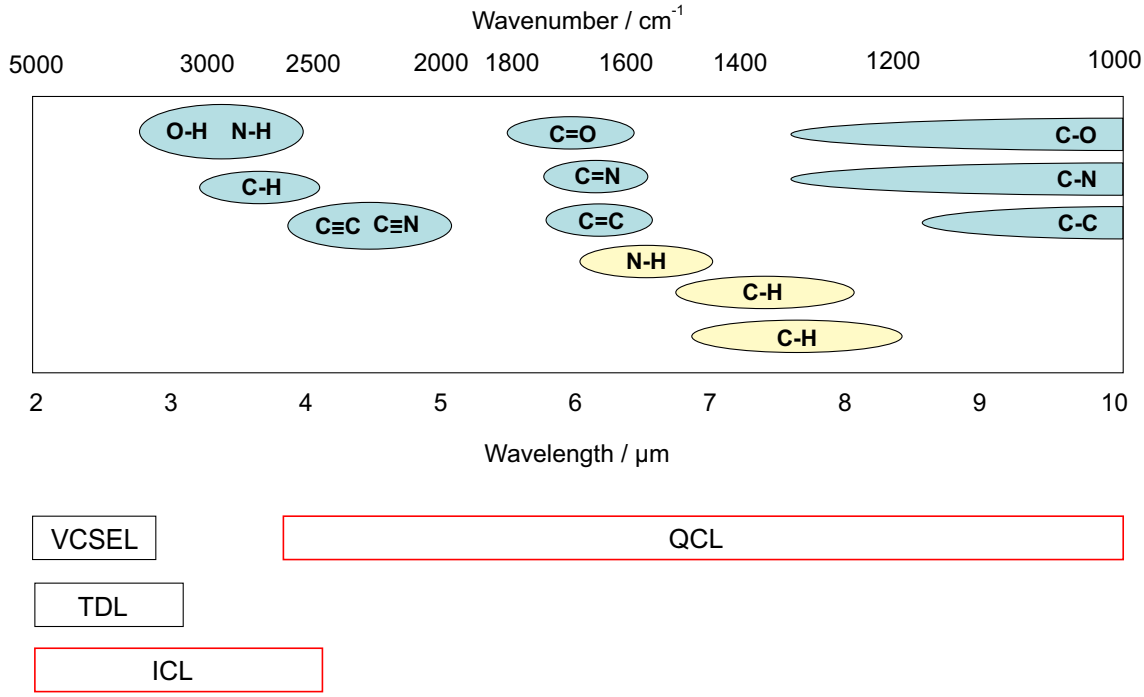

Figure 1.4: Schematic of typical frequencies for vibrational modes involving common groups adapted from Waynant *et al.*[31] Stretching vibrations are indicated in blue, while fundamental bending modes are in yellow. Below are the regions currently covered by commercially-available laser systems. Absorption spectroscopy based on ICLs and QCLs, indicated in red, is included in this thesis. Note: TDL = tunable diode laser; VCSEL = vertical-cavity surface-emitting laser.

sources for mid-infrared spectroscopy and are attractive alternatives to gas lasers or non-linear systems (see Table 1.1). Unlike diode lasers, QCLs have a single charge carrier mechanism (*i.e.* only electrons instead of electrons and holes). This eliminates broadening due to spontaneous recombination, and so QCLs intrinsically have narrow linewidths (gain spectra) typically on the order of a few MHz without any active stabilization.[33,34] The primary fundamental limitation is phonon broadening, though in practice noise on the laser drivers determines the laser linewidth.[35] Linewidths as low as 5.6 Hz have been achieved by beating two QCLs locked to optical cavities, though even simply locking a single laser to a transition or cavity has been shown to decrease the linewidth to 10s of kHz.[33,36,37] Thanks to rapid improvements in design, commercially-available lasers can emit hundreds of mW of power while operating at room temperature or with a simple thermoelectric cooling system. The lasers are compact – the chip itself is only on the order of a few cubic millimetres. The light is linearly polarized when emitted from the semiconductor chip edge with an astigmatic divergence that can easily be rectified using an aspheric lens for collimation.[38] The intersubband transition mechanism makes it possible to fabricate broadband QCLs with different layers; unlike interband semiconductors, the intersubband transition does not absorb at the high (or low) frequency end of its gain spectrum and the unipolar mechanism facilitates cascading even through different active regions.[39] Short wavelength QCLs ($\leq$ 4 μm) are limited, particularly at room temperature, by the requirement for a very high conduction band offset, and the development of different layer compositions has only recently been shown to produce QCLs with output wavelengths down to 3 μm.[40,41]

1.3.5 ICLs

Commercially-available QCLs are still limited at short wavelengths ($<$ 4 μm), which has left a gap in the semiconductor market between about 2 – 4 μm, a key spectral region for many hydrocarbons as shown in Figure 1.4. The introduction of interband cascade lasers (ICLs) filled this gap between QCLs and near-infrared diode lasers in the 2.7 – 5.5 μm window.[42] This makes them ideally suited for probing important C-H stretches in the 3 μm spectral region. First proposed in 1995, ICLs are still a nascent technology and only recently became available with single mode cw output and room temperature operation.[43–46] The

Table 1.1: Key features of light sources commonly used for high resolution infrared spectroscopy. Lead salt solid state lasers, though used widely in previous years, have become obsolete due to the requirement of cryogenic temperatures for cw operation.
* *Values often limited by drivers*
† *Beams are intrinsically divergent, however optics can be inserted near the laser facets to minimize this effect*
‡ *This is the Doppler linewidth at room temperature – the linewidth of specific lasers will depend on the pressure of the gas mixture used*

	QCL	ICL	CO_2	DFG/OPO
Output power	>200 mW (DFB)	3 mW (DFB)	100 kW	1 mW
Linewidth	< MHz*	< MHz*	60 MHz‡	1 MHz
Single mode	✓	✓	✓	✓
Tunable wavelength	✓	✓	X	✓
Low noise	✓*	✓*	X	✓
Good beam quality	✓†	✓†	✓†	✓
Fast modulation	✓	✓	✓	✓
Room temperature	✓	✓	✓	✓
Compact size	✓	✓	✓	✓
Cost	£4,500	£10,000	£15,000	≥ £10,000

lasing mechanism is essentially a hybrid between QCL and diode technology. As for diode lasers, the photons are emitted upon the recombination of an electron-hole pair across a band gap. These type II semiconductors are sometimes referred to as "W" diode lasers due to the unique shape of the potential in the active region, shown in Figure 1.3 (b).[47,48] However, as for QCLs, a series of potential wells in series are used to stimulate laser emission. The current state of technology does limit room-temperature (or thermoelectrically cooled), single mode, cw DFB-ICLs to output powers in the few mW range. Small-scale commercial production of these lasers is maturing and active research in the area promises significant improvements in power and stability – and decreases in cost – in the coming years.

1.4 Detection

Detection is clearly a key component of absorption spectroscopy. A good detector for gas absorption spectroscopy measurements must be able to detect mid-infrared photons at low photon-densities and have a fast response time.

Optimal detector performance can be characterized by a number of parameters.[11] The

simplest perhaps is the quantum efficiency (η), which is the ratio of the charge carriers produced per photon absorbed. A large η ensures that small photon number densities will still produce a sufficient current to be measurable above baseline noise. This can be converted into a current per photon energy value, termed the responsivity ($\mathcal{R}^*$):

$$\mathcal{R}^* = \frac{e\eta}{h\nu}. \tag{1.14}$$

For measurements requiring high time resolution, it is necessary to also have a fast response time, or rise time, so that the finite time delay between signal change and measurement is as short as possible. This is related to the bandwidth of the detector, such that detectors with fast response times will have large bandwidths (Δf). The detectivity (D^*) of a detector takes this factor into account:[11]

$$D^* = \frac{V_s}{V_n} \frac{1}{I\sqrt{A\Delta f}} \tag{1.15}$$

where V_s and V_n are the voltage amplitudes of the signal and noise, respectively, I is the incident optical field intensity, and A is the detector area. Detectivity and response times of detectors used in this work are given in Table 1.2.

1.4.1 Detectors

For studies requiring sensitive detection, photovoltaic devices are the most common mid-infrared detectors. These are a type of photodiode that work essentially as the reverse of a diode light source: a photon impinging on the semiconductor surface causes an electron to jump from the valence to the conduction band at a p–n junction, which is detected as a change in electric potential across the chip.[11] The devices are generally run with a reverse bias across the junction, meaning a positive voltage on the n-type side, for a more linear response. The band gap determines the spectral limit of the device – the energy of the photon absorbed must be greater than the band gap in order to be detected. Mercury cadmium telluride (MCT) is the most common semiconductor material used for mid-infrared detection as the amount of Cd doping in the alloy allows band gap tunability over the 1 – 25

Table 1.2: Manufacturers' specifications for detectors used in this work. Data for MCT detector applies to $\lambda = 8$ μm.

Detector	Wavelength	Detectivity	Response time
PVMI-3TE-10.6 (VIGO)	1–11 μm	1.8×10^9 cm Hz$^{-1/2}$ W^{-1}	≤ 3 ns
PVI-2TE-6 (VIGO)	2–7 μm	3.5×10^9 cm Hz$^{-1/2}$ W^{-1}	≤ 15 ns
PVI-2TE-4 (VIGO)	2–4 μm	3.3×10^{11} cm Hz$^{-1/2}$ W^{-1}	≤ 20 ns
WinCamD-FIR2-16-HR (DataRay)	2–16 μm	NA	16 ms
MCT J15D12-M204-S01M-10-CAF2 (EG&G)	2–12 μm	1×10^{10} cm Hz$^{-1/2}$ W^{-1}	0.5 μs

μm spectral range. Although AC and DC MCTs often require liquid N_2 or water cooling, room temperature devices are also available.[49]

Beam imaging in the mid-infrared can be achieved with bolometers. A bolometer contains a sensing surface composed of a material with a high temperature coefficient of resistance, which means the potential across the detector is highly dependent on temperature.[11] An array of individual, temperature-dependent pixels allows imaging of the beam's spatial profile. These devices have a much slower time constant compared to photovoltaic devices and are more susceptible to thermal disturbances. They are, therefore, typically used for analysis of beam quality rather than for measuring signal intensity. Characteristics of specific detector models used in this thesis are given in Table 1.2.

1.4.2 Quantifying sensitivity

Consistently, accurately, and precisely measuring spectra is a constant battle against numerous sources of noise and errors. It should be noted here that, for semiconductor lasers, the amplitude and laser frequency are interrelated so deviations of one will also be manifest to some extent in the other. White noise or slow drifts of laser output can be introduced through any of the devices that control the laser, including the current and temperature drivers and signal generators. Mechanical or acoustic disturbances from nearby laboratory equipment, particularly the vacuum pumps required for many experiments, can also contribute a source of random noise. Any time-dependent alteration of the sample – for example leaks from a sample cell or temperature fluxes – will limit the value of averag-

ing data and may result in inaccurate measurements. The detector signal may drift over time as the sensing elements warm up, thereby adding its own white electrical noise to the output; mid-infrared detectors are especially susceptible to voltage changes caused by thermal fluctuations due to the necessary low band gaps. Though not a type of noise *per se*, the acquisition bandwidth is often a significant limitation to optimizing the system due to processing times, finite sampling rates, and bit noise from analogue-to-digital conversion.

Countless ways of assessing sensitivity for trace gas measurement are reported in the spectroscopy literature with different authors favouring different ways of quantifying the quality of their methods. There is no universal way to quantify the sensitivity and stability of measurements, however determining a set of values that assess different uncertainties, such as those listed in Table 1.3, can provide a fairly complete picture of the potential of a technique and quality of a measurement.

The Allan-Werle variance analysis is a widely accepted way of assessing temporal stability and identifying contributions to uncertainty – indeed, it is almost taken for granted in the spectroscopy community that an Allan-Werle variance plot will be presented when reporting on a new study. This statistical method was first introduced in the field of atomic clocks with a paper by David Allan in 1966.[50] In this article, he laid out the fundamental idea: the variance of a measurement – in this case of oscillator frequency – is determined for a range of averaging times and plotted on a log–log scale. Nearly three decades later, Werle *et al.* applied this principle to tunable diode laser absorption spectroscopy.[51] In this seminal work, the authors proposed using Allan plots to identify different sources of noise and identify the optimal averaging time for gas concentration measurements.

Different types of noise will show different averaging time dependence, as shown in Figure 1.5. For an ideal measurement when random white noise is the only source of uncertainty, the variance decreases linearly with averaging time on the log-log scale due to the relationship $\sigma^2 \sim \tau^{-1}$ for frequency-independent noise. Any $1/f$ frequency-dependent noise will contribute a constant variance with no averaging time dependence. An upward slope on the plot for longer averaging times indicates drifts in the system and may create a turning point in the plot that limits the optimal averaging time for minimum variance.

Table 1.3: Definitions and units of commonly quoted sensitivity values.

Sensitivity value	**Symbol**	**Units**
Minimum detectable concentration	c_{min}	ppm (or similar)
Minimum detectable absorption coefficient	α_{min}	cm^{-1}
Minimum detectable absorption	MDA	[unitless]
bandwidth normalized		$Hz^{-1/2}$
Standard deviation (Allan-Werle)	σ_{AW}	[intensity units]
Residual of fit	σ_{res}	[unitless] or cm^{-1}
Noise equivalent absorption sensitivity	NEAS	$Hz^{-1/2}$ cm^{-1}

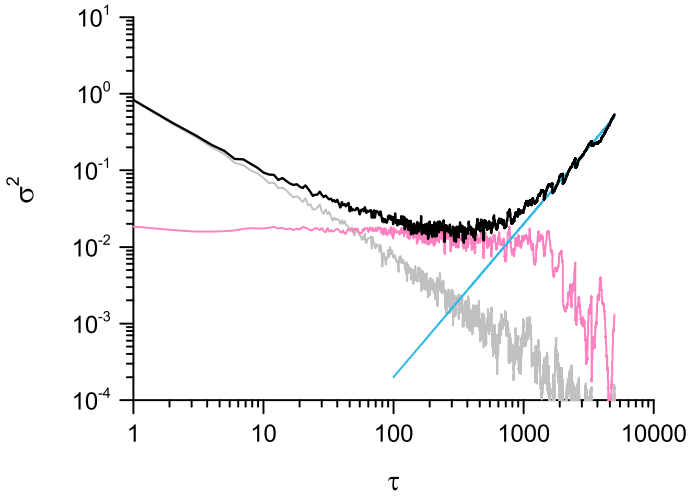

Figure 1.5: Sample Allan-Werle variance plot with the normalized signal variance (black) calculated as a sum of white noise (grey) and $1/f$ noise (pink), as well as long-term drift (blue).

In laser spectroscopy, the Allan-Werle analysis is a commonly-used statistical tool at many stages of an experiment. New lasers, laser current drivers, and detectors are subjected independently to Allan-Werle tests to ensure that the output demonstrates only low-level white noise over extended time periods without any drifts that will impact experimental measurements. When an experiment is set up for measuring gas concentration, the optimal signal averaging time can be determined by either analysing the variance of the measured signal amplitude or the calculated concentration of the gas. This can often help identify ways to improve the experiment.

Allan-Werle variance analysis only demonstrates the stability of the system and is not a true representation of the accuracy or precision of the method. For example, a consistent etalon feature on a baseline will increase the uncertainty of the spectral fit but will not

contribute to a variance dependent on averaging time. Therefore, it is also necessary to quantify the quality of the fit and signal-to-noise ratio (SNR) of the measurement.

One common way to report sensitivity is by the minimum detectable absorption (MDA), which is simply the 1σ value of a specified fit to absorption data (σ_{res}) for a stated averaging or acquisition time.[52] A bandwidth-normalized value is an even more rigorous way of defining the sensitivity – in this case, the MDA is normalized to the limiting bandwidth of the system. In most cases, the limiting bandwidth is determined either by the data sampling (acquisition) rate or the operating bandwidth of the detector. Performing identical experiments with two different detectors may give different MDA values if the bandwidths of the two sensors are very different, which accounts for the signal being smoothed out when using low bandwidth detection. Typically, bandwidth-normalized values are called "noise equivalent".

In the analyses presented here, $1\sigma_{\text{res}}$ values of absorption spectra measurements are determined using a non-linear fit, unless otherwise indicated. The data (y) are fit to an appropriate function (y^o) – typically a Voigt profile as noted in Section 1.2.2 – and the residual of the fit determined ($|y^o - y|$). As is typical in non-linear variance analysis, the standard deviation (σ_{res}) takes into account the number of degrees of freedom of the fit, which is equal to the number of data points in the fit (n) less the number of fitting parameters that can be changed in the fitting routine (n_{fit}):[53]

$$\sigma_{\text{res}} = \left(\frac{\sum_{i=1}^{n} (y_i^o - y_i)^2}{n - n_{\text{fit}}} \right)^{1/2}. \tag{1.16}$$

When an instrument is designed for a specific application, or at least for a specific target molecule, the scientist making the measurement mostly cares about whether it is capable of measuring sufficiently low concentrations for a particular study. Therefore, a minimum detectable concentration (c_{min}) is a practical value to report. This is only useful when comparing techniques that measure the same gas molecule; since each species will have different cross-sections in a given spectral window, the same MDA may result in different c_{min} values for different gases.

1.5 Techniques

In its most basic form, a laser absorption gas measurement involves the laser source, a sample cell, and a detector. As the laser frequency is scanned, the intensity reaching the detector will decrease relative to the amount detected without the presence of the absorbing gas, and the Beer-Lambert law (Equation 1.13) can be applied. This basic method is suitable when a large volume fraction of the target species is present and the laser frequency excites a transition with a large cross-section. In many scenarios, however, there is only a small amount of the target species present, which means there will only be a small change in the signal intensity on the detector and the signal-to-noise ratio of the system may be insufficient to accurately measure a concentration. Therefore, trace gas species measurements often require more advanced spectroscopic techniques.

1.5.1 Long distances

There are two ways to increase sensitivity: increasing absorption signal or reducing the noise on the signal. The value of σ is limited by the transitions accessible to the laser free from complications arising from interference with absorption from other species. Since the concentration is the independent variable, the only additional adjustable parameter to change in Equation 1.13 is the path length; the method by which the path length is increased varies on the application and environment.

In atmospheric chemistry, it is possible to collect the laser beam after it has travelled kilometres through the air. Light detection and ranging (LIDAR) was initially developed to take long distance meteorological measurements.[54] Since then it has proven to be an extremely important tool in a wide variety of fields from seismology to archaeology to public safety. LIDAR, also known as laser radar, uses echoes – reflections of laser light – to determine distances and properties of targets far away in the same way that sonar (sound waves) and radar (radio waves) work. While gases do not effectively reflect light, simultaneous measurements at two different wavelengths can be used to semi-quantitatively resolve concentrations of a particular species.[55]

In most cases, however, it is not practical or possible to make measurements along a straight path of such long distances. Multipass cells offer one option for enhancing optical path length within a compact system. These systems use special configurations of mirrors to reflect light through the sample several times before being detected. One of the earliest incarnations of this type of system was the White cell, introduced in 1942.[56] A single large spherical mirror is placed opposite a pair of smaller spherical mirrors in such a way that a beam directed past the edge of the single mirror onto one of the pair will bounce back-and-forth several time before exiting past the opposite edge. Small adjustments to the mirrors allows easy tunability of the number of passes, and thus the path length, within the sample volume. This type of cell is still widely used for modern laser absorption spectroscopy. A similar system developed in 1965, called a Herriott cell, uses only two spherical mirrors but operates on a similar principle.[57] The beam, in this case, enters and exits through a hole in the centre of one mirror, and the number of passes is controlled by the mirror separation.

Multipass cells using cylindrical mirrors are an attractive alternative due to their compact size and easy path length tunability. The beam enters and exits through central holes in the opposing mirrors, and a dense optical pattern of beam reflections can be tuned by both the relative rotation of the mirrors, as well as the separation distance.[58] The diminutive size of these systems, which can be small as a few cm^3, makes them particularly attractive for field and clinical applications. Absorption in multipass cells follows essentially the same behaviour as single pass absorption since successive passes do not overlap significantly in space. The total path length is limited by the number of discrete passes that can be traversed without overlap or a portion of the beam being clipped by the edge of the mirrors or entrance and exit holes; typical optical path lengths range from metres to hundreds of metres depending on the length of the cell and diameter of the mirrors.

Optical cavities are popular for sensitive absorption spectroscopy where even longer path lengths are desired. Briefly, an optical cavity is composed of a set of mirrors coated with a high reflectivity dielectric coating at the laser wavelength deposited upon a slightly transparent substrate. A small portion of an incident field will be injected into the cavity, and these photons will bounce back-and-forth along the same path many thousands or tens

of thousands of times on average before leaking out of the cavity through one of the mirrors. While cavity-based techniques have the added complication of interference of the intracavity field, it is quite common to achieve optical path lengths of kilometres on an optical bench. Chapters 3 – 5 discuss the theory and implementation of various cavity-based methods for trace gas sensing.

1.5.2 Modulation

If it is not possible or practical to increase the signal, SNR can be improved by reducing the noise. There are various sources of noise, as mentioned in Section 1.4. Averaging the signal decreases effect of white noise, however this is of limited value if the signal drifts or exhibits low frequency fluctuations. Another major contributor is $1/f$ noise, or pink noise, that increases for lower frequency measurements. There are many contributions to this, for example from interactions of current carriers, diffusion, or imperfections on the detector. This noise can be alleviated by applying a high frequency modulation to the laser; after demodulation of the signal, which can be accomplished electronically, the original signal is retrieved without interference from low frequency noise.

Frequency modulation spectroscopy (FMS) and wavelength modulation spectroscopy (WMS) are the simplest variants, with a single, high frequency voltage applied to the laser, in most cases *via* the driving current.[59] The detected signal is demodulated at the same frequency using a lock-in amplifier to produce a harmonic signal, which is effectively a first or higher order derivative of the original absorption signal. Absolute concentration measurements can only be made after the spectrometer has been calibrated or the experiment has been quantitatively modelled. Frequency and wavelength modulation techniques are discussed more comprehensively and examples given in Chapter 2.

Another modulation-based technique is photoacoustic spectroscopy (PAS).[60–62] This fascinating marriage of light and sound uses amplitude-modulated laser radiation to excite vibrations in a target molecule which manifest as temperature changes oscillating at the same frequency. Pressure waves in the gas are generated by the temperature fluctuations and picked up by a microphone or other sound-sensitive device. Recently, quartz tuning

forks, which are produced cheaply for watches and other commercial electronics, have been shown to be excellent, low-noise detectors for this technique in a variation called quartz-enhanced photoacoustic spectroscopy (QEPAS).[63,64]

Free radicals are chemically reactive species that are very important in kinetics and atmospheric chemistry. Faraday modulation spectroscopy (FAMOS) is a suitable method for selectively detecting molecules these molecules by exploiting characteristics of unpaired electrons.[65,66] In this case, an external magnetic field around the sample oscillates at a high frequency ($\sim$ kHz). This produces an oscillation in the measured light polarization when an appropriate absorbing molecule is present that can be demodulated using a lock-in amplifier.

Some of the best sensitivities achieved in trace gas sensing have been reported using noise-immune cavity-enhanced optical heterodyne molecular spectroscopy (NICE-OHMS). This technique takes advantage of the noise-reduction benefit of frequency modulation and the path length enhancement offered by optical cavities; by carefully selecting the modulation frequency, FMS can be performed inside an optical cavity, effectively eliminating signal amplitude noise.[67,68] NICE-OHMS does, however, require a rather complicated experimental set-up with precise electronics, and is generally only suitable for laboratory-based studies.

1.5.3 Alternative methods

Laser-based absorption spectroscopy is not the only trick up the metaphorical sleeve for trace gas measurements. Upon absorption of radiation, molecules may relax in a variety of ways. Radiative relaxation mechanisms, such as fluorescence, provide alternative measurement signatures. Laser-induced fluorescence has proven robustness for atmospheric field measurements.[69] Notably, the technique has been employed very successfully for *in situ* measurements of OH and HO_2 radicals in the troposphere.[70] Coherent anti-Stokes Raman spectroscopy (CARS) is another sensitive non-linear technique based on emission at the anti-Stokes frequency of a Raman-active transition stimulated by multiphoton absorption.[71,72] As this technique typically requires two or three high power, pulsed beams and

precise alignment conditions, it is unsuitable for many applications. Only gas molecules with strong Raman transitions or transitions with a high quantum efficiency for relaxation by fluorescence can be measured with these techniques, so their applicability is limited.

Mass spectrometry (MS) is the major rival methodology to optical techniques that uses molecular mass (m) and charge (z) rather than energy levels to identify samples. Whereas most sensitive laser-based spectrometers target a specific molecule, MS measures all species within the sample. This creates its own problems since fragmentation can lead to many species having the same m/z value within a given ionized sample. Additionally, established ionizing techniques were, for many years, not compatible with continuous, on-line sampling required for breath analysis and some *in situ* atmospheric measurements. The recent developments of selected ion flow tube mass spectrometry (SIFT-MS) and proton-transfer reaction mass spectrometry (PTR-MS) have now opened up this possibility.[73,74] These rely on soft chemical ionization, usually targeting specific types of molecules such as volatile organic compounds (VOCs), followed by transport in a buffer gas through a drift flow tube. Both techniques have been used with some success in real-world applications, including atmospheric and physiological measurements; indeed, PTR-MS has become a routine method for measuring VOCs in the atmosphere.[75–77] However, while the sensitivity of these techniques is high and continually improving, the instruments are still bulky, expensive, and require technical expertise to operate and interpret data.

1.6 Examples of applications

Mid-infrared spectroscopy has proven to be an important measurement technique that can be adapted across a wide gamut of gas sensing applications – an exhaustive discussion of all the fields utilizing the technique is far beyond the scope of this thesis. The breadth of research applications based on various types of mid-infrared spectroscopy with different light sources is testament to its growing importance. A few examples of gas sensing applications using mid-infrared laser absorption spectroscopy are listed here.

One of the main motivations for the development of very sensitive gas spectrometers is the need to understand the changes in atmospheric composition and properties as a result of

industrialization and a rapidly growing human population. Atmospheric gas measurements have focused on four areas: changes in composition, chemical reactions, identification of sources and sinks, and monitoring of air quality. For example, flux measurements of CH_4 isotopes using a DFB-QCL and multipass absorption cell provide information about sources, important for estimating uncertain CH_4 emissions.[78] Similarly, scientists demonstrated that more open, outdoor pig farms were a less significant source of CH_4 and N_2O compared to closed-in farms using manure slurries using a quantum cascade laser-based instrument.[79] Ground measurements are fairly straightforward, but measurements over larger areas and higher altitudes require launching the instruments on balloons, aircraft, or spacecraft where they must remain functional – without adjustment – while experiencing extreme mechanical disturbance and temperature changes. Lead salt tunable diode lasers and mid-infrared QCLs have been transported to the stratosphere on high-altitude balloon and aircraft for accurate measurements of CH_4 and N_2O profiles that would be impossible from ground-based observation[80–84]

Air quality is an important safety concern, especially where air is scarce. Recently, a tunable diode laser-based spectrometer was sent to the International Space Station to monitor O_2, CO_2, NH_3, and water vapour for crew safety.[85] Gas sensors are necessary to sniff out explosive materials, and are particularly useful for assessing people or objects metres away. For example, it is important to check vehicles for traces of explosives at security checkpoints – this motivation led to the development of an OPO-based spectrometer for detection of TNT, RDX, and other traces species commonly used for bomb-making.[86] The capabilities of mid-infrared spectroscopy to measure acetone, C_2H_6, CO, NO, NH_3, CH_4, COS, and CO_2 isotopes have already been demonstrated using various techniques, with many groups continuing to pursue research in this area.[87–92]

Gas sensors are not only used for passive monitoring. Semiconductor manufacturing requires precise control of levels of different components in plasma reactors. DFB-QCLs have been used to make continuous measurements of industrial plasma and actively control the amounts of C_4F_8 and SiF_4 in the chamber using mass flow controllers.[93] As a further example, the full potential of human breath analysis for medical diagnostics is only starting

to be realized.[94,95]

These are only a few examples that give a flavour of the wide variety of applications that have benefited from mid-infrared laser spectroscopy. There are numerous other applications where mid-infrared laser-based absorption spectroscopy may usurp other gas detection methods in the future from food safety to geology to forensics.[96–102]

1.7 Target gas species

Target gas species included in this thesis were primarily selected for their physiological or atmospheric relevance. Physicians and physiologists are increasingly appreciating the power of breath analysis for health diagnostics, and certain trace components of breath can serve as an early warning indicator of disease or can be used to track the effectiveness of treatment.[95] Atmospheric studies also rely heavily on trace gas detection, both for studying chemistry and transport in the troposphere and stratosphere, and for monitoring emissions for health or regulatory purposes. Key greenhouse gases (GHGs) that affect the radiative forcing of the planet have been identified, and quantifying sources and sinks is vitally important for predicting future changes to the climate and oceans.[103] Volatile gases, which must be tested at the source or in the laboratory, cannot be overlooked as products of reactions with other species may include GHGs and secondary pollutants. Detailed descriptions of the molecular properties and relevance of target species are included in subsequent chapters.

1.8 Outline of thesis

The thesis is divided into four chapters of results, grouped by methodology:

- In Chapter 2, frequency and wavelength modulation techniques are described. A 8.2 μm distributed feedback quantum cascade laser (DFB-QCL) is frequency stabilized using a LabVIEW program that generates an error signal to keep the laser frequency locked to a transition of CH_4 in a low-pressure reference cell. Long-term drifts in laser frequency were mitigated with this protocol, making this technique useful for measurements requiring long-term averaging. The second experiment used a 5.3 μm DFB-QCL to measure NO using frequency modulation spectroscopy (FMS). Despite

residual amplitude modulation distorting the measurement, the FMS signal could be fit to a theoretical model and demonstrated an improvement in signal-to-noise ratio compared to the direct absorption measurement.

- Chapter 3 delves into cavity-enhanced absorption spectroscopy (CEAS). A 5.3 μm DFB-QCL was used to measure CO_2 in an off-axis linear cavity arrangement. Residual mode structure, often the limiting factor determining sensitivity, was effectively removed by applying a broadband radio frequency perturbation to the laser driving current. The uncorrelated noise, supplied by a simple device introduced between the current driver and laser, broadened the apparent linewidth of the laser. This addition of noise both enhanced the sensitivity ten-fold compared to the unperturbed condition and made the system more robust. This broadband perturbation is more effective than the usual method of applying a single frequency perturbation as it both shows a greater enhancement in sensitivity and is more flexible for adaptation in a range of systems.

- After introducing the theory of optical-feedback cavity-enhanced absorption spectroscopy (OF-CEAS) with V-shaped cavities, Chapter 4 presents the first demonstrations of this technique with distributed feedback interband cascade lasers (DFB-ICLs) and an external cavity quantum cascade laser (EC-QCL). Experiments were performed with a 3.24 μm DFB-ICL at INP Greifswald and resulted in the first peer-reviewed publication of OF-CEAS with an ICL. Subsequent experiments in Oxford used a 3.29 μm DFB-ICL for measurements of several VOCs, and demonstrated improved sensitivity. OF-CEAS was also performed for the first time with a 5 μm EC-QCL. Although spectra of N_2O were measured with similar levels of precision, persistent mode-hopping of this early-generation laser prevented further study.

- The final results chapter, Chapter 5, combines theory and experimental data to demonstrate the use of a linear optical cavity for OF-CEAS trace gas measurements. Simulations of this new variation of OF-CEAS were developed that agree well with measured results. Spectra of CO_2 collected with a high power 5.3 μm DFB-QCL yielded an experimental sensitivity on par with the best V-shaped cavity QCL-based

systems. Since other cavity-based experiments can easily be converted to linear OF-CEAS systems, establishing the precision and robustness of this simple geometry may open the door for more groups to utilize this trace detection technique.

- Conclusions and future work are then presented in Chapter 6.

Chapter 2

Frequency Modulation: Laser Stabilization and Gas Detection

White, pink, violet, and grey noise – in any quantitative measurements, the challenge of differentiating true signals from a rainbow of systemic fluctuations is universal. In semiconductor-based devices, including lasers and detectors, performance is often limited by noise that scales with $1/f$, also known as pink noise. The magnitude of the fluctuations therefore decreases for higher signal frequencies. However it is not practical to increase the rate of laser scans indiscriminately as distortions and acquisition issues may arise if the laser is scanned too quickly over an absorption feature. Other tricks must be applied in order to increase frequency without affecting the accuracy of the measurements. One way of achieving this is to increase the frequency by applying a high frequency modulation to the signal for heterodyne detection.

Modulation can be applied in a number of ways, including at the laser source in frequency or amplitude variations,[59,104] on the sample itself with an oscillating magnetic field[65] or electric field[105], or by using an optical chopper to interrupt the signal.[106] By selectively measuring signal components at the applied modulating frequency, the desired absorption signature can be recovered with low frequency noise efficiently filtered out. The demodulation to select the right frequency components can be accomplished electronically using a simple demodulator, or in the case of quartz-enhanced photoacoustic methods, by a tuning fork resonant at the modulation frequency.[63] Lock-in amplifiers, as discussed below, are one

of the most powerful and versatile instruments available for phase-sensitive detection and Fourier component demodulation.

In this chapter, the general theory of modulation spectroscopy techniques is discussed and two experiments involving laser modulation of QCLs are described. In the first, a rapid laser frequency modulation allows derivative-like signals from a reference gas cell to be used to actively lock an 8.2 μm DFB-QCL and prevent drifts in emitted wavelength. Frequency modulation spectroscopy is demonstrated for detecting NO with a 5.3 μm DFB-QCL in the second.

2.1 Theory

2.1.1 Frequency modulation spectroscopy

Frequency modulation spectroscopy (FMS) is a type of optical heterodyne detection technique developed in the early 1980s.[107–109] Originally, the technique involved applying a phase modulation *via* an external modulator at frequency ν_m to a laser emitting at ν_c, the carrier frequency, to generate a pure frequency-modulated signal. As a reminder, throughout this thesis the convention used for frequency variables is: ν is frequency in Hz and $\tilde{\nu}$ is frequency in wavenumber (cm^{-1}). While similar modulation techniques had been well-established, FMS is distinguished by a radio frequency (RF) modulation that is significantly larger than the linewidth of the spectral absorption line.[109,110] The technique was extended to semiconductor lasers a few years later with modulation occurring initially *via* the injection current.[111,112] While it was convenient to apply modulation to the laser-driving current, this introduced an additional amplitude modulation coupled to the frequency variation. Despite this, with careful experimental execution, it was shown that semiconductor laser FMS could achieve shot noise-limited sensitivity for trace gas detection.[112–115]

The radiation field of the laser can be modelled as:[108]

$$E(t) = E_o \exp(i2\pi\nu_c t) \sum_{n=-\infty}^{\infty} J_n(M_\nu) \exp(i2\pi n\nu_m t) \tag{2.1}$$

where J_n are Bessel functions of the first kind. The laser linewidth ($\sim$ MHz) is narrower than

the modulation frequency, and can therefore be neglected in these calculations. When the modulation index (M_ν) is small ($M_\nu \ll 1$), J_n is negligible for $n > 1$ and the field consists of only one pair of sidebands. The application of an oscillation on top of an electromagnetic field with sinusoidally varying phase generates a pair of sidebands with frequencies of $\nu_c \pm \nu_m$ and with a π rads phase difference. If ν_m is sufficiently small, relative to ν_c, sidebands can be generated for harmonics of ν_m. By using a small modulation index, a single pair of well separated sidebands can be generated on either side of the carrier:

$$E(t) = E_o \left[\frac{-M_\nu}{2} \exp\left(i2\pi(\nu_c - \nu_m)t\right) + \exp(i2\pi\nu_c t) + \frac{M_\nu}{2} \exp\left(i2\pi(\nu_c + \nu_m)t\right) \right]. \quad (2.2)$$

Under the correct conditions, one sideband can probe the transition without interference from the carrier band.[109] Interactions between the field and absorber are defined by a dimensionless attenuation factor ($\delta = \alpha L/2$) and phase shift (ϕ), both frequency-dependent parameters:

$$\begin{aligned} E(t) =& E_o \left[\exp(-\delta_{-1} - i\phi_{-1}) \frac{-M_\nu}{2} \exp\left(i2\pi(\nu_c - \nu_m)t\right) + \exp(-\delta_0 - i\phi_0) \exp(i2\pi\nu_c t) \right. \\ & \left. + \exp(-\delta_1 - i\phi_1) \frac{M_\nu}{2} \exp\left(i2\pi(\nu_c + \nu_m)t\right) \right]. \end{aligned} \quad (2.3)$$

When the attenuation experienced by the sidebands is equal, the two contributions cancel since the sidebands are π radians out of phase. However, if the laser is scanned over an absorption profile, the sum is non-zero with a magnitude determined by the absorption coefficient and modulation index as depicted in Figure 2.1. The intensity of light incident to the detector, assuming weak absorption ($\delta_i \ll 1$), can be approximated as:[108,109]

$$I(t) = \frac{c|E_o^2|}{8\pi} \exp(-2\delta_0) \left[1 + (\delta_{-1} - \delta_1) M_\nu \cos(2\pi\nu_m t) + (\phi_{-1} + \phi_1 - 2\phi_0) M_\nu \sin(2\pi\nu_m t) \right]. \quad (2.4)$$

A few aspects of this result are worth commenting on. Firstly, there is a DC component independent of the modulation parameters in addition to two contributions which oscillate sinusoidally at the modulation frequency. Secondly, the sine term is proportional to the difference of the carrier phase compared to the average of the sidebands, while the cosine term

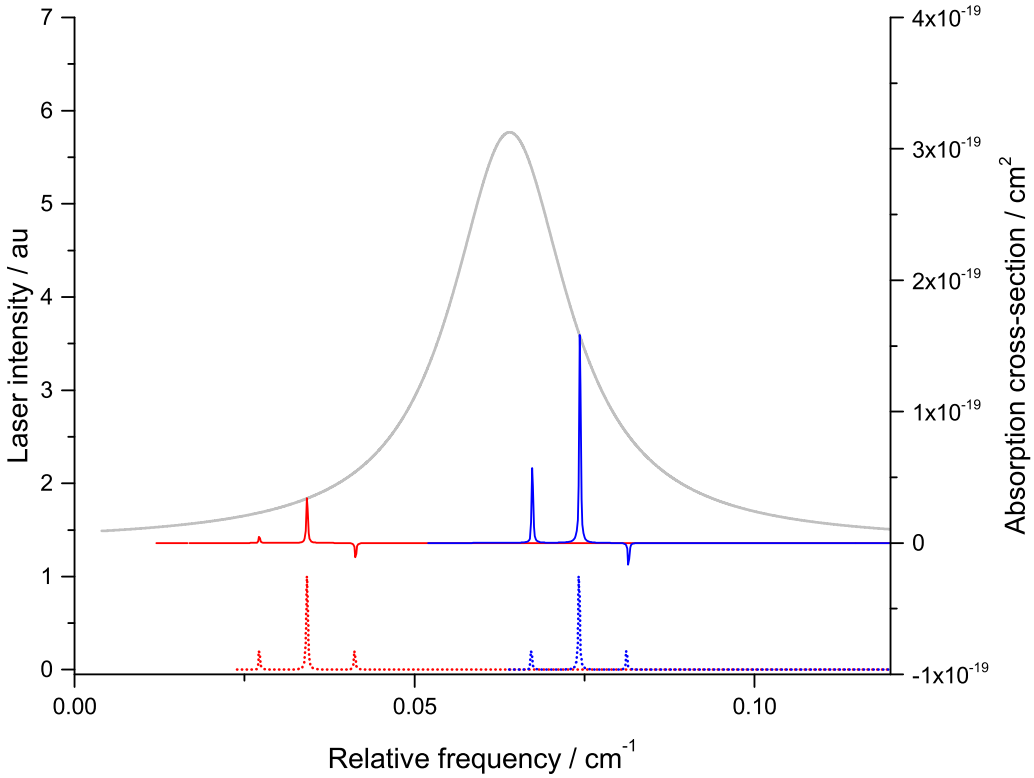

Figure 2.1: Schematic of simulated FMS. The intensity of the laser with one pair of sidebands is shown in dashed lines (corresponding to left-hand axis) at two different carrier frequencies. The laser emission is modelled as a Lorentzian function with a linewidth of 6 MHz. The frequency modulation occurs at 200 MHz with a modulation index of ~ 0.4. The grey trace (solid line) indicates a simulated molecular absorption profile with a linewidth of 0.021 cm^{-1} and integrated cross-section of 1×10^{-20} cm^2 cm^{-1}. The solid blue and red traces show the relative contributions of the sidebands for the two corresponding carrier frequencies.

is dependent on the difference in attenuation between the upper and lower sidebands.[108] These two terms represent the dispersion (D_{fm}) and absorption (A_{fm}) of the transition, respectively. Phase-sensitive electronics, such as a lock-in amplifier or demodulator, can be used to select the Fourier component of the signal at ν_m, or an integer multiple, as the laser carrier frequency is scanned.[110] In general, Equation 2.4 to be written simply as:

$$I(t) \propto A_{fm}(\nu)\cos(2\pi\nu_m t) + D_{fm}(\nu)\sin(2\pi\nu_m t) \tag{2.5}$$

where the absorption and dispersion terms are given by:

$$A_{fm}(\nu) \propto [\delta(\nu_c - \nu_m) - \delta(\nu_c + \nu_m)]\,; \tag{2.6}$$

$$D_{fm}(\nu) \propto [\phi(\nu_c - \nu_m) + \phi(\nu_c + \nu_m) - 2\phi(\nu_c)]\,. \tag{2.7}$$

Absorption and dispersion functions are related by Hilbert transforms.[116] In practice, one measures the in-phase (I_{fm}) and quadrature (Q_{fm}) signals, which are directly related to A_{fm} and D_{fm}:

$$I_{fm}(\nu) \propto [A_{fm}(\nu)\cos\theta + D_{fm}(\nu)\sin\theta] \tag{2.8}$$

$$Q_{fm}(\nu) \propto [A_{fm}(\nu)\sin\theta - D_{fm}(\nu)\cos\theta] \tag{2.9}$$

with θ representing the phase shift between the lock-in reference and detected signal. This represents the most simple case with a single pair of sidebands, no amplitude modulation, and weak absorption and dispersion. Under these conditions, absolute concentrations of a target gas can be determined by calibrating the system to determine the proportionality between A_{fm} and the measured signals.

The theory was later extended to the case when amplitude and frequency are modulated simultaneously;[59,111,114] this is typically true for current modulation of semiconductor lasers. In this scenario, the field is:

$$E(t) = E_o[1 + M_a\sin(2\pi\nu_m t + \psi)]\exp[i2\pi\,(\nu_c t + M_\nu\sin(2\pi\nu_m t))]. \tag{2.10}$$

M_a is the amplitude modulation index, and ψ is the phase shift between the amplitude modulation (AM) and frequency modulation (FM). Following a similar route as before, this

leads to the intensity on the detector being:[111,112]

$$\begin{aligned} I(t) =& \frac{c|E_o^2|}{8\pi} \exp(-2\delta_0)\Big(1 + [M_\nu(\delta_{-1} - \delta_1) + M_a(\phi_{-1} - \phi_1)\cos\psi \\ & + M_a(2 + 2\delta_0 - \delta_{-1} - \delta_1)\sin\psi]\cos(2\pi\nu_m t) \\ & + [M_\nu(\phi_{-1} + \phi_1 - 2\phi_0) + M_a(2 + 2\delta_0 - \delta_{-1} - \delta_1)\cos\psi \\ & - M_a(\phi_{-1} - \phi_1)\sin\psi]\sin(2\pi\nu_m t)\Big). \end{aligned} \tag{2.11}$$

In the case where $\psi = 0$, this can be simplified:

$$\begin{aligned} I(t) =& \frac{c|E_o^2|}{8\pi} \exp(-2\delta_0)\Big(1 + [M_\nu(\delta_{-1} - \delta_1) + M_a(\phi_{-1} - \phi_1)]\cos(2\pi\nu_m t) \\ & + [M_\nu(\phi_{-1} + \phi_1 - 2\phi_0) + M_a(2 + 2\delta_0 - \delta_{-1} - \delta_1)]\sin(2\pi\nu_m t)\Big). \end{aligned} \tag{2.12}$$

It is evident in this case that the absorption-free signal may be non-zero. Indeed, in some cases the residual amplitude modulation (RAM) leads to baseline signals that are much larger than that of the absorption.[59] The RAM can be minimized by optimizing the phase difference between the detector and phase-sensitive lock-in reference, although sensitivity is still limited by ψ.[114,117] RAM lessens the suitability of FMS for absolute trace concentration measurements as it introduces two extra parameters in the model and requires detectors with a large, linear dynamic range.

An alternative FMS method uses two modulation frequencies such that $|\nu_{m1} - \nu_{m2}|$ is much smaller than both component frequencies.[59,117] This is particularly useful for pressure-broadened measurements which require $\nu_m \geq$ few GHz for a single sideband to probe the transition at any one time or when the bandwidth of the detector is only a few MHz or less. In contrast to traditional single-tone FMS, two-tone FMS signals have even symmetry and only the quadrature term (Equation 2.9) can be determined. Even with a pure FM spectrum, there is a non-zero absorption-free baseline proportional to M_ν^2. Due to these reasons, and the more complex electronics required, only one-tone FMS was employed in these experiments.

FMS is most useful when the quantum noise of the detector is one of the limitations

of sensitivity. As this is a frequency-dependent noise – becoming more significant for low frequency signals – adding a modulation in the MHz to GHz range significantly attenuates its contribution. FMS is particularly well-suited to applications requiring detection of very weak absorption signals.

2.1.2 Wavelength modulation spectroscopy

Wavelength modulation spectroscopy (WMS), also called harmonic or derivative spectroscopy, is similarly based upon frequency modulation of the radiation field, but is useful for different types of measurements. WMS is characterized by a modulation frequency that is much smaller than the spectral linewidth, though the product $M_\nu \nu_m$ must be significantly larger than the laser linewidth in order to treat the instantaneous emitted frequency as a delta function.[59] In WMS, the sinusoidal variations in laser wavelength lead to an oscillating signal that can be described as a sum of Fourier components at the harmonics of the modulation frequency.[118] For small oscillations, the n^{th} Fourier component at the n^{th} harmonic of ν_m is proportional to the n^{th} derivative, $d^n\alpha(\nu)/d\nu^n$ where the absorption coefficient can be thought of as the signal measured. The Fourier components at specific harmonics can be selectively picked out using a lock-in amplifier, as described in the next section.

The lower modulation frequencies of WMS (typically kHz) relieve the requirement of a high bandwidth detection scheme characteristic of single-tone FMS. Though the $1/f$ noise will intrinsically be more significant for WMS compared to FMS, it is possible to eliminate much of this by splitting the beam and normalizing the WMS signal against a reference measurement of the laser output.[119] The derivative signal is useful if, for example, the baseline value varies across the scan, which will not affect higher order harmonics. It is advantageous in some circumstances to have a zero crossing at the transition centre which can be satisfied using any odd harmonic.

2.1.3 Lock-in amplifiers

Lock-in amplifiers are powerful instruments for detecting small AC signals that use phase-sensitive detection to selectively measure signal at a single reference oscillation frequency.[120] In its most basic form, a lock-in amplifier is simply a frequency multiplier followed by a low-frequency filter. To work, the signal must be modulated by a single frequency (ν_m); usually this is accomplished by applying a high frequency modulation to the current applied to the laser. Detectors are intrinsically more sensitive to signals at high frequencies (which can easily be seen by the $\mathrm{Hz}^{-1/2}$ units of detectivity, see Section 1.4). The detector signal is input into the lock-in and multiplied by a sine wave at a lock-in reference frequency (ν_r). The output (V_{LI1}) can then be represented by:

$$\begin{aligned} V_{\mathrm{LI1}} = &\quad V_s \sin(2\pi\nu_m t + \phi_s)\sin(2\pi\nu_r t + \phi_r) \\ = &\quad \tfrac{1}{2}V_s \cos\left[2\pi(\nu_m - \nu_r)t + \phi_s - \phi_r\right] - \tfrac{1}{2}V_s \cos\left[2\pi(\nu_m + \nu_r)t + \phi_s + \phi_r\right] \end{aligned} \tag{2.13}$$

where ϕ_i values are the relative phase of the reference and signal and V_s is the signal amplitude from the detector. The low-frequency filter then removes AC components. If the modulation and reference frequencies are the same ($\nu_m = \nu_r$), the only non-zero component will be a DC signal that is proportional to the signal amplitude on the detector while still taking advantage of the improved sensitivity of high frequency measurements:

$$V_{\mathrm{LI1}} = \frac{1}{2}V_s \cos(\phi_s - \phi_r). \tag{2.14}$$

This output is still dependent upon the relative phase of the signal and reference oscillator. More advanced lock-in amplifiers, such as those used here, incorporate a second phase-sensitive detector to remove this dependency. In this case the second system takes the same input from the detector and multiplies it by a reference sine wave that is shifted $\frac{\pi}{2}$ radians from the first, and the frequency-filtered output voltage from this (V_{LI2}) will be proportional

to the input signal amplitude:

$$V_{\mathrm{LI2}} = \frac{1}{2} V_s \sin(\phi_s - \phi_r). \tag{2.15}$$

The signal, regardless of phase conditions, can then be extracted by summing the two components in quadrature. Alternatively, without applying this second multiplier, the phase of the reference oscillation can be adjusted on the lock-in amplifier to the condition $\phi_r = \phi_s$, thereby ensuring that the lock-in output will be optimized.

While this amplification method is useful for DC signals, it is not particularly good for measuring spectral lineshapes while scanning the laser frequency. However, if an integrator is used instead of a basic low-pass filter, the amplifier can be set up to measure absorption features. In order to effectively filter out unwanted structure, it is important for the modulation frequency to be orders of magnitude faster than the scan rate of the laser. With the integrator, the harmonics (where $\nu_r = n\nu_m$) display derivative-like behaviour, *i.e.* the second harmonic of an absorption signal will have the same overall appearance as the second derivative of the lineshape. This feature makes lock-in amplifiers particularly useful for stabilization techniques, since the odd harmonics of an absorption profile will have a zero crossing point at the centre of the transition.[121] It is therefore quite easy to generate an error signal when the laser frequency drifts, which will be reflected in a shift of the zero crossing in the time domain from scan to scan. For example, if the zero crossing occurs at $t_0 + \Delta t$ in one scan (where t_0 is the start of the scan), a non-zero signal measured at the $t_0 + \Delta t$ of subsequent scans will indicate a frequency drift; additionally, the sign and amplitude of the signal will indicate the direction and magnitude of the shift.

2.2 DFB-QCL frequency stabilization

In applications requiring long-term frequency stability for accurate measurements of fluxes or long-term averaging, drifts in laser frequency and output power can be problematic. Long-term fluctuations can arise from slight changes in, for example, temperature or current. An active feedback loop for frequency stabilization that prevents drifts in laser output would improve the sensitivity of these absorption measurements.

The simplest method for active frequency stabilization utilizes a reference sample with known absorption profile to lock the laser frequency relative to the reference transition. Yanagawa *et al.* locked a 1.5 μm diode laser to a NH_3 absorption and Richter *et al.* used a methanol transition to stabilize a far-infrared Fabry-Pérot QCL at 2.5 THz.[121,122] Both of these techniques demonstrated enhanced stability over approximately second to minute timescales. In order to implement a similar type of stabilization, a WMS-based feedback loop was developed and tested on a mid-infrared DFB-QCL for the study of CH_4. In this section, *stabilization* refers to maintaining a consistent frequency scan in successive measurements (*i.e.* pinning the start frequency of the ramp); this is distinct from other types of frequency stabilization, like Pound-Drever-Hall techniques, which have much more rapid error responses to (typically) maintain a single laser frequency.

2.2.1 8.2 μm DFB-QCL characterization

Each QCL chip must be carefully characterized in order to determine the most appropriate running conditions for each experiment and ensure that variability in the laser emission will not be a limiting factor to spectroscopic sensitivity. Before discussing the laser chip itself, however, it is important to consider the electronics controlling the temperature and current of the chip; the quality of the current driver may, in some cases, determine the operating linewidth of the laser. Custom, low-noise temperature and current drivers were designed and built in-house for the DFB-QCL systems. An overview of these drivers and the custom laser mounts used for many of the laser systems is given here.

The temperature controller allows monitoring of the laser housing temperature with or without actively adjusting the voltage applied to the Peltier element. A Peltier module consists of p and n-doped semiconductors connected in series such that current flows through the junction n $\rightarrow$ p on one side and through the reverse on the opposite side. The semiconductors lie on a single plane sandwiched between two ceramic plates. Due to the thermoelectric effect, the ceramic plate on the first side acts as a heat sink, while the plate on the opposite side acts as a heat source. By tuning the voltage across the semiconductor layer, it is possible to finely tune the rate and direction of heating and cooling. The

temperature driver output voltages that allowed temperature tuning of the ceramic plate nearest the laser were between -30°and 9°C.

The current driver, housed in a separate module, was designed to apply currents between 0 and 1000 mA across a QCL chip, though a maximum current limit could be set below 1 A to prevent damaging the laser. The DC current level could be adjusted manually on the controller, and a low frequency (< MHz) signal could be added on top of this to scan the laser. The QCL chips require a reverse voltage across the anode and cathode, so the current applied is actually negative, which means that applying a positive voltage ramp causes a decrease in the magnitude of the applied current. Earlier analysis of the noise output of the current driver demonstrated a current deviation of < 0.1 mA when 400 mA was applied across a 25 Ω test resistor.[123] The homemade device was consistently less noisy than two similar commercial devices (Wavelength Electronics QCL1500 and ILX Lightwave LDX 3232), with ten times less noise measured over averaging times up to 30 s.

An 8.2 μm (8.175 – 8.250 μm) cw single mode DFB-QCL (Alpes, sbcw835DN) was supplied on a copper NS submount (1.9 x 0.7 x 0.2 cm dimensions). The laser is soldered at the midpoint of the long axis near one edge of the submount such that the emitting facet of the chip faces out with the optical axis perpendicular to the long axis of the submount. Raised contact ridges on either side are connected to the anode or cathode of the chip by thin gold wires. The QCL housing was custom designed and fabricated in-house. The whole submount is screwed onto a copper base with a layer of indium foil in between to ensure efficient and homogeneous thermal conductivity across the surface. The copper base is placed on one of the Peltier's ceramic plates. Spring-loaded pins pressing against the contact ridges connect the laser to the current driver circuit. All the components are sealed inside an aluminium box with a water cooling system to dissipate excess heat. Water (∼12°– 15°C) flows continuously through the cooling system, and the compartment which houses the laser is evacuated using a mini-pump (KNF N84.3ANE-K). The vacuum removes water vapour from the compartment to prevent damage to the delicate semiconductor layers by condensation and freezing. A 9-pin D-sub connector joins the internal components – thermocouple, Peltier, anode, and cathode – to the temperature and current drivers. A

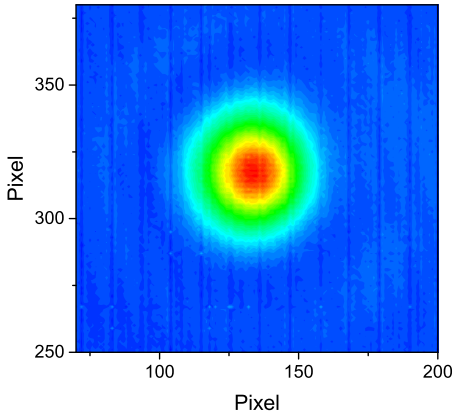

Figure 2.2: Beam profile of collimated 8.2 μm DFB-QCL measured 50 cm from the collimating lens using a microbolometer with colour contours representing intensity in arbitrary units. Each pixel has an area of 35 μm $\times$ 35 μm.

BaF_2 window allows transmission of the laser emission out of the housing. The box is clamped into a custom, anodized aluminium base that is bolted to the optical table with the laser beam at a working height of $\sim$ 15 cm. A bracket fixed to the base supports the collimating lens holder to ensure the laser remains collimated even when moved to a different optical bench.

The laser beam is collimated by using a microbolometer to image the beam profile at varying distances from the laser facet. A 1.27 cm diameter aspheric collimating lens (Thorlabs, $f = 4$ mm) is placed in an XYZ lens positioner to allow fine adjustments such that the laser beam exhibits a symmetric, two-dimensional Gaussian profile horizontally and vertically, and maintains approximately the same beam diameter over distances ≥ 1 m. A sample intensity profile of the collimated 8.2 μm QCL measured 50 cm from the collimating lens is shown in Figure 2.2.

Power and I-V curves (Figure 2.3) are measured to check that the laser behaviour agrees with the manufacturer's specifications. At various operating temperatures, the laser current is tuned from its threshold level to near maximum (typically $\sim$ 300 – 560 mA for QCLs) while simultaneously reading the applied voltage – displayed on the current driver – and output power measured using a power meter (Melles Griot, Broadband 13PEM001). The power measured is typically $\sim$ 20% lower than expected, which is reasonable as some losses can be expected due to the large divergence of the beam, the finite aperture of the

BaF_2 window, absorption by the BaF_2, and the limited size of the collimating lens. The levelling off and slight decrease of the laser power near the maximum current occur due to thermal effects and the so-called Stark roll-over, where the upper state and injector level of the QCL potential wells become misaligned.[124]

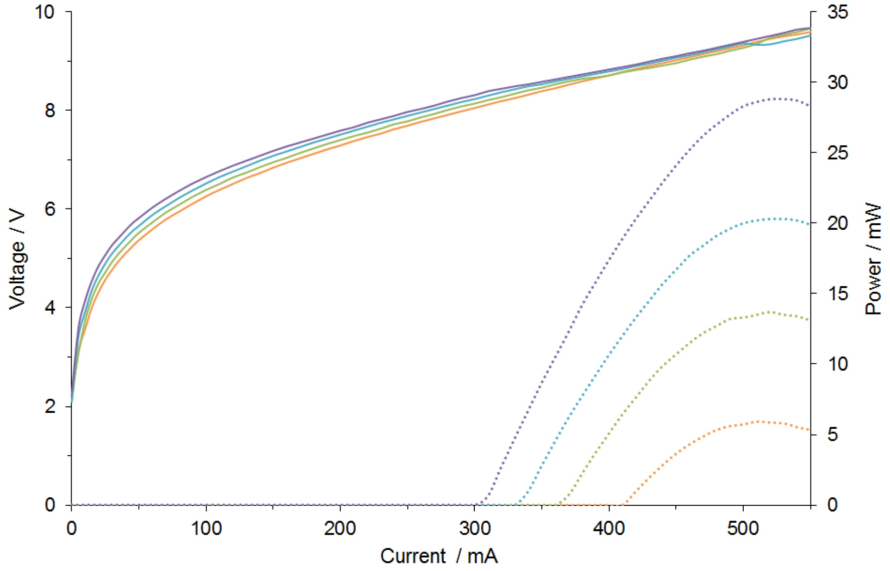

Figure 2.3: Voltage (solid lines) and power (dotted lines) of the 8.2 μm DFB-QCL as a function of applied current at four laser operating temperatures: 0°C (orange); -10°C (green); -20°C (blue); -30°C (purple).

2.2.2 Methane properties

Methane is an important greenhouse gas with many times the global warming potential of CO_2 due partly to its much longer tropospheric lifetime. In contrast to CO_2, it is the sources of CH_4 that require further investigation.[103] There are obvious anthropogenic sources – *e.g.* natural gas leaks and anaerobic processes in agriculture – but some sources are less well understood, such as the methane hydrate reservoirs in melting permafrost.[125] Biologically, low CH_4 levels in breath and other expelled gases can indicate stomach or intestinal problems.[126]

CH_4 has nine vibrational degrees of freedom and four normal modes; these are the symmetric stretch (ν_1), triply-degenerate asymmetric stretch (ν_3), doubly-degenerate "wagging" bend (ν_2), and triple-degenerate "scissoring" bend (ν_4). Three of these lie within the region

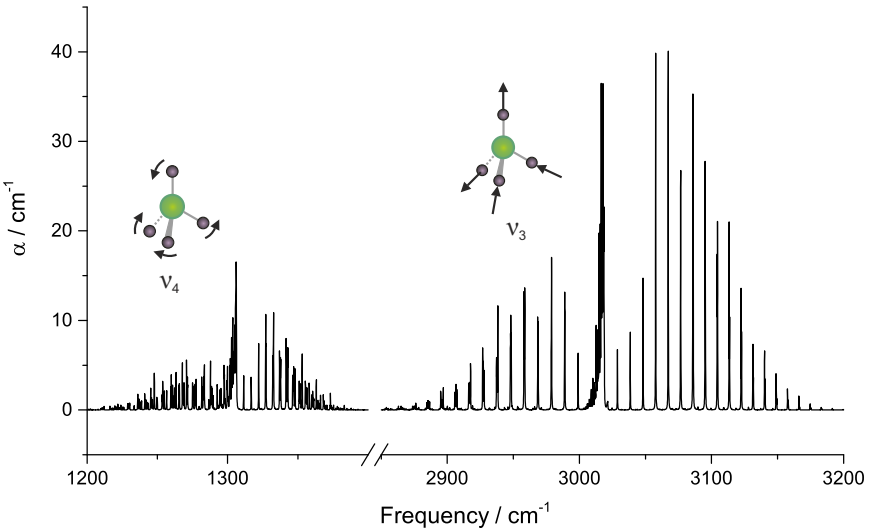

Figure 2.4: HITRAN absorption coefficient spectrum of CH_4 in regions corresponding to ν_3 asymmetric stretch and ν_4 bend vibrational modes.[6] Data presented are for 760 Torr pure CH_4.

covered by the mid-infrared QCLs, and the asymmetric stretch and scissoring mode transitions are shown in Figure 2.4. Although only the ν_3 and ν_4 fundamental transitions are infrared-active, Coriolis interactions, as well as higher order effects, distort the permanent molecular dipole and split the ro-vibrational transitions This allows some ro-vibrational bands to be observed even for fundamentally inactive modes.[127–129] For notation, in addition to the vibrational state excited, CH_4 levels are characterized by local quanta J, C, and α_{JC}, which represent the total angular momentum quantum number, the molecular spin symmetry, and the index number for transitions with the same J and C respectively.

2.2.3 Experiment

In this experiment, shown in Figure 2.5, an 8.2 μm cw QCL was stabilized to the P(12) ν_4 CH_4 transition at 1219.65 cm^{-1}. The laser was housed under vacuum in a custom mount at a constant temperature of -30°C maintained by a Peltier element. After collimation by an aspheric lens (Thorlabs, f = 4.0 mm), the 15 mW beam was split by a wedged CaF_2 window. The transmitted beam (∼90% incident intensity) passed through a 30 cm long cell containing a sample of 150 Torr 0.3% CH_4 in air and focused onto a photovoltaic detector (VIGO PVMI-3TE-10.6) using an off-axis parabolic mirror. The signal was sent to a lock-in amplifier (LI1; Stanford SR830) for second harmonic ($2f$) demodulation, which

was recorded on an oscilloscope (LeCroy WaveSurfer). About 7% of the original beam was reflected off the front surface of the window through a 5 cm long reference cell with 12 Torr pure CH_4 onto a mercury cadmium telluride (MCT) detector (EG&G J15D12) connected to a second lock-in amplifier (LI2; Stanford SR510) with a time constant between 300 and 1000 μs.

The current applied to the laser was a combination of three inputs: fast modulation, slow scan, and DC error signal. A low-amplitude (100 mV) 10 kHz signal from LI2 modulated the laser for lock-in amplification, while a function generator (TTi TG230) produced a 400 mV peak-to-peak triangle wave at 2 Hz that scanned the laser frequency across the CH_4 transition. As described previously, the derivative-like lock-in signal is ideal for this locking scheme due to the flat baseline and the zero crossing of the odd harmonic. The third harmonic ($3f$) of the reference signal (LI2) was sent to a DAQ (NI-PCI-6036E) and used by a self-written LabVIEW program to determine the error signal. The program fixed a point in the scan to the centre frequency of the transition. The amplitude and sign of the $3f$ signal at this point indicated the magnitude and direction of wavelength drift. The program averaged four scans and continuously adjusted a DC voltage applied to the current controller to minimize the $3f$ signal at the set point. The $2f$ signal of the sample arm was measured simultaneously to demonstrate the potential of the technique for concentration measurements.

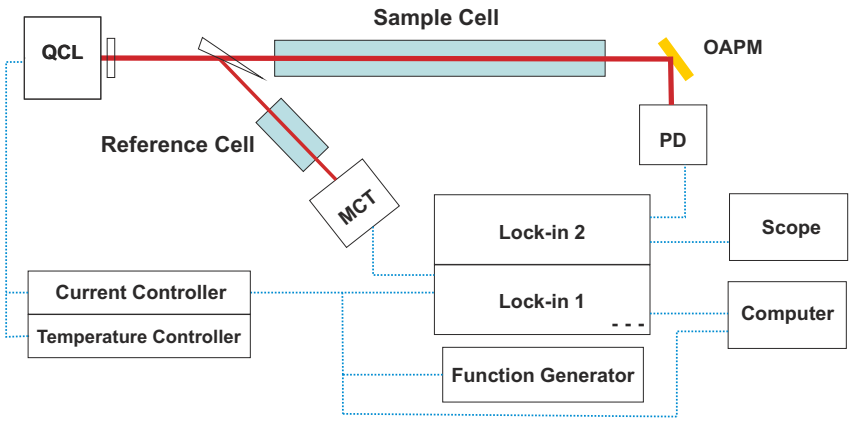

Figure 2.5: Schematic of frequency stabilization experiment with 8 μm DFB-QCL. Note: MCT = mercury cadmium telluride detector; PD = photodiode detector.

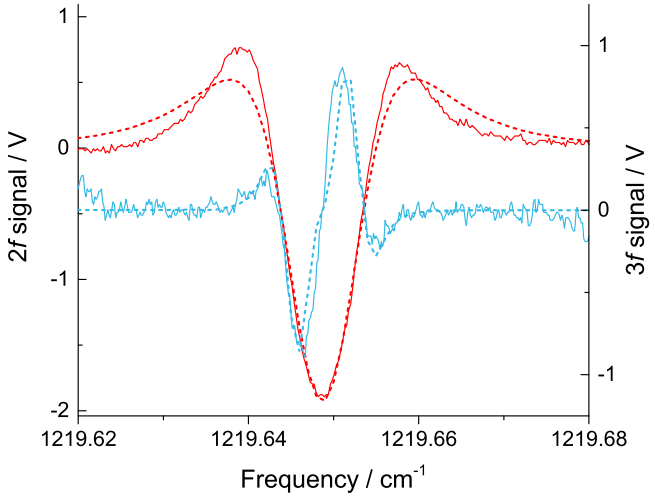

Figure 2.6: Mathematical model (dotted) and experimental (solid) second (red) and third (blue) harmonic signal from scanning across molecular transition. The model amplitude scales were adjusted to match experimental signal amplitudes. The asymmetry in the data is likely caused by distortions due to the time constant of the lock-in amplifiers.

2.2.4 Results

Sample traces of the $3f$ reference signal and $2f$ sample signal, measured simultaneously, are shown in Figure 2.6. A simulation of the second and third derivatives of the absorption by CH_4 in the two cells is overlaid to demonstrate that there is an excellent qualitative match with the lock-in amplifiers' $2f$ and $3f$ output. Asymmetry in the measured signal can arise from a non-linear baseline and distortions from the lock-in if the time constant selected is too long. The stabilization routine required an odd harmonic to take advantage of the centre zero-crossing for error signal generation; the third harmonic was chosen to eliminate all baseline effects without unnecessarily diminishing the signal amplitude. The $2f$ signal was chosen for the sample arm where the magnitude of the signal is important and the symmetry is irrelevant.

To assess the usefulness of the technique, the frequency excursion of the laser relative to the transition centre was measured over long ($\sim 10^2$ s) times. As mentioned in Section 1.4, Allan-Werle variance plots are a common metric for measuring the stability of a system over time.[50,51] Figure 2.7 shows the variability in the centre of the sample signal, and Figure 2.8 the corresponding variance as a function of averaging time. It is clear that enabling the frequency-locking feedback scheme greatly enhances the stability of the output laser frequency for averaging times $>$ 30 sec, but has little impact for shorter averages. For

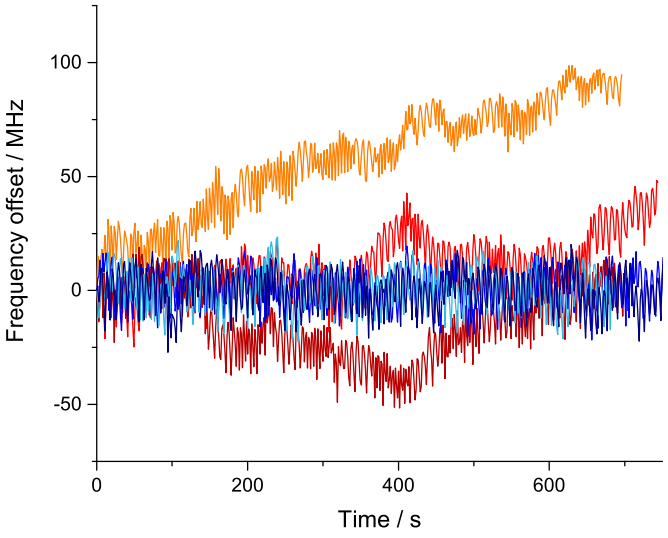

Figure 2.7: Frequency variability of methane transition line centre measured in reference cell over time. Red and orange lines represent measurements taken without feedback; blue were measured with the stabilization feedback loop enabled.

example, the standard deviation in output frequency after two minute averaging is 3 MHz with feedback enabled and 100 MHz without, while in both cases the variation is about 50 MHz for 10 second averaging. In Figure 2.9, the Allan-Werle variance is computed for each point across the $2f$ spectrum individually. With the feedback loop disabled, there is a clear increase in the variance at the points in the waveform with large gradients with a negligible variance at the centre minimum. This indicates, as expected, that frequency drifts rather than amplitude fluctuations are responsible for the changes in variance.

This method is relevant for experiments susceptible to long-term (up to several hours) laser drifts due to subtle changes in temperature or current. The response time of the feedback circuit is insufficient to improve short-term variation between consecutive scans but is easily adequate for monitoring samples of ambient air. The method is limited by the range of frequency drifts that can be corrected. Short-term variation in the frequency output must be much smaller than the linewidth of the transition for the reference sample for the error loop to function properly. For short-term stabilization requiring a fast feedback loop, the Pound-Drever-Hall method could be employed. In this method, phase corrections due to a high finesse Fabry-Pérot resonator allow fast corrections that are not limited by the laser response time.[130]

The marked improvement in laser stability with the active feedback loop shows that frequency stabilization using laser modulation is an effective method for preventing drifts in laser frequency. This method can be easily adapted for other QCLs with the use of an appropriate reference gas.

2.3 DFB-QCL FMS

Measurements of trace gases using WMS have been demonstrated using both pulsed and cw mid-infrared DFB-QCLs.[131,132] Using the $2f$ signal, minimum detectable concentrations of <1 ppb were achieved for CO, N_2O, and acrylonitrile (CH_2CHCN). In both studies, the technique proved robust but overall sensitivity was limited partly by spectral asymmetry due to RAM.

It has proven somewhat more challenging to successfully utilize FMS in the mid-infrared with semiconductor lasers. Gagliardi *et al.* demonstrated sensitive detection of N_2O and CH_4 isotopes using a cryogenically-cooled QCL at 8 μm with a modulation frequency of 170 MHz.[133] However, Borri *et al.* reported severe degradation to a low temperature Fabry-Pérot QCL after applying high frequency modulation (50 – 600 MHz).[134] Both single and two-tone FMS were used for the detection of N_2O and CH_4, respectively. Poor coupling of high frequency modulation into the laser head and the non-linear, inhomogeneous frequency

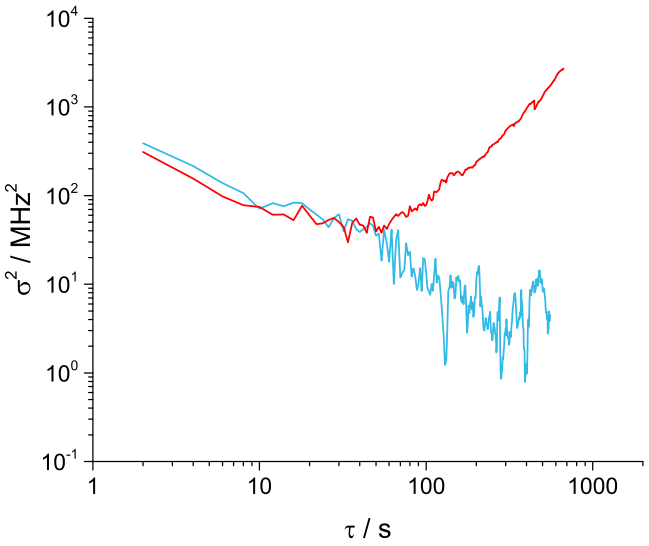

Figure 2.8: Allan-Werle variance of the measured frequency excursion of the laser. As before, blue represents active stabilization loop enabled and red represents measurement without stabilization.

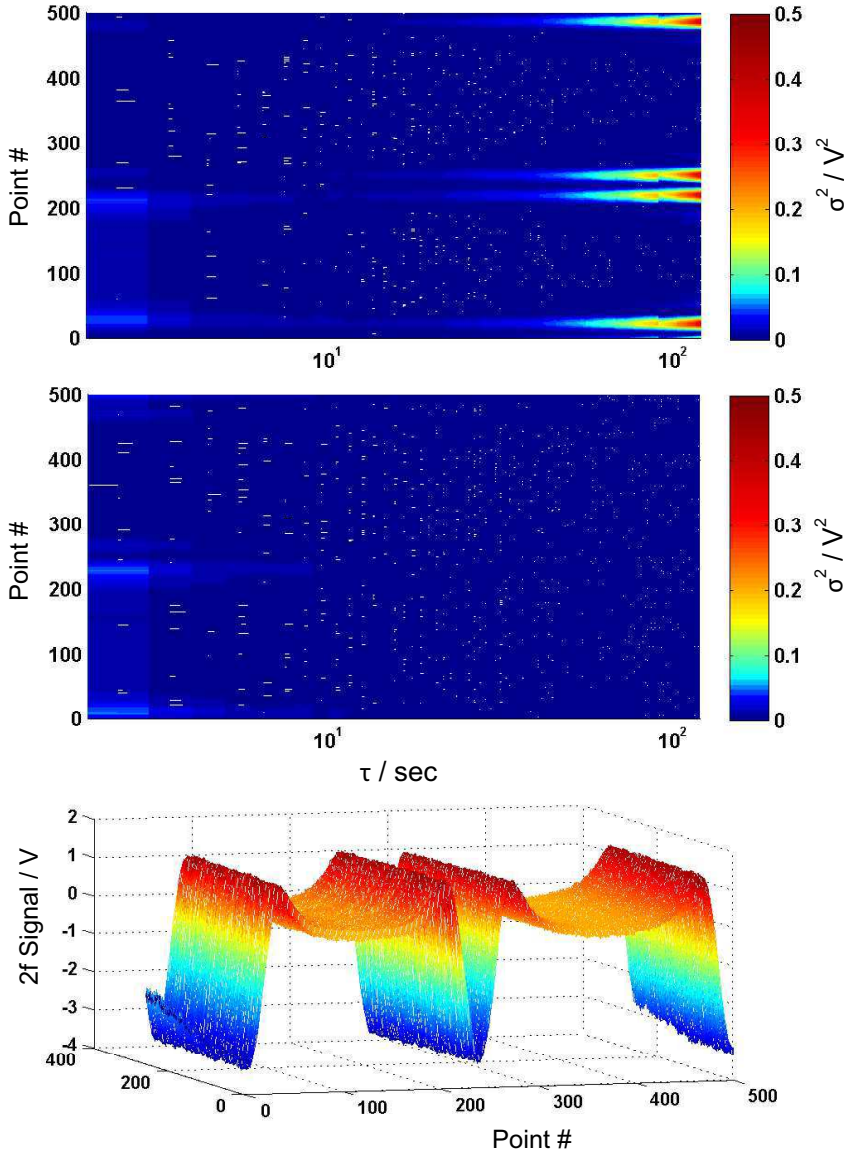

Figure 2.9: 2D Allan-Werle variance of the $2f$ spectra measured through the sample cell. The upper two plots show the Allan-Werle variance for each individual point across the scan without (upper) and with (lower) the active feedback loop enabled. The variance values are indicated by the colour bar. The trace on the bottom shows the corresponding points across the scan.

response observed limited the sensitivity, with MDA values in the 10^{-4} – 10^{-3} range. More recently, a THz Fabry-Pérot QCL was used to perform single-tone FMS (v_m = 50 MHz) on methanol.[135] While RAM was again observed, the authors noted that the frequency modulation dominated over the amplitude modulation.

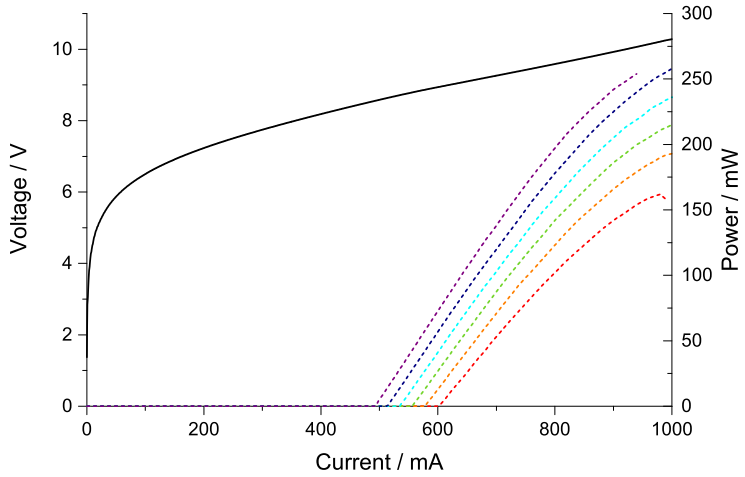

Figure 2.10: Power curves (dashed lines) of 5.26 μm DFB-QCL as a function of current for the following temperatures: -15°C (purple); -10°C (dark blue); -5°C (light blue); 0°C (green); 5°C (orange); 10°C (red). The voltage (black line) as a function of current is the average of the six data sets.

2.3.1 5.26 μm DFB-QCL characterization

The QCL used in this experiment was a 5.26 μm cw, single mode DFB-QCL (Maxion, M575AH) supplying up to 260 mW power. This was supplied on a nearly identical NS submount as the 8 μm laser, and was set up with the same housing, base, and controllers as described in Section 2.2.1. I-V and the power curves of the device are shown in Figure 2.10. Due to the high power of this laser, it was not possible to measure the beam profile without using filters, which distort the measured profile, to prevent damage to the microbolometer sensor. The laser was operated between -15°and 10°C with a limiting current of 1 A.

2.3.2 Nitric oxide properties

Nitric oxide, a free radical, is one half of the important NO_x double-act (NO + NO_2) that determines so much of the chemistry in the lower troposphere. In the presence of volatile organic compounds (VOCs), NO_x will react to form photochemical smog, a harmful pollutant that can aggravate lung issues. The relative amounts of NO_x and VOCs determines tropospheric ozone production – another pollutant that causes oxidative stress in both plants and animals, including humans. NO_x compounds are partly responsible for the formation

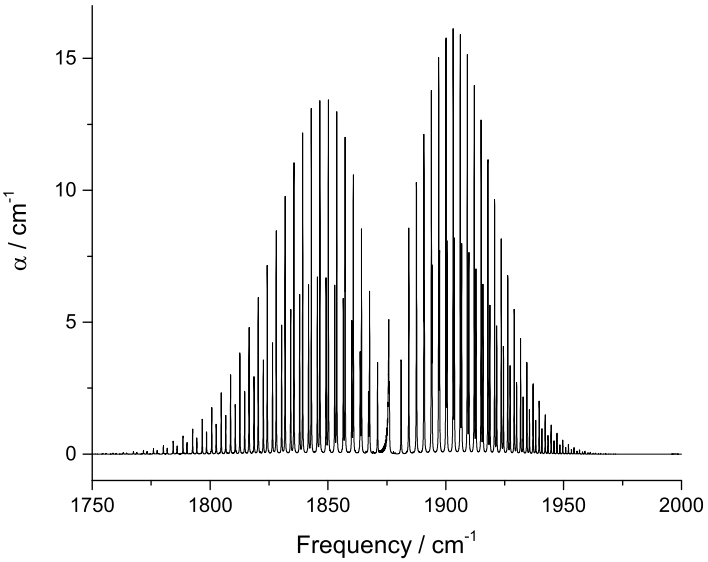

Figure 2.11: HITRAN spectrum of fundamental NO stretch. Absorption coefficients given correspond to pure NO at 760 Torr.

of acid rain upon reaction with O_2 and H_2O.[136] Emission sources vary significantly by region, and as a highly reactive free radical species it is not well mixed on any significant transport scale. In heavily populated and industrialized areas, the major source is usually transportation due to the oxidation of N_2 or nitrogen-containing compounds in fuel at high temperatures found in combustion engines.

NO is somewhat unique among the gases explored in that it is commercially available in the health sector as a vasodilator drug, including for neonates.[137] It is also used by physiologists in studying lung diffusing function and identifying lung disease.[138] As a diatomic molecule, NO has a single fundamental stretching mode at ~ 1880 cm^{-1}, shown in Figure 2.11, that is strongly infrared-active. The neutral molecule has an unpaired electron, making it an attractive molecule for techniques using magnetic fields, such as Faraday modulation spectroscopy.[65] For this experiment, however, more broadly applicable frequency modulation was used rather than magnetic modulation.

2.3.3 Experiment

FMS was performed to detect NO with a Peltier-cooled 5.26 μm cw DFB-QCL (Maxion) sealed in a custom mount. The laser was scanned with a 1.5 V triangle ramp (corresponding

to ~ 1.5 cm^{-1}) at 50 Hz using an external function generator (TTi, TG230) connected to a custom current controller. A bias tee was introduced between the laser head and the connection to the temperature and current drivers in order to couple in the modulation voltage. The homemade bias tee is a simple T-junction circuit with a 10 mH inductor in the branch connected to the laser drivers to prevent high frequency current from travelling back up the channel. The high frequency modulation passed through a 0.1 μF capacitor, to de-couple the signal from the laser, and a 50 Ω resistor to improve impedance-matching with the driver. The fast modulation was combined with the slow ramp after the driver to avoid attenuation due to low-pass filters within the driver circuitry. For these experiments, the modulation was supplied by a signal generator (Marconi Instruments, 10 kHz – 1.01 GHz) with a colourful history in the Royal Navy aboard the HMS Collingwood. The laser was collimated using an aspheric lens (Thorlabs, $f = 4$ mm) and passed through a 70 cm long cell onto a 20 MHz-bandwidth DC photodetector. The cell was connected to a vacuum pump and pressure gauge (Leybold Ceravac, $\leq$1 Torr) and filled with 20 – 200 mTorr pure NO (BOC). The output of the detector was recorded on a 400 MHz-bandwidth oscilloscope (LeCroy WaveSurfer 44MHxs-A).

2.3.4 Results

Before applying modulation to the laser current, direct absorption spectra were recorded at two different regions: a single feature centred at 1900.52 cm^{-1} identified as the $^2\Pi_{3/2}$ R(6.5) transition with contributions from both Λ doublets well-overlapped; and a doublet feature centred at 1900.07 and 1900.08 cm^{-1} assigned to the $^2\Pi_{1/2}$ R(6.5) transition where the two Λ doublet resolved transitions are clearly separated.[6] After applying the Beer Lambert law (Equation 1.13), the spectra were fit well using a Gaussian model as shown in Fig. 2.12 with the expected thermal linewidth broadening (FWHM = 0.0058 cm^{-1}). The Gaussian lineshape is an appropriate model in this case due to the low pressure of the sample.

For FMS, the signal generator applied a high frequency, typically 20 MHz (limited by detection bandwidth) with an applied modulation depth of 50 mV. This modulation frequency is much broader than the laser linewidth. The output of the detector was sent

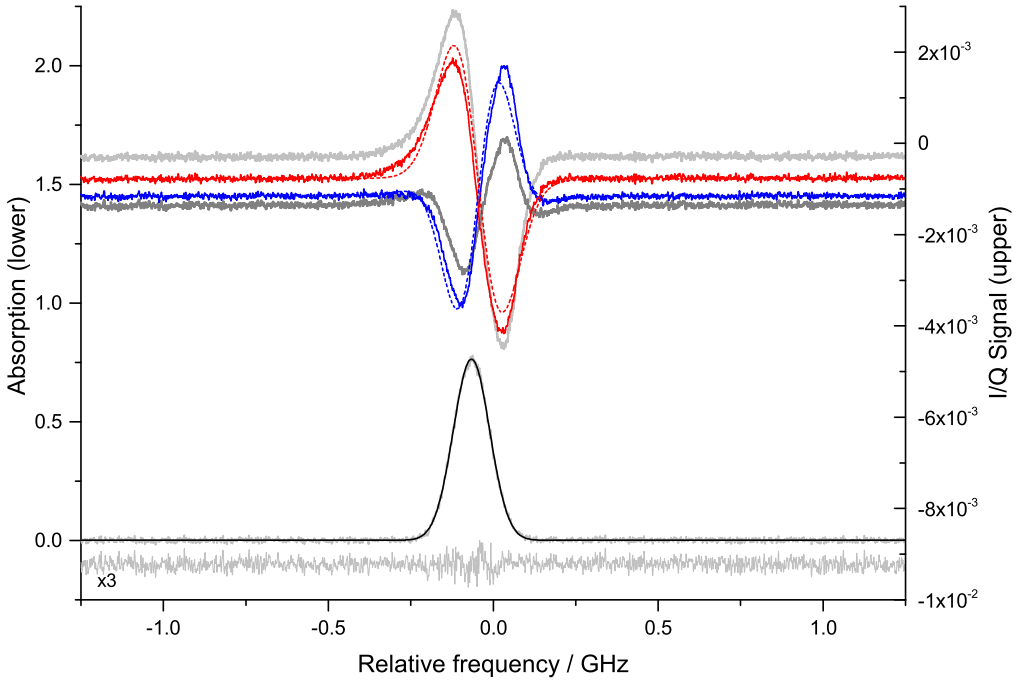

Figure 2.12: A direct absorption measurement (lower) at 1900.52 cm^{-1} ($^2\Pi_{3/2}$ R(6.5) NO transition) is compared with corresponding FMS data (upper). The lower panel shows a Gaussian fit (black line) to the direct absorption data (grey line) of 40 mTorr NO at 1900.52 cm^{-1} which yields a linewidth of 0.13 GHz. The residual is shown below, offset for clarity and magnified by a factor of three. The upper panel shows the corresponding FMS measurements. The I_{fm} (blue) and Q_{fm} (red) data (solid lines) were fitted (dashed lines) using the MATLAB program described in the text, yielding a fitted linewidth of 0.16 GHz, indicating some broadening with laser frequency modulation. The pure absorption (light grey) and dispersion (dark grey) are also shown, calculated from Equations 2.8 and 2.9. For the FMS data, the laser was modulated with 50 mV at 20 MHz.

to a homemade demodulator which generated I_{fm} and Q_{fm} signals using a local oscillator reference input from the signal generator. The relative phase of the two input signals, which determines the relative contributions of the A_{fm} and D_{fm} to the I_{fm} and Q_{fm} signals, was changed by using different length cables.[135] The phase was adjusted so the I_{fm} and Q_{fm} exhibited similar magnitudes. A sample FMS measurement is shown in Figure 2.12. As expected, RAM resulted in signal asymmetry. This is an intrinsic side effect of current modulation on semiconductor lasers, and therefore could not be eliminated without having the ability to finely tune the signal phase.

Despite this effect, it was possible to use a MATLAB model to extract lineshape parameters from I_{fm} and Q_{fm} signals using an iterative fitting algorithm.[139] The simulation

assumed a Gaussian lineshape to produce values of centre frequency, Gaussian linewidth, demodulation frequency, phase, scale factor, and offset values for I_{fm} and Q_{fm}. Comparison of the Gaussian linewidths of the direct absorption spectra with those determined from the modulated I_{fm} and Q_{fm} indicate some broadening of the lineshape due to the modulation. As shown in Figure 2.12, the direct absorption lineshape matched the expected thermal Doppler linewidth (130 MHz), whereas the FM spectra yielded a linewidth of 160 MHz. The broadening of the FMS signal is expected due to the contribution of both sidebands (of opposite phase) to the signal because the sideband separation is smaller than the absorption linewidth (see Figure 2.1). In an ideal case, where the modulation frequency is greater than the absorption linewidth, no broadening of the FMS signal would be expected.

Both FM and direct absorption spectra were collected for the gas at a range of pressures, shown for the singlet R(6.5) $^2\Pi_{3/2}$ transition around 1900.5 cm^{-1} in Figure 2.13. For $P \leq 60$ mTorr, the signal increased linearly with pressure (see Figure 2.14), though at higher pressures of NO, nearly 100% absorption was observed near the transition centres, causing distortions to the direct absorption lineshape. The FM spectra also exhibited distortions at these pressures and could not be fitted well by the MATLAB program.

To estimate the sensitivity of the FMS measurements, the maximum amplitude of the I_{fm} or Q_{fm} fit from the MATLAB program was compared to the baseline noise. After fitting the experimental I_{fm} and Q_{fm}, the phase was adjusted in the simulation to maximize the amplitude of one of the components. The SNR was then taken to be this amplitude divided by the standard deviation of the baseline signal. For example, the maximum I_{fm} signal of an FM spectrum of 70 mTorr NO was 15 mV with a baseline standard deviation of 0.037 mV, yielding a SNR of about 400. This is a slight improvement to the a direct absorption measurement at a similar pressure (66 mTorr), where comparison of the maximum absorption and baseline standard deviation gives a SNR of 240. The minimum detectable pressure of NO is roughly 170 μTorr for a 320 ms FMS measurement, or more generally $\alpha_{min} = 7 \times 10^{-7}$ cm^{-1}. It should be noted, however, that this sensitivity estimate neglects the influence of RAM on the accuracy of fits.

The limitations to sensitivity are not associated with the QCL *per se*, but with other

electronic components of the system. A detector with a similar detectivity but faster time response would allow application of a higher modulation frequency, allowing an increased sideband separation and ensuring that only one sideband is scanned over the absorption transition at any one time. Increasing the modulation frequency would require making

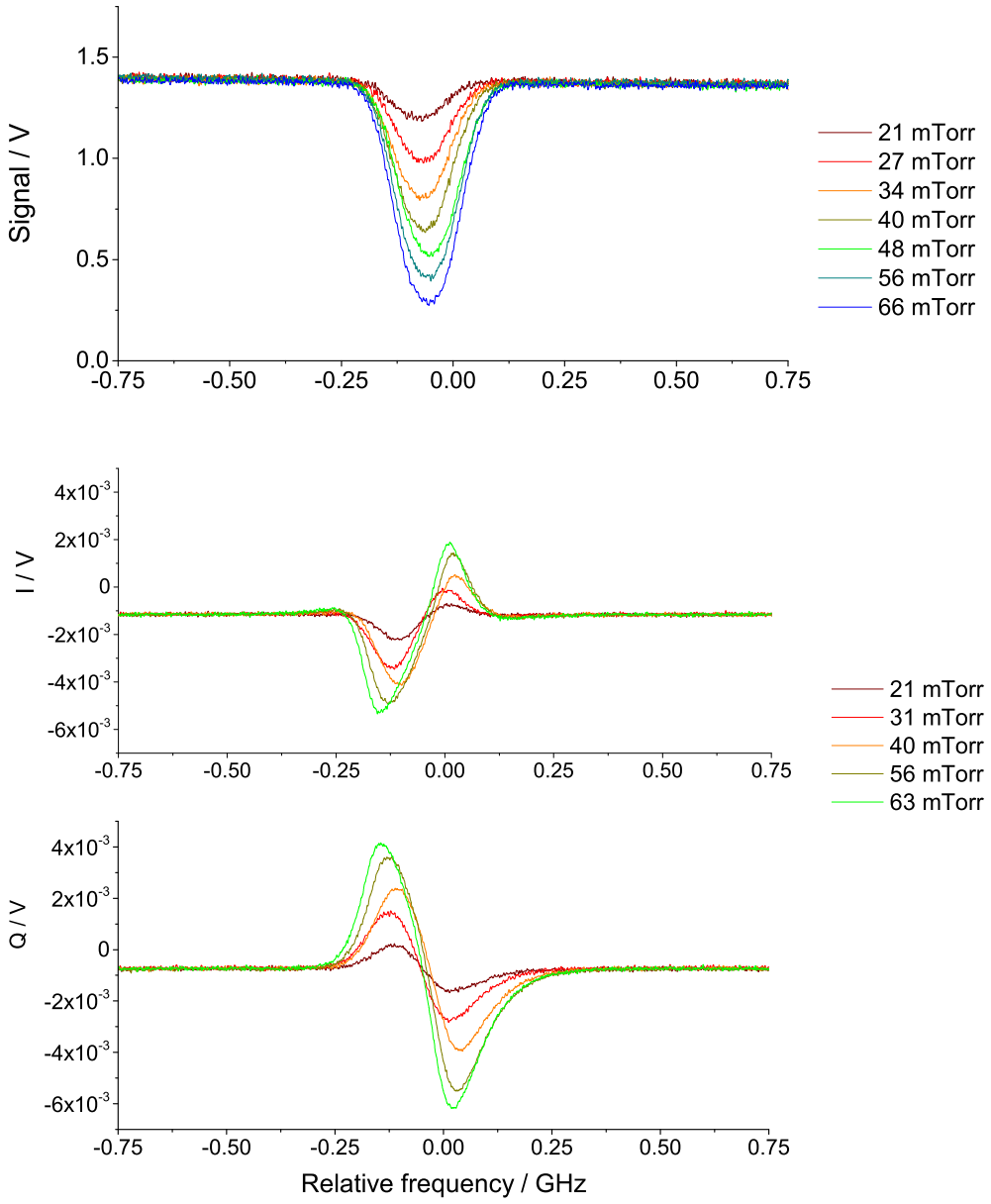

Figure 2.13: Direct absorption (upper) and FM (lower) spectra at varying NO pressure showing increase in FMS signal with increasing pressures (number densities) of NO. The transition is the same as Figure 2.12.

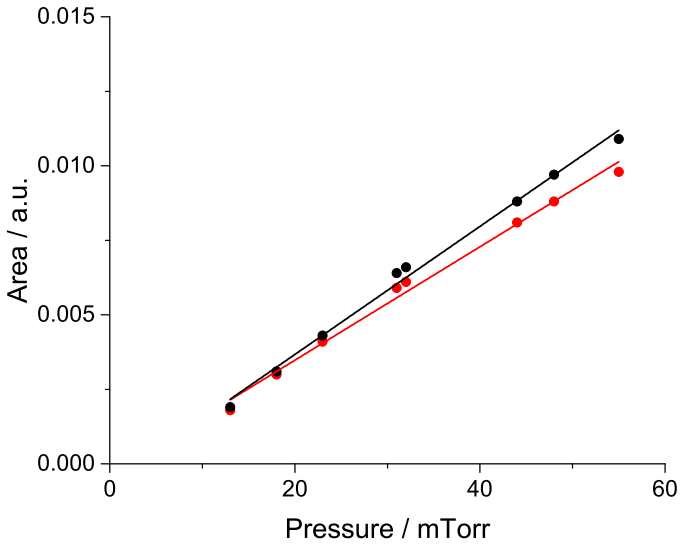

Figure 2.14: Derived area from MATLAB fits of I_{fm} and Q_{fm} measurements shown in Figure 2.13 up to 60 mTorr. Black and red represent data collected with laser frequency ramped up and down, respectively. Both data sets fit to linear function that does not cross the origin, likely due to an offset on the pressure sensor.

adjustments to the bias tee to eliminate parasitic effects at high modulation frequency described extensively in the next chapter. Based on adjusting the simulations shown in Figure 2.12, increasing the modulation frequency to well over the absorption linewidth (*e.g.* 10 GHz) would result in a factor of five increase in the SNR. Signal processing could be further improved by using a variable demodulator offering both modulation frequency and phase tunability. There is hope in innovative laser technology – recently, an electrically tuned, pulsed, THz QCL was developed that maintains a constant optical power output as the frequency is scanned, and would therefore not be susceptible to RAM.[140]

While FMS can be a powerful technique for high sensitivity gas detection, it suffers from a number of drawbacks that make it unsuitable for some applications. Perhaps most crucially for gas sensing, it is not straightforward to extract absolute concentration values from the measured spectra without careful calibration. The accuracy depends on the demodulation electronics utilized. Furthermore, in an ideal case the relative phase of the local oscillator and signal could be tuned to ensure minimal RAM effects. FMS is poorly suited to measure spectra with broad, overlapping features due to the optimal condition that the sideband separation is larger than the spectral linewidth. Instead, methods for increasing the optical path length must be used in order to achieve sensitivities surpassing those of single pass direct absorption methods. The next chapter introduces some of these cavity-based spectroscopy techniques.

2.4 Conclusions

An active frequency stabilization system based on locking to a methane transition was developed for an 8.2 μm DFB-QCL. The feedback program prevents laser output drifts over $\geq$30 s, a capability particularly useful for WMS experiments requiring averaging over minute time scales. With the system stabilized, variation in laser frequency was limited to 3 MHz over two minutes. The experimental set-up is quite simple, and the LabVIEW program developed can be easily adapted to other laser systems. Future experiments requiring stable wavelengths over an extended period of time can be significantly improved by implementing frequency stabilization.

Frequency modulation spectroscopy was demonstrated with a 5.3 μm DFB-QCL for measurements of NO. Despite the low modulation frequency (20 MHz) relative to the NO absorption linewidth, the measured I_{fm} and Q_{fm} signal could be modelled reasonably well using a MATLAB program. Some RAM was observed, however changing the relative phase of the signal and local oscillator minimized its contribution. An α_{min} of 7×10^{-7} cm^{-1} for 320 ms measurement (SNR = 400) was estimated for the technique, and some potential avenues of improvement were discussed. This is on par with a similar QCL-based FMS experiment, which achieved an MDA of 2×10^{-6} Hz$^{-1/2}$ in a 17 cm cell.[133] FMS is an effective technique for reducing low-frequency noise in order to sensitively measure trace species at low sample pressures with QCLs.

Chapter 3

Off-axis CEAS: Sensitivity Enhancement by RF Current Perturbation

3.1 Introduction to optical cavities

Sensitivity in trace gas measurements can be improved not only by minimizing electrical noise on the detected signal, but also by enhancing the magnitude of the absorption signal. In some cases, it is appropriate to pre-concentrate the sample,[141] but many applications require rapid data acquisition with no alteration of the gas sample. Instead of increasing the number density of molecules, signal can be boosted by increasing the path length of the radiation through the gas in order to increase the number of molecules with which the field can interact. As evident in Equation 1.13, attenuation of radiation linearly increases with L in the limit of low absorption. Multipass cells can be used to increase path lengths by one or two orders of magnitude, as mentioned in Section 1.5.1, however further extensions in path length require an often undesirable increase in volume to prevent beam overlap. Optical cavities offer a powerful method for achieving long optical path lengths without the need for a large footprint.

Fundamentally, an optical cavity is a set of mirrors set up such that reflections within the inter-mirror space overlap. Optical cavities are useful because of their bigger-on-the-inside quality: within a benchtop sample container that is centimetres long, it is possible to achieve long effective optical path lengths – the average distance a photon travels through

the sample – on the order of many kilometres. With mirror reflectivities (the fraction of light intensity reflected off the surface) commonly > 0.999, the lifetime of the intracavity field is at least three orders of magnitude longer than the round-trip time of a single pass.

The most basic optical cavity is a Fabry-Pérot resonator, which can be found inside many laser systems as a coherent amplification mechanism. This type uses two highly polished surfaces as reflecting planes separated by a short distance to form a cavity. The term *optical cavity* is colloquially used when referring to systems where the reflector separation is large compared to mirror thickness and curved cavity mirrors are used.[35]

Cavities are often described by a finesse ($\mathcal{F}$), which defines the ratio between the free spectral range (FSR) and cavity bandwidth at resonance ($\Delta\nu_{\text{cav}}$) based on the reflectivity of the mirrors (R):

$$\mathcal{F} = \frac{FSR}{\Delta\nu_{\text{cav}}} \approx \frac{\pi\sqrt{R}}{1-R}, \tag{3.1}$$

indicating that narrow bandwidth (high finesse) cavities require high reflectivity mirrors with R values close to unity.[142] Effective optical path lengths scale as $L/(1-R)$, which means that a 1 metre-long cavity composed of mirrors with $R = 0.99998$ (commercially available in the visible and near-infrared) allows the intracavity light field to interact with the sample the distance of a marathon (42 km)!

The magnitude of the intracavity field is the sum of all the fields within the cavity, which is a combination of components with varying phase. If the incident radiation satisfies the condition $\nu = \frac{Nc}{2L}$, where N in this case is an integer, then it excites a longitudinal mode of the cavity. In this case, the resonant intracavity field behaves in a similar manner to a particle-in-a-box with stationary nodes established at each end mirror and a standing wave generated with complete constructive interference, as shown in Figure 3.1. Light in resonance with a longitudinal mode of the cavity has a well-defined spatial intensity profile, called a transverse electromagnetic mode (TEM_{mn}), in the plane perpendicular to the optical propagation axis. Concave cavity mirrors are required to generate these well-behaved transverse modes. Stable cavities cannot be formed by solely flat mirrors as these lead to poorly-behaved, unpredictable transverse mode structures with higher losses.[35]

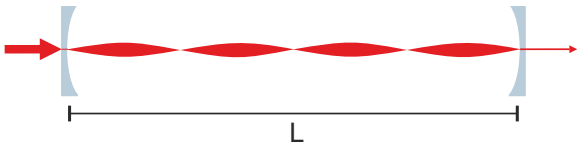

Figure 3.1: Schematic of an intracavity field in linear cavity when incident wavelength is resonant with and excites a longitudinal mode. In a typical cavity-based experiment, light is coupled in through one mirror and the field leaking out is detected on the opposite end as indicated.

3.2 Cavity-based techniques

Two families of cavity-based spectroscopy techniques have been widely adopted: cavity ring-down spectroscopy (CRDS), developed by O'Keefe and Deacon in 1988,[143] and cavity-enhanced absorption spectroscopy (CEAS), which came about a decade later.[144–146] CRDS uses the exponential decay of light intensity emerging from an optical cavity to measure absorption, scattering, and other losses incurred by the sample or mirrors.[147] The decay of the intracavity intensity and light leaking out can be described in the time domain by:

$$I(t) = I_0 \exp(-t/\tau_{RD}). \tag{3.2}$$

If the only loss mechanisms are due to mirror transmission $(1 - R)$ and absorption by some sample (αL), the ring-down time (τ_{RD}) is defined as:

$$\tau_{RD} = \frac{L}{c(1 - R + \alpha L)}. \tag{3.3}$$

Thus, any attenuation of light within the cavity will cause I to decrease more quickly from the absorption-free value (I_o). It is common practice to account for the loss effects of the mirrors by comparing the ring-down times with and without the sample in the cavity, with the latter baseline value denoted τ^o_{RD}:

$$\alpha = \frac{L}{c}\left(\frac{1}{\tau_{RD}} - \frac{1}{\tau^o_{RD}}\right). \tag{3.4}$$

One of the main attractions of CRDS is its relative immunity to changes in the intensity of light coupled into the cavity. Thus, laser amplitude fluctuations are not a source of noise in the signal. CRDS requires a way to turn off the light coupled into the cavity in order to

measure a decay; it is convenient to use pulsed lasers,[143] however cw lasers can also be used as sources along with a fast switch mechanism such as an acousto-optic modulator (AOM) or rapid current modulation for diode lasers.[142,148–150] To take a complete spectrum of an absorption feature, the ring-down time must be measured across a range of discrete laser frequencies.

In contrast, CEAS, also known as integrated cavity output spectroscopy (ICOS), is best suited to cw laser sources and allows continuous, rapid scanning across an absorption profile. In this case, the cavity transmission is simply measured and time-integrated as the laser wavelength is continuously scanned.[142,146,151–154] When the laser beam is not aligned to propagate along the central axis, the incident laser field will overlap with and couple into higher order TEM_{mn} modes at slightly varying frequencies for a given longitudinal mode. The technique is thus usually referred to as off-axis CEAS to highlight this deliberate misalignment.[152] If sufficient higher order modes are efficiently populated, there will be a near continuous output from the cavity with the intensity related to losses in the cavity, such as from molecular absorption, by:[142]

$$\frac{I_o(\nu)}{I(\nu)} - 1 = \frac{\alpha(\nu)L}{(1-R)}. \tag{3.5}$$

In this case, I_o represents the cavity transmission intensity without the absorber in the optical path.

The use of both CEAS and CRDS is widespread in many fields, particularly atmospheric science and physiology. An excellent review of applications of CEAS and CRDS to atmospheric science was published by Brown in 2003,[155] and Wang and Sahay provided a comprehensive overview of laser spectroscopic gas detection for breath analysis in 2009.[94]

A new approach to off-axis CEAS is presented in this chapter. A related method, optical-feedback CEAS, is described and demonstrated in Chapters 4 and 5.

3.3 DFB-QCL off-axis CEAS

3.3.1 Introduction to off-axis CEAS

Off-axis CEAS is a compact, simple technique that offers quantitative measurements without strict alignment or mechanical stability requirements.[146,152,154] Several studies have demonstrated the feasibility of achieving high sensitivity using off-axis CEAS with cw DFB-QCLs despite increased diffraction losses at longer wavelengths. Moyer *et al.* built a field-ready instrument with a 6.7 μm QCL and 90 cm long, high finesse (∼15,700) cavity that achieved a noise-equivalent absorption sensitivity of 2.4×10^{-11} cm^{-1} Hz$^{-1/2}$.[52] This is a somewhat unrealistic value as it is normalized against the sample rate of individual points rather than the scan rate. Applying the same method of estimating sensitivity as used later in this thesis yields a sensitivity of $\alpha_{min} = 4.5 \times 10^{-8}$ cm^{-1} for a 4 s measurement based on the minimum detectable absorption (MDA) and effective path length given in the paper. Similar instruments at 5.2 μm were developed for online breath-by-breath measurements of nitric oxide and achieved sensitivities < 1 ppb ($\sim 2 \times 10^{-10}$ cm^{-1} Hz$^{-1/2}$).[156,157]

The limiting factor determining sensitivity is often residual mode structure. This occurs when the laser preferentially couples into certain cavity modes leading to an inhomogeneous mode population. In order to reduce this noise, Liu *et al.* modulated piezo-mounted cavity mirrors to increase the density of excited modes to achieve 1.62×10^{-8} cm^{-1} Hz$^{-1/2}$ sensitivity with a DFB-QCL.[158] Modulation can also be applied to the laser frequency for wavelength-modulated integrated cavity output spectroscopy (WM-ICOS), which has been shown to enhance the SNR by as much as a factor of five in the mid-infrared.[156,159,160] While these methods enhance sensitivity, it is often at the expense of large set-ups, additional mechanical requirements, or more complex analysis.

Recently, an alternative method using RF white noise perturbation of the laser current was developed in our group and demonstrated improved SNR in off-axis CEAS measurements using a 100 MHz-bandwidth 764 nm vertical-cavity surface-emitting laser (VCSEL) and moderate finesse (∼700) cavity.[161] Inducing random, uncorrelated fluctuations in the laser frequency has the beneficial effect of promoting efficient wash-out of residual mode

structure by increasing the effective linewidth of the laser. This is the noise paradox: noise is added to the laser in order to reduce noise in the signal. The following section describes an extension of this technique to mid-infrared QCL sources with a significant improvement in off-axis CEAS sensitivity demonstrated for measurements of CO_2. In parallel, the broadening of the effective QCL linewidth caused by the RF perturbation was explored using a pump-probe technique, and the effects of high frequency modulation on the laser examined. The QCL study was published in 2014.[162]

3.3.2 5.29 μm DFB-QCL characterization

A 5.29 μm (1884 – 1897 cm^{-1}) cw single mode DFB-QCL (Maxion, M575AY), similar to the one characterized in Section 2.2.1, was set up in identical housing with the same temperature and current drivers. The laser was operated between -30°and 9°C with a maximum current of 990 mA. Measured I-V and power curves are shown in Figure 3.2. By carefully increasing the driving current just above the threshold level, it was possible to measure the beam profile without damaging the microbolometer elements. Figure 3.3 shows typical collimated beam profile 50 cm from the collimating lens.

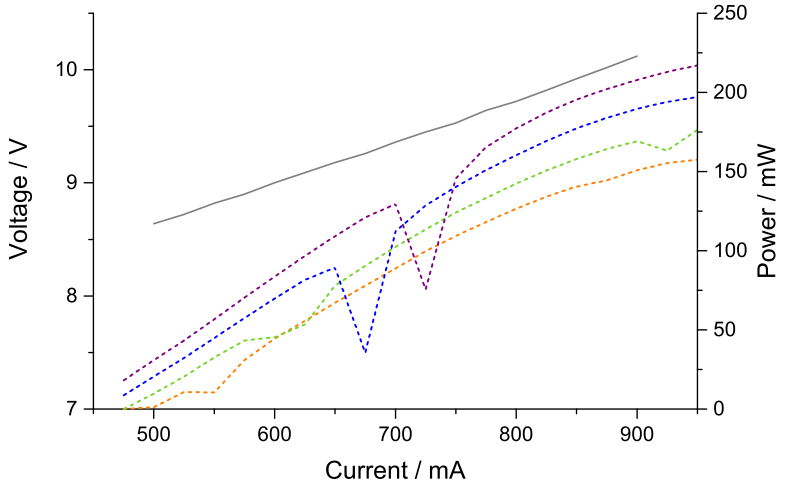

Figure 3.2: Measured output power (dashed lines) of the laser system as a function of driving current for the 5.29 μm DFB-QCL at the following operating temperatures: -5°C (purple); 0°C (blue); 5°C (green); 9°C (orange). The applied voltage (grey solid line) at 9°C is also shown. The drops in measured laser output power (*i.e.* at 725 mA driving current with -5°C operating temperature) occur when the laser frequency scans over the strongly absorbing (6,4,3) ← (5,3,2) ν_2 water vapour transition at 1889.6 cm^{-1}.

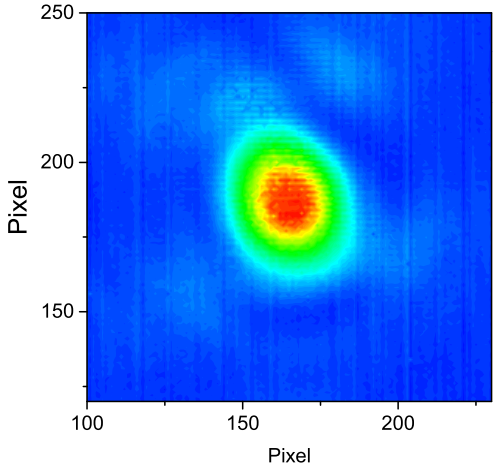

Figure 3.3: Beam profile of collimated 5.29 μm DFB-QCL measured 50 cm from collimating lens. Contours show beam intensity in arbitrary units, with each pixel separated by 35 μm.

3.3.3 Carbon dioxide properties

Carbon dioxide was used as a model gas for these proof-of-principle tests. CO_2 is the infamous culprit of the growing greenhouse effect rapidly changing the planet's radiative balance. As the second most prevalent greenhouse gas (behind water vapour), it is present in unadulterated air in quantities that probably push the definition of "trace" – average global levels in the atmosphere surpassed the 400 ppm mark for the first time in early 2015.[163] Atmospheric CO_2 has been measured for over 100 years, so there is clearly no desperate need for an atmospheric sensor. Measurements are still useful as, for example, there are still uncertainties in quantifying its sinks. Comparisons of the amount of $^{12}CO_2$ and $^{13}CO_2$ in an air sample will vary seasonally and regionally for different plant uptakes and, on a global scale, the ratio is an important indicator of the ocean-atmosphere exchange rates.[164] The gas is also of interest for physiologists as the relative amounts of CO_2 in exhaled breath can be used as an indicator of gas exchange and blood flow in the lungs.[165]

CO_2 is a good exemplar gas for proof-of-principle experiments since it is easy to obtain, safe to use, and has strongly absorbing transitions throughout the spectral region covered by QCLs. As a linear triatomic molecule, CO_2 has four vibrational degrees of freedom, which are accounted for by three normal modes: symmetric stretch (ν_1), antisymmetric stretch (ν_3), and doubly-degenerate bend (ν_2). The transition notation used here is based

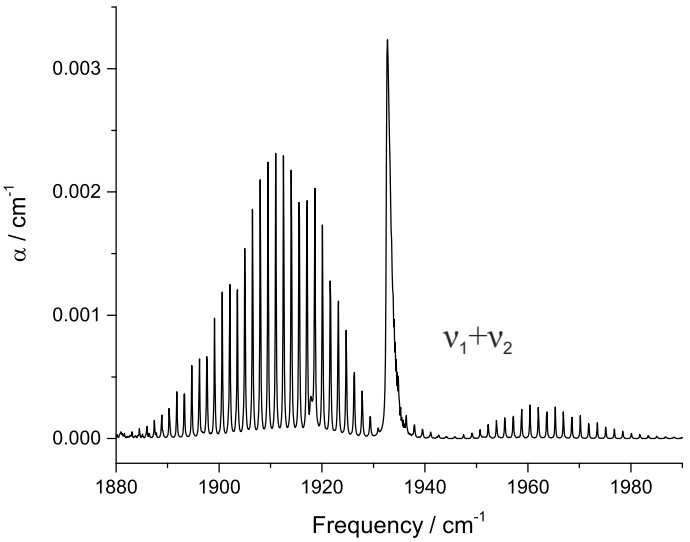

Figure 3.4: Absorption coefficient spectrum of pure CO_2 at 760 Torr showing the $\nu_1 + \nu_2$ combination band.[6]

on that used by HITRAN given by five digits: $\nu_1\nu_2^l\nu_3 r_F$.[166] The additional terms are l, the angular momentum of the bending mode, and r_F, a term included due to a strong Fermi resonance effect in CO_2 between ν_1 and the second overtone of ν_2.[167] The region used for CEAS experiments corresponds primarily to excitation of the $\nu_1 + \nu_2$ combination band (see Figure 3.4).

3.3.4 Experiment

For the CEAS experiment, depicted in Figure 3.5, the 5.29 μm cw DFB-QCL (Maxion) was placed in a custom-built, Peltier-cooled mount. The frequency of the laser could be tuned between 1883 and 1896 cm^{-1} using temperature and current controllers built in-house. A bias tee combined the driving current with the high frequency signal from a broadband noise source. The initial source was an amplified (3×Mini-circuits 10-1500 MHz amplifiers, ZKL-1R5) high-frequency (1 – 1500 MHz) noise generator (RF Design, BBGen). Later experiments used the amplified (2×Mini-circuits 10-1500 MHz amplifiers, ZKL-1R5) output of a broadband (50 kHz – 500 MHz) white noise generator (Noise Brick NB3). The maximum total current noise in the range 10 – 500 MHz was about 300 mA, only a small fraction of which was transferred to the QCL, *vide infra*. The broadband noise generator was replaced with a high frequency signal generator (Marconi Instruments, 2022E) to compare with single frequency current modulation. In both cases the laser frequency was scanned

typically 0.8 cm^{-1} at 200 Hz using a sawtooth voltage applied to the current driver by a function generator (TTI TG230).

The output beam, with a power of up to 220 mW, was collimated by an aspheric lens (f = 4 mm) and directed into an optical cavity composed of two high reflectivity ZnSe mirrors (Los Gatos Research Inc.). A steering mirror in front of the cavity was mounted on a translation stage to allow for easy adjustment of the beam alignment into the cavity. The 22 cm long cavity was enclosed by a stainless steel tube with an outlet port to a diaphragm vacuum pump and an inlet port connected to a pressure gauge (Leybold Ceravac CTR 90) and valve to allow introduction of the sample gas. For this study, the cavity was filled to 60 Torr with a calibrated mixture of 10% CO_2 in a N_2/O_2 mixture (BOC). The beam transmitted through the cavity was focused onto a photovoltaic detector (VIGO, PVMI-3TE-10.6) by an off-axis parabolic mirror. The output of the detector was amplified (Femto DHPCA-100) and sent to a 20 MHz-bandwidth oscilloscope (LeCroy WaveSurfer), which averaged scans and recorded data.

For the pump-probe experiment, conducted in parallel, a 5.26 μm cw DFB-QCL (Maxion, DQ5-M575AH-NS) was operated under similar conditions at an output power of 140

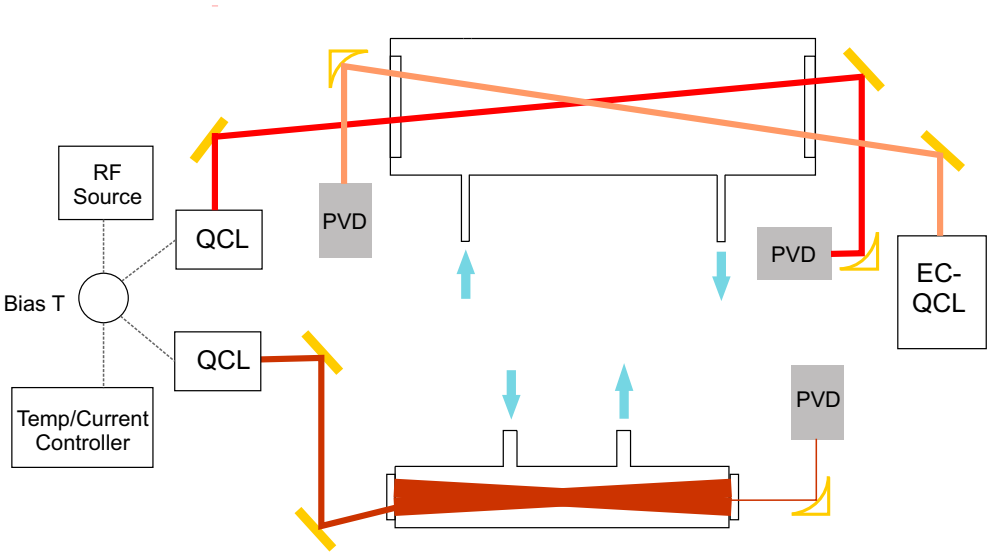

Figure 3.5: Experimental set-up of pump-probe (upper) and off-axis CEAS (lower) experiments. The experiments used different DFB-QCLs run under very similar conditions with the current combined with RF modulation in the bias-T. Arrows indicate inlets and outlets for gas samples and vacuum pump.

mW and a fixed frequency within the e component of the $R(6.5)_{\frac{1}{2}}$ $v = 1 \leftarrow 0$ ro-vibrational transition in NO at 1900.07 cm^{-1}. An external cavity (EC) QCL (Daylight Solutions) outputting 100 mW optical power was tuned across the $P(7.5)_{\frac{1}{2}}$ $v = 2 \leftarrow 1$ transition at a relatively slow rate (0.344 kHz/ns) using a function generator (TTi TG1304) output applied to the diffraction grating actuator. The beams counter-propagated through a 70 cm long cell filled with NO to a pressure of 43.5 mTorr, as shown in Figure 3.5, and the EC-QCL signal was collected by a photovoltaic detector (Vigo PVMI-3TE-10.6). This configuration results in a sub-Doppler velocity group being pumped from the ground vibrational state into the first excited state by the DFB-QCL, which is then probed by the EC-QCL. The width of the measured absorption is therefore a convolution of the velocity selected width (determined by the pump laser linewidth) and the linewidth of the probe laser ($\sim$2 MHz).[168] Approximately 100 scans of the probe laser were taken with various levels of RF applied to the DFB-QCL. The signals were averaged using a post processing program in MATLAB to identify the absorption maxima and re-centre them to account for phase fluctuations in the function generator. The frequency tuning rate was measured using a Ge etalon with a free spectral range of 490 MHz at the working wavelength.

3.3.5 Results

The effect of the RF noise on the linewidth of the 5.26 μm pump laser is shown in Figure 3.6. Increasing the amplitude of the RF noise leads to an increase in the observed linewidth as expected. With no RF noise applied the width of the absorption feature is measured as 6 ± 0.01 MHz by fitting with a Gaussian profile. The linewidth is observed to increase to 20 ± 0.02 MHz with 27 dB of amplification applied to the RF noise generator, and to 27 ± 0.03 MHz with 30 dB amplification. At 80 dB RF amplification (300 mA across 10 – 500 MHz), which is the RF power corresponding to the CEAS results, the line profile was similar to the Doppler width of the transition (130 MHz) and therefore could not be quantitatively measured using this method.

The extent of broadening to the 5.29 μm DFB-QCL was analysed under similar perturbation conditions using a low pressure reference gas. A portion of the laser output

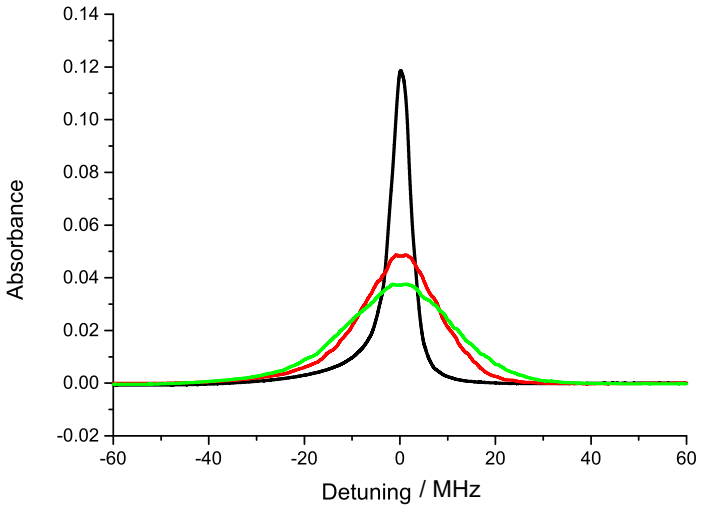

Figure 3.6: The hot band absorption from a pump-probe spectroscopy experiment with increasing amounts of RF noise applied to the pump laser. The signal with no RF (black) has a width of 6 MHz, increasing to 20 MHz with 27 dB noise (red) and 27 MHz with 30 dB noise (green) applied to the laser. All are plotted against the detuning of the probe laser from two-photon resonance.

was directed through a 5 cm long glass cell with BaF_2 windows containing a few Torr of pure NO. The laser was scanned over the NO doublet absorption feature, consisting of several overlapping hyperfine transitions centred at 1890.707 and 1890.719 cm^{-1}. The signal was measured on a photodiode (VIGO, PVMI-3TE-10.6) and recorded on an oscilloscope (LeCroy WaveSurfer). The separation of the features (350 MHz) is larger than the linewidth of the unperturbed laser (few MHz) and the linewidth of the transitions (∼130 MHz), so the features are clearly separated in the black spectrum shown in Figure 3.7. In the first case, 85 kHz modulation was applied to the laser through the bias tee according to a similar experiment recently reported by van Helden *et al.* using an EC-QCL.[169] It is clear from Figure 3.7 that the modulation depths used in the previous study are not pragmatic for this DFB-QCL system; the spread of signal upon modulation indicates that frequency

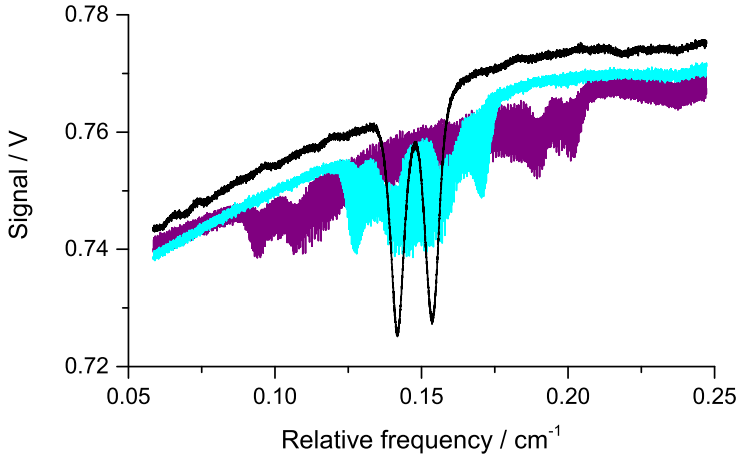

Figure 3.7: NO $^2\Pi_{1/2}$ and $^2\Pi_{3/2}$ R(3.5) transitions at 1890.707 and 1890.719 cm^{-1} respectively (*i.e.* $\Delta\tilde{\nu} \approx 0.0117$ cm^{-1}) measured with the laser modulated at 85 kHz with amplitudes of 0 mV (black), 100 mV (blue), and 300 mV (purple).

excursions of the laser are on the order of GHz, which will lead to significant broadening of measured absorption profiles. The broadened spectra are quite noisy relative to the unperturbed laser.

The effect of broadband noise used in these experiments on the laser behaviour was markedly different and is shown in Figure 3.8. The NO spectrum with the laser unperturbed is again shown with a black line. The other spectra were collected with the amplified BBGen noise generator perturbing the QCL with different bandwidths of noise applied. The unfiltered RF noise (1 – 1500 MHz) had a negligible effect on the measured spectrum (red line), and no change was observed when a 50 MHz high pass filter was inserted before the bias tee (green line). There was a clear broadening of the spectrum – and thus presumably the effective laser linewidth – when 30 MHz (dark blue) and 11 MHz (light blue) low pass filters were applied to the RF noise. This behaviour reveals an interesting phenomenon – the application of high frequency noise does not cause have the same effective linewidth

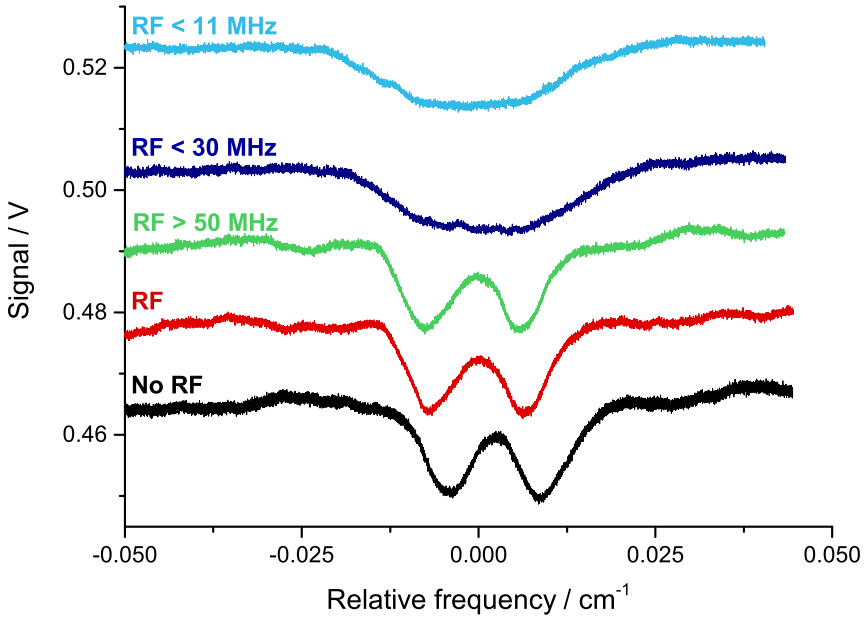

Figure 3.8: Spectra of ≈ 2 Torr NO in a 5 cm long reference cell. The QCL was scanned at a rate of 100 Hz with no RF modulation (black), amplified RF modulation (red), RF modulation ≥50 MHz (green), RF modulation ≤30 MHz (dark blue), and RF modulation ≤11 MHz (light blue). Data are offset for clarity.

broadening effect, and it also prevents low frequency components from affecting a change. This indicates that some parasitic elements in the circuit affect the frequency response of the system, however these are not problematic if the applied modulation frequency is kept below ∼30 MHz. Based on these results, we elected to proceed with the lower frequency Noise Brick noise generator, which effectively broadened the laser without any bandwidth filtering. A comparison of the frequency distribution of the two noise sources was performed by taking a Fourier transform of an absorption-free portion of the spectrum with amplified RF noise applied to the laser. The integrated area of each is approximately the same: 1.22×10^4 V Hz for the BBGen device with 30 MHz low pass filter compared to 1.13×10^4 V Hz for the Noise Brick. As expected from the manufacturers' specifications, the Noise Brick output was weighted more heavily to low frequency noise.

To determine the effect of this linewidth broadening on CEAS measurements, the 5.29 μm laser was scanned over the P(56) $11^102 \leftarrow 00^001$ transition (1890.330 cm^{-1}) and the P(36) and P(37) $12^202 \leftarrow 01^101$ transitions (1890.337 and 1890.490 cm^{-1} respectively) of CO_2. The absorption was calculated from the transmitted intensity (I) using the usual CEAS formula assuming that the sample absorption is weak compared to the mirror loss:[149,150]

$$\left(\frac{I_o}{I} - 1\right) = \frac{\alpha L}{(1-R)}. \tag{3.6}$$

The absorption coefficient (α) can therefore be determined based on the physical cavity length (L) and measured effective reflectivity of the mirrors (R). The reference signal (I_o) was determined by fitting the baseline to a third order polynomial in the frequency domain. The average mirror reflectivity (geometric mean) was determined to be 0.99930 by measuring the ring-down time under the same alignment conditions as the absorption measurements ($\tau^o_{RD} = 1.0490 \pm 0.0225\ \mu s$). The cavity field was turned off for the ring-down measurement by applying a sawtooth voltage ramp so that the laser current dropped below the threshold level; the rate at which the current changed was much faster than the ring-down time, and therefore does not affect the exponential decay. Figure 3.9 shows raw data of CO_2 absorption features at 1890 cm^{-1} with the corresponding absorption spectra shown in Figure 3.10 for three laser current perturbation regimes: unperturbed (NP, blue),

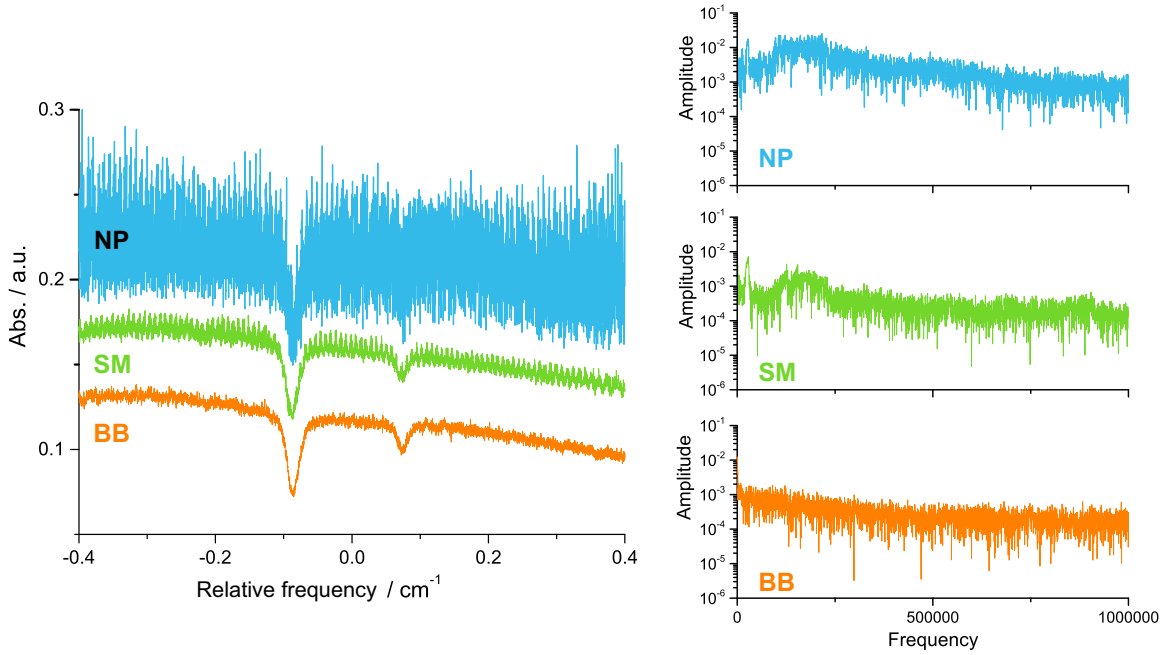

Figure 3.9: (left) Raw off-axis CEAS data (20 scans averaged) collected with laser frequency decreasing at a scan rate of 200 Hz and represent 20 scans averaged (100 ms acquisition time) corresponding to no perturbation (NP, blue), 1 MHz single frequency modulation (SM, green), and broadband RF perturbation (BB, orange) applied to the laser current. Data are offset for clarity. (right) Fast Fourier transform (FFT) analysis of baseline noise for the spectra shown. While the single frequency modulation (SM) diminished the broad shoulder around 100 – 200 kHz, the broadband perturbation (BB) completely eliminated this low frequency noise feature and the frequency distribution appears homogeneous. The spike at low frequency corresponds to the FSR of the cavity. Frequency in the FFT analysis given in Hz.

single frequency modulation (SM, green) and broadband (BB, orange) RF perturbation. The difference in the quality of the data is readily apparent. The data shown here are the average of 20 consecutive scans, which allowed for a significant improvement in SNR compared to single shot measurements without significantly prolonging acquisition time. The frequency axis was determined using the Ge etalon.

Each spectrum was fit with three Voigt lineshape profiles, with the Lorentzian component of the lineshape fixed to the theoretical pressure-broadened width based on HITRAN broadening parameters.[6] The laser lineshape is likely to experience a Gaussian broadening due to the finite bandwidth of the noise.[170,171] Taking the Gaussian linewidth to be the Doppler profile and allowing the Lorentzian component to vary did not affect the overall results. Due to the significant overlap between the transitions at 1890.330 and 1890.337 cm^{-1}, the centre frequency separation and line strength ratio were fixed in the fitting rou-

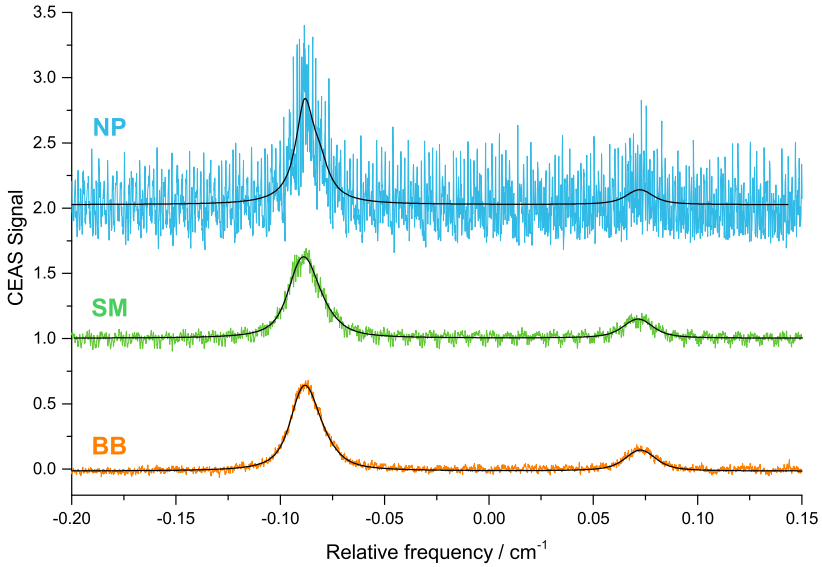

Figure 3.10: Cavity-enhanced absorption spectra measured with no RF (blue), 1 MHz (green), and broadband (orange) perturbation of the laser frequency (data offset for clarity) with Voigt profile fits. All data were collected with laser frequency decreasing at a scan rate of 200 Hz and represent 20 scans averaged (100 ms acquisition time). Data are offset for clarity.

tine. The parameters of the fits shown in Figure 3.10 are given in Table 3.1. The narrow fitted linewidth of the low wavenumber transition with the unperturbed laser is attributed to the high noise level on this spectrum.

The SNR enhancement from the white noise generator was compared with 1 MHz single frequency noise applied to the current. The modulation amplitude was 100 mV (compared to the $\approx$ 6 V ramp for the entire frequency scan), which causes a similar degree

Table 3.1: Fitted integrated absorption, Voigt linewidths, and minimum detectable absorption (MDA) for spectra shown in Figure 3.10. The transitions are given in order of increasing energy: 1890.330, 1890.338, and 1890.490 cm^{-1}. The expected linewidths, based on HITRAN broadening coefficients, are 0.01296, 0.01340, and 0.01422 cm^{-1}, respectively. In all fits, Lorentzian linewidths, centre frequency separation, and ratio of transition areas were fixed in fitting routine.

Noise condition	**A**	**FWHM** / cm^{-1}	**MDA** per 100 ms
NP (No perturbation)	0.01191	0.01049	5.8×10^{-2}
	0.00398	0.01129	
	0.00248	0.01540	
SM (1 MHz single frequency modulation)	0.01155	0.01608	9.9×10^{-3}
	0.00386	0.02057	
	0.00346	0.01717	
BB (Broadband RF)	0.01183	0.01542	5.5×10^{-3}
	0.00395	0.01871	
	0.00384	0.01757	

Table 3.2: Derived spectral linewidths from a Gaussian fit to data collected under the three perturbation conditions and over different averaging times. The last column gives the mean absolute residual to the fit.

Noise condition	# averages	FWHM / s	σ_{res} / V
NP	1	1.31×10^{-4}	1.11×10^{-1}
	10	1.07×10^{-4}	6.14×10^{-2}
	100	1.03×10^{-4}	1.89×10^{-2}
	2000	1.06×10^{-4}	4.87×10^{-3}
SM	1	1.16×10^{-4}	1.34×10^{-2}
	10	1.15×10^{-4}	7.86×10^{-3}
	100	1.15×10^{-4}	3.47×10^{-3}
	2000	1.05×10^{-4}	1.31×10^{-3}
BB	1	1.15×10^{-4}	1.22×10^{-2}
	10	1.13×10^{-4}	3.19×10^{-3}
	100	1.13×10^{-4}	1.68×10^{-3}
	2000	1.20×10^{-4}	1.12×10^{-3}

of lineshape broadening compared to the noise source (~30% broader than the unperturbed regime) as indicated in Table 3.2. This degree of linewidth broadening corresponds to a current excursion of approximately 3 mA, indicating that only about 1% of the RF power is injected into the laser. It was not possible to precisely measure the coupling efficiency because the laser chip was housed in a sealed unit. The low coupling efficiency estimated is reasonable since the previous study using a VCSEL found an RF noise coupling efficiency of 1% using a similar set-up.[161]

Using the treatment described by Moyer *et al.*, acquisition bandwidth-corrected minimum detectable absorption (MDA) values were determined for the three different conditions of laser frequency perturbation based on the data and fits shown in Figure 3.10.[52] Using the standard deviation of the residual to the fit as σ_{res}, the MDA for 1 MHz single frequency modulation is 9.95×10^{-3} $Hz^{-1/2}$ based on the 100 ms measurement, which itself represents a twentyfold improvement of the MDA from a similar study with an EC-QCL.[169] The broadband RF source provided an even greater improvement in sensitivity, with an MDA of 5.54×10^{-3} $Hz^{-1/2}$. This is more than a factor of ten better than the same measurement with no RF perturbation. Furthermore, fast Fourier transform (FFT) analysis of the baseline (Figure 3.9) shows that the broadband perturbation homogenized the frequency distribution of the noise.

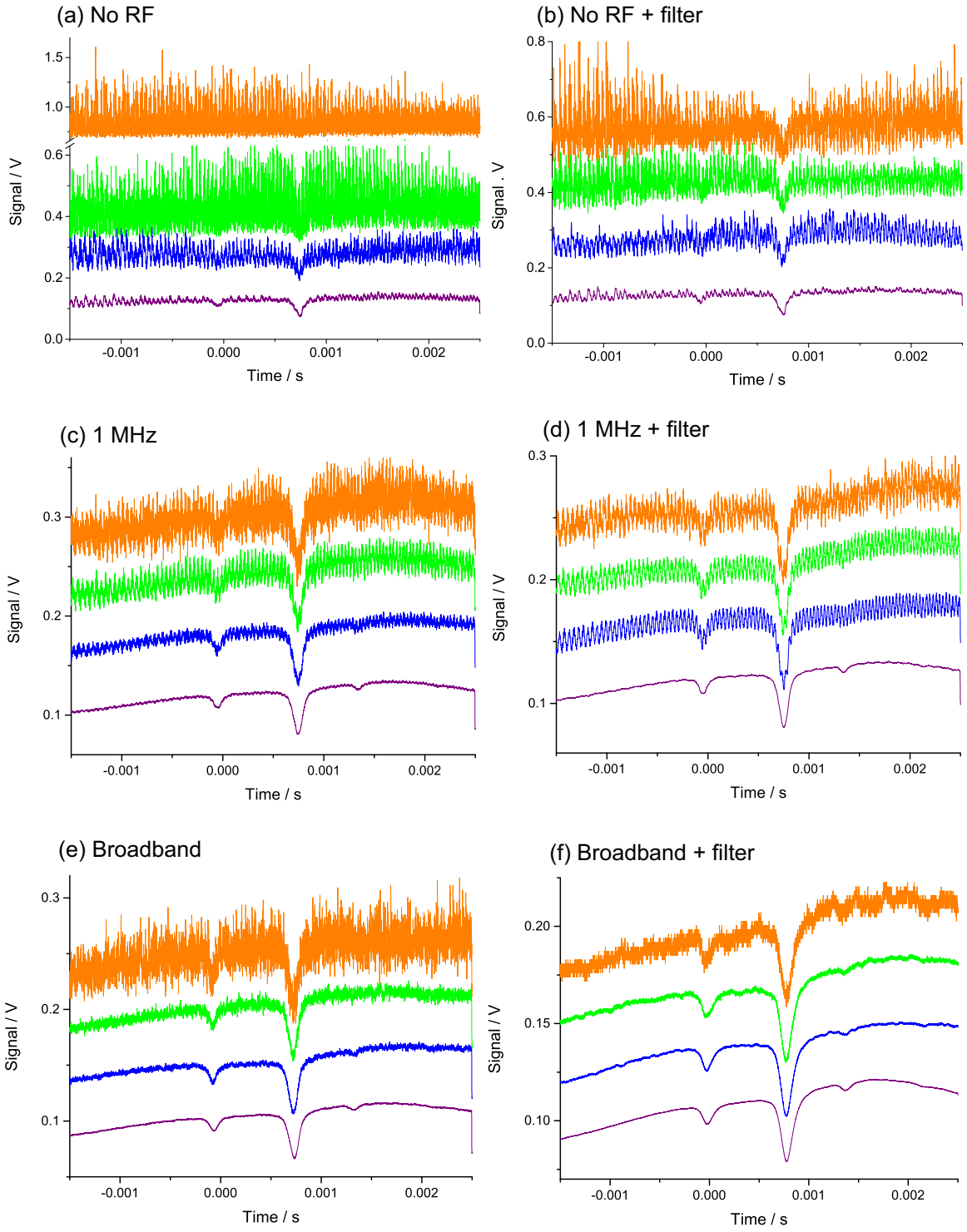

Figure 3.11: Comparison of off-axis CEAS cavity transmission signal for different noise conditions and averaging times. Data averaged over 2000 (purple), 100 (blue) and 10 (green) scans are shown with a single scan (orange). The noise conditions were: (a),(b) unperturbed; (c),(d) 1 MHz modulation; (e),(f) broadband RF perturbation. A 15 kHz low-pass filter was used to reduce high frequency noise in (b), (d), and (f).

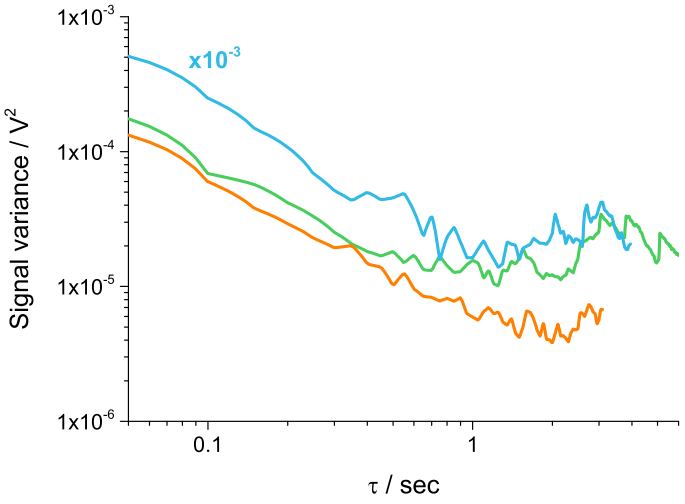

Figure 3.12: Allan-Werle plot of signal variance for off-axis CEAS with no RF perturbation (blue), 100 mV modulation at 1 MHz (green), and broadband RF perturbation with 80 dB amplification (orange). The typical signal amplitude in all cases was about 150 mV. The NP variance has been scaled by three orders of magnitude for clarity. Each line is an average of the signal variance at six or more points across the scanned region.

Where rapid acquisition is not required, the SNR can be further enhanced by longer signal averaging. Figure 3.11 shows a series of measurements varying the number of scans averaged for the three laser current conditions. The single point Allan-Werle variance (Figure 3.12) indicates an improvement in sensitivity up to two seconds averaging time.[50,51] Not only is there a substantial improvement with single frequency or broadband perturbation, in agreement with the values in Table 3.2, the noise also pushes the minimum in the variance curves to longer averaging times. Thus, the sensitivity can be improved by averaging over longer periods when current perturbation is applied. This shows that, with a broader laser linewidth, the signal intensity is less vulnerable to, for example, changes due to mechanical disturbances or temperature variations.

Long-time measurements are subject to baseline drifts, which can be minimized with improved thermal isolation and mechanical stability of the detector and cavity. To measure an optimal sensitivity, 400 scans were averaged with a 15 kHz low pass filter on the signal to eliminate high frequency noise. While the filter effectively reduced high frequency noise on the signal (see Figure 3.11), the absorption profile signal was broadened by a further $\sim 20\%$. A cubic baseline fit yields a standard deviation of 1.92×10^{-3}, which results in a minimum measurable absorption coefficient (α_{min}) of 6.1×10^{-8} cm^{-1} corresponding to a minimum detectable CO_2 concentration of 314 ppm at 60 Torr. For comparison, a similar baseline fit of the unfiltered spectra averaged over 20 scans yields an α_{min} of 5.7×10^{-7} cm^{-1}. This is lower than the α_{min} value associated with the MDA given above as this solely accounts for

baseline noise and does not include errors due to the quality of the lineshape fit.

3.4 Conclusions

Off-axis CEAS measurements of CO_2 with a DFB-QCL were significantly enhanced by applying a perturbation to the driving current, which was shown to broaden the effective linewidth of the laser. Both broadband and single RF modulation of the laser frequency significantly improved the SNR compared to the control experiment without laser perturbation, however the white noise demonstrated several advantages in experimental robustness and sensitivity. An MDA of 5.54×10^{-3} $Hz^{-1/2}$ was achieved with an acquisition time of 100 ms, demonstrating a tenfold improvement over the unperturbed condition. The fast acquisition time makes this technique suitable for studies requiring rapid, real-time measurements such as breath diagnostics or atmospheric monitoring. Allan-Werle analysis demonstrated that the laser current perturbation extends the optimal averaging time since the random current fluctuations that broaden the linewidth ease restrictions on the stability of the cavity. RF perturbation can be improved with further investigations of the frequency response of the QCL system and adjustments to the bias tee circuitry in order to determine the most effective RF range for modulation and eliminate parasitic electronic effects. The technique may be used to tune the effective linewidth of the QCL for applications benefiting from specific linewidths broader than the intrinsic bandwidth of the laser. Broadband perturbation is an ubiquitous tool that can be applied to a range of experiments with varying alignments and scanning conditions without making any alterations to the modulation conditions. The relaxation of cavity alignment tolerances makes this technique particularly attractive for field applications where *in situ* adjustments are difficult. In the fight against noise, sometimes more noise is the solution.

Chapter 4

V-shaped Cavity OF-CEAS: Extension to New Mid-infrared Laser Sources

4.1 Introduction to OF-CEAS

Laser spectroscopists have long lamented problems arising from inadvertent reflections returning to the laser facet. When a sufficient amount of phase-matched light within the gain spectrum of the semiconductor laser is coupled into the laser cavity, a phenomenon known as optical feedback occurs. The external field acts as injection seeding, causing the laser frequency to deviate from the free running condition dictated by the current and temperature applied.[172–174] Under the influence of optical feedback, a continuously scanning laser will exhibit discontinuous jumps in emitted wavelength and spectral information will be lost.

The simplest type of optical feedback originates from a single reflection off an external reflector. This type of feedback is a pervasive, often unwanted, effect and has been studied extensively in diode lasers, notably in a seminal article published by Roy Lang and Kohroh Kobayashi in 1980.[173,174] They laid the groundwork for theoretical descriptions of the behaviour of a feedback-coupled laser, which will be discussed further *vide infra*. In this paper, the authors noted multistability in laser frequency arising from interfering effects – due to a broad gain spectrum and sensitive dependence of laser medium refractive index on temperature and carrier density – which leads to a characteristic sawtooth-like power and frequency output as the laser current is scanned. The sawtooth arises from pe-

riods of retarded frequency tuning, relative to the free running rate, interjected by nearly instantaneous frequency jumps.[175]

Feedback can arise from sources other than direct reflections, such as high finesse optical cavities. Optical-feedback cavity-enhanced absorption spectroscopy (OF-CEAS), first demonstrated by Jérôme Morville *et al.* in 2005, exploits optical feedback to couple the laser with an optical cavity containing an absorbing gas.[176] When the laser is aligned on-axis with an optical cavity, a resonant feedback field arises if the laser wavelength excites a longitudinal mode of the cavity, stimulating laser emission at the resonant wavelength. If the cavity has a high finesse, this returning field has a narrow linewidth ($\sim$10s – 100s of kHz) relative to the free running linewidth of the laser ($\sim$ few MHz for QCLs, typically determined by the quality of the current controller). Thus, a resonant cavity field in phase with the laser induces a narrowing of the emitted linewidth, even beyond the cavity bandwidth.[176–179] The laser becomes "locked" to the cavity frequency. This term can be misleading as it describes the condition when the laser frequency is being tuned at a rate proportional to the inverse square of the ring-down time; for most optical cavities, this change is much smaller than the linewidth of the field and the laser frequency is treated as a single value.[179] The passive locking of the laser to the resonant cavity allows a build-up of intracavity intensity and, correspondingly, an increase in the measured transmission signal. The narrowed linewidth enhances injection efficiency into the resonant cavity field as the portion of laser power within the cavity linewidth increases, creating a positive feedback loop until an equilibrium is reached. At this point, signal amplitude noise arising from laser frequency fluctuations is eliminated.[179] The cavity remains in resonance much longer than the average photon lifetime of the system before discontinuously returning to its free running condition (dictated solely by electronic drivers).

As the laser frequency is scanned, it comes into and out of resonance with the cavity, forming a comb of frequencies that can be used to probe molecular absorptions of gases within the cavity. The resonant cavity modes are separated by the FSR of the cavity, which is simply determined by its physical length (L), the refractive index of the intracavity

medium (n_i), and the speed of light (c):

$$\mathrm{FSR} = \frac{n_i c}{2L}. \tag{4.1}$$

The FSR is usually on the order of the Doppler linewidth of the sample gases at ambient temperatures (~ 50 – 300 MHz in the mid-infrared), making this technique best suited for pressure-broadened systems typical of sensing applications.

The next section introduces the theoretical basis of OF-CEAS, followed by a description of three different V-shaped OF-CEAS experiments and the results obtained. These systems represent the first successful demonstrations of OF-CEAS with DFB-ICL and EC-QCL sources, and the viability of these lasers for optical feedback experiments is discussed.

4.2 OF-CEAS theory

4.2.1 Feedback effects

Understanding the physical basis of OF-CEAS requires developing quantitative descriptions of the laser and intracavity radiation fields. The time-varying laser field (E) under the influence of optical feedback can be modelled as:[173,180]

$$\frac{d}{dt}\left(E(t)\exp(i2\pi\nu t)\right) = E(t)\exp(i2\pi\nu t)\left[\frac{i\pi c}{n_o \ell} + \frac{1}{2}\left(G(N) - \Gamma_o\right)\right] + \kappa E(t-\tau)\exp(i2\pi\nu(t-\tau)) \tag{4.2}$$

where variables include the carrier density-dependent gain factor ($G(N)$), the laser cavity loss (Γ_o), the refractive index of the gain medium (n_o), the laser cavity length (ℓ), and the laser frequency (ν). The last term on the right-hand side was added by Lang and Kobayashi in order to account for feedback effects, scaled by κ and delayed by some time constant τ.[173] One can derive an expression relating the free running laser frequency (ν_o) to the feedback-coupled laser frequency (ν_{fb}):

$$\nu_o = \nu_{fb} + \frac{\sqrt{\beta}(1-R_o)c}{2\ell n_o \sqrt{R_o}}\left[\mathrm{Re}(h_{fb})\sin\left(\frac{4\pi L'\nu_{fb}}{c}\right) - \mathrm{Im}(h_{fb})\cos\left(\frac{4\pi L'\nu_{fb}}{c}\right)\right]. \tag{4.3}$$

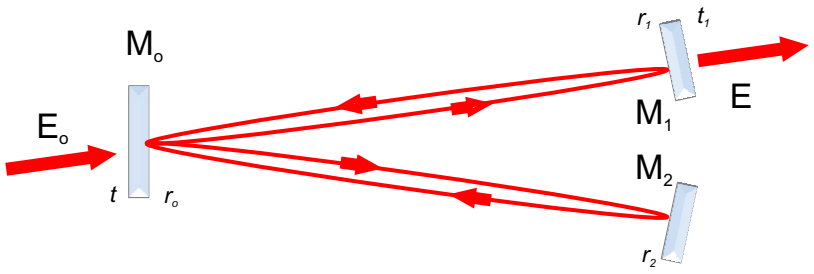

Figure 4.1: Schematic of V-shaped optical cavity where light is injected through M_0 and is reflected in a V pattern with a small angle between the two cavity arms. In this case, the cavity transmission through M_1 is measured, however the signal can be measured after M_2. The reflection (r) and transmission (t) coefficients are labelled individually for the three cavity mirrors as shown.

The full derivation is given in the Appendix. The expression given assumes $\alpha_H = 0$, such as for QCLs, however application of a $\sqrt{1+\alpha_H^2}$ scale factor to the numerator of the right hand term can account for linewidth broadening effects in other types of lasers. Feedback is dependent on the reflectivity of the laser facet (R_o), the laser–cavity distance (L'), the feedback rate (β), and the feedback transfer function (h_{fb}). The feedback rate is the ratio of the power of feedback light coupled back into the laser to the power emitted by the laser.

The transfer function describes changes to the field intensity and phase due to external optics, and is therefore determined by the characteristics of the optical cavity. The first OF-CEAS experiments utilized V-shaped optical cavities comprised of a central folding mirror, through which the incident light enters, and two end mirrors as shown in Figure 4.1. This geometry ensures that only light leaking from the cavity will return back to the laser facet since the reflection of the emitted beam incident on M_0 is directed away from the laser. Cavity transmission can be measured from light leaking out of either – or both – end mirrors. The field returning to the laser is the sum of light leaking through M_0 (from the M_1 arm) on each round-trip pass:

$$\begin{aligned} E_{fb} = E_i \quad & \left[t^2 r_1 \exp\left(-(2ik+\alpha)L_1\right) + t^2 r_o^2 r_1^2 r_2 \exp\left(-(2ik+\alpha)(2L_1+L_2)\right)\right. \\ & \left. + t^2 r_o^4 r_1^3 r_2^2 \exp\left(-(2ik+\alpha)(3L_1+2L_2)\right) + \ldots\right] \end{aligned} \tag{4.4}$$

where E_i is the incident field, α is absorption coefficient, and the transmission (t) and reflection (r) coefficients are as indicated in Figure 4.1. The phase factor term k is defined as $2\pi/\lambda$. On each pass, the field undergoes an odd number of π phase shifts off the dielectric

mirror and an even number of π Gouy phase shifts through an intracavity waist if all mirrors are concave (or an odd number if M_0 is flat while M_1 and M_2 are curved). It is important to note here that r_i and t_i refer to reflection and transmission coefficients, which apply to the electric field, whereas R_i and T_i are the reflectivity and transmissivity of the intensity such that, for example, $R_i = |r_i|^2$. Using an approximation for the infinite sum, which is valid when $\alpha \ll 1$, the feedback transfer function can be written as:

$$h_{fb,V} = \frac{E_{fb}}{E_i} \approx \frac{t^2 r_1 \exp\left(-(2ik+\alpha)L_1\right)}{1 - r_o^2 r_1 r_2 \exp\left(-(2ik+\alpha)(L_1+L_2)\right)}. \tag{4.5}$$

In order to calculate its value based on measurable quantities, it is reasonable to assume that an average reflectivity can be used for all mirrors ($R = |r_1|^2 = |r_2|^2 = |r_o|^2$). Furthermore, typical V-shaped optical cavities have arms of equal length ($L_1 = L_2 = \frac{1}{2}L$), and so the transfer function is:

$$h_{fb,V} = \frac{T\sqrt{R}\exp\left(-(2ik+\alpha)\frac{L}{2}\right)}{1 - R^2\exp\left(-(2ik+\alpha)L\right)}. \tag{4.6}$$

When the laser is on resonance, this simplifies to:

$$h_{fb,V} = \frac{T\sqrt{R}\exp\left(-\alpha\frac{L}{2}\right)}{1 - R^2\exp(-\alpha L)} \tag{4.7}$$

or, in the case of zero absorption:

$$h^o_{fb,V} = \frac{T\sqrt{R}}{1-R^2}. \tag{4.8}$$

The transfer function in Equation 4.3 is therefore only dependent on cavity length, laser frequency, mirror reflectivity, and intracavity absorption.

Next, it is necessary to consider how the absorption is calculated when the radiation field overlaps itself as it passes through the sample. In contrast to multipass cells where the beam interacts with a different region of the sample volume on each pass, some of the gas molecules along the overlapping beam path will already be internally excited by absorption. To determine an expression relating molecular absorption to a change in measured cavity transmission, a similar method is applied as above to find a transfer function describing the

transmitted field. The cavity transmission can be measured after either M_1 or M_2, which have slightly different transfer functions labelled h_{V1} and h_{V2} respectively given by:

$$h_{V1} = \frac{tt_1 \exp\left(-(2ik+\alpha)\frac{L}{4}\right)}{1 - r_o^2 r_1 r_2 \exp(-(2ik+\alpha)L)} \tag{4.9}$$

and

$$h_{V2} = \frac{tt_2 r_o r_1 \exp\left((2ik+\alpha)\frac{3L}{4}\right)}{1 - r_o^2 r_1 r_2 \exp(-(2ik+\alpha)L)}. \tag{4.10}$$

As the signal measured is an intensity, it is more useful to determine the ratio between the transmitted and incident laser intensity. At a resonant frequency this ratio of light intensity measured on the M_1 arm, for example, is:

$$\frac{I_\alpha}{I_i} = |h_{V1}|^2 = \frac{T^2 \exp\left(-\alpha\frac{L}{2}\right)}{\left(1 - R^2 \exp(-\alpha L)\right)^2} \tag{4.11}$$

while in the case where no absorbing species is present:

$$\frac{I_o}{I_i} = |h_{V1}^o|^2 = \frac{T^2}{(1-R^2)^2}. \tag{4.12}$$

The amount by which absorption attenuates the transmitted light intensity can then be inferred by finding the ratio:

$$\frac{I_o}{I_\alpha} = \frac{|h_{V1}^o|^2}{|h_{V1}|^2} = \frac{T^2\left(1 - R^2\exp(-\alpha L)\right)^2}{T^2\exp\left(-\alpha\frac{L}{2}\right)(1-R^2)^2}. \tag{4.13}$$

Assuming $\exp(-\alpha\frac{L}{2}) \approx 1$ and applying the approximations $\ln(1-x) \approx -x - \frac{x^2}{2}\ldots$ and $(1-x^2) \approx 2(1-x)$ leads to a simple expression relating the absorption coefficient to measured signals:

$$\alpha = \frac{(1-R^2)}{L}\left(\sqrt{\frac{I_o}{I_\alpha}} - 1\right) = \frac{2(1-R)}{L}\left(\sqrt{\frac{I_o}{I_\alpha}} - 1\right). \tag{4.14}$$

Equation 4.14 is the same for both h_{V1} and h_{V2}.

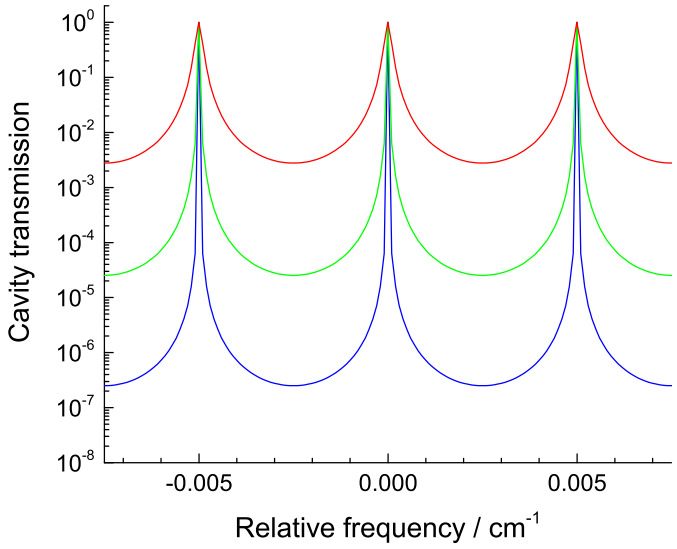

Figure 4.2: Sample Airy function model of cavity transmission for three different values of R: 0.999 (blue), 0.99 (green), and 0.9 (red). An optical cavity length of 100 cm is assumed in all cases, and the cavity transmission is normalized against incident light intensity.

4.2.2 Optical cavity theory

The width of the resonance, or cavity bandwidth, is determined by the mirror reflectivity, as seen in Equation 3.1 which defines the cavity finesse. The cavity transmission (I) for light injected at normal incidence can be described by an Airy function:[181]

$$I = I_i \left(1 + \frac{4R}{(1-R)^2} \sin^2 \left[\frac{2\pi\nu L}{c}\right]\right)^{-1} \tag{4.15}$$

where I_i is the incident power and $\tilde{\nu}$ is laser frequency in Hz. Calculated Airy functions for typical optical cavities in Figure 4.2 clearly show a narrowing in cavity bandwidth as R increases. For OF-CEAS, the laser bandwidth is much smaller than the FSR of the cavity and the cavity length is fixed while the laser frequency is scanned. In other systems, particularly with broader laser sources, the laser wavelength is fixed and the cavity length is scanned by mounting a mirror on a movable platform or piezoelectric actuator.[142]

4.2.3 Phase matching

Models must consider phase effects carefully since feedback must be in phase with the laser emission in order to stimulate emission and lock the frequency. In addition to the phase

development arising from the distance covered by the intracavity field, the intracavity field will undergo a π Gouy phase shift at its focal point located at z_o.[35] As long as each round-trip pass of the cavity involves an even number of Gouy phase shifts, there is no destructive interference from this effect. For the V-shaped systems, it was assumed that TEM_{00} are the dominant transverse modes.[179]

The cavity mirrors alter the phase of the field reflected off the high reflectivity surface. Cavity mirrors are typically fabricated from high quality, optically transparent substrates with specialized coatings for the wavelength of interest. In the mid-infrared, common substrate materials include ZnSe, CaF_2, and BaF_2. On the front face of the mirror – the surface on the inside of the cavity – a dielectric film is deposited that results in high reflectivity at the target wavelength. This coating is a series of alternating layers of thin dielectric films with two different refractive indices ($n_1 > n_2$), beginning and ending with the more optically dense material (n_1). If the optical thickness of each layer is equivalent to $\lambda/4$, *i.e.* $n_1 l_1 = n_2 l_2 = \lambda/4$, then all reflections will be in phase as shown in Figure 4.3.[10] Multiple layers result in a large fraction of the incident light being reflected with constructive interference between beams reflected from each interface. Similarly, an anti-reflection coating can be applied to a substrate where a dielectric material with a refractive index between that of the substrate and air is sandwiched between the two media. If this layer has a thickness equivalent to $\lambda/4$, then complete destructive interference will occur between the reflected beams.

Phase-matching should be optimized for as many excited longitudinal modes as possible in the ideal case. To ensure that each consecutive longitudinal mode has the same phase as the laser, the laser–cavity distance (L') is set to an integer multiple of the cavity length. Or, more specifically, it should satisfy $2L' = N\lambda$ at each wavelength of the cavity where N is a positive integer.

The picture becomes slightly more complex in a V-shaped cavity. The beam follows the pattern $M_1 \rightarrow \boxed{M_0} \rightarrow M_2 \rightarrow M_0 \rightarrow M_1 \rightarrow \boxed{M_0} \rightarrow M_2 \ldots$ where any field that leaks out through M_0 on the passes in boxes can return to the laser. Thus, if the total cavity length is L with symmetric arms, the feedback field traverses $L + 2nL$ before exiting the cavity.

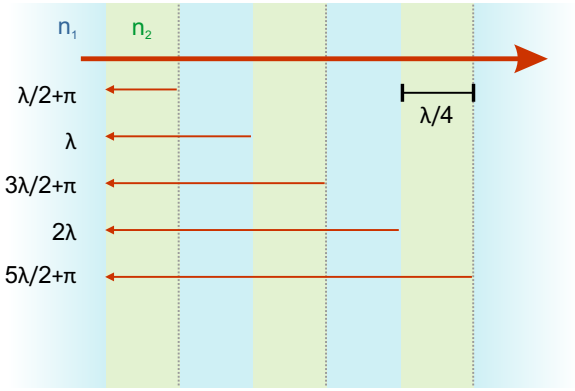

Figure 4.3: Schematic of reflections from dielectric coating. The coating consists of alternating high (blue) and low (green) refractive index materials ($n_1 > n_2$) such that there is a π phase shift for reflections from the low-to-high interfaces (indicated by grey dashed lines). Each layer has a thickness of $\lambda/4$ where λ is the wavelength of incident light.

Considering the case where $L' = nL$, the condition given above would only be true for even n and only every other longitudinal mode would be in phase at the laser. To make sure the laser frequency locks to each consecutive longitudinal mode, $L' = \frac{1}{2}L + nL$ is required.

In Section 3.1, an analogy was drawn between the resonant intracavity field of a simple two-mirror optical cavity and the quantum mechanical particle-in-a-box. For a V-shaped system, one can imagine folding the linear system about the halfway point, where the central folding mirror is inserted. If the total cavity length is equal to an even integer multiple of the laser wavelength, the resonant standing wave will have a node on the central mirror; on the other hand, an odd integer of the wavelength will result in an antinode at the mirror. The reflectivity of dielectric films is subtly phase-dependent, so the reflection coefficient for resonant light at even and odd harmonics can be different. If every mode is excited, even and odd harmonics must be separated and treated as two data sets with different corresponding R values. Armed with this background theory, we now investigate how well the technique works.

4.3 History

The first OF-CEAS experiment was performed by researchers at Lyon and Grenoble.[176] They reported $\alpha_{min} = 2 \times 10^{-10}$ cm^{-1} (10 s average) for measurements of ambient water vapour using a 1312 nm diode laser and 88 cm long V-shaped optical cavity. The good

sensitivity achieved demonstrated the potential power of the technique for trace gas studies. A number of studies using V-shaped systems and diode lasers soon followed which reported similar α_{min} values for measurements of several important trace species summarized in Table 4.1. Using a very high finesse ($\mathcal{F} > 140,000$) cavity, Landsberg *et al.* achieved the best OF-CEAS sensitivity published at this time, $\alpha_{min} = 5.7 \times 10^{-11}$ cm^{-1} Hz$^{-1/2}$.[182] It should be noted that noise can further be reduced by performing FMS in combination with OF-CEAS – similar to the NICE-OHMS technique – with an estimated α_{min} of 2.1×10^{-11} cm^{-1} Hz$^{-1/2}$ in the first study.[183]

OF-CEAS has proven to be useful in field applications. CH_4, CO, and δ^2H/CH_4 signatures in ice cores from Greenland and Antarctica have been measured using diode laser-based systems.[184–186] A breath analyser using a single OF-CEAS system measured CO, CH_4, and NH_3 in hospitalized patients with detection limits of ≤ 25 ppb.[90]

Though first developed with diode lasers, several researchers quickly recognized the opportunity to use OF-CEAS to overcome shortcomings in mid-infrared cavity-enhanced spectroscopy. Optical feedback allows a large build-up of intracavity intensity due to laser linewidth narrowing and frequency locking, which results in a transmitted signal intensity that is much greater than for other cavity-enhanced techniques. Detectivity in the mid-infrared is inherently more limited than for shorter wavelengths since thermal fluctuations are more likely to be significant. OF-CEAS requires pressure-broadened gas samples for ac-

Table 4.1: Table of V-shaped diode laser studies. All experiments were conducted with DFB diode lasers unless noted otherwise.

	λ (nm)	Gases detected	Sensitivity	Finesse
Morville, *et al.*[176]	1312	H_2O	2×10^{-10} cm^{-1} (10 s)	20,000
Kerstel, *et al.*[187]	1392	H_2O isotopes	4×10^{-10} cm^{-1} Hz$^{-1/2}$	20,000
Romanini *et al.*[188]	1659	CH_4	2×10^{-9} cm^{-1} (200 ms)	21,000
Courtillot *et al.*[189]	411*	NO_2	3.5×10^{-9} cm^{-1} (70 ms)	35,000
Baran *et al.*[178]	1596	H_2O, CO_2	5.8×10^{-9} cm^{-1} Hz$^{-1/2}$	3,500
Cermak *et al.*[190]	2.3 μm**	H_2O, CO_2, CH_4	2.5×10^{-8} cm^{-1} (260 ms)	15,000
Desbois *et al.*[191]	1603 nm	CO_2	5×10^{-10} cm^{-1} (4 s)	24,000
Landsberg *et al.*[182]	1.4 μm	H_2O isotopes	5.7×10^{-11} cm^{-1} Hz$^{-1/2}$	>140,000

* Extended cavity diode laser

** Vertical-cavity surface-emitting laser

curate measurements; moving to a spectral region where lines are more separated alleviates problems from overlapping transitions.

The linewidth and stability of a semiconductor laser subject to feedback can be classified by five regimes based on the feedback rate (ratio of feedback to output laser power) and phase as depicted in Figure 4.4.[192] For feedback rates as low as 10^{-8}, the laser linewidth may broaden or narrow depending on the phase of the feedback; apparent broadening can occur due to rapid mode-hopping when the feedback is out of phase. Feedback rates in two regimes between approximately 10^{-5} – 10^{-4} and > 0.1 lead to narrowed, single mode emission.[192,193] The range in between ($\sim 10^{-4}$ – 0.1) is termed Regime IV and is characterized by coherence collapse. When subject to significant feedback intensities, the natural relaxation oscillation damping of the laser is weakened leading to sidebands in the laser emission separated by this oscillation frequency.[194,195] This leads to chaotic behaviour, experimentally observed as significant broadening of the laser linewidth.[192,193,196] Diode lasers exhibit broadening due to spontaneous phase shifts enhanced by relaxation oscillations, indicated by the linewidth broadening coefficient α_H introduced by Charles Henry (typically ~ 5 – 7 for diode lasers).[171,195] In contrast, the single charge carrier mechanism of QCLs allows for very fast relaxation, resulting in $\alpha_H \approx 0$. QCLs are therefore immune to coherence col-

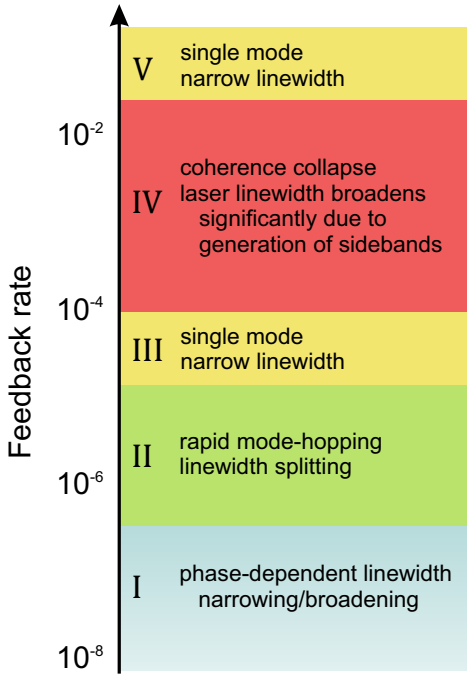

Figure 4.4: Schematic of operating characteristics of diode lasers in five feedback regimes.[192] Regimes I and II are dependent on the feedback phase and the transition between them depends on the round-trip distance of the feedback field. Regime IV is distinguished by chaotic laser emission and occurs for lasers with non-zero linewidth enhancement factors. Only Regimes III and V are suitable for OF-CEAS.

lapse and can exhibit single mode linewidth narrowing even at high feedback rates.[193,197] Interband cascade lasers (ICLs) have a very low broadening coefficient ($\alpha_H = 0.71$) so may be insensitive to coherence collapse, though no studies have been conducted (to my knowledge) on ICL feedback response.[198] Since strong feedback rates do not lead to a chaotic break-down of linewidth narrowing in QCLs (and potentially ICLs), these new lasers exhibit single mode, narrowed linewidth emission for all feedback rates above Regime II (see Figure 4.4) without any maximum limit. As these lasers are well-behaved even under very high feedback rates, they are very attractive for OF-CEAS.

V-shaped OF-CEAS using mid-infrared DFB-QCLs was first reported by two separate groups in 2010. Hamilton *et al.* used a 7.84 μm DFB-QCL for measurements of N_2O and CH_4, and demonstrated $\alpha_{min} = 5.5 \times 10^{-8}$ cm^{-1} for 1 s averaging.[199] Maisons *et al.* also detected N_2O at a shorter wavelength, 4.46 μm, achieving a 1 s-averaged sensitivity of 3×10^{-9} cm^{-1}.[200] In more pragmatic terms, the detectable concentration limit of the former study was 2 ppb at 1 bar compared to 35 ppt at 40 Torr for the latter; since the measurements were taken under very different conditions, it is impossible to scale them by number density alone with confidence as the lineshape will change significantly. Later, Gorrotxategi-Carbajo *et al.* measured H_2CO using a 5.65 μm DFB-QCL with a sensitivity of 1.6×10^{-9} cm^{-1} for a single 100 ms scan.[201]

The work presented in this chapter builds upon these previous OF-CEAS studies. First, the model of the optical feedback-driven laser–cavity coupling is refined to verify the basic assumptions that lead to Equation 4.14. The technique is then extended to DFB-ICLs and an EC-QCL; demonstration of OF-CEAS with these sources has previously been unreported in the literature.

4.4 Refining the feedback model

The relationship between the laser and cavity is one of the elegant features of OF-CEAS. The co-dependence of laser linewidth and feedback rate can only be described using a dynamic model as static equations cannot account for the quasi-positive feedback cycle that determines the equilibrium conditions. Initially, when the laser comes into resonance with

a high finesse cavity, only a small fraction of the light can be coupled into the resonant intracavity field since the laser linewidth ($\sim$ few MHz for the semiconductor lasers used here) is much broader than the cavity bandwidth ($\sim$ 10s kHz). The feedback rate to the laser will therefore be limited to some extent by this poor overlap. As the laser starts to experience phase-matched feedback, the linewidth of the laser emission begins to narrow. Under conditions limited by $1/f$ noise, Morville *et al.* provide the following relationship between the locked laser linewidth ($\Delta\nu_{\text{locked}}$) and the free running laser linewidth ($\Delta\nu_o$):[179,202]

$$\Delta\nu_{\text{locked}} = \Delta\nu_o \left[\beta\epsilon^2 h_{fb}(1+\alpha_H^2)\right]^{-1/2} \left(\frac{\tau_{\text{las}}}{\tau_{RD}}\right). \tag{4.16}$$

The extent of line narrowing is determined by the ratio of the laser and cavity bandwidths, represented by the laser photon lifetime (τ_{las}) and cavity ring-down time (τ_{RD}), the overlap of the intracavity and incident laser fields (ϵ^2), the transfer function for feedback from the cavity (h_{fb}), and the feedback rate coefficient (β). The β value is a frequency-independent scaling factor determined by the losses of the feedback light due to diffraction and the finite size of the laser facet aperture. The term in brackets can be thought of as an effective feedback rate experienced by the laser. The overlap term (ϵ^2) increases as the laser emission narrows, which enhances coupling into the resonant cavity field, and so the feedback rate rises as the linewidth narrows. As seen in Equation 4.16, an increased feedback rate will further narrow the laser linewidth, generating a quasi-positive feedback cycle (see Figure 4.5) until the laser linewidth is well below the cavity bandwidth and the feedback rate reaches an equilibrium. Due to these coupled effects, an iterative algorithm is required to quantitatively determine the equilibrium field overlap and feedback rate.

A LabVIEW program was written to model the relationship between coupled laser linewidth and feedback rate using an iterative loop. The cavity field (I_{cav}) was modelled, as explained in Section 4.2.2, by an amplitude-normalized Airy function (Equation 4.15) with the finesse determined by the reflectivity of the mirrors and absorption losses within the cavity. The laser field intensity (I_L) was simulated using an area-normalized Lorentzian

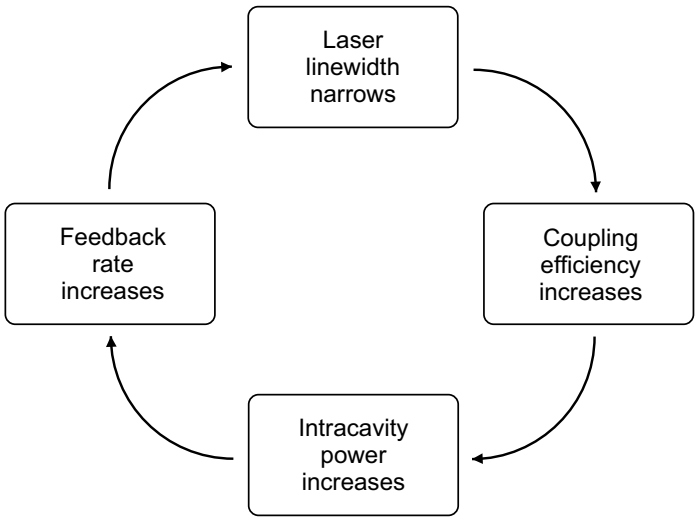

Figure 4.5: Flow diagram showing co-dependence of laser and cavity characteristics in the feedback model.

function:[179]

$$I_L(\nu) = \frac{2}{\pi \Delta\nu_L} \left(1 + 4 \left(\frac{(\nu - \nu_o)}{\Delta\nu_L} \right)^2 \right)^{-1} \tag{4.17}$$

where $\Delta\nu_L$ is the FWHM and ν_o is the centre frequency of the laser. The overlap of the two fields was calculated using an overlap integral:

$$\epsilon^2 = \frac{|\int I_L(\nu) I_{\text{cav}}(\nu) d\nu|^2}{\int I_L(\nu) d\nu \int I_{\text{cav}}(\nu) d\nu}. \tag{4.18}$$

Equation 4.6, giving the feedback transfer function for a V-shaped cavity, was used for h_{fb} in Equation 4.16.

Absorption alters the radiation in several ways. When an absorbing species is present in the cavity, the lifetime of the intracavity light is decreased and the cavity bandwidth is broadened. At the same time, the feedback rate is decreased, which leads to less significant narrowing of the laser linewidth compared to the absorption-free condition. Both the change in cavity bandwidth and laser linewidth will alter the coupling efficiency of light into the cavity. Looking back at Section 4.2.1, Equation 4.13 was determined under the assumption that the light incident on the cavity is the same regardless of whether or not an absorbing species is present inside. If the overlap term (ϵ^2) is highly dependent on α, this assumption may not be valid. The LabVIEW program was therefore used to calculate equilibrium

overlap conditions for a range of α and β values to determine the validity of the assumption.

The system modelled was based on a 3040 cm^{-1} ICL using the α_H value of 0.71 reported by Lerttamrab *et al.*.[198] Though the linewidth of ICLs has not been precisely measured, the DFB structure should result in the emitted linewidth similar to DFB-QCLs, typically on the order of a few MHz (10^{-4} cm^{-1}). Under these conditions, the laser does not contribute to the spectral lineshape even in the Doppler-limited regime ($\Delta\nu \approx 150$ MHz). The ICL chip size was estimated to be approximately 1 mm, giving a laser photon lifetime of 3 ps. The model assumed a cavity with an average mirror reflectivity of 0.999 and total cavity length (including both arms) of 100 cm, as well as phase matching between the laser and intracavity fields. It was assumed that the absorption feature is much broader than the cavity linewidth such that α is constant over a single cavity mode. An enhanced feedback rate, defined by the expression in square brackets in Equation 4.16, and coupled laser linewidth (Equation 4.16) were calculated to account for changes in laser–cavity coupling. Up to 100 iterations were completed until there was clear convergence of the laser linewidth and feedback enhancement to equilibrium values. For each value of α, the model additionally computed results for an absorption-free system with the same β .

As expected, the model predicted a broader laser linewidth when an absorbing species is present compared to the absorption-free condition. For example, the laser linewidth is

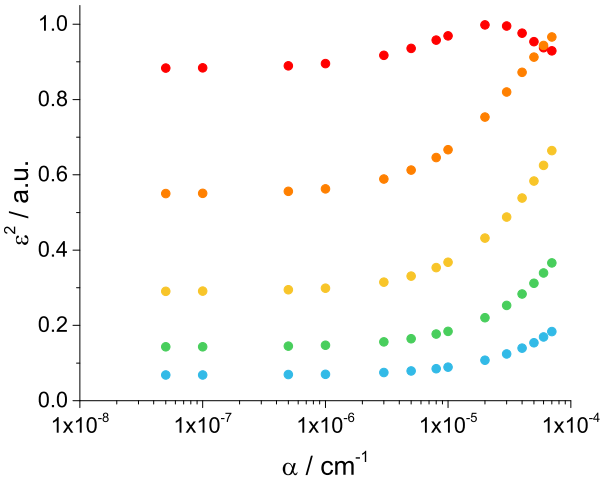

Figure 4.6: Cavity and laser spectral overlap calculated as a function of absorption coefficient for β values of: 10^{-2} (blue), 10^{-3} (green), 10^{-4} (yellow), 10^{-5} (orange), and 10^{-6} (red). Overlap increases dramatically at high α values due to broadening of both the coupled laser linewidth and cavity bandwidth due to absorption. The turning point for the lowest feedback rate (red circles) indicates that the coupled laser linewidth actually becomes larger than the cavity bandwidth for $\alpha > 2 \times 10^{-5}$ cm^{-1} leading to a decrease in overlap.

13 – 14% broader than the absorption-free condition when $\alpha = 10^{-6}$ cm^{-1} (*e.g.* 4.7 kHz compared to 4.1 kHz when $\beta = 10^{-4}$). In addition to this broadening in laser linewidth, absorption leads to broadening of the cavity bandwidth. This allowed better spectral overlap such that coupling is actually higher with absorption, and ϵ^2 becomes dependent on α at high values as shown in Figure 4.6. The final enhanced feedback rate only decreases by 7 – 8% for β values ranging from 10^{-2} – 10^{-6}. The effects become more significant for larger α values, and the change in coupled laser linewidth becomes slightly more pronounced for low feedback rates. Therefore, Equation 4.14 is not valid for strongly absorbing samples. A coupling efficiency parameter γ_{fb} must be introduced to take into account the changes in laser and cavity linewidths:

$$\alpha = \frac{2(1-R)}{L}\left(\sqrt{\gamma_{fb}\frac{I_o}{I_\alpha}} - 1\right). \tag{4.19}$$

The scaling factor γ_{fb} is related to the spectral overlap of the incident radiation and resonant cavity transmission lineshape with and without an absorbing species, and is generally ≥ 1. Assuming $\gamma_{fb} = 1$ in all cases (as is normally done) may therefore result in an underestimation of α near the line centre of strongly absorbing transitions. The model suggests γ_{fb} only becomes significantly different from unity for $\alpha \geq 5 \times 10^{-6}$ cm^{-1} under the conditions assumed in the model. The absorption values measured in the OF-CEAS experiments presented here are generally within the regime where this assumption holds true. In a few cases, however, lineshape distortions and underestimations in the measured absorption under conditions where $\alpha > 5 \times 10^{-6}$ cm^{-1} indicate that these *feedback enhancement effects* can indeed influence measurements, and these are discussed further *vide infra*.

4.5 DFB-ICL V-shaped OF-CEAS: Greifswald

4.5.1 3.24 μm DFB-ICL characterization

The initial ICL-based OF-CEAS studies were performed at the Leibniz-Institut für Plasmaforschung und Technologie e.V. (INP Greifswald) within the Process Monitoring Research Programme.[203] A 3.24 μm cw single mode DFB-ICL (Nanoplus) emitting up to 3

mW was housed in a TO3 can with collimation lens enclosed and mounted on a custom-made water-cooled heat sink. The collimating lens could not be adjusted without opening the laser housing, however measurements with a microbolometer (WinCamD) verified negligible divergence over a path length of $\sim$ 1.5 m. The temperature was set between 10 – 20°C and thermoelectrically controlled (Wavelength Electronics, PTC10K-CH). Current from a threshold level of $\sim$ 75 mA up to a maximum 200 mA was supplied by a commercial driver (Wavelength Electronics, QCL1000). This range allowed a frequency tuning range of $\sim$ 10 cm^{-1} around 3086 cm^{-1}. An Allan-Werle variance plot of normalized laser output intensity demonstrated that white noise is the main contributor when a single current is applied to the ICL.

4.5.2 Experiment

For the OF-CEAS experiment, a function generator (Hewlett Packard 33120A) was used to scan the 3.24 μm ICL $\sim$ 0.35 cm^{-1} with a sawtooth function at 50 Hz. All data were collected with the laser scanning to lower wavenumber. As shown in Figure 4.7, the beam was directed through a BaF_2 window into a sealed aluminium box with one steering mirror mounted on a piezoelectric transducer (PZT) for fine control of the feedback phase. The windows were tilted with respect to the optical axis to reduce reflections returning to the laser. The box had inlet and outlet ports for gas sample introduction and evacuation,

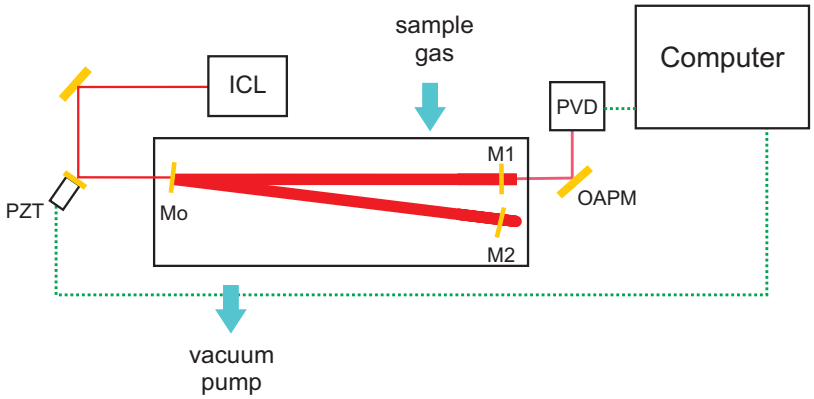

Figure 4.7: Schematic of the OF-CEAS experimental set-up with V-shaped optical cavity. The shaded box indicates the sealed sample container and the green dashed line shows the phase-locking electronic control loop. Note: M_i = spherical mirrors, PVD = photovoltaic detector, OAPM = off-axis parabolic mirror, PZT = piezoelectric transducer.

and was connected to a pressure gauge (MKS capacitive transducer). Inside the box, a V-shaped cavity with 40 cm long arms was constructed from three spherical mirrors. The 2.54 cm diameter cavity mirrors (CRD Optics) used a high reflectivity dielectric coating ($R > 0.9997$ specified at 3.3 μm) on ZnSe substrates with 1 m radius of curvature. The beam was injected into the cavity at the folding mirror (M_0), with the laser-to-cavity distance set equal to one cavity arm length. An off-axis parabolic mirror (OAPM) ($f = 2.54$ cm) outside the box focused the light leaking through M_1 onto a DC-coupled photovoltaic detector (Neoplas Control IRDM-DCA-5). The transmitted signal was amplified with a gain of five (Stanford Research Systems SR455) before being recorded and averaged five times on a 1 GHz-bandwidth oscilloscope (LeCroy HDO 6104). Further averaging and processing of the data was performed using custom LabVIEW routines. The LabVIEW program, similar to the one described later in Section 4.6.4, generated an error signal for the PZT for each recorded average of 5 scans on the oscilloscope, and a data acquisition card (DAQ, National Instruments PXI 6704) applied a voltage to the PZT to maintain phase-locking.

The laser was scanned across three strong CH_4 transitions around 3086 cm^{-1} (see Table 4.2). CH_4 is the simplest VOC, and is important both for planetary radiative balance and physiology as mentioned in Section 2.2.2. Two different samples were measured with nominal mixing ratios of 180 ppb and 360 ppb CH_4 in buffer gas. The samples were formed by buffering laboratory air with N_2 inside the sample box; the ambient laboratory air has a concentration of 1.8 ppm CH_4, verified previously with a QCL-based CEAS experiment.[169] Homogeneous gas mixing was assumed. In order to obtain a pressure broadened absorption lineshape covering a sufficient number of cavity FSRs for spectral analysis, spectra of both samples were collected at various pressures from 40 to 190 Torr.

4.5.3 Results

A typical cavity transmission spectrum averaged over 100 scans of a 190 Torr sample with 360 ppb CH_4 is shown in Figure 4.8. Over 20 ms, the ICL locked to 40 successive cavity modes with a locking time, estimated by the FWHM, of 80 μs, much longer than the ring-down time (typically 3.2 μs). The time between modes was $\sim$ 200 μs (Fig. 4.8(a)). No

Table 4.2: Molecular absorption parameters for transitions scanned in 3.24 μm ICL V-shaped OF-CEAS experiment.[6] The CH_4 transitions are all assigned to the fundamental ν_3 transition of the most abundant isotope, and a single overlapping H_2O ν_2 2 ← 0 transition is indicated in blue. Cross-sections assume natural isotopic abundances from HITRAN.

Frequency / cm^{-1}	**Transition**	**Cross-section / cm^2 cm^{-1}**
3085.832	7 A_2 10 ← 6 A_1 1	1.69×10^{-19}
3085.861	7 F_2 25 ← 6 F_1 1	1.01×10^{-19}
3085.894	7 F_1 26 ← 6 F_2 2	1.01×10^{-19}
3086.031	7 A_1 8 ← 6 A_2 1	1.66×10^{-19}
3086.072	7 F_1 27 ← 6 F_2 1	1.00×10^{-19}
3086.086	7 E 17 ← 6 E 1	6.67×10^{-20}
3087.192	(6,2,5) ← (6,3,4)	2.07×10^{-22}

broadening of the modes was observed due to averaging of the transmission spectra. There is a clear amplitude oscillation in the transmitted signal for alternating modes due to even and odd modes having a different phase at the folding mirror as explained in Section 4.2.3. Even and odd designations are applied arbitrarily to the two data sets as the cavity path length is not known with sufficient precision to correlate laser frequency and longitudinal mode harmonic order.

It should be noted that a significant non-zero signal is observable even when the laser is not in resonance with the cavity. This is attributed to a combination of a DC detector offset and an additional contribution that is suspected to arise from non-resonant cavity transmission. Figure 4.9 highlights the two offset components by comparing the cavity

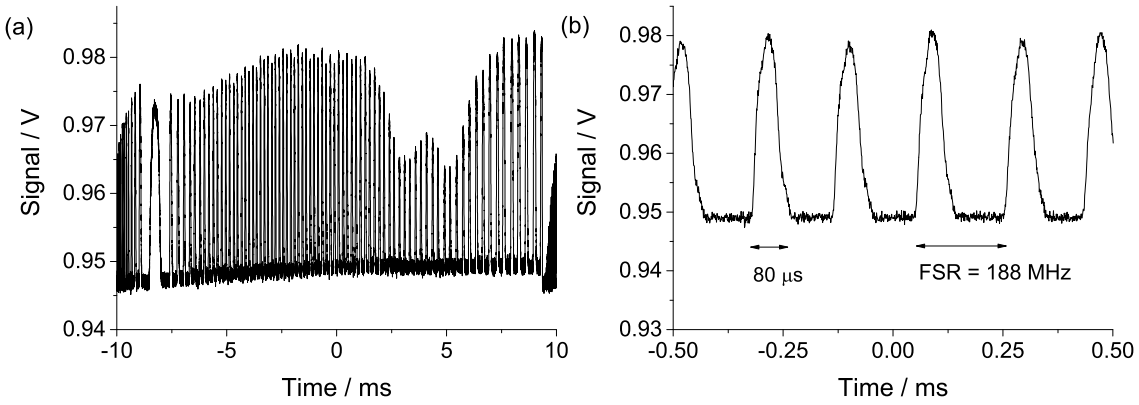

Figure 4.8: (a) Cavity transmission for 360 ppb CH_4 in buffer gas at a total pressure of 190 Torr while the laser is scanning to lower wavenumber. This transmission spectrum is the average of 100 scans. (b) A close-up section of the scan. The locking range (duration of locking) is about 80 μs and the FSR separation of the modes is 188 MHz.

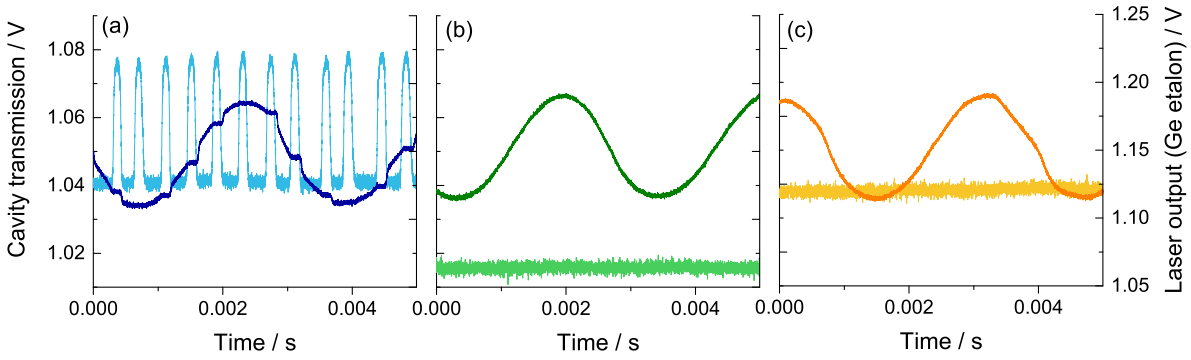

Figure 4.9: Comparison of laser output passed through a Ge etalon (dark traces, right-hand axis) with cavity transmission (light traces, left-hand axis) measured nearly simultaneously for the following conditions: (a) laser locked to resonant cavity and in phase feedback field; (b) cavity blocked; (c) laser locked to resonant cavity and out of phase.

transmission and frequency tuning of the laser under different conditions. The frequency tuning of the laser was measured by sending a small portion of the output beam through a Ge etalon and onto a detector. When the cavity is blocked (b), the measured transmission signal only arises from the DC offset intrinsic to this detector. There is an additional contribution to the signal when the resonant cavity feedback field is out of phase with the laser (c), even though cavity transmission from excited longitudinal modes is not observed. When the feedback field is phase-matched to the laser (a), the signal returns to the same level in between cavity modes. The amplitude of this non-resonant signal increases a small amount from left to right across the scan, corresponding to an increase in laser output power as the current is increased. Adjustments of the beam steering between laser and cavity cause observable changes to this component, however fine adjustments for phase control had no effect. Covering the detector with a dark cloth to prevent the photodiode from picking up any stray scattered light had no effect.

It is possible that amplified spontaneous emission (ASE) in the laser output field is responsible for this signal. The ASE contribution may contain frequency components that are very different from the centre frequency of the laser. The dielectric films on the cavity mirrors allow efficient reflections only for a relatively narrow range of wavelengths. Light outside this band will have a much lower reflectivity coefficient, and therefore the transmission efficiency will be larger (assuming lossless interactions with the mirror substrate). Thus, compared to the centre frequency, a greater fraction of ASE may be able to pass

straight through M_0 and M_1 without building up in the cavity. While we were unable to observe any sidebands when the laser beam was measured by a Fourier-transform infrared (FTIR) spectrometer, even weak, broadband ASE beyond the resolution of the spectrometer may affect the weak cavity transmission signal.

The V-shaped cavity in principle prevents light reflected off the backside of the in-coupling cavity mirror from returning to the laser, however Figure 4.9 shows that the laser output is being modified by an unknown feedback field that does not arise from the high finesse cavity resonance. Directing a portion of the laser output beam through a Ge etalon onto the photovoltaic detector provides insight into the frequency tuning of the laser. When a beam block is placed between the second steering mirror and cell window (b), the sinusoidal variation in the laser output signal indicates a smooth rate of frequency change. When the box is unblocked and the resonant cavity feedback field allowed to return to the laser facet (a), horizontal steps in the laser signal indicate frequency locking to the longitudinal mode of the cavity when the feedback is in phase. Under the same alignment conditions with the PZT adjusted so that the cavity feedback field is out of phase with the laser (c), one would expect to see the same signal as case (b). However, distortions in the etalon signal show that the laser frequency is not tuning in a smooth, linear fashion. It is possible that this behaviour arises from non-resonant reflections returning to the laser. Given the evidence of ASE discussed in the preceding paragraph, reflections of ASE – from M_1 for example – may be affecting the stimulated emission of the ICL. While the ASE should be outside the gain spectrum of the laser, and therefore unable to injection seed emission, this may be an interesting avenue of future research given the lack of comprehensive studies on ICL feedback response.

For this experiment, stable feedback locking was achieved without applying mode matching. Mode matching, discussed later in Section 5.2.2, could allow better coupling of the mid-infrared light into the cavity and enhanced signal intensity. Measurements of laser output showed that the laser power variation due to intracavity absorption reducing the optical feedback was negligible ($< 1\%$) and so no correction for this effect was required. Furthermore, the feedback rate to the ICL resulted in a frequency locking range smaller

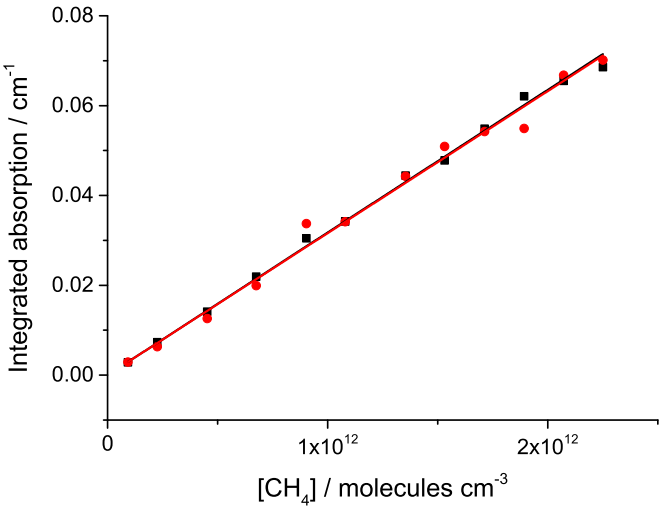

Figure 4.10: Integrated absorption based on Voigt fits as a function of CH_4 number density. Black and red data indicate even and odd harmonics, which are analysed separately. The intercept was set as the origin and the slope was used to determine reflectivity: slope= $\frac{L\sigma}{2(1-R)}$.

than one cavity FSR without any attenuation of the feedback rate ensure excitation of successive modes.

To produce an absorption spectrum, the mode amplitude (I) was compared to the corresponding mode amplitude when the cavity was evacuated (I_o) to determine the absorption A (the term in square brackets in Equation 4.14). The cavity mode amplitudes are typically determined using an Origin algorithm for finding the local maxima in both the positive and negative direction with 3-point smoothing. The values determined using alternative methods, for example by looking at the second derivative, yielded equivalent values within experimental noise. The effective reflectivity (R) was determined independently for even and odd harmonics.

The spectral feature measured consists primarily of three transitions in the R branch of the ν_3 asymmetric stretch of CH_4, although weaker neighbouring lines were included in the model to fit the spectra (see Table 4.2). Fitting was performed in Origin with the relative centre frequencies and relative areas of the seven CH_4 transitions and Gaussian linewidths (Doppler broadening) fixed, and the Lorentzian linewidths larger or equal to those predicted using the HITRAN database[6] to account for any experimental broadening. The slope of integrated absorption plotted as a function of CH_4 number density for the R(6) ν_3 fundamental transition at 3086.031 cm^{-1} with a line strength of 1.66×10^{-19} cm^2

cm^{-1} is shown in Figure 4.10. A linear function with intercept at the origin was fit to each set of data to determine R using the relationship $A/[CH_4] = \sigma L/2(1-R)$. The retrieved R value for both even and odd modes was 0.99958 ($\pm$0.00002). This agrees with ring-down measurements with a typical decay time of 3.2 μs, corresponding to $R = 0.999583$. This gives a finesse of the V-shaped cavity of 7500 and an effective path length of 1900 m. Figure 4.11 shows a cumulative fit to the measured absorption coefficient spectrum of 360 ppb CH_4 in buffer gas at a total pressure of 190 Torr averaged over 100 scans. Based on the standard deviation of the residual of the cumulative fit $\alpha_{min} = 1.1 \times 10^{-7}$ cm^{-1} for 2 s averaging, or a detection limit of 8 ppb at 190 Torr.

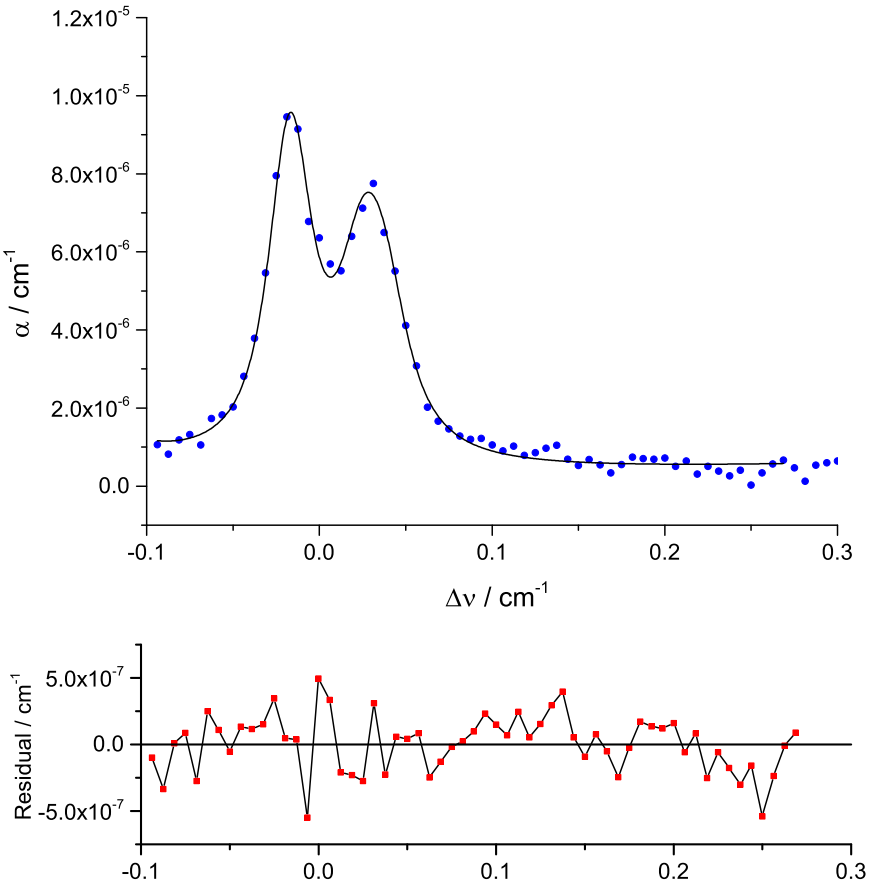

Figure 4.11: Absorption coefficient spectrum from 2 s averaged measurement of 360 ppb of CH_4 in buffer gas at a total pressure of 190 Torr together with a composite fit taking into account the 8 transitions which contribute to the observed absorption feature. Also shown is the residual of the fitted absorption profile, shown below. The standard deviation of the residual of the fit shown gives $\alpha_{min} = 1.4 \times 10^{-7} cm^{-1}$.

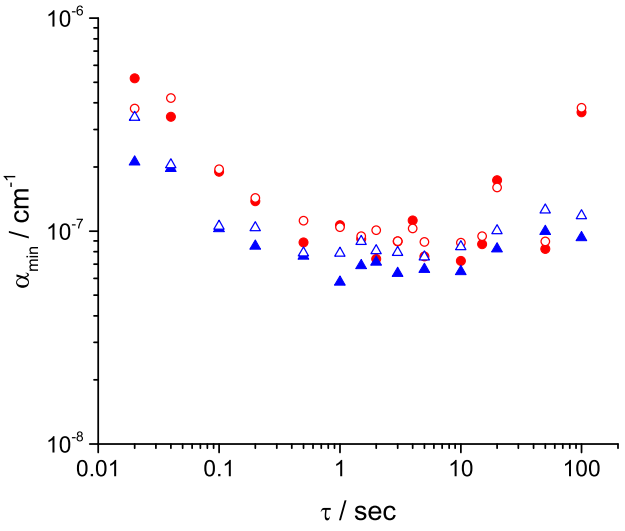

Figure 4.12: Allan-Werle variance plot of the minimum detectable sensitivity, α_{min}, derived from a polynomial fit to the evacuated cavity transmission, as a function of averaging time. Red circles correspond to data collected with the phase-locking control loop enabled and blue triangles with this loop disabled. Filled and open data points indicate odd/even harmonics.

An Allan-Werle analysis on the minimum detectable absorption coefficient (α_{min}) was performed to determine the optimal averaging time for measurements. The cavity transmission through an evacuated cavity was measured with different averaging duration, and the odd and even cavity mode amplitudes were fitted separately to second order polynomial functions to account for the non-linear variation in laser intensity across the scan. Using the standard deviation of the fit as a minimum detectable signal, the resulting α_{min} was plotted against theoretical averaging time (number of scans $\times$ acquisition time). Due to non-instantaneous processing times, the actual time elapsed was somewhat longer. This Allan-Werle analysis was performed with and without the phase-locking control loop enabled, and both demonstrated similar sensitivity for all averaging times. Fig. 4.12 shows the Allan-Werle plot with a broad minimum in α_{min} starting from approximately 100 scans averaged ($\tau = 2$ s). The average α_{min} with and without phase-locking control enabled for the region $\tau = 2 - 10$ sec was determined to be $(4.0 \pm 0.5) \times 10^{-8}$ cm^{-1}. The rise in α_{min} for longer averaging times is likely due to slow fluctuations in the baseline rather than loss of phase-matching. It is interesting to note that there is little difference within the error in the measurements with or without controlling the phase, which could indicate some level of laser self-locking or simply a very stable apparatus.

While this α_{min} is relatively high compared to other OF-CEAS studies with diode lasers and QCLs,[176,200,201,204,205] the strong 3 μm transitions lead to a minimum detectable con-

centration of 8 ppb CH_4 at 190 Torr, which is comparable to previously reported OF-CEAS instruments.[188,204] This is a good example of the benefits of the mid-infrared spectral region – despite young technology and relatively poor optics the strong absorption cross-sections accessible allow for very low minimum detectable concentrations of a trace hydrocarbon gas.

4.6 DFB-ICL V-shaped OF-CEAS: Oxford

4.6.1 3.29 μm DFB-ICL characterization

Following on from the initial studies performed in Greifswald, a second ICL OF-CEAS system was set up in Oxford for detection of N_2O and VOCs. The full tuning range of this 3.29 μm cw single mode DFB-ICL (Nanoplus) is 3039 – 3046 cm^{-1}. The laser emits up to 4 mW and was purchased without collimating optics within the laser package. An anti-reflection coated aspheric lens (Thorlabs C036TME-E, $f = 4$ mm) was mounted next to the laser to collimate the beam over $\sim$ 1.5 m using the microbolometer (WinCamD).

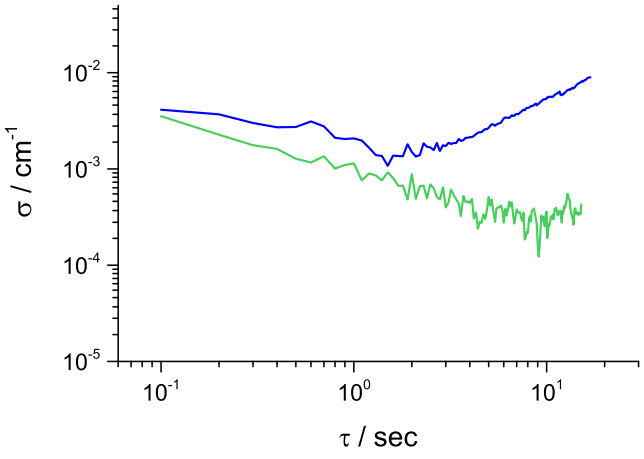

Figure 4.13: Allan-Werle plot showing standard deviation of laser frequency as a function of averaging time for a commercial driver (blue) and a custom driver (green). Laser frequency was determined by scanning the laser across the transition at 3042.58 cm^{-1} within the $\nu_2 + \nu_4$ combination band of CH_4 under low pressure.

The temperature conditions required were the same as for the first Nanoplus ICL (10 – 20°C), however the maximum operating current of this laser was 50 mA – only 25% of the maximum operating current of the 3.24 μm laser. Given that the two lasers were manufactured by the same company and have similar wavelengths and output powers, it is unknown why the 3.29 μm laser required significantly lower driving current. The low threshold current is, however, not wholly surprising as Meyer *et al.* predicted that ICLs

should have a tenfold lower threshold current density compared to QCLs.[44] A decreased current indicates increased wall-plug efficiency, so in principle this laser more effectively converts current density to photon density. However, the lower current makes the laser frequency and intensity more sensitive to current noise. The commercially available Wavelength Electronics current driver (QCL1000) can output up to 1 A to QCL or ICL chips, and is therefore designed for lasers with higher current thresholds that are less susceptible to small fluctuations. A pair of temperature and current controllers was customized in-house for this ICL, and the performance compared to the commercial driver. The laser frequency variability was determined by measuring two $\nu_2+\nu_4$ combination band transitions at 3042.40 and 3042.58 cm^{-1} in a sample of low pressure ($\sim$ 20 Torr) pure CH_4 in a 40 cm long cell. An Allan-Werle variance analysis was performed to analyse the consistency of the time at which the maximum absorption was measured in successive scans. Figure 4.13 shows the standard deviation in laser frequency as a function of averaging time for both drivers, determined by converting time variance to frequency variance using the separation of the two transitions. With the commercial driver, the increase in standard deviation for $\tau > 2$ s demonstrates that the laser frequency clearly drifted over time. When the laser is driven by the custom controller, on the other hand, there is no discernible drift up to 10 s. The frequency deviation is about a factor of two lower, even for short averaging times, indicating better shot-to-shot stability. In addition to covering several CH_4 transitions, this laser could be used for measurements of N_2O.

4.6.2 Nitrous oxide properties

Nitrous oxide is another species that absorbs across nearly the entire mid-infrared region. As for CH_4, N_2O is a long-lived greenhouse gas whose atmospheric levels have increased rapidly in recent decades. The greatest anthropogenic source is over-fertilization in agriculture, which overwhelms the natural nitrogen processing cycle. N_2O that reaches the stratosphere enhances ozone depletion as a source of catalytic NO_x.[206,207]

Of course, N_2O is more commonly known as "laughing gas" due to its effects on the brain that produce a euphoric feeling upon inhalation.[208] It is used as a mild general anaes-

thetic, and is often given to pregnant women during labour in concentrations of around 50%. More recently, it has been investigated in Oxford as a useful indicator gas for measuring cardiac output and lung homogeneity.[209]

N_2O is a linear triatomic molecule with four vibrational modes: one bending mode (doubly degenerate) and two stretching modes. It therefore shares a similar family of modes with CO_2, however its lack of an inversion centre means it has $C_{\infty v}$ symmetry and the stretching modes do not have the "symmetric" and "asymmetric" labels of $D_{\infty h}$ molecules (*i.e.* CO_2). Vibrations are labelled by $\nu_1\nu_2^l\nu_3$ where l indicates the angular momentum of the bending mode.

4.6.3 Experiment

The 3.29 μm cw single mode DFB-ICL, driven by the custom controllers, was ramped by a function generator (TTI TG1304) applying a triangle function at a rate of 10 Hz. In addition to the laser, several other key components were changed from the previous set-up. The DC-coupled photovoltaic detector (VIGO PVI-2TE-4/VPDC-0.1l) used here did not require amplification and only exhibited a small non-zero offset ($\sim$ 30 mV).

Two sets of plano-convex cavity mirrors were implemented: infrared-transmissive quartz mirrors (Layertec) with a reported reflectivity > 0.997; and higher reflectivity ($R > 0.999$) ZnSe mirrors (CRD Optics), described in the previous section. Both sets had an anti-reflection coating on the flat surface of the mirror with 1 m radius of curvature on the high reflectivity side. The terms *moderate finesse* and *high finesse* will be used to differentiate between the mirror sets respectively.

The optical cavity was enclosed within an aluminium and plexiglass box. This system does not allow optimization of cavity mirror alignment while the box is under controlled pressure, but it is very robust – cavity alignment does not vary with sample pressure even for $P > 1$ atm – and therefore suitable for proof-of-principle studies. Reflections from the windows did not return feedback to the laser. The box had three external connections: a gas sample inlet, an outlet to vacuum pump (Leybold TRIVAC D8B), and a pressure gauge (Leybold Ceravac CTR 90 1000 Torr or 100 Torr). In this set-up, the mirrors were mounted

on gimbal mounts within the box.

The sensitivity and stability were characterized using CH_4 and N_2O as test gases. Very strong CH_4 transitions were not accessible to this laser, so a standard mixture of 3000 ppm CH_4 with C_2H_2 and CO in N_2 (BOC) was buffered in additional N_2 to obtain samples with concentrations from 200 – 3000 ppm at *ca.* 100 Torr. N_2O measurements were performed with a mixture of 5% N_2O in N_2 (BOC).

4.6.4 Locking algorithm

The optical feedback phase-locking algorithm is adopted from the work of Ohshima and Schnatz who first proposed using the symmetry of transmitted cavity modes to lock a laser to an optical cavity.[210] The same principle has been applied in locking algorithms used for other OF-CEAS studies.[176,204]

Signal from the cavity transmission detector is sent to a LabVIEW program *via* a DAQ, with data acquisition triggered by the function generator applying the laser voltage ramp. A portion of the measured transmission, usually spanning across about 10 – 20 FSRs, is normalized to a maximum amplitude of unity, as shown in Figure 4.14(a). This transmission signal is then clipped such that only the top 20% (*i.e.* normalized signal between 0.8 – 1.0) is analysed (b). The program computes the gradient between consecutive points (c) and then saturates the derivative such that positive gradient is set to $+a$ and negative to $-a$ where a is a constant (d). The program then integrates across (e) and multiplies the result by a user-set scaling factor (f). The resulting error signal is added to an analogue output voltage sent to a PZT that can change the laser–cavity distance. The sign of the scaling factor determines the direction the PZT moves. The saturation step is required for a non-zero integral. The program essentially compares the number of data with positive slope to the number with negative slope. When the phase is optimized, cavity modes are symmetric, resulting in a net integral of nil and no error signal is applied to the PZT.

The scaling factor to convert the computed error to voltage depends on the voltage-to-length conversion of the piezoelectric stack and wavelength of light. In some cases, a PZT amplifier is connected between the computer and PZT if the 10 V error signal range from

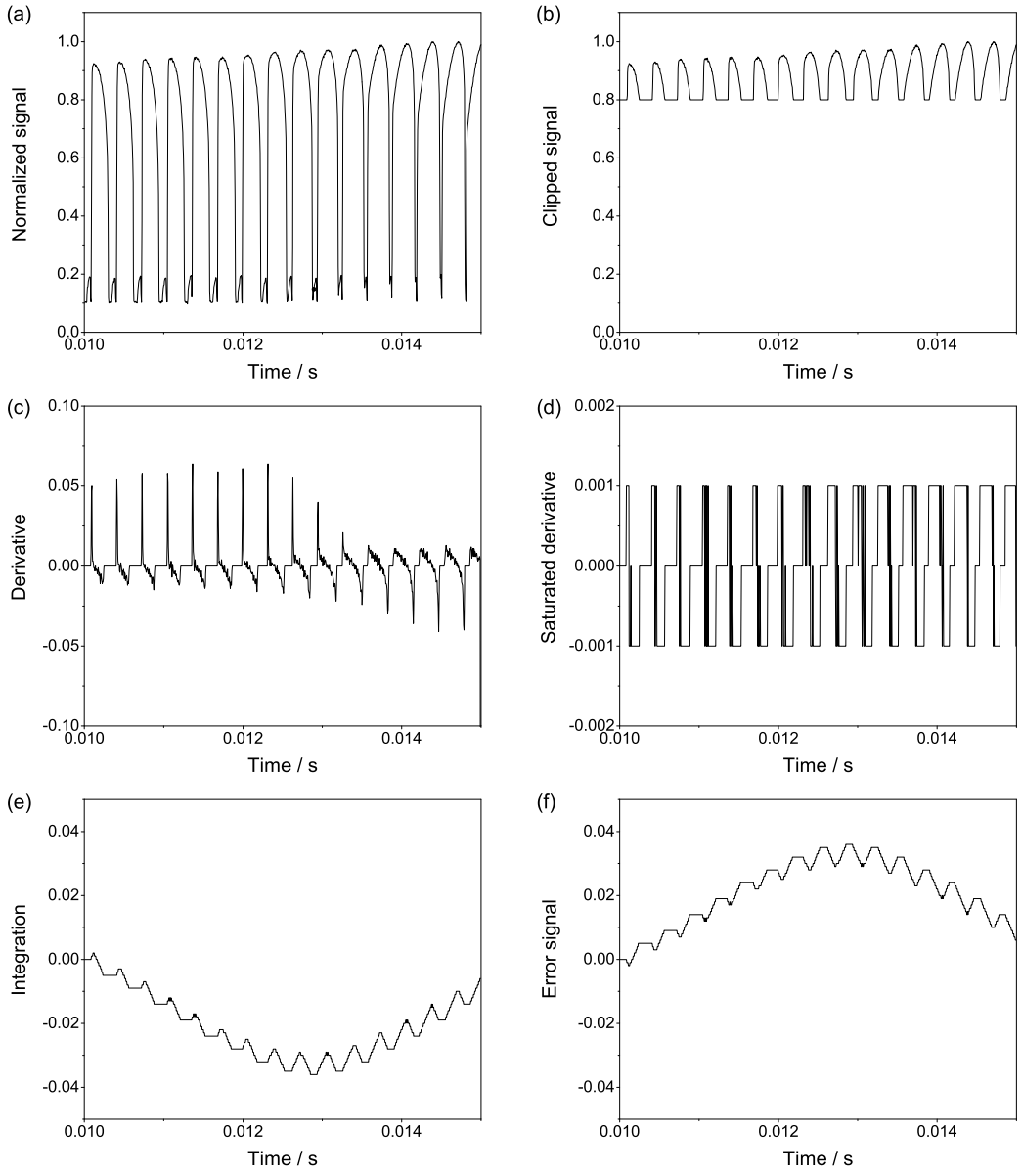

Figure 4.14: OF-CEAS locking algorithm: (a) Normalized signal segment; (b) clipped signal; (c) derivative; (d) saturated derivative; (e) integration; (f) error signal.

the DAQ is insufficient. The tunability of the PZT length should be at minimum one phase cycle (*i.e.* λ). If small shot-to-shot variations in phase – which are too fast to be corrected by this method – add unwanted fluctuations to the error signal, the program can be set to apply a running average of the error signal over several laser scans.

User-defined parameters are optimized for each experiment. The region of the cavity transmission used for analysis is typically located around the middle of one frequency ramp and away from any strong absorption lines. The scaling factor and integrating time are determined empirically by adjusting values until stable phase-locking is observed.

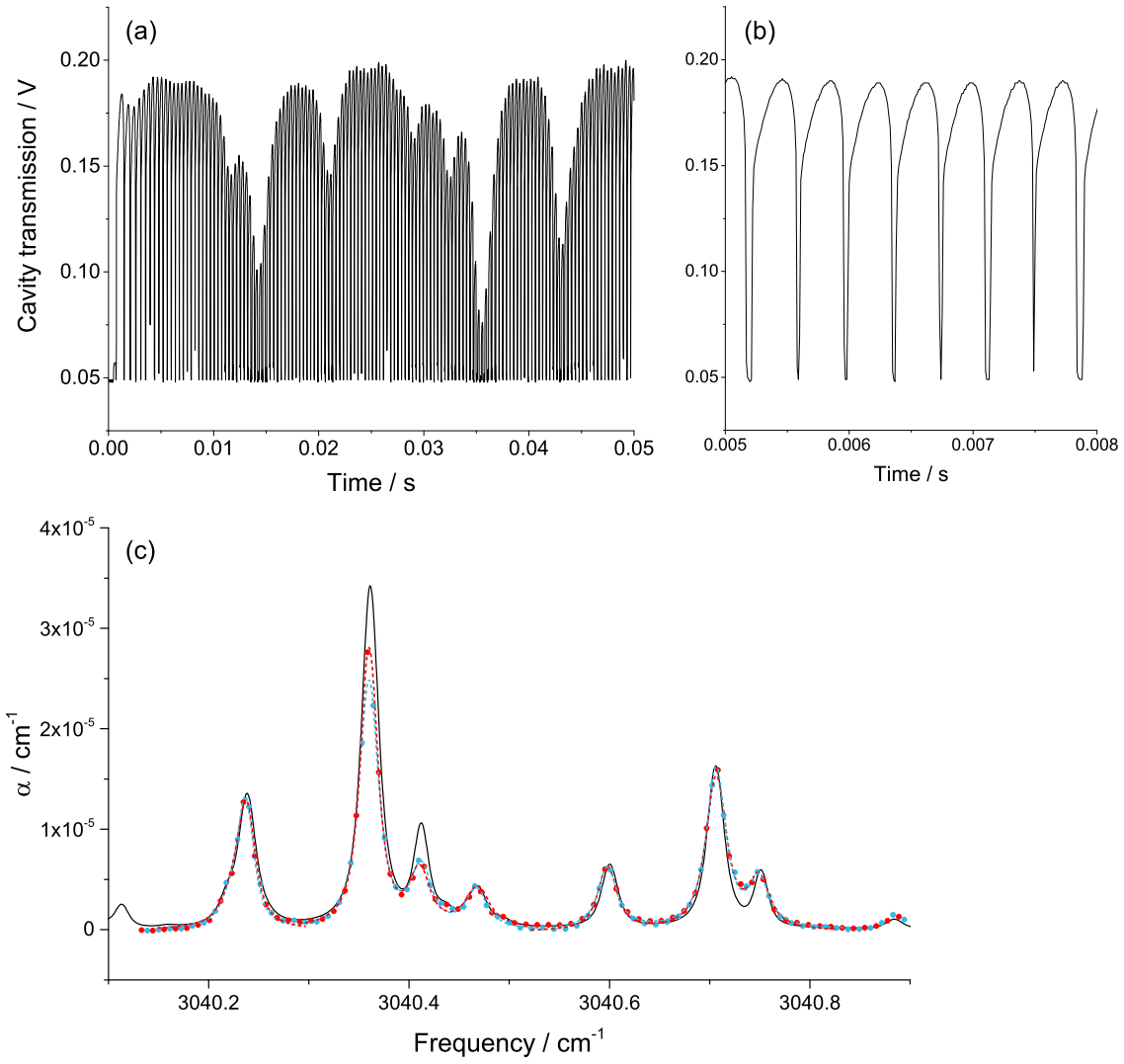

Figure 4.15: (a) Sample cavity transmission measurement with no averaging. (b) Close up of a few cavity modes showing the long locking range and improved SNR compared to previous measurements. The FSR in this case is 170 MHz. Note that there is a 30 mV DC offset from the detector. (c) Corresponding absorption spectrum of 0.3% CH_4 at 101 Torr. The red and blue dashed lines show Voigt fits corresponding to the even/odd harmonic data (circles). The black line shows a HITRAN simulation.

4.6.5 Results

The first results presented were measured under moderate finesse conditions, using the Layertec cavity mirrors. A sample cavity transmission from a single scan of the laser at 10 Hz through a sample of 0.3% CH_4 at 115 Torr is shown in Figure 4.15. There is a DC offset of 30 mV and an additional contribution of < 10 mV from ASE or some other light leaking through the cavity. The frequency tuning range of this ICL covered a much weaker region of the CH_4 absorption spectrum compared to the previous one, therefore higher concentrations of the gas were required for similar absorption levels. The data shown here include the transitions given in Table 4.3. The SNR however is significantly better compared to earlier measurements (*i.e.* Figure 4.8), especially given these data were collected over 50 ms with no averaging or amplification of detector signal. The laser jumps directly from one longitudinal mode to the next without returning to the free running condition since the locking range is approximately equal to the time to cover one FSR.

Figure 4.15 (c) shows the corresponding absorption spectrum. A fit of Voigt profiles to the transitions listed in Table 4.3 and HITRAN simulation (black line) are also shown. Due to the large number of lines in the region, Voigt models were optimized in three spectral regions across the scan for each harmonic. The feature at 3040.41 cm^{-1} arises from a CH_3D absorption, and the clear decrease in the absorption compared to the HITRAN simulation indicates that the sample in the cylinder contained less than the 0.06% CH_3 isotopic abundance assumed by HITRAN. The poor fit in the region around 3040.73 cm^{-1} is likely due to overlapping absorption from residual acetonitrile or water vapour in the box or tubing. The reflectivity of these mirrors was measured to be 0.9990 using a concentration series as described previously. The photovoltaic detector used for these measurements has a bandwidth of 100 kHz, and was therefore too slow for accurate measurements of ring-down decays.

The sensitivity is better characterized by looking an an absorption spectrum that is less congested. To demonstrate the sensitivity, a spectrum is shown of 45 Torr 5% N_2O in N_2 (Figure 4.16). The absorption at 3039.4 cm^{-1} due to the P(8) transition of the $\nu_1 + 3\nu_2$

Table 4.3: Molecular absorption parameters for methane transitions scanned and fit in 3.29 μm ICL V-shaped OF-CEAS experiment.[6] The first three transitions are part of the $\nu_2+\nu_4$ fundamental band, while those in the following section are due to the fundamental ν_3 transition (with $\nu_2 = 1$). Cross-sections assume the natural isotopic abundances from HITRAN, and the absorption due to deuterated methane (CH_3D) is shown in grey.

Frequency / cm^{-1}	**Transition**	**Cross-section / cm^2 cm^{-1}**
3040.238	14 F_1 37 ← 13 F_2 3	3.00×10^{-23}
3040.361	13 F_1 39 ← 12 F_2 3	8.12×10^{-23}
3040.469	13 F_1 39 ← 12 F_2 2	8.42×10^{-24}
3040.219	8 F_1 44 ← 2 F_2 3	5.02×10^{-24}
3040.600	3 F_2 42 ← 2 F_1 3	1.42×10^{-23}
3040.706	3 A_2 16 ← 2 A_1 2	3.81×10^{-23}
3040.751	E 29 ← 2 E 2	9.61×10^{-24}
3040.412	ν_4 1 ← 0 R(2)	1.87×10^{-23} (0.06%)

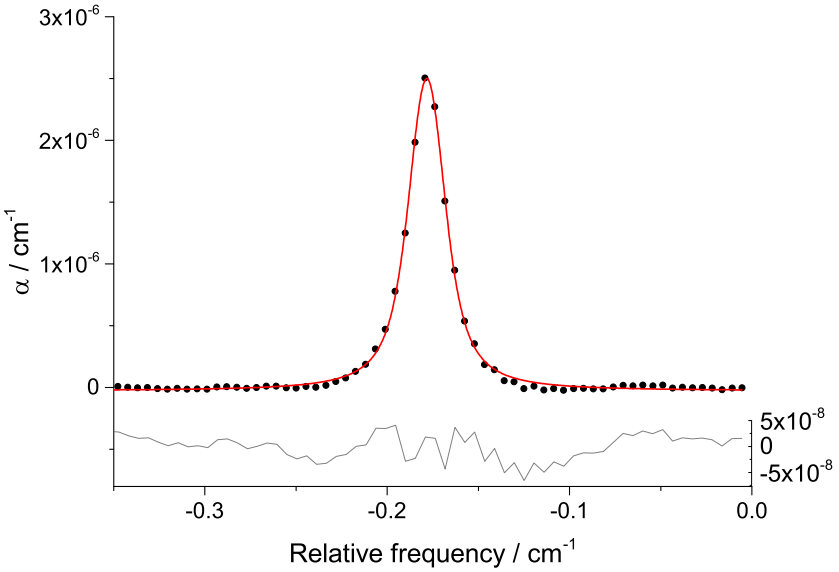

Figure 4.16: Spectrum of N_2O absorption coefficient for the P(8) $\nu_1 + 3\nu_2$ combination band transition at 3039.4 cm^{-1}. Data measured using the moderate finesse OF-CEAS cavity (black circles) is compared to a Voigt fit (red line) with the residual (grey) shown below.

combination band is isolated, and the spectrum can be fit well to a single Voigt function. Using the mean absolute residual as an estimate for α_{min} gives 2.5×10^{-8} cm^{-1} for a single 100 ms measurement. Despite the relatively short path length, the high SNR of the cavity transmission signal allows for sensitive detection.

Figure 4.17 shows an Allan-Werle analysis of the cavity transmission stability with

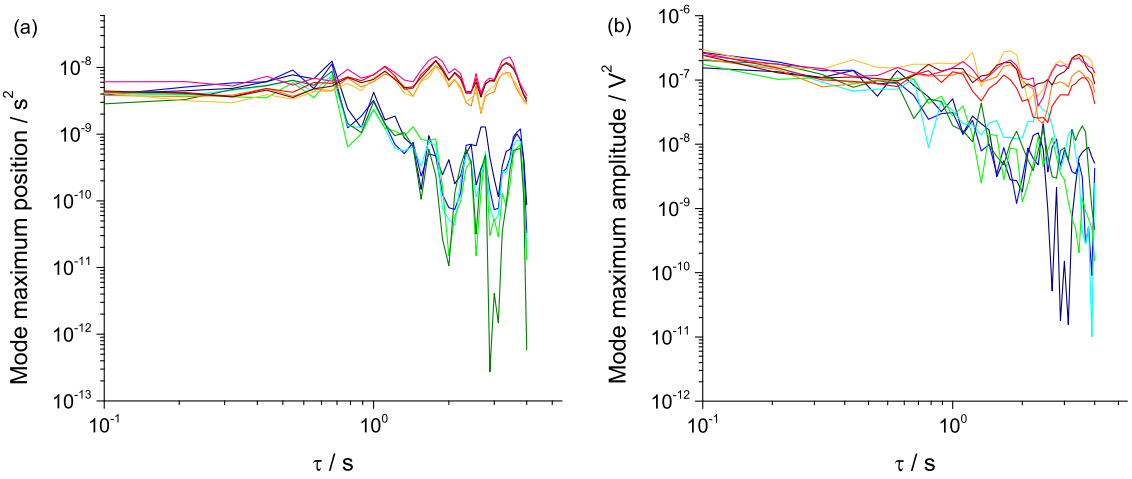

Figure 4.17: Comparison of cavity transmission stability with (blue/green) and without (red/orange) active error loop enabled to maintain optimal phase matching using PZT. (a) Allan-Werle variance of cavity mode maximum position along time axis, which represents the frequency stability of the laser and cavity from scan-to-scan. The typical time between resonant cavity modes (time span to cover FSR) is 500 μs. (b) Allan-Werle plot of amplitude of cavity mode maximum. The average amplitude is 110 mV.

and without the locking program (Section 4.6.4) enabled. Since the algorithm maintains symmetric modes, there is an enhanced stability in both the amplitude of the cavity modes (b), as well as the x-axis position of the maxima (a). The latter is observable as a horizontal jitter of modes when the locking loop is disabled arising from noise on the phase matching between the feedback and laser fields.

While OF-CEAS is traditionally performed by scanning the laser frequency over one or more ro-vibrational transitions of the target species, it is possible to remain fixed on a single mode and measure the change in transmission signal due to absorption at a single frequency. The system was sufficiently stable that the laser could remain locked to a single cavity mode without any active locking mechanism for several seconds. The laser frequency was set near the line centre of the ν_3 R(2) CH_4 transition at 3040.706 cm^{-1} with the current fixed to a single value for the measurements shown in Figure 4.18 (a). The cavity transmission signal was recorded for a range of CH_4 sample concentrations, all buffered in N_2 to a total pressure of 70 Torr to eliminate variations in pressure broadening. Using Equation 4.14, the measured signal was converted to absorption by comparing with the transmission through an evacuated cavity. The linearity in the plotted absorption versus CH_4 concentration (Figure

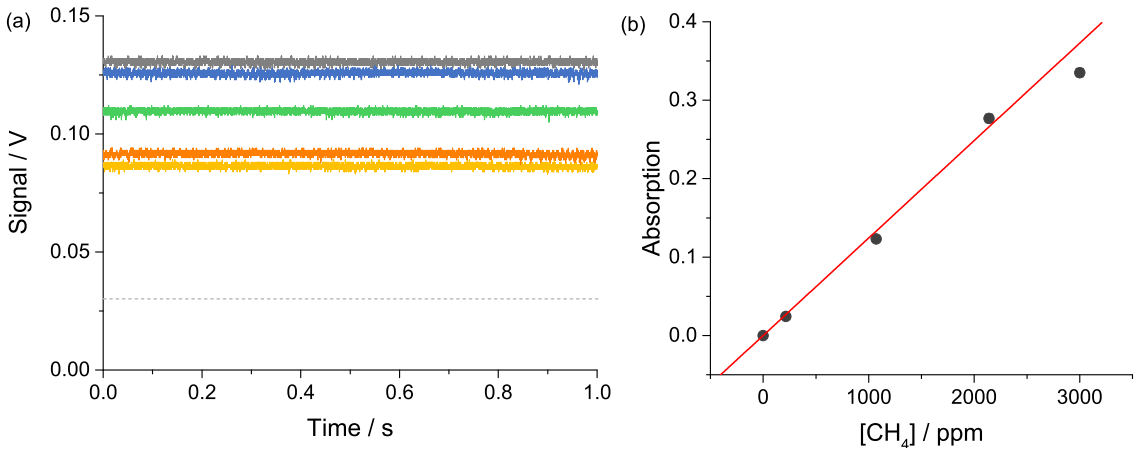

Figure 4.18: (a) Single frequency measurement of CH_4 at varying volume fractions in a total volume of 70 Torr: 3000 ppm (yellow), 2140 ppm (orange), 1070 ppm (green), and 214 ppm (blue). The grey line was measured with cavity evacuated. The laser remains locked to a single longitudinal mode throughout the entire duration without any active control. The dotted line represents the DC offset of the detector. (b) Plot of absorption as a function of CH_4 volume fraction with linear fit (red) that passes through the origin.

4.18 (b)) validates that this is an alternative way of implementing OF-CEAS for accurate gas measurements. The highest concentration corresponds to an α of about 7×10^{-6} cm^{-1}, and therefore is within the high feedback rate regime where feedback enhancement effects can lead to underestimations of the absorption. The standard deviation of the signal is low ($\sim$ 0.9 mV), and so the limiting factor is the pressure gauge which has a precision of only 1 Torr.

Without any active locking, the cavity transmission signal did vary over timescales of $\sim$ 1 minute as shown in Figure 4.19. A fast Fourier transform (FFT) analysis of the signal clearly shows significant noise contributions at two frequencies around 100 Hz. Low frequency fluctuations are generally mechanical rather than optical, and it is suspected that these instabilities arise from vibrations of instruments in the vicinity of the cavity. An evaluation of the noise of the mains electricity determined that fluctuations are far too small to have the observed effects.

The α_{min} values for the moderate finesse cavity are limited somewhat by the effective path length, so experiments were performed with a higher finesse cavity using the CRD Optics cavity mirrors. These mirrors are composed of a different substrate (ZnSe) with a dielectric coating that gives a higher reflectivity in this wavelength region. By inserting

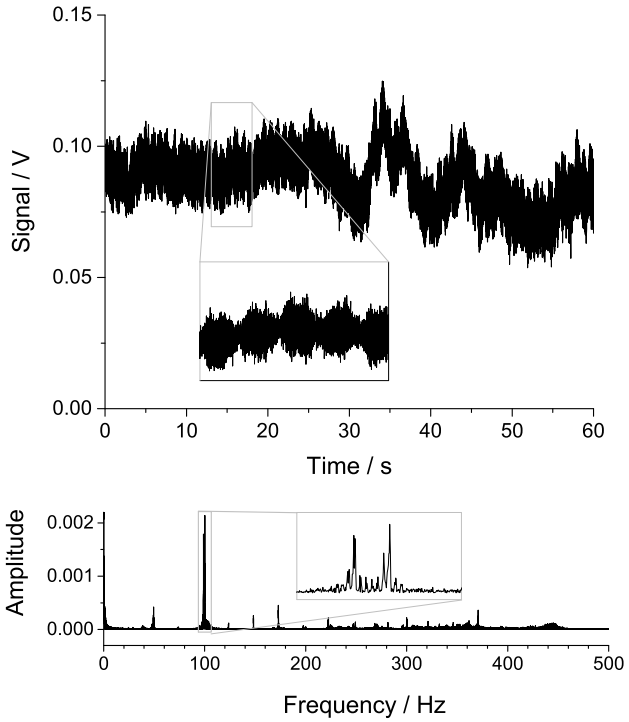

Figure 4.19: Continuous cavity transmission signal (upper) measured with no voltage ramp applied to laser current or active locking program to maintain phase matching. An FFT analysis of the signal (lower) revealed two strong frequency contributions (inset) near 100 Hz, likely due to mechanical disturbances. The two frequency contributions are sufficiently similar to create a clear beating effect in the signal noise (upper inset).

these mirrors into the same set-up, it was possible to study changes to feedback and spectral resolution that arise primarily from differences in cavity bandwidth and mirror transmissivity. The quartz mirrors have a transmissivity at 3 μm of 80% (10 mm thick) while ZnSe has a transmissivity of approximately 70% (5 mm thick) at the same wavelength, though these values ignore effects from the anti-reflection coatings. ZnSe has a higher refractive index, and will therefore intrinsically reflect more incident radiation.[211,212]

A sample cavity transmission spectrum measured with the high finesse cavity is shown in Figure 4.20. In this experiment, the cell was filled with 5% N_2O buffered in N_2 at a total pressure of 90 Torr. Due to the alignment, the signal amplitude for odd and even harmonic longitudinal modes is markedly different. The locking range is significantly shorter with the higher finesse mirrors, likely due to the decreased transmission efficiency of ZnSe compared to the quartz substrate.

The measured absorption spectrum of the 3042.00 cm^{-1} P(5) transition in the $\nu_1 + 3\nu_2$ combination band of N_2O is shown in Figure 4.21. The effective reflectivity of these mirrors,

determined again by a concentration series as before, was determined to be 0.99975. This is slightly higher than measured previously due to cleaning and smaller angle-of-incidence at the folding mirror. The resultant sensitivity, based on the Voigt fit, is 2.5×10^{-8} cm^{-1} for a 100 ms scan. It is interesting to note that the limit of detection is (coincidentally) the same for both the high and moderate finesse cavities. Despite the longer path lengths associated with the higher reflectivity mirrors, the additional losses due to absorption in the ZnSe substrate reduced the transmitted signal and feedback intensity, and so the advantages of the extended path length were offset by the reduced SNR. An ideal system would utilize mirrors with both a high reflectivity and high transmission efficiency at the laser wavelength.

4.6.6 Acetonitrile detection

Acetonitrile is a unique organic species with strongly hydrophilic and hydrophobic moieties that is ubiquitous as a solvent in many analytical techniques such as high performance liquid chromatography (HPLC) and hydrophilic interaction chromatography (HILIC).[213,214] It is a symmetric rotor with eight vibrational modes, four of which are doubly degenerate. In particular, the infrared-active symmetric and doubly degenerate anti-symmetric methyl stretches absorb in the 3 μm region at 2954 cm^{-1} and 3009 cm^{-1} respectively.[215]

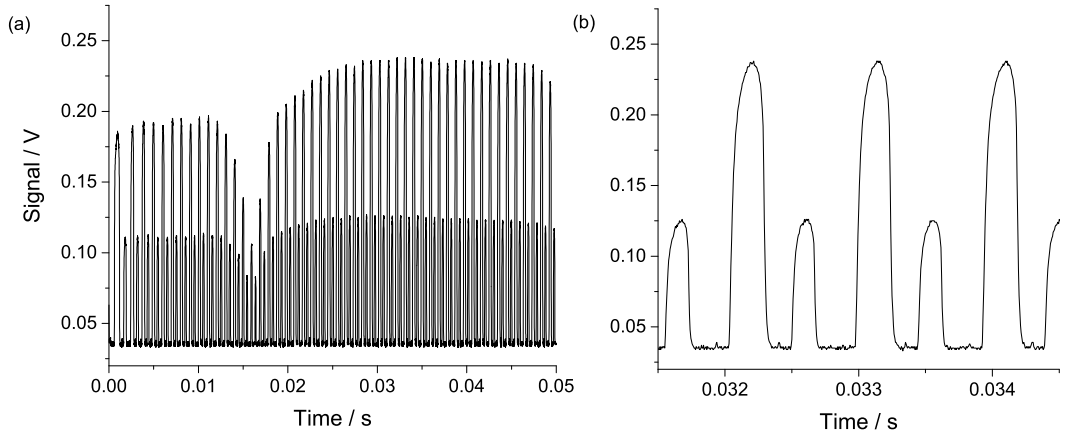

Figure 4.20: (a) Sample cavity transmission measurement with no averaging. (b) Close-up of a few cavity modes showing high SNR and locking range. The FSR in this case is approximately 170 MHz, and there is a clear distinction between the mode amplitude of even and odd harmonic longitudinal modes likely due to inhomogeneities in the folding cavity mirror. Note there is a 30 mV DC offset from the detector.

In the atmosphere, CH_3CN is a long-lived species with a lifetime of 20 years in the stratosphere.[216] CH_3CN is emitted at the surface from biomass burning, particularly forest fires, and is transported into the lower stratosphere by cloud convection.[216] Its main stratospheric sink is reaction with OH, but CH_3CN in the lower troposphere can be lost by dry deposition.[217] The ocean has been identified as being both a sink and a source, and therefore may act as a transport conduit.[217] The biogeochemical cycle is still poorly understood, however, and requires further investigation. Background levels of CH_3CN in the lower troposphere are around 40 ppt, but can rise to a few hundred ppt in some areas.[217]

CH_3CN has been linked to a few physiological studies. Proton transfer reaction mass

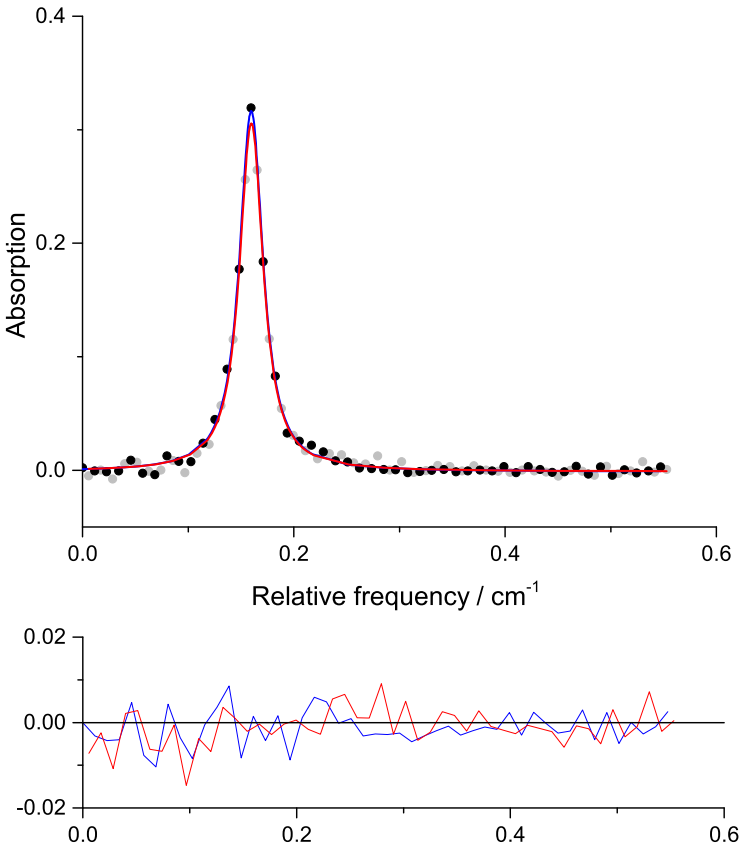

Figure 4.21: Absorption spectrum (upper) and residual (lower) of 5% N_2O in N_2 mixture at 90 Torr measured by OF-CEAS in V-shaped optical cavity. The grey and black circles represent data for even and odd modes, while the red and blue lines show the Voigt profile fit and residual for the same. This gives an MDA of 4.4×10^{-3}, which is equivalent to $\alpha_{min} = 2.5 \times 10^{-8}$ cm^{-1}. The x axes are the same for both plots.

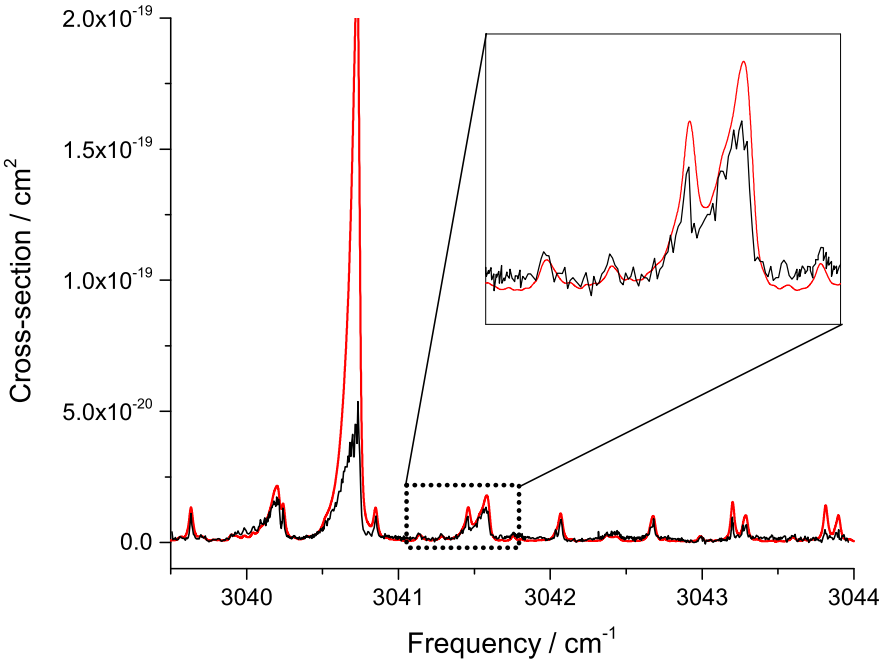

Figure 4.22: The black line shows an acetonitrile spectrum, converted to absorption cross-section per molecule, measured using the moderate finesse cavity ($R = 0.999$) with 30 Torr of 1000 ppm CH_3CN in the cavity. The overlaid HITRAN data set (red) is for CH_3CN at 217 K and 50 Torr (red).[6]

spectrometry (PTR-MS) measurements of the breath of smokers and non-smokers indicated that CH_3CN is present in higher concentrations in smokers' breath for up to a week after smoking ceases.[218] Typical concentrations for non-smokers were under 15 ppb, while smokers' breath contained as much as 200 ppb directly after smoking a cigarette. More recently, studies suggest that CH_3CN levels in breath may be used for diagnosing cystic fibrosis and/or monitoring patients to improve therapy.[219]

Acetonitrile absorbs in the region covered by this laser, although detailed tables of transition cross-sections and broadening parameters are not available. Nevertheless, an OF-CEAS absorption spectrum of a calibrated 1000 ppm sample buffered in synthetic air (BOC) measured in the moderate finesse cavity agrees well with HITRAN data (Figure 4.22). Although the measured spectrum was collected under different pressure and temperature conditions to the reference data, there is still general agreement with more structure visible in the lower pressure OF-CEAS spectrum. The inset highlights the high spectral resolution of the OF-CEAS data, which picks up individual features that are smoothed out

in the reference spectrum due to increased pressure broadening and lower frequency resolution (0.015 cm^{-1}). The notable exception to the good agreement between experiment and reference is the large feature at ~ 3040.6 cm^{-1} which is fit poorly for two reasons. Firstly, the large absorption cross-section and high mixing ratio of the calibrated sample translate to large α values ($\alpha_{max} \sim 5 \times 10^{-5}$ cm^{-1}) which are susceptible to feedback enhancement effects. Secondly, the transitions are highly temperature dependent in this region (for example the maximum amplitude of this spectral feature drops by about 10% at 217 K compared to 207 K based on HITRAN reference spectra), and so the expected maximum cross-section is likely to be much closer to the measured result. Using the Boltzmann distribution to correct for differences in temperature, it is estimated that the amplitude under these experimental conditions would be about half that of the reference spectrum. This ignores other effects such as overlapping transitions and temperature-dependent lineshapes.

Based on the calculated sensitivity of the system (2.5×10^{-8} cm^{-1}), the minimum detectable concentration of CH_3CN at 30 Torr is 500 ppb, assuming the maximum cross-section measured. This is insufficient for detection CH_3CN in breath in real-time, however pre-concentration techniques could be readily employed to increase the species to detectable levels.[219] While the volume of the current set-up makes it impractical for breath measurements at the moment, the development of a smaller volume V-shaped cell would open up opportunities for sensitive detection of CH_3CN in breath using ICL-driven OF-CEAS.

4.7 EC-QCL V-shaped OF-CEAS

4.7.1 5 μm EC-QCL characterization

While external-cavity QCLs (EC-QCLs) use essentially the same type of laser chip as DFB-QCLs, the wavelength selection mechanism makes them function quite differently. The EC-QCL used here is an early Daylight Solutions product broadly tunable between 1776 – 1962 cm^{-1} with up to 150 mW emitted power. The output wavelength is determined by three parameters: laser chip temperature, applied current, and external grating alignment. The first two control the family of frequencies that can be emitted by the cascading electrons, while the latter selects a single wavelength from the laser gain spectrum. This EC-QCL

has a double-ended Littrow grating configuration, shown in Figure 4.23. This configuration was designed to ensure that the direction of the output laser beam does not depend on the grating position, and therefore alignment and collimation are maintained across the entire frequency range of the laser.

This laser was purchased within its own commercial housing including the collimation lens, external cavity, Peltier and water cooling for laser chip. The combined current and temperature control unit was purchased from the laser manufacturer (Daylight Solutions). This controlled the applied driving current, Peltier temperature, and position of the external grating by a PZT. Small amplitude, fast modulation ($>$ 10 kHz) could be applied *via* current modulation, while slow modulation ($<$ kHz) of the laser output could be achieved by tuning the grating PZT. Fast modulation across the entire frequency range is not possible with EC-QCLS as it is with DFB-QCLs. Conversely, EC-QCLs can cover far more absorption lines, therefore offering a great deal more flexibility in optical frequency coverage.

Until recently, mode hops have been one of the limitations to EC-QCL utility.[220] Mode-hops occur due to longitudinal mode competition for dominance within the gain spectrum of the laser. When one longitudinal mode suddenly "wins", a jump in the emitted frequency to the new resonant mode frequency occurs with a small frequency interval skipped. These hops prevent smooth, well-controlled tuning.

4.7.2 Experiment

There is no evidence in the literature that an EC-QCL has been successfully used for OF-CEAS experiments. To investigate this possibility, the Daylight EC-QCL was scanned over $\sim$ 0.5 – 1 cm^{-1} using the internal piezoelectric transducer (PZT) driven by an external function generator (TTI TG230) outputting a 5 Hz sinusoidal signal. A collimating lens enclosed in the housing ensured a collimated output beam with an emitted power typically

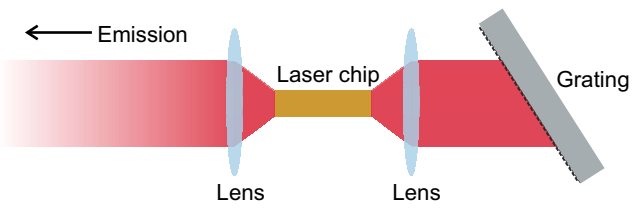

Figure 4.23: Patented double-ended Littrow configuration for EC-QCL grating. This configuration with the grating maintains emission alignment as the grating is tuned to select different wavelengths.

around 100 mW. The current was typically set to a value between 290 – 340 mA, well above threshold and below the maximum allowable level. The beam was directed onto the folding mirror of a custom-made V-shaped cavity constructed from 2.54 cm diameter stainless steel tubing. The two end mirrors were mounted on bellows that allowed adjustability with the mirrors forming part of the outer cell seal. The folding mirror was fixed in place.

A delay line on one pair of steering mirrors allowed coarse tuning of the laser–cavity distance to match the length of each cavity arm (46 cm), and a CaF_2 window in front of the cavity reflected a small amount of light onto a photovoltaic detector (VIGO, PVI-2TE-10.6). Gas was flowed through the sealed cavity *via* an outlet port at the M_1 bellows and an inlet port at the M_2 bellows. The outlet port was connected *via* a valve to a barotron (Leybold Ceravac CTR 90) and a diaphragm vacuum pump; the inlet port was connected to a gas cylinder containing 5% N_2O in N_2 (BOC). The custom dielectric-coated ZnSe cavity mirrors (Lohnstar Optics, $R > 0.999$) included one plane mirror at the centre turning point (M_0) and plano-concave mirrors (1 m radius of curvature) at the M_1 and M_2 positions. An off-axis parabolic mirror ($f = 2.54$ cm) was placed after M_2 and focused light leaking out of the cavity onto a second photovoltaic detector (VIGO, PVI-2TE-10.6).

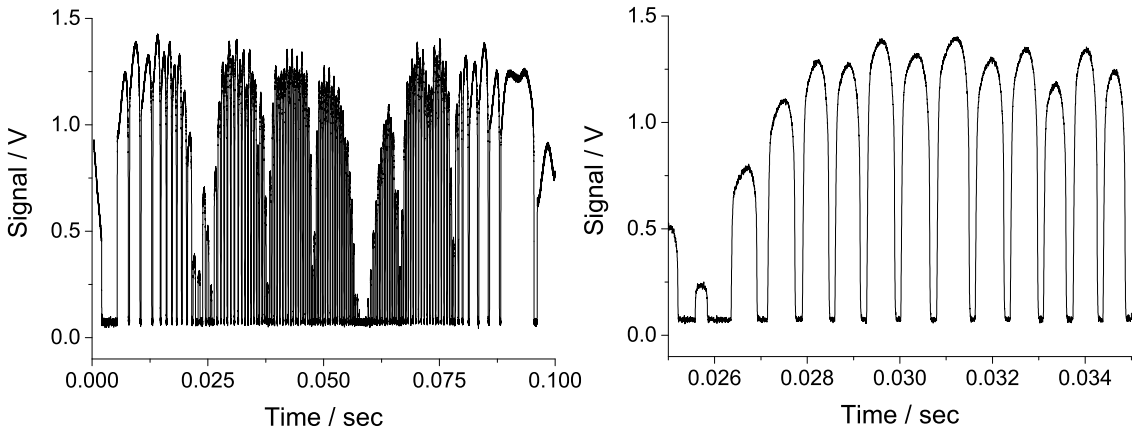

Figure 4.24: (left) Typical cavity transmission collected over a single scan (200 ms) through an evacuated cavity as the laser frequency is ramped down. The modes last for a longer amount of time towards the turning points of the piezo range (at $\sim$ 0 and 0.1 s) with the shortest modes in the middle; this is due to the non-linear frequency tuning. The oscillation in amplitude is due to an etalon between the detector and near cavity mirror. (right) A close-up view of the mode shapes in the same scan.

4.7.3 Results

A typical cavity transmission spectrum measured through an evacuated cavity is shown in Figure 4.24. It is clear that the feedback rate allows for the laser to remain locked to the resonant cavity for just less than one FSR, which maximizes the build-up of intracavity power while still allowing for excitation of consecutive modes. In this case, the FSR is 169 MHz with both even and odd harmonic longitudinal modes excited. The symmetric modes and long locking range (relative to the ring-down time) are evidence that an EC-QCL responds well to optical feedback. Indeed, it is possible, as shown in Figure 4.25, to lock the laser to the cavity for a relatively long time when no ramp is applied. While the cavity transmission is maintained, the laser is frequency-narrowed and emits at a wavelength within the linewidth of the high finesse cavity.

The signal does exhibit a very regular fluctuation with a frequency of about 100 Hz. This fluctuation is evident in the laser output intensity, indicating that it is a laser rather than a cavity effect. It is likely noise introduced by mechanical vibrations from adjacent equipment or the internal piezo as this is roughly the response time of the actuator. Due to this fluctuation, a longer locking range and higher feedback rate is likely required to maintain long-term locking. Nevertheless, the ability to maintain locking over seconds is a promising feature that may be useful in future experiments.

The primary purpose of OF-CEAS, however, is trace gas detection by measuring absorption spectra. In this respect, the EC-QCL was not sufficiently consistent for reproducible gas concentration measurements. For the pressure-broadened samples typically measured using this technique, one needs to scan over at least 0.5 cm^{-1} to fully cover an absorption feature. There were very few current and wavelength conditions under which the laser did not exhibit mode hops when the piezo was ramped over this range. While the Littrow configuration allowed for stable locking across the entire tuning range of the laser without realignment, the mode hopping was more frequent at lower wavenumber and so the spectra shown here were collected at centre frequencies above 1850 cm^{-1}. The mode jumps were not consistent from scan-to-scan, as shown in Figure 4.26, and therefore averaging

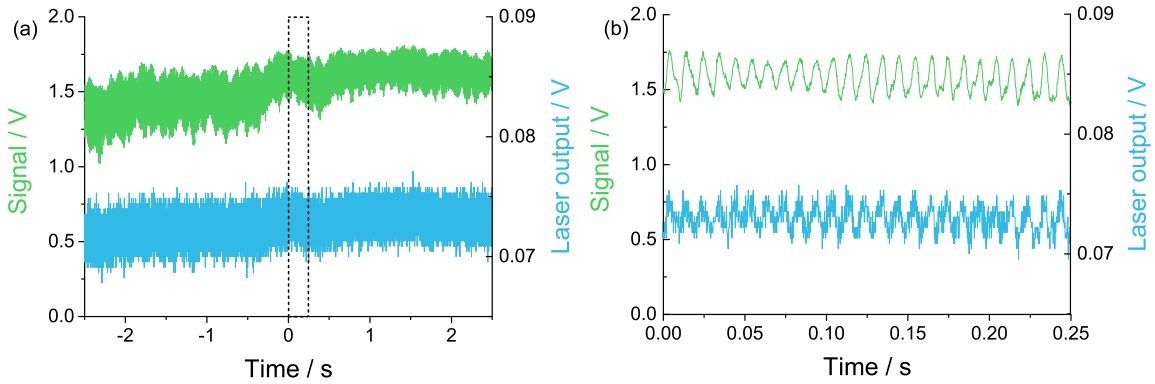

Figure 4.25: (a) Plot of cavity transmission (green) with the laser emitting at a single wavelength, shown with the laser output (blue) measured by reflecting a portion of the beam onto a second detector in front of the cavity. The laser signal has been smoothed using a 20 point moving average. No active adjustments were required to keep the laser locked to the cavity for the full measurement. (b) A more detailed view of the signals (dashed box) showing oscillations in both the laser output and cavity transmission. These fluctuations have a frequency of about 100 Hz, and are likely caused by mechanical disturbances.

spectra was not possible. The phase of feedback affected where mode-hops were observed across a scan, likely due to small changes in refractive index and/or temperature of the laser chip associated with the returning feedback light.

The spectrum shown in Figure 4.27 covers transitions given in Table 4.4. The mirror reflectivity was measured by ring-down to be 0.999785. For the Voigt profile fits of the

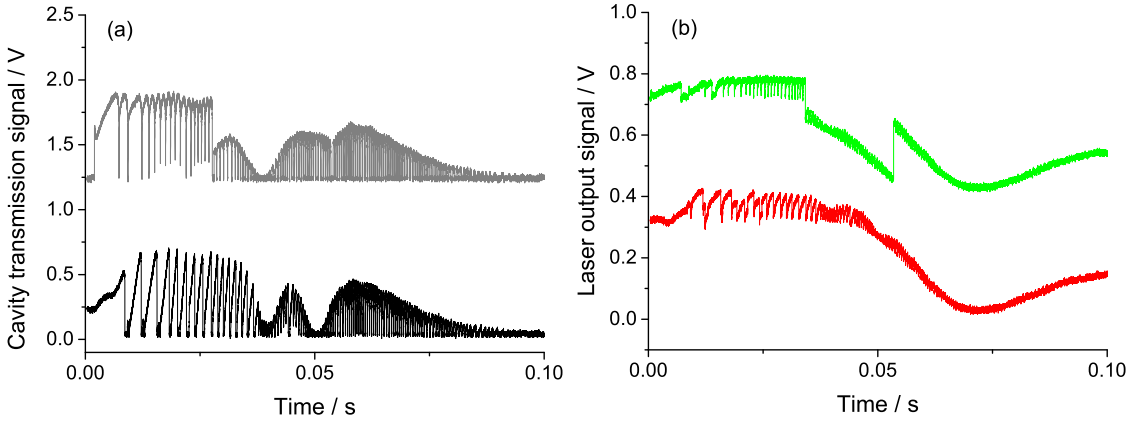

Figure 4.26: (a) Cavity transmission through V-shaped cavity containing 5% N_2O at low pressure. In the upper, light grey trace there is a clear mode hop at about 0.025 s, and a second at 0.055 s. (b) Laser output showing similar behaviour, with the lower, red trace measured while the laser tuned continuously, and the upper, green trace measured when the laser mode-hopped at two points during the scan. Note that the broad etalon is an artefact of reflections interfering in the set-up, and is not due to fluctuations in output laser intensity. No adjustments were made to the system between measurements.

Table 4.4: Details from HITRAN of the main N_2O transitions within the spectral region scanned. All transitions for the most naturally abundant isotope.[6]

Frequency / cm^{-1}	**Transition**	**Cross-section / cm^2 cm^{-1}**
1911.210	1110 ← 0000 R(39e)	1.17×10^{-23}
1911.297	1330 ← 0220 R(24e)	4.15×10^{-25}
1911.297	1330 ← 0220 R(24f)	4.02×10^{-25}
1911.319	1220 ← 0110 R(31f)	2.15×10^{-24}
1911.371	1220 ← 0110 R(30e)	2.34×10^{-24}

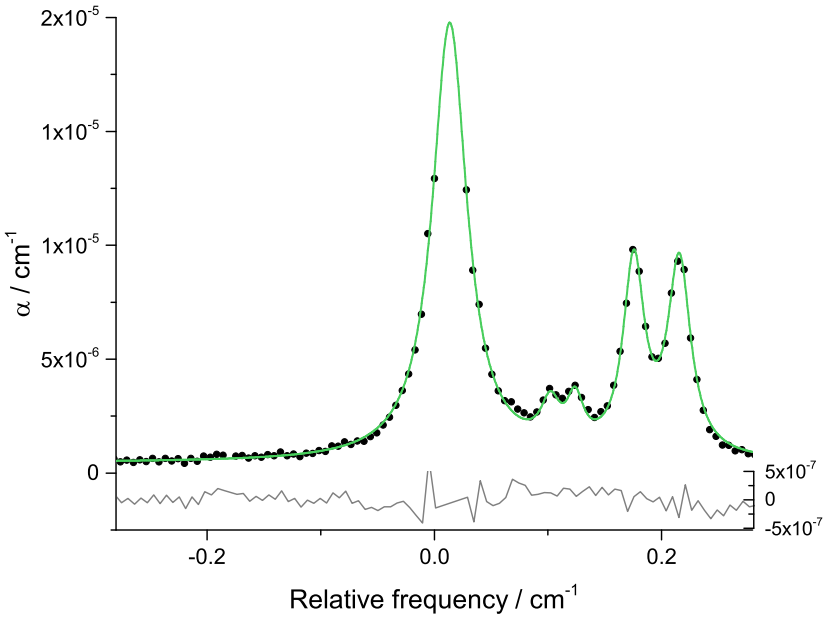

Figure 4.27: Absorption coefficient spectrum of gas sample containing 5% N_2O in N_2 at 100 Torr total pressure. The data (black circles) are fit well by the Voigt profile simulation (green), as shown in the fairly homogeneously distributed residual (below). The fit gives $\alpha_{min} = 1 \times 10^{-7}$ cm^{-1}. Data points are missing in the region around 0.0 cm^{-1} frequency due to nearly complete absorption of the intracavity light.

data, the Gaussian linewidths were set according to the Doppler broadening, and the centre frequencies and areas of overlapping features scaled according to HITRAN.[6] The cavity modes near line centre of the strongest transition were too weak to measure accurately. The lineshape of this large transition, in particular, is broad (0.04 cm^{-1} FWHM), which may indicate that attenuation of feedback enhancement (as discussed in Section 4.4) causes lineshape distortions at these high absorption levels. The resulting mean square residual

of the spectrum gives $\alpha_{min} = 1.0 \times 10^{-7}$ cm^{-1} at 100 Torr. This sensitivity clearly does not match the performance achieved with diode lasers, however it is similar to the earliest studies with ICLs. This laser was produced in one of the earliest generations of EC-QCLs manufactured by Daylight, and since then the company has made great strides in enhancing the robustness of their systems and decreasing mode-hopping; the technique may therefore be more successful with a newer version of this laser that does not suffer the same mode instability limitations.

4.8 Conclusions

Trace gas detection using OF-CEAS with DFB-ICLs and EC-QCLs has been demonstrated for the first time. Using a V-shaped optical cavity to ensure pure feedback from the high finesse resonance, DFB-ICLs at 3.24 μm and 3.29 μm were shown to sensitively measure several VOCs. Measurements of standard N_2O mixtures demonstrated sensitivity down to $\alpha_{min} = 2.5 \times 10^{-8}$ cm^{-1} in 100 ms. Acetonitrile, which is of growing interest for medical studies, was successfully measured. The first demonstration of EC-QCL-based OF-CEAS was less successful. Although a limited sensitivity of $\alpha_{min} = 1 \times 10^{-7}$ cm^{-1} in 100 ms was achieved for N_2O measurements, spontaneous and inconsistent mode-hopping of the laser frequency could not be eliminated. The results represent a promising step towards achieving high quality OF-CEAS measurements with broadly tunable EC-QCLs.

Chapter 5

Linear Cavity OF-CEAS: A Simple and Novel Approach

5.1 Introduction to linear cavity OF-CEAS

5.1.1 Alternative geometries for OF-CEAS

V-shaped optical cavities have been the most popular configuration for OF-CEAS experiments over the past decade, partly because a comprehensive theoretical foundation has been established specifically for this design.[176,179] However, optical cavities can be formed in a wide variety of shapes and styles, and it is interesting to explore the potential of using other types of cavities that may be more suitable for some applications of OF-CEAS. Indeed, a number of other high finesse cavity configurations (shown in Figure 5.1) have already been shown to allow stable locking and sensitive gas detection.[199,221]

A triangular optical cavity with circular intracavity light propagation (Figure 5.1 (b)), also known as a ring cavity, is one alternative that has been used for OF-CEAS measurements.[199] This three-mirror ring cavity is similar to the V-shaped cavity with M_1 and M_2 angled such that the light propagates in the order $M_0 \rightarrow M_1 \rightarrow M_2 \rightarrow M_0$. Hamilton *et al.* used a three-mirror triangular cavity with a retro-reflector behind one mirror to allow bidirectional propagation around the ring to establish stable standing waves when the laser is on resonance.[199] Although a four-mirror bow tie-shaped ring geometry (Figure 5.1 (c)) has not yet been used for OF-CEAS, it is reasonable to expect that this could work in a

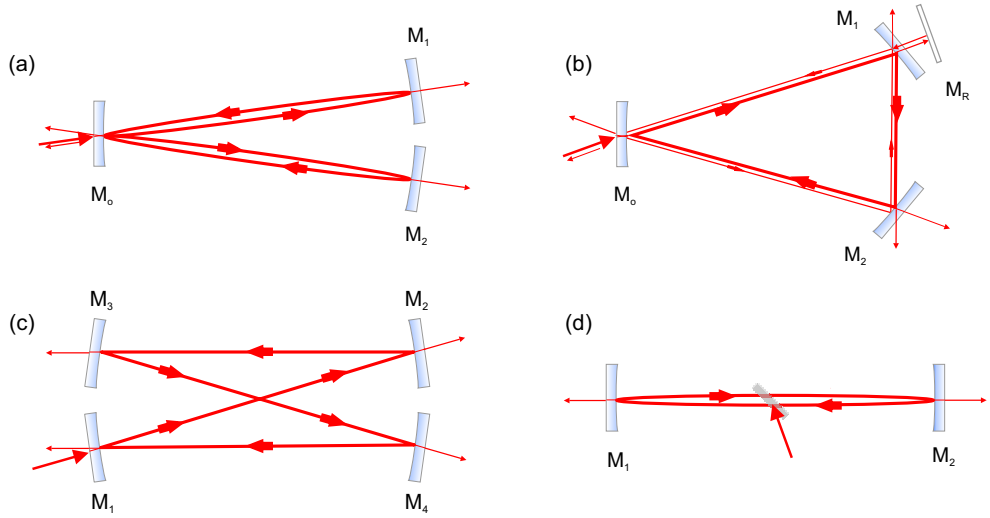

Figure 5.1: Schematic of a variety of optical cavity geometries with beam propagation: (a) V-shaped cavity discussed in previous chapter; (b) triangular ring cavity with retroreflector (M_R) positioned to re-inject counter propagating light through M_1;[199] (c) bow-tie ring cavity, with mirrors numbered in order of beam propagation, which has been used for similar techniques and functions as a folded ring cavity;[148] (d) Brewster angle linear optical cavity where light is injected *via* a glass plate at Brewster angle, indicated in grey.[221] Note that overlapping lines are displaced for clarity.

similar way.[148] One of the limitations of these techniques is the weak intensity of the feedback field due to losses upon re-injection of the retro-reflected light, as well as the multiple mirror reflections on each pass. Additionally, the reflectivity of dielectric mirror coatings is highly dependent on the angle of incidence of the radiation, and can fall off significantly as the angle deviates from normal incidence.

OF-CEAS has been performed with a Brewster angle cavity.[221] In this configuration (shown in Figure 5.1 (d)), an intracavity glass plate allows Brewster-polarized laser light injected at a specific angle to be reflected many times along an optical axis between two high reflectivity mirrors when the laser wavelength is in resonance with the cavity. While this technique can be used with visible light, it is difficult to find optical materials with sufficiently high transmittivity in the mid-infrared, and the intracavity loss resulting from this would severely limit the sensitivity of this OF-CEAS variant with QCLs.

In terms of construction complexity, a linear, two-mirror cavity with on-axis injection through one end mirror is the simplest optical cavity design. This is the geometry explored in depth in this chapter.

5.1.2 Linear cavity OF-CEAS

Using a high finesse linear optical resonator for OF-CEAS has many advantages over the more common V-shaped set-ups. For the V-shaped system, as described in the previous chapter, the sample can either be enclosed in a box surrounding the optical cavity – which requires a relatively large sample volume – or a customized sample cell must be fabricated to enclose the optical path. The latter requires skilled glass blowing or metalworking and, depending on the method used, there may be fabrication restrictions on the central angle where the two arms join together. While a custom cell can minimize the required volume, it is not conducive for smooth flow conditions due to the sharp angle at the folding mirror. Increasing the central angle is not desirable since the reflectivity of dielectric coatings can fall off sharply with increasing angle of incidence, and the s- and p-polarized components will experience different reflectivity efficiencies.[11]

A linear cavity can easily be constructed with a single tube connecting the two opposing cavity mirrors. This configuration is commonly used for CRDS and other variants of CEAS – indeed, cavity mirrors are often sold in pairs – so in principle CRDS or CEAS experimental set-ups could easily be repurposed for OF-CEAS experiments. The geometry is conducive to near-laminar gas sample flow through the single, straight tube, which can have a minimal volume close to the volume of the intracavity field. It should be noted that *linear cavity* here refers to a system where the intracavity field propagates along a single axis between two mirrors that are positioned parallel to each other and normal to the optical axis. It is possible to have different optical paths within a cavity that physically has a linear geometry. For example, Dahmani *et al.* demonstrated locking a diode laser using a V-shaped beam propagation within a linear, confocal cavity.[222] While this configuration could ease some of the disadvantages of V-shaped systems, the finesse of the cavity was limited.

OF-CEAS measurements are theoretically more efficient with linear cavities compared to V-shaped cavities. In a V-shaped cavity there are four turning points where light leaks through the cavity mirrors, meaning that the maximum theoretical signal intensity on the detector is 25% of the incident light.[179,204] With a linear cavity, on the other hand, all the

light leaking out of the cavity is utilized – light leaking out of the injection mirror (M_1) is the feedback field that locks the laser frequency, and light leaking out the opposite mirror (M_2) is detected. One can argue that the spectral resolution is higher for linear systems. Clearly, the FSRs of a linear system and V-shaped system with the same total path lengths are equivalent. In practice if the laser–cavity distance is an even integer of the cavity arm length the laser will only lock to alternating modes, halving the spectral resolution (*i.e.* $2 \times$ FSR); alternatively, if the laser–cavity distance is an odd integer of arm lengths and the laser locks to every cavity resonance, the even and odd harmonic resonant frequencies must be analysed independently resulting in two data sets with half the resolution of the equivalent linear system.

Linear optical cavities have been used for feedback-based experiments in the past. Over a decade ago, a linear cavity system was used to frequency-lock a diode laser for mirror birefringence measurements.[223] More recently, a similar system was developed to lock a diode laser to a linear cavity for Raman scattering spectroscopy.[224,225] In these experiments, one or two Faraday isolators were placed between the laser and cavity to reduce unwanted reflections returning to the laser. Optical isolators not only add a cost and space burden to the apparatus, they are not well-developed in the mid-infrared spectral region with poor isolation efficiency and high transmission losses.

For many years the prevailing belief in the scientific community was that it would be impossible to stably lock a mid-infrared laser to a high finesse linear cavity for OF-CEAS measurements.[223] Unlike the configurations used previously for OF-CEAS, the laser beam must be at normal incidence to the injection mirror. This means that light not injected into the cavity will be reflected straight back along the incident trajectory and return to the laser. This reflected field acts as "bad" feedback – the linewidth of the returning light has not been narrowed and the amplitude of the feedback field will be the same for all laser frequencies. For typical cavity injection efficiencies, the intensity of reflected light must be much greater than that of the field leaking out of the high finesse cavity. While little work has been conducted on the effects of competing feedback fields, it has been widely accepted that the much more intense reflected feedback field must dominate and prevent

stable locking to the weaker feedback field returning from the resonant cavity.

Despite the dire predictions, linear cavity-based OF-CEAS was successfully demonstrated in this group, and the first studies were published in 2013.[205] In this work, a 3 mW DFB-QCL at 5.5 μm was locked to a 77 cm long linear cavity for measurements of NO and N_2O. For this proof-of-principle experiment, the sensitivity was similar to other OF-CEAS studies using QCLs ($\alpha_{min} = 2 \times 10^{-8}$ cm^{-1} Hz$^{-1/2}$), however the locking range was short, indicating a low feedback rate.[199]

In this chapter, a theoretical foundation for linear-based OF-CEAS is first developed to explain how the laser can stably lock to a high finesse cavity in the presence of a competing feedback source. Experimental measurements using a 200 mW 5.3 μm DFB-QCL are then compared to the model, and the potential of the technique discussed. A selection of results in this chapter were reported in the literature.[226]

5.2 Theory

5.2.1 Linear cavity transfer function

The theoretical framework developed here is based on a cavity as shown in Figure 5.2 where the laser light is incident on M_1 and detected after M_2. The feedback model development starts from the equation for the coupled laser frequency introduced earlier (Equation 4.3) where h_{fb}, the feedback transfer function, depends on the cavity configuration. Feedback can return to the laser in three ways: reflected from the first, flat surface of M_1, reflected from the curved surface of M_1, or leaking out of the cavity when a resonant intracavity field is excited. The first can be disregarded, as shown *vide infra*. The feedback transfer function

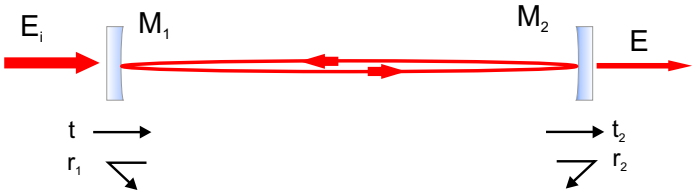

Figure 5.2: Schematic of linear cavity where light is injected through M_1 and measured after M_2. The transmission (t_i) and reflection (r_i) coefficient labelling scheme is shown.

therefore has two major components: a *non-resonant* term due to the light reflected from the curved face of the mirror:[173]

$$h_1 = \sqrt{R} \tag{5.1}$$

and a second term from the *resonant* cavity.

Following the analysis by Davis, the field leaking back through M_1 is related to the incident field by:[227]

$$E_{fb} = E_i \left[t^2 r_2 \exp(-(2ik + \alpha)L) + t^2 r_1 r_2^2 \exp(-2(2ik + \alpha)L) + \dots \right] \tag{5.2}$$

where t, r_i, and L are the transmission coefficient, reflection coefficients, and cavity length as labelled in Figure 5.2. The phase factor is the same as previously defined ($k = 2\pi/\lambda = 2\pi\tilde{\nu}$), and α is the absorption coefficient. Using similar approximations as applied previously, this can be simplified to find the transfer function representing the resonant feedback from the high finesse cavity (h_2):

$$h_2 = \frac{t^2 r_2 \exp(-(2ik + \alpha)L)}{1 - r_1 r_2 \exp(-(2ik + \alpha)L)}. \tag{5.3}$$

Assuming that $T \approx 1 - R$ and all mirrors are identical leads to:

$$h_2 = \frac{(1 - R)\sqrt{R} \exp(-(2ik + \alpha)L)}{1 - R \exp(-(2ik + \alpha)L)}. \tag{5.4}$$

Combining Equations 5.1 and 5.4 yields:

$$h_{fb,L} = C_1 \sqrt{R} + C_2 \frac{(1 - R)\sqrt{R} \exp(-(2ik + \alpha)L)}{1 - R \exp(-(2ik + \alpha)L)} \tag{5.5}$$

where C_1 and C_2 are introduced as scaling factors to account for different losses as the fields return to the laser.

Equation 4.3 assumes that the laser–cavity distance (L') is equal to the cavity arm lengths (L) such that phase-matching between the laser and feedback is optimized. This means the reflected and resonant cavity feedback fields will generally be in-phase on the return to the laser as each experiences an odd number of π phase changes due to reflections

from dielectric coatings.

It is useful to first understand how each feedback field affects the laser individually. Figure 5.3 shows how the behaviour of a 5.3 μm QCL changes when only reflected light acts as feedback. The plot shows the output frequency of the laser subject to external feedback injection seeding as a function of free running laser frequency according to Equation 5.1 and 4.3. The grey line is the reference condition where the laser frequency follows the set temperature and current control. The free running frequency is the emitted frequency when no feedback affects the laser, and can be considered a proxy for time when the laser current is tuned linearly. The dashed line accounts for injection seeding from a reflection from an external reflector located 77 cm from the laser source with a feedback rate 5×10^{-5}. The laser frequency must scan monotonically, and the green and red lines show the progression of the laser frequency as the free running laser frequency is decreased or increased respectively. The frequency changes sharply at intervals corresponding to $c/2L'$ where L' is the laser–reflector distance. This is the same as the behaviour reported by Lang and Kobayashi and

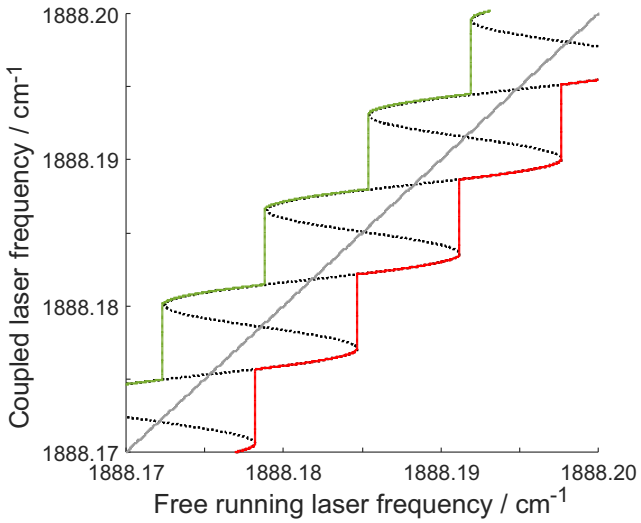

Figure 5.3: Simulated laser frequency output when subject to reflections returning to the laser cavity from an external reflector. The plot shows the coupled laser frequency – the emitted laser frequency stimulated by feedback injection seeding – as a function of free running frequency dictated by current and temperature control. The grey solid line represents a laser not coupled to any feedback where the actual frequency matches the free running. The black dashed line is the curve predicted by Equation 5.6. Due to the requirement for monotonic frequency change, there is a hysteresis in the emitted frequency: the red line follows the curve as the frequency is scanned from low to high wavenumber, and green follows the curve from high to low. In this simulation, $\beta = 4 \times 10^{-5}$ and $L' = 77$ cm.

other studies.[173,175,228] The sinusoidal contours arise because of the multistability of the semiconductor subject to feedback that affects both the shape of the gain spectrum and refractive index of the semiconductor gain medium. The discontinuities in frequency occur at different points depending on the direction of scanning – this hysteresis arises because the laser must monotonically ramp in a single direction.

Feedback from a high finesse cavity causes a laser to deviate from free running conditions only over a very narrow wavenumber range corresponding to a resonant longitudinal mode within the cavity, as shown in Figure 5.4. The plot shows a coupled laser response to linear cavities under three different conditions of finesse ($\mathcal{F}$) and feedback rate (β): $\mathcal{F} = 10500$, $\beta = 4 \times 10^{-5}$ (solid black); $\mathcal{F} = 10500$, $\beta = 8 \times 10^{-5}$ (dashed grey); and $\mathcal{F} = 3000$, $\beta = 4 \times 10^{-5}$ (dotted grey). As the laser frequency is increased from left-to-right across the plot the coupled and free running frequency of the laser match until it reaches a resonant frequency. At this point the laser frequency remains at nearly a single value for an extended time. As the bandwidth of the cavity decreases (*i.e.* $\mathcal{F}$ increases), the range of frequencies over which the laser frequency can be locked decreases. The feedback rate only

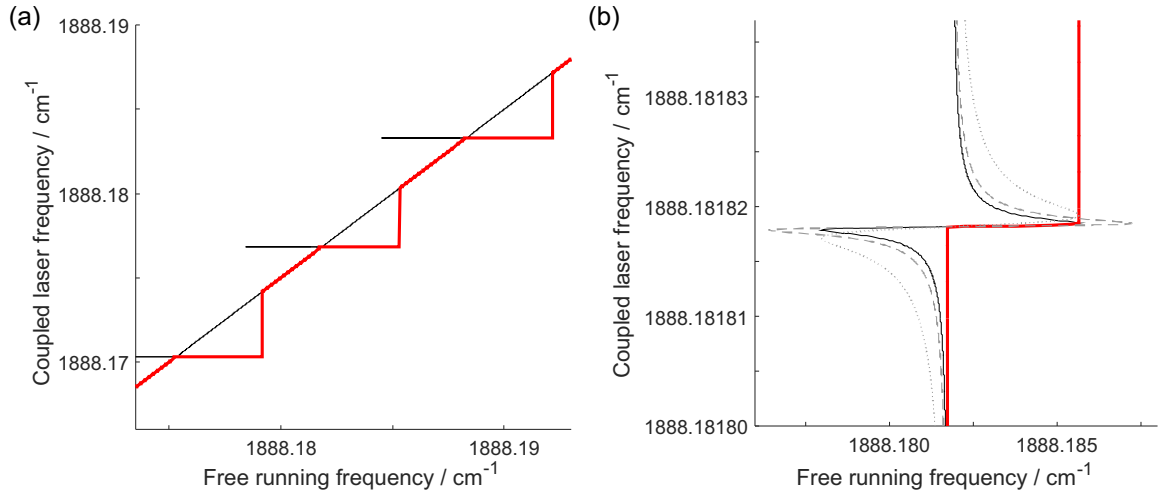

Figure 5.4: (a) Simulated laser frequency output when subject to only feedback from a high finesse linear cavity. (b) Close-up of region around a resonant frequency of the cavity. The solid black line represents the coupling of the laser with a 77 cm-long cavity with $\mathcal{F} = 10500$ ($R = 0.9997$) and $\beta = 4 \times 10^{-5}$, and the red line shows the emitted frequency as the laser is tuned from low to high wavenumber under these conditions. The grey dotted line represents a cavity with $\mathcal{F} = 3000$ ($R = 0.999$) and $\beta = 4 \times 10^{-5}$; and the grey dashed line represents a cavity with $\mathcal{F} = 10500$ and $\beta = 8 \times 10^{-5}$. The feedback is assumed to be in phase with the laser when it re-enters the laser cavity.

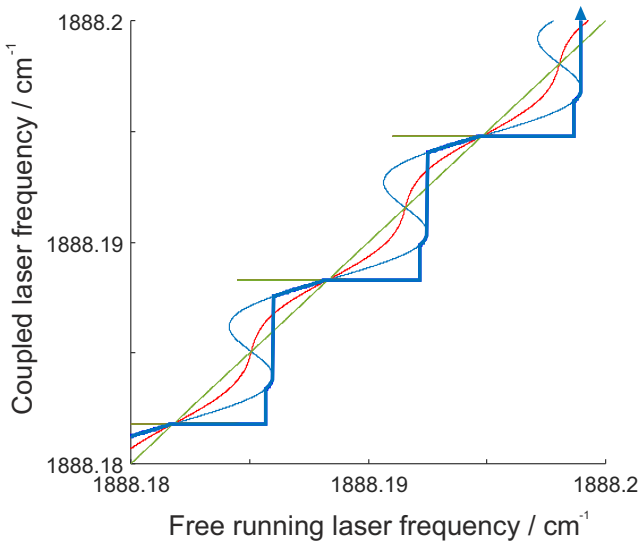

Figure 5.5: Feedback model of coupled laser frequency subject to both resonant and non-resonant feedback compared to free running condition. In all simulations, $\beta = 10^{-5}$, $C_2 = 1$, and $R = 0.9997$. Three values of C_1 were modelled: 0.0 (green), 0.1 (red), and 0.3 (blue). The thick blue line shows the emitted frequency as an upward ramp is applied for the scenario with the highest non-resonant feedback rates. The laser frequency increases monotonically (direction shown by arrow), leading to jumps as shown.

affects the locking range, or the range of the free running frequency over which the laser can be locked, which corresponds experimentally to the length of time the laser is locked relative to the time to scan between successive longitudinal modes.

Figure 5.5 shows simulations of the frequency tuning of a feedback-coupled 5.3 μm QCL over two cavity resonances under different feedback conditions with both resonant and non-resonant contributions. In all simulations, $R = 0.9997$, $C_2 = 1$, and $\beta = 10^{-5}$ with varying non-resonant feedback strengths ($C_1 = 0 - 0.3$). This range of feedback rates was chosen based on estimates reported in previous studies.[176,197,201] The laser behaviour can be predicted from the model by following the appropriate curve in the direction corresponding to the applied current ramp. The green curve in Figure 5.5 corresponds to feedback arising from a system where no reflections return to the laser ($C_1 = 0$), such as a V-shaped optical cavity. The blue and red lines indicate the tuning with different feedback rates for the non-resonant field ($C_1 = 0.3$ and $C_1 = 0.1$ respectively), and show that the frequency locking feature arising due to the high finesse optical cavity is superimposed on an oscillation due to the non-resonant reflection with an amplitude determined by C_1. The presence of the non-

resonant field leads to additional frequency jumps. When the laser comes to the end of the locking range, the frequency nearly instantaneously returns to the free running frequency until the next resonant frequency. Clearly, the figure shows that it is still theoretically possible for the "good" resonant locking to occur under the correct conditions. One can also see that the amplitude of the non-resonant feedback becomes irrelevant once the laser is locked to the cavity.

The phase of the feedback is an important consideration in simulations based on Equation 5.6. Even if L and L' are nominally equal, very small deviations can alter the phase of the feedback fields relative to the laser. A phase term (Φ) can therefore be introduced to Equation 4.3 to account for these small changes in length that affect the feedback phase:

$$\nu_o = \nu_{fb} + \frac{\sqrt{\beta}(1-R_o)c}{2\ell n_o\sqrt{R_o}}\left[\mathrm{Re}(h_{fb})\sin\left(\frac{4\pi L'\nu_{fb}}{c}+\Phi\right) - \mathrm{Im}(h_{fb})\cos\left(\frac{4\pi L'\nu_{fb}}{c}+\Phi\right)\right]. \tag{5.6}$$

The variables in this equation include the laser cavity length (ℓ), the laser medium refractive index (n_o), the laser facet reflectivity (R_o), and the feedback rate (β). A MATLAB program was written to simulate the coupled laser behaviour based on this equation. It is difficult to directly measure the frequency and amplitude of the fields returning to the laser, and so the model simulated the cavity transmission. This required determining the transfer function of the field transmitted through the cavity and detected after M_2. Proceeding along a similar route as previously, the transmitted field can be described by:

$$E = E_i\left[tt_2\exp\left(-(2ik+\alpha)\frac{L}{2}\right) + tt_2r_1r_2\exp\left(-3(2ik+\alpha)\frac{L}{2}\right)+\ldots\right] \tag{5.7}$$

in agreement with Lehmann and Romanini.[229] The transmitted field generally experiences an odd number of π Gouy phase shifts and even number of reflections before leaking out through the output mirror. The transfer function of the field passing through M_2 is therefore:

$$h_L = \frac{E}{E_i} = \frac{tt_2\exp\left(-(2ik+\alpha)\frac{L}{2}\right)}{1-r_1r_2\exp(-(2ik+\alpha)L)}. \tag{5.8}$$

Equation 5.8 was used to simulate cavity transmission intensity for different phase con-

ditions, as shown in Figure 5.6, similar to previous analysis for V-shaped cavity OF-CEAS.[176,179,230] In each panel, the upper figure shows the theoretical coupled laser frequency (dashed line) with bold line indicating the coupled laser tuning as it is scanned from low to high wavenumber; the lower figure shows the corresponding simulated cavity transmission. The condition that gives the most symmetric cavity transmission profile and longest locking range (b) is not a perfect phase match between the laser and feedback fields (a).[176] If the feedback phase is more significantly different to the laser, then the cavity transmission will appear asymmetric (c). When the feedback is out-of-phase with the laser field (d), no sustained locking occurs.

The change in the general appearance of the simulated cavity modes reflects distortions of the coupled laser frequency curve that arise when the feedback field is not phase-matched to the laser. This can be seen clearly in Figure 5.7 where the frequency tuning curves for three phase angles are shown along with the corresponding cavity transmission simulations, which are all scaled to a maximum amplitude of unity and therefore do not account for changes in cavity transmission intensity due to increased coupling of the laser into the resonant cavity field.

Following on from Equation 5.8, one can derive an equation to determine absorption in the intracavity path, and thereby the concentration of a target gas. The measured intensity is

$$\frac{I_\alpha}{I_i} = |h_L|^2 = \frac{T^2 \exp(-\alpha L)}{(1 - R\exp(-\alpha L))^2} \tag{5.9}$$

when there is an absorber present, or

$$\frac{I_o}{I_i} = |h_L^o|^2 = \frac{T^2}{(1-R)^2} \tag{5.10}$$

when no absorbing species is present. The absorption coefficient can again be determined by comparing the transmitted intensity with and without the target species:

$$\frac{I_o}{I_\alpha} = \frac{T^2\,(1 - R\exp(-\alpha L))^2}{T^2\exp(-\alpha L)\,(1-R)^2}. \tag{5.11}$$

Rearranging and using the approximation $\ln(1-x) \approx -x$ yields:

$$\alpha = \frac{(1-R)}{L}\left(\sqrt{\frac{I_o}{I_\alpha}} - 1\right). \tag{5.12}$$

This expression is similar to the formula derived for the V-shaped system (Equation 4.14) and in agreement with Bergin *et al.*.[205]

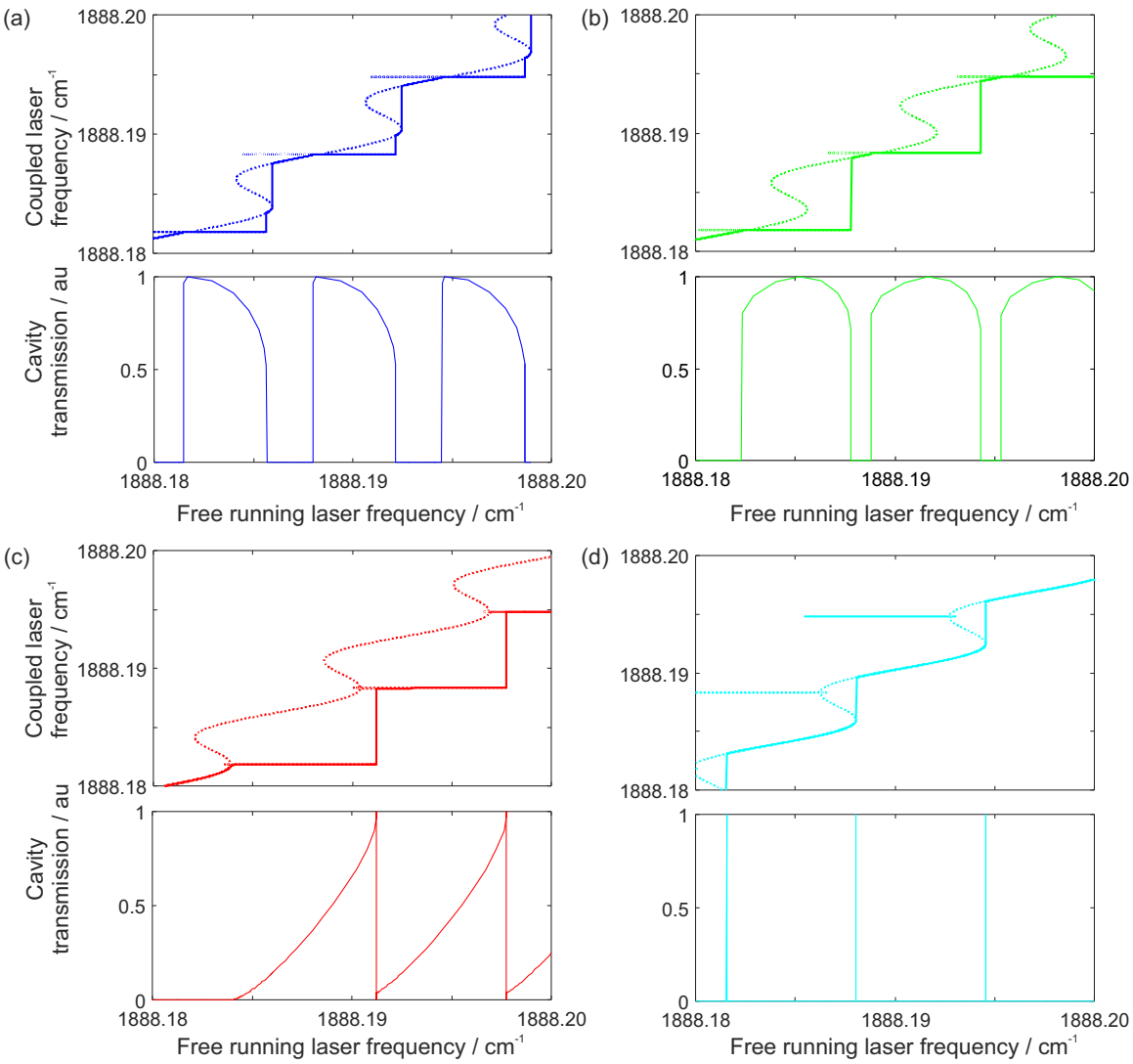

Figure 5.6: Complementary coupled laser frequency (upper) and cavity transmission simulations (lower) for different phase conditions: (a) $\Phi = 0$ rad; (b) $\Phi = 0.18$ rad; (c) $\Phi = +1.0$ rad; (d) $\Phi = -1.0$ rad. For all simulations, $\beta = 4 \times 10^{-5}$, $C_1 = 0.3$, $C_2 = 1.0$, and $R = 0.999$. Note that the longest locking range and optimal mode symmetry does not correspond to zero phase offset. The thick line in the feedback model plots indicates the laser frequency tuning as the laser is scanned from lower to higher wavenumber.

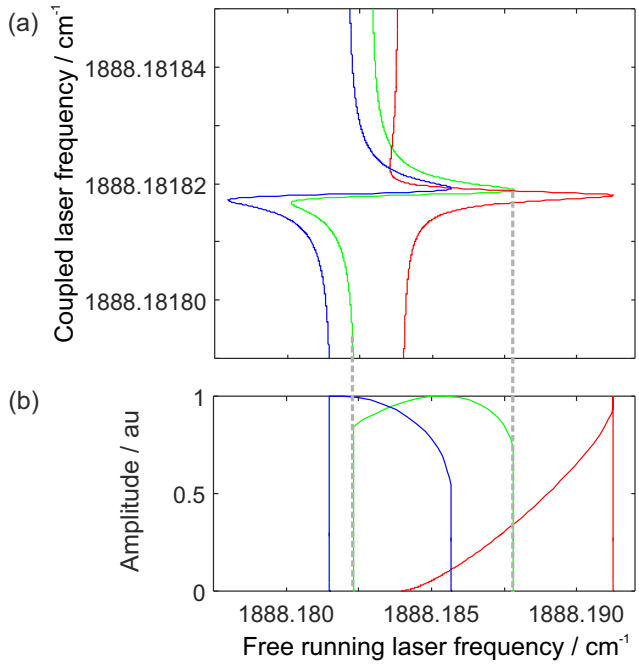

Figure 5.7: (a) Feedback model of the coupled laser frequency compared to free running with different phase shared by both feedback contributions. In all simulations, $\beta = 4 \times 10^{-5}$, $C_1 = 0.3$, $C_2 = 1$, and $R = 0.999$. Three phase (Φ) conditions were modelled: 0 rad (blue), 0.18 rad (green), and 1.0 rad (red). (b) Simulations of the cavity transmission for same settings as above. Grey dashed lines have been added to highlight the correlation between the frequency locking range of the laser and the cavity transmission for the $\Phi = 0.18$ rad condition.

Theoretical feedback models show that the amount of feedback from the resonant cavity and non-resonant reflection determines whether or not stable locking can occur. The next section deals with mapping the beam propagation to predict feedback losses in order to determine whether a linear OF-CEAS set-up can achieve the feedback rates required for the resonant field to win over the non-resonant field.

5.2.2 Modelling the intracavity field

As discussed in Section 4.4, the extent to which incident light couples into a high finesse cavity is related to the overlap between the resonant intracavity field and the laser field at the input mirror. The coupling efficiency – the fraction of incident light that fulfils the conditions of the resonant cavity field – is maximized when the incident beam is mode-matched to a specific resonant cavity mode. Mode-matching is defined as a special state when one "match[es] the field distribution of the incident light to that of the recipient cavity mode." [231] This means the cavity field and incident field must have the same phase front

curvature and spot size at the in-coupling cavity mirror.

In order to set up mode-matching, it is first necessary to quantitatively describe the resonant intracavity fields. The changing radius of curvature ($\mathcal{R}$) and size (w) of the Gaussian intracavity field can be described quite conveniently as a function of position along the central axis using a complex beam parameter q:[11]

$$\frac{1}{q(z)} = \frac{1}{\mathcal{R}(z)} - \frac{i\lambda}{\pi w(z)^2}. \tag{5.13}$$

The spot size (w) is defined as the radius at which the field intensity falls to $1/e^2$ of its maximum value, assuming a two-dimensional Gaussian distribution. Due to the curvature of the mirrors, the intracavity field will have a waist (w_o), or a minimum size, at some point z_o, which is

$$w_o = \sqrt{\frac{\lambda}{2\pi}\left(L(2\mathcal{R}_M - L)\right)^{1/2}} \tag{5.14}$$

in the case of a symmetric cavity composed of mirrors with radius of curvature $\mathcal{R}_M$. At this focal point, the wave-front is planar, which implies:[11]

$$q_o = \frac{i\pi w_o^2}{\lambda}. \tag{5.15}$$

The radius of curvature of the wave-front at some arbitrary point along the intracavity optical axis can then be determined from the waist:

$$\mathcal{R}(z) = z\left[1 + \left(\frac{\pi w_o^2}{\lambda z}\right)^2\right] \tag{5.16}$$

as can the spot size:

$$w = \sqrt{w_o^2\left(1 + \left(\frac{\lambda z}{\pi w_o^2}\right)^2\right)}. \tag{5.17}$$

In order for the intracavity field to have a well-defined waist, it must fulfil the stability condition based on the cavity length and radii of curvature of the two cavity mirrors ($\mathcal{R}_1$ and $\mathcal{R}_2$):[11]

$$0 < \left(1 - \frac{L}{\mathcal{R}_1}\right)\left(1 - \frac{L}{\mathcal{R}_2}\right) < 1. \tag{5.18}$$

The fundamental Gaussian beam solution of the paraxial wave equation describing the distribution of the field (Ψ) can be written as a function of the complex beam parameter:[11,35]

$$\Psi(r,z) = \exp\left[-i\left(p(z) + \frac{k}{2q(z)}r^2\right)\right]. \tag{5.19}$$

The phase factor (p) satisfies $\frac{dp}{dz} = \frac{-i}{q}$. This fundamental equation describes the simplest solution with a single Gaussian distribution. For linearly polarized semiconductor lasers, higher order transverse modes are described most accurately using the Hermite-Gaussian TEM_{mn} model where the indices m and n denote the mode order along the x and y Cartesian axes respectively. Hermite polynomial ($\mathcal{H}$) factors adjust the paraxial solution to describe these higher transverse modes, which are eigenmodes of the linear propagation eigenfunction of the resonator:[10,11,35,231]

$$\Psi(x,y,z) = \mathcal{H}_m\left(\frac{\sqrt{2}x}{w}\right)\mathcal{H}_n\left(\frac{\sqrt{2}y}{w}\right)\exp\left[-i\left(P(z) + \frac{k}{2q(z)}(x^2+y^2)\right)\right]. \tag{5.20}$$

The first Hermite polynomials ($\mathcal{H}_i$) are:

$$\mathcal{H}_0(x) = 0 \quad \mathcal{H}_1(x) = x; \quad \mathcal{H}_2(x) = 4x^2 - 2; \quad \mathcal{H}_3(x) = 8x^3 - 12x. \tag{5.21}$$

Theoretical intensity profiles of the fundamental and higher order Hermite-Gaussian modes in the xy plane are shown in Figure 5.8. The x and y indices indicate the number of nodes along the corresponding axis in the intensity profile. Higher order transverse modes exhibit resonant longitudinal mode excitation at slightly different frequencies – which allows for the dense population of excited cavity modes used for off-axis CEAS in Chapter 3. The shift arises due to the transverse momentum dependence of the Gouy phase shift through the intracavity waist.[232] As the incident beam typically has a Gaussian profile, perfect mode-matching is experimentally only possible for TEM_{00} transverse modes unless highly specialized optics are available. The paraxial equation can also be solved for axisymmetric profiles with cylindrical symmetry, termed Laguerre-Gaussian modes.

The field that propagates from the collimated laser to the cavity can be described by

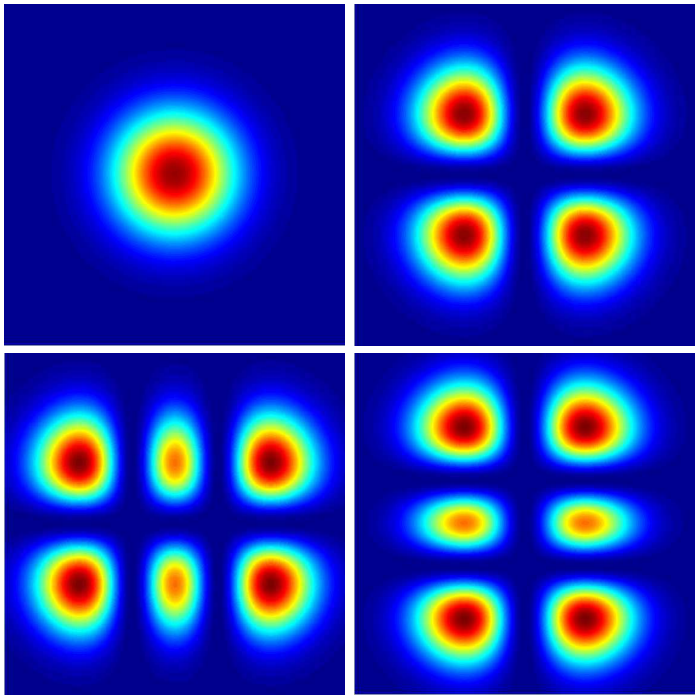

Figure 5.8: Theoretical intensity distributions of Hermite-Gaussian transverse modes of various orders including (clockwise from top left) TEM_{00}, TEM_{11}, TEM_{12}, and TEM_{21}. x nd y axes are taken to be across the width and along the length of the page respectively.

a complex beam parameter ($\widetilde{q}(z)$). Mode-matching requires that the $\widetilde{q}(z_{M1})$ of the incident beam from the laser matches $q(z_{M1})$ of a resonant intracavity Gaussian field at M_1. The beam from the laser is altered by focussing optics and propagation through optics and free space. In order to account for effects from these components, ray transfer matrix analysis is applied to describe the evolution of the field from an arbitrary point z_1 to z_2:[11,35]

$$\widetilde{q}(z_2) = \frac{A\widetilde{q}(z_1) + B}{C\widetilde{q}(z_1) + D} \tag{5.22}$$

where the ray transfer matrix ($\mathbf{M}$) is:

$$\mathbf{M} = \begin{pmatrix} A & B \\ C & D \end{pmatrix}. \tag{5.23}$$

$\mathbf{M}$ describes the development of the beam size and wave front, and is calculated as the product, in reverse order, of individual matrices describing propagation through different media or through focussing optics. The calculation of $\mathbf{M}$ for this experiment was written

into a MATLAB routine and is given in the Appendix. Ray trace analysis can be used to select the positions and focal lengths of optics to maximize mode-matching. Since this method of analysis allows the beam properties to be determined at any point along the optical propagation axis, it is possible to calculate C_1 and C_2 values at the laser facet to account for losses to the feedback fields.

In order to test that the model predictions are correct and explore the potential sensitivity of linear OF-CEAS, an experiment using a 5 μm DFB-QCL to measure CO_2 and H_2O as example target gases was set up. H_2O is an excellent test molecule as it can be introduced *via* laboratory air and the ν_2 bending mode absorbs strongly around 1885 cm^{-1}.

5.3 DFB-QCL Linear-cavity OF-CEAS

5.3.1 Experiment

The linear OF-CEAS set-up, shown in Fig. 5.9, is similar to one described previously but utilizes a newer, more powerful QCL, described in Section 3.3.2.[205] This 5.3 μm cw single mode DFB-QCL (Maxion, M575AY), which emits light between 1883 and 1896 cm^{-1} with a power of up to 220 mW, was placed in a custom-made mount and Peltier-cooled to an operating temperature selected from within the range -30 to 9°C. Both the temperature of the chip and current supplied were controlled by custom electronics built in-house. The current was modulated by a function generator (TTI TG230) which applied a triangular ramp to scan over the selected transitions at a rate of 10 Hz. The laser was normally operated well above the threshold current (429 mA at -10°C under free running conditions).

The output beam was collimated by an aspheric lens (Thorlabs $f = 4$ mm) and focused down to an intermediate beam waist by an off-axis parabolic mirror (OAPM). An iris was placed at the beam waist to spatially filter unwanted reflections. A PZT attached to the steering mirror that directed the beam into the cavity allowed fine control over the phase of the feedback fields. A polarizer was placed in the beam path before the cavity to tune the feedback rate and simultaneously measure the laser output signal with a photovoltaic detector (VIGO, PVMI-3TE-10.6) collecting the reflection as shown. The

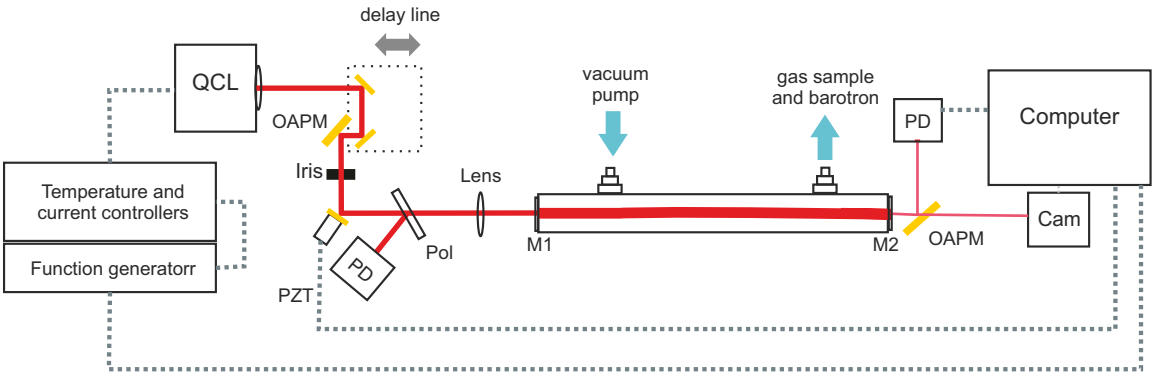

Figure 5.9: Experimental set-up for linear OF-CEAS with a 5.3 μm DFB-QCL. The laser–cavity distance is controlled by the delay line and PZT, which is connected to the computer for active control of the feedback phase. Note: PD = photovoltaic detector; Cam = infrared camera; Pol = polarizer. Grey dashed lines indicate electronic connections.

77 cm long optical cavity was formed using two high reflectivity ZnSe mirrors (Los Gatos) with radii of curvature of 50 cm. A CaF_2 lens (f = 15 cm) was set at a slight angle to the beam axis and focused light into the cavity. The cavity was enclosed by a 1-inch diameter stainless steel tube with the cavity mirrors mounted in bellows connected to a vacuum pump, pressure gauge (Leybold Ceravac CTR 90), and inlet for gas samples. The beam exiting the cavity was focused by an OAPM onto a second photovoltaic detector (VIGO, PVMI-3TE-10.6). This OAPM was placed on a flip-mirror to allow imaging of the transmitted beam profile by an infrared silicon microbolometer camera (WinCam). The laser–cavity distance was set using an optical delay line and the PZT to be equal to the cavity length. The detector output was sent to a data acquisition card (National Instruments, PCI-6221), and a LabVIEW program recorded the signal. Resonant cavity modes were maintained by applying a DC error signal generated in a LabVIEW program to the PZT to maintain optimal phase matching and symmetric cavity mode transmission, as described in Section 4.6.4. Simultaneous measurements from multiple detectors were recorded on an oscilloscope (LeCroy WaveRunner 6100A, 1 GHz bandwidth).

To demonstrate the potential of the technique, the cavity was filled with 20 – 125 Torr of a 10% ($\pm \leq 0.5\%$) CO_2 mixture with O_2 and N_2 (BOC). Further studies on H_2O relied on introducing laboratory air into the cavity.

5.3.2 Results

Figure 5.10 shows an example cavity transmission measurement when no absorbing species is present in the cavity. The data shown are measured from a single 100 ms laser scan with 6 V triangle voltage ramp applied at an acquisition rate of 100 kHz. The amplitude of the applied current is increasing and laser frequency decreasing from left to right. The feedback rate was attenuated with the polarizer to ensure excitation of consecutive cavity modes, though the feedback rate is still sufficiently high that the locking range is nearly the full duration of one FSR. No frequency calibration is required, as each cavity mode is separated by one FSR (0.0065 cm^{-1}), as indicated in the close-up image of the cavity modes in Figure 5.10(b). Measurements of the laser output indicated that the power of the laser was not significantly affected by changes in feedback rate due to absorption in the cavity, and so the signal was not normalized to output power.

As described in the previous chapter, Origin software was used to find the amplitude of each cavity mode (grey circles). For this experiment, the signal was very large – due to both the high power of the laser and good coupling efficiency into the cavity – and the signal-to-noise ratio (SNR) sufficiently high that no averaging was necessary. The red line

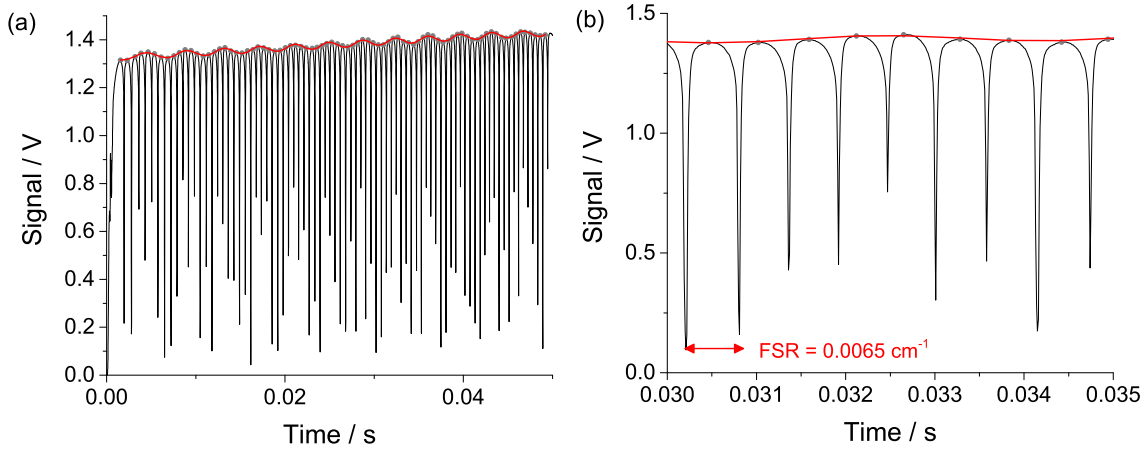

Figure 5.10: (a) Example cavity transmission for linear OF-CEAS with no absorbing species in the cavity. The cavity transmission does not return to zero in between modes since the locking range is (just) equal to the full FSR of the cavity (0.0065 cm^{-1}). The red line shows a fourth order polynomial plus sine function fit to the cavity mode maxima. (b) Close-up of cavity modes highlighting high SNR and long locking duration.

in Figure 5.10 shows a fit of the data (in the frequency domain) to the sum of a fourth order polynomial and sine wave. Similar functions have been used in the past.[188,201] This non-linear function describes the data well, with a mean absolute deviation of 3.3 mV giving a SNR of 420 or $\alpha_{min} = 5 \times 10^{-9}$ cm^{-1}. The sinusoidal component takes into account the clear etalon, which arises from reflections between the window of the photovoltaic detector and back of M_2. This is a persistent problem that has been mentioned by others.[179] The etalon fringes can be minimized by adjusting the alignment of the detector, however they cannot be completely eliminated. Attempts to eliminate the etalon by jittering the OAPM before the detector added noise so it was deemed better to minimize the fringing and make sure that the analysis accounted for it correctly.

The frequency locking of the laser was investigated using a 3-inch solid Ge etalon with FSR of 495 MHz at 5 μm. By sending the reflection off the attenuating polarizer through the Ge etalon onto the second photovoltaic detector, the frequency tuning behaviour of the laser could be observed simultaneously with cavity transmission, as shown in Figure 5.11. The cavity transmission, shown in red, indicates when in-phase feedback from a resonant linear cavity is injection seeding the laser. The simultaneous laser output signal, in blue, exhibits a stepwise behaviour with the duration of the step corresponding to the duration of locking and intense cavity transmission. This is juxtaposed on top of a reference signal (grey) measured with the cavity blocked and the laser tuning dictated by a linear voltage ramp. This clearly shows that the optical feedback from the resonant cavity is responsible for the step-like frequency tuning behaviour.

The locking program described in Section 4.6.4 helped maintain stable cavity modes and Figure 5.12 shows the Allan-Werle plot of the normalized variance of cavity mode maxima. While averaging up to 1 second improves the sensitivity, the flattening of the curve suggests that $1/f$ noise dominates thereafter. For one second averaging, the SNR of the mode amplitude is about 10^{-3}.

The threshold current of a semiconductor laser decreases with increased feedback rate, and so measurements of this threshold reduction provide some insight into the amount of feedback the laser experiences.[173,175] With the laser operating at -10°C, the threshold

current decreased by 3.8% from 429 mA to 411 mA with non-resonant feedback only (*i.e.* no cavity transmission signal). When the laser frequency was locked to a resonant cavity, this change increased to 4.2% indicating that the total feedback rate increased, as expected.

Following the analysis of Morville *et al.*, the effect of tuning rate on cavity injection efficiency was examined by simultaneously measuring the laser output, feedback light intensity, and cavity transmission at varying feedback rates and free running frequency tuning rates.[176,179] The feedback rate could be adjusted with the polarizer in front of the cavity. The amplitude of the cavity transmission under optimal phase-matching conditions was used as a proxy for the injection efficiency. As shown in Figure 5.13, the critical tuning rate – the maximum frequency tuning rate at which feedback is still observed – increases with increased feedback rate as expected. For a typical feedback rate used for the experiments shown, there is a sharp decrease in injection efficiency as the tuning rate exceeds 1000 GHz/s, which is similar to previous observations for OF-CEAS systems using V-shaped cavities and diode lasers.[176] All spectra shown throughout this chapter were collected with a much slower tuning rate than this maximum limit to ensure stable feedback locking.

As demonstrated for the V-shaped cavity systems, the robust stability of the linear cavity and high feedback rate allowed continuous locking of the laser frequency to a single mode over relatively long times (seconds) with no active error loop. If the emitted wavelength is resonant with the cavity, the duration of the lock is solely determined by noise or drifts in

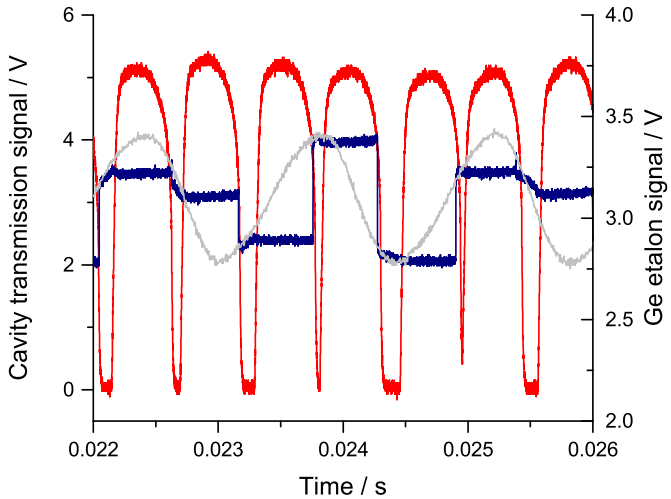

Figure 5.11: Changes in emitted laser frequency tuning shown by comparing laser output through Ge etalon with (blue) and without (grey) resonant feedback from the linear optical cavity. The red line shows the cavity transmission signal measured simultaneously with blue laser output line.

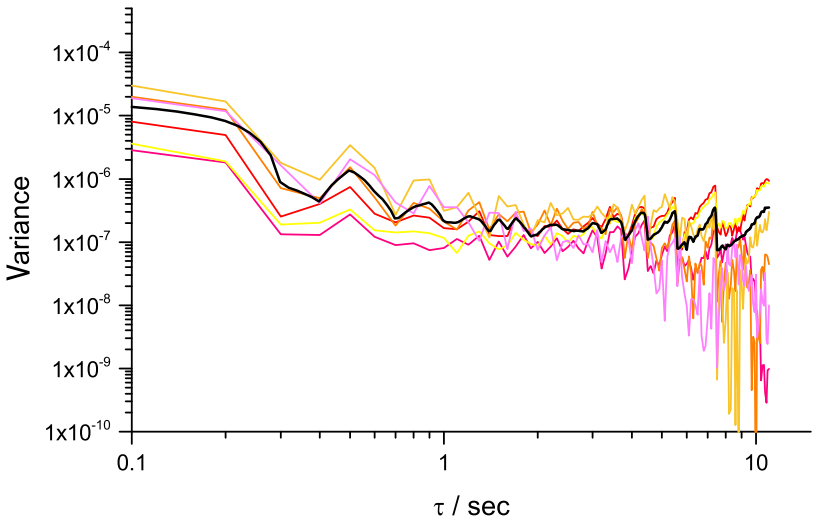

Figure 5.12: Allan-Werle variance of individual cavity mode maxima normalized to average value for individual modes (coloured lines) shown with average (black).

the system, from mechanical, thermal, or electrical sources. Figure 5.14 shows a long-term measurement at a single resonant frequency, with the amplitude of the signal compared to a normal cavity transmission spectrum for reference. This was easily be achieved by simply removing all current modulation to the laser and adjusting the phase manually with the PZT until the laser frequency was resonant with the cavity. The measurement was then collected with no other adjustments to the system. With a simple error loop to maintain the correct phase and frequency, it should be possible to actively maintain intracavity excita-

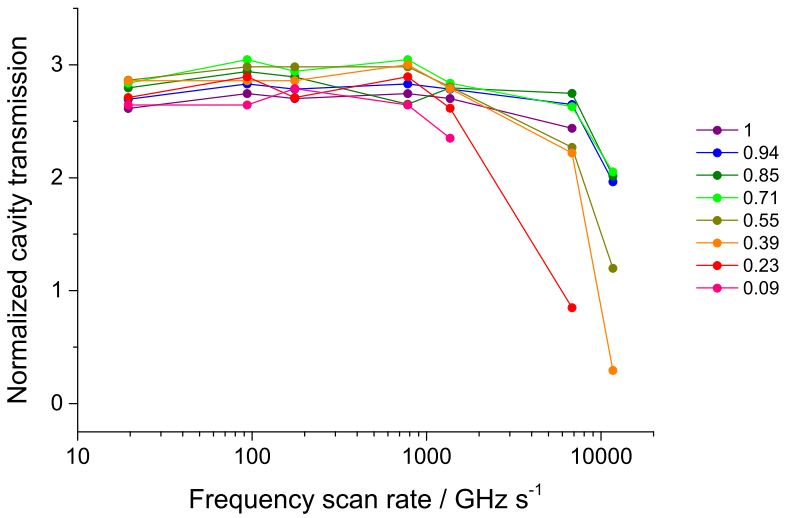

Figure 5.13: Plot showing drop-off in injection efficiency at high frequency scanning rates for different amounts of feedback. The legend indicates relative power transmission through the polarizer (normalized to a maximum of unity). The cavity transmission, which is used as a proxy for coupling efficiency of the incident laser into the intracavity field, has been normalized to the square-root of the fractional incident power.

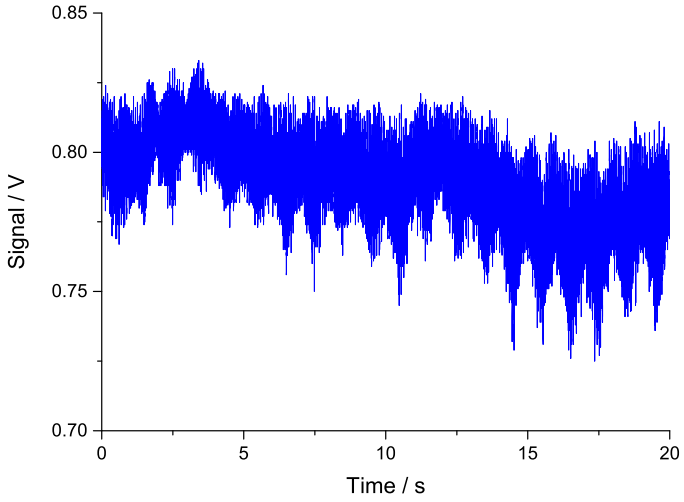

Figure 5.14: Cavity transmission as the laser frequency remains locked to a single longitudinal cavity mode. For this measurement, no voltage modulation was applied to the laser and no error signal applied to maintain phase matching. The standard deviation of the signal is 0.018 V, or approximately 2% of the mean.

tion and frequency locking for significantly longer times. Given that the intracavity power is quite high (up to 250 W), this capability may be attractive for applications requiring continuous measurements under high powers with precise frequency resolution.[35,223]

The high power of this DFB-QCL allowed sufficient transmitted power for monitoring the excited transverse mode profile using the mid-infrared microbolometer (WinCamD) placed after the cavity. Small adjustments to the cavity alignment allowed different TEM_{mn} modes to be selectively resonant in the cavity, as shown in Figure 5.15. As expected, the signal amplitude and locking range decreased when higher modes were preferentially excited, illustrating that increased diffraction losses lead to a lower feedback rate. As evidence of this, cavity ring-down times decreased as the mode order increased as shown in Figure 5.16. The abscissa is an effective mode order magnitude equal to $\sqrt{m^2 + n^2}$, which is approximately proportional to the theoretical maximum mode amplitude. The ring-down decays were measured in two ways: by applying a sharp, nearly instantaneous drop in current below threshold, or by measuring the decay rate as the laser jumps off resonance and returns to free running. Both methods returned comparable values for a given alignment.

It is striking that the laser was able to lock stably to higher order resonant transverse cavity modes. In previous studies, most authors have reported only TEM_{00} or TEM_{01} modes for OF-CEAS, though in many cases the fundamental mode was simply assumed.[176,183,201,204] Hamilton *et al.* recorded excitation of TEM_{10} and TEM_{20} modes

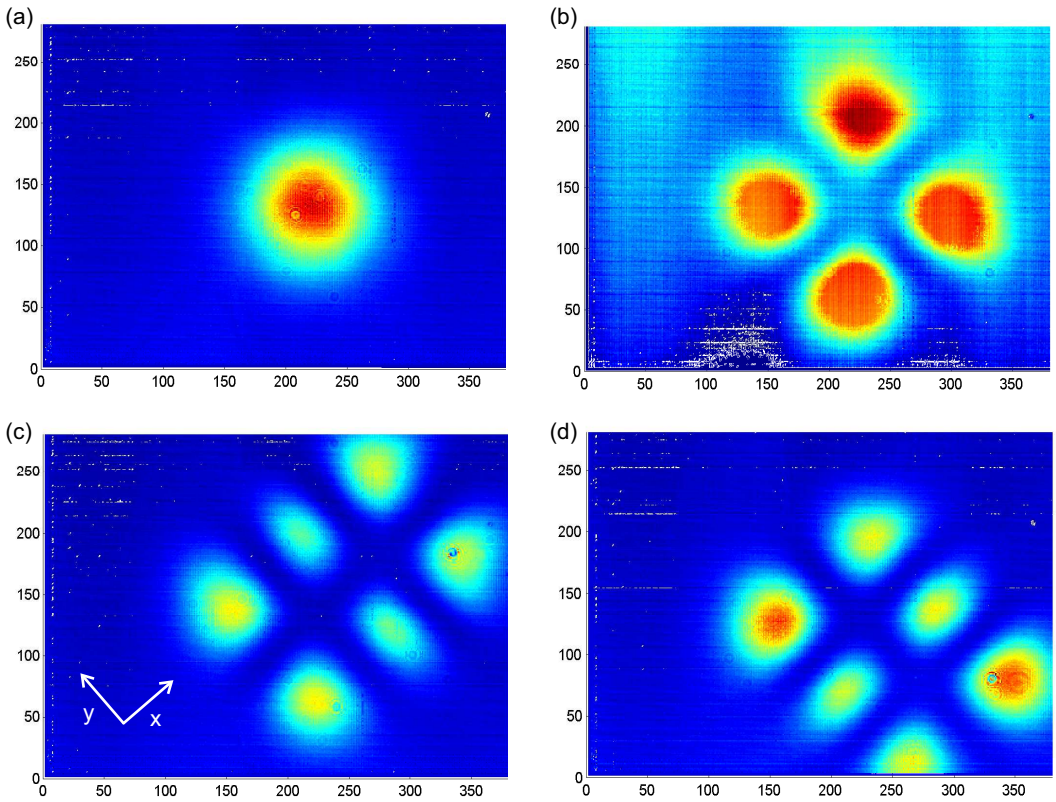

Figure 5.15: Sample transverse cavity modes experimentally measured from light leaking out. The transverse modes are assigned as: (a) TEM_{00}; (b) TEM_{11}; (c) TEM_{21}; (d) TEM_{12}. Each pixel along the camera's Cartesian coordinates corresponds to 35 μm. Colour contours represent variations in intensity in arbitrary units. These data show excellent agreement with theoretical calculations of Hermite-Gaussian mode profiles shown in Figure 5.8.

in a three-mirror ring system.[199] The ring-down time – and therefore the effective path length – decreases if higher order modes are selectively excited, so it is important to know which TEM_{mn} is excited in each measurement in order to retrieve an accurate absorption coefficient and concentration.

All spectra presented here were collected with TEM_{00}, TEM_{01}, or TEM_{02} Hermite-Gaussian transverse modes excited in the cavity, verified by the microbolometer, as these allowed stable locking to successive modes over a range of powers incident on the cavity. TEM_{00} modes required a much greater attenuation of light incident on the cavity to ensure that the feedback rate maintained feedback locking for less than one FSR. Additionally, it is possible that the Gouy phase shift allowed higher order modes to compete more favourably for injection seeding due to the resulting phase offset between the resonant and non-resonant

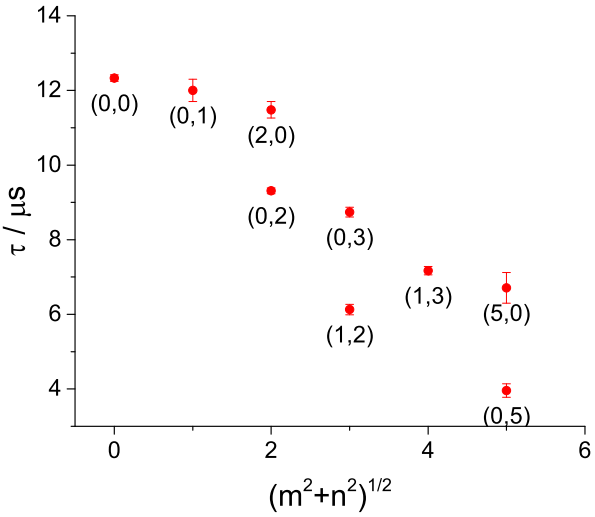

Figure 5.16: Measured ring-down times (τ_{RD}) for different Hermite-Gaussian mode orders TEM$_{mn}$ labelled by (m,n). The abscissa is an effective mode order magnitude equal to $\sqrt{m^2+n^2}$ and error bars show the standard deviation of repeated measurements.

feedback fields.

5.3.2.1 Comparison to model

In order to test that the feedback models accurately simulate the experiment, the relative power of resonant and non-resonant light coming back towards the laser while the cavity is in resonance was estimated (see Figure 5.17). To do this, the total output power of the laser, the power transmitted through the polarizer, and the power of the light transmitted through the cavity were recorded. The latter could be accurately measured due to the ability to remain locked to a cavity mode for a long time (seconds) when not applying a current ramp. After checking that the signal on the detector matched the amplitude of the cavity modes observed during a scan, a power meter was placed after the cavity to measure the total power of this light. For example, with a current of 840 mA and temperature of -10°C

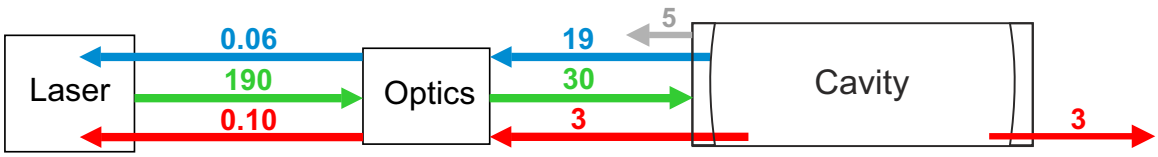

Figure 5.17: Schematic of linear OF-CEAS experiment showing the intensity of light passing along each section. Green indicates outgoing light emitted by the laser, blue indicates non-resonant reflections off the curved surface of the cavity mirror, red indicates light from the high finesse linear cavity, and grey indicates reflections off the flat surface of the cavity mirror. Optics include the focussing optics, iris, and polarizer between the laser and the cavity. Arrows going into laser take into account spatial filtering by the laser facet aperture. All powers are given in mW.

applied to the laser, the average power emitted from the laser (through the collimating lens) is 190 mW. For a typical polarizer setting used for measurements of absorption spectra, the power was attenuated to 30 mW incident on the cavity. The first reflection off the flat surface of the ZnSe mirror accounted for a 17% loss. Therefore, the maximum power being reflected off the second surface when the cavity is not in resonance (and injection efficiency is negligibly small) is 20.8 mW. When the laser frequency was locked to resonant TEM_{01} transverse modes excited in the cavity, the maximum power transmitted through the cavity was 3.0 mW. It is reasonable to estimate that the out-coupling efficiency would be equal for both cavity mirrors, implying that 6.0 mW of light was initially coupled into the cavity field or up to 30% injection efficiency.

In order to verify these estimates, simultaneous measurements of cavity transmission and the light reflected off the input cavity mirror were recorded. The reflection was measured by collecting the reflection off the polarizer on the cavity side using an additional photovoltaic detector. This light is estimated to be proportional to the sum of all feedback fields. As shown in Figure 5.18, a drop in signal is observed as the cavity comes into resonance, with a shape that is roughly the inverse of the transmitted signal. At the minimum

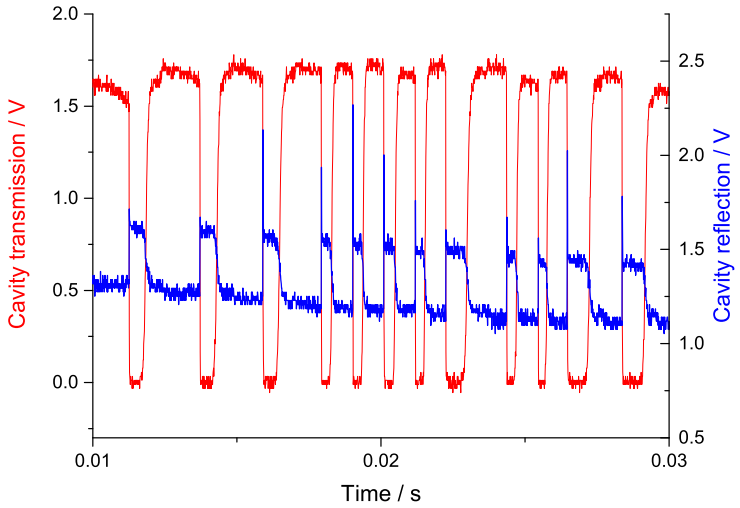

Figure 5.18: Overlay of cavity transmission (red) and simultaneous measurement of light reflected back from the cavity (blue). The latter was measured using a reflection off the cavity-side of the polarizer onto a second photovoltaic detector, and contains both the non-resonant reflected field and resonant feedback when the laser frequency is on resonance. The spike in light coming from the cavity at the end of each mode likely arises from the increase in non-resonant light reflected off the mirror in addition to the decaying resonant field leaking out.

– where coupling efficiency is presumably highest due to linewidth narrowing – the intensity is reduced by 12% from the signal collected off resonance. Continuing to use the figures mentioned above, this means that the power of light coming from the cavity – the non-resonant feedback – decreases from 20.8 mW to 18.3 mW, or a reduction of 2.5 mW. The change in signal is a combination of a reduction of reflected light due to increased coupling into the cavity, as well as the addition of resonant light leaking out of the cavity. Assuming, as before, that the out-coupling rates are the same at both cavity mirrors this gives a coupling efficiency of 24%, indicating that the estimate of 3 mW returned resonant feedback power is reasonable. Thus, the feedback coming from the cavity is heavily skewed towards the non-resonant contribution from reflection off the curved surface of M_1. In order for the resonant feedback to dominate at the laser, mode-mismatching and spatial filtering are required to separate the two feedback fields and preferentially attenuate the non-resonant contribution.[233]

The OAPM and lens were positioned between the laser and cavity to allow for mode-mismatching of the incident light into the intracavity field. *Mode mismatching* here refers to a condition whereby the incident laser beam and intracavity field have very different

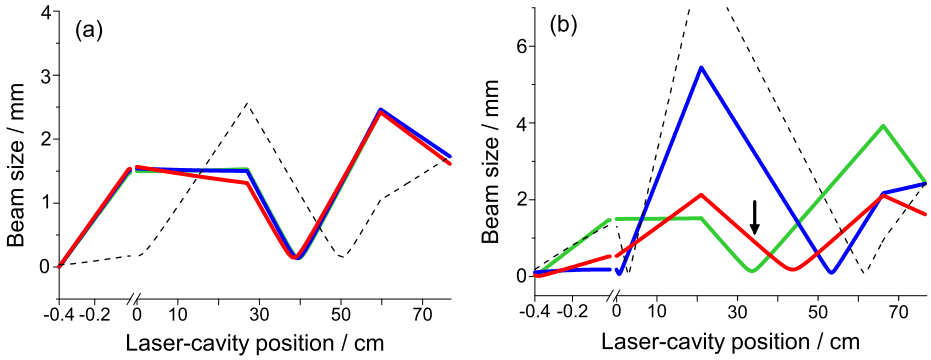

Figure 5.19: These plots show beam size as a function of the position along the laser–cavity path for four different beams: laser output (green), reflection off flat face of M_1 (dashed black), non-resonant feedback reflection off curved face of M_1 (blue), and resonant cavity field (red). In (a) the off-axis parabolic mirror and lens are positioned such that the incident beam is nearly mode-matched into the cavity. In (b), which simulates the experimental set-up used here, the incident beam is mismatched in order to change the spatial distribution of the beams to allow for preferential filtering of the non-resonant feedback field by the laser facet and iris at position indicated by arrow. Note, the beam size is defined as the half-width at $\frac{1}{e}$ magnitude of the field assuming a spherical Gaussian profile, and 0 cm is the location of the collimation lens positioned 4 mm in front of the laser facet.

spatial profiles at the input mirror. A Gaussian ray trace matrix analysis of the experiment was used to model the size and curvature of the beams for the region between the laser and cavity.[11] The beam waist after the collimating lens was estimated to be 1.5 mm with the microbolometer. Figure 5.19 shows the modelled beam size for the various field contributions as a function of position between the laser facet and inner surface of the input cavity mirror. A comparison is shown between the case where the beam is mode-matched into the cavity (a) and the set-up used here (b) where the mode is mismatched in order to separate the focal points of the non-resonant and resonant fields for spatial filtering. An iris was placed at the focal point of the output beam (33 cm) in order to preferentially attenuate the non-resonant feedback. As evident in this figure, the beam size of the non-resonant feedback (blue) was much larger than the resonant (red) at the iris position, and so a greater fraction of the resonant power will be transmitted through the iris aperture (2 mm). It is worth noting that the reflection off the flat, uncoated surface of the mirror (dashed black line) diverges quickly and is virtually all lost either at the iris or off the edges of the optics.

The key spatial filtering occurs at the laser facet. The laser facet size is specified as 5.8×2 μm (Maxion). The ray trace analysis was extended beyond the collimating lens to predict the size of the various fields at the facet, located approximately 4 mm in front of the aspheric lens. Due to the mode-mismatching conditions set, both the resonant and non-resonant fields are clipped at the facet. The size of the non-resonant beam is approximately 100 μm at the facet compared with a resonant beam size of 30 μm, which means that the portion of the resonant field intensity entering the laser facet is greater than that of the non-resonant field by more than a factor of ten. This attenuation is sufficient such that the resonant field feedback rate is greater than the non-resonant field at the laser cavity.

The coupled laser feedback model could then be used to simulate the experiment based on these calculated feedback rates, and the expected behaviour of the coupled laser was compared with experimental measurements of changes in laser output. Figure 5.20 (a) shows a theoretical coupled laser frequency tuning curve given the estimated feedback rates of the system. As discussed earlier, it is clear that the sharp feature due to the high finesse optical cavity is superimposed on the oscillatory tuning curve characteristic of the

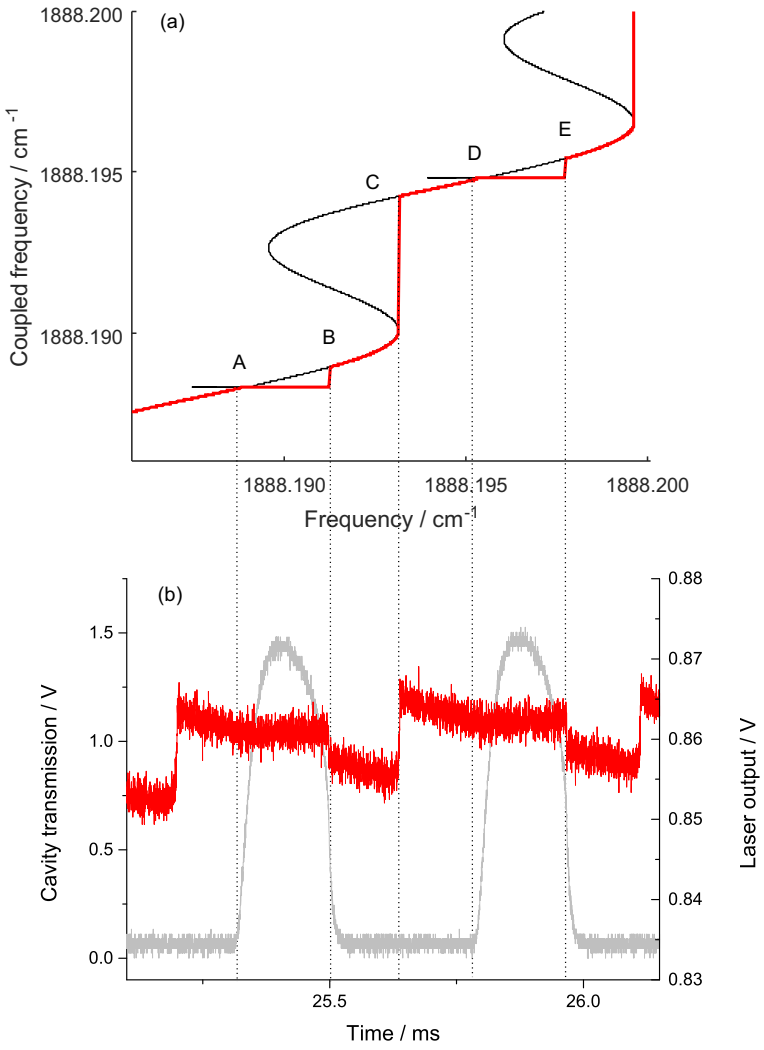

Figure 5.20: (a) Feedback model and (b) experimental measurements demonstrating the effect of non-resonant and resonant feedback on the laser. Based on the experimental parameters and Gaussian ray trace analysis, the two feedback rates were estimated to be $C_2\beta = 3.5 \times 10^{-7}$ and $C_1\beta = 3 \times 10^{-7}$ for this measurement with $\Phi = 0.1$ rad. The dashed lines indicate corresponding changes in the laser output at the labelled points in the coupled frequency plot. In (b), the grey trace is a cavity transmission signal measured after the exit mirror of the cavity, with the laser output intensity (red) measured simultaneously from a portion of light reflected off the polarizer.

multistable laser cavity experiencing non-resonant feedback from an external reflector.[173] Figure 5.20 (b) shows experimental measurements of the laser output power (red) overlaid on the cavity transmission signal (grey) collected simultaneously to indicate when the laser is resonant with the cavity as the frequency is scanned. The laser output follows a similar sawtooth-like pattern, as seen previously in diode laser studies, as well as a clear locking range where the output power remains stable.

It is possible to interpret the laser output measurement shown in Figure 5.20 based on the theoretical feedback model. Starting at point A, the laser frequency comes into resonance with the optical cavity and stays locked at this frequency until reaching point B where the laser discontinuously jumps out of resonance with the cavity to a frequency dictated by the non-resonant feedback field. The tuning rate of the laser frequency continues to be slower than for the free running system, and the difference between the coupled and free laser frequency increases. At point C, the laser suddenly mode hops to another point on the tuning curve, as seen in previous studies.[173] It continues tuning at an attenuated rate until reaching point D, at which time the optical cavity is resonant and the laser responds to this new, dominant feedback field until the end of the locking range at point E. Measurements of the laser output filtered through a Ge etalon verified that frequency, as well as amplitude, did not measurably vary through the duration of locking to the resonant linear cavity.

Simultaneous measurements of laser output through the etalon and cavity transmission demonstrate the expected variation as a function of phase, adjusted manually using the PZT. The modelled transmission (Figure 5.6) very accurately reproduces the measurements observed (Figure 5.21), demonstrating both the asymmetry of the cavity modes and frequency jumps at predicted points in the laser ramp. The linear cavity OF-CEAS simulations therefore paint a complete picture of the feedback effects exhibited by the QCL.

5.3.3 Trace gas measurements

The next step is to demonstrate the technique for gas concentration measurements. Figure 5.22 shows a cavity transmission signal when an absorber is present, in this case CO_2. The spectral region around 1888 cm^{-1} covers five CO_2 transitions, including transitions of ^{18}O and ^{17}O isotopologue species (see Table 5.1). The example spectrum shown in Figure 5.23 was collected with 100 Torr of the 10% CO_2 mixture in the cavity and the laser scanned over 0.5 cm^{-1} with a 10 Hz triangular ramp. Absorption values were calculated using Equation 5.12, with each point representing one cavity mode. Data were fit to a combination of Voigt profiles to account for each transition. In order to accurately simulate the physical

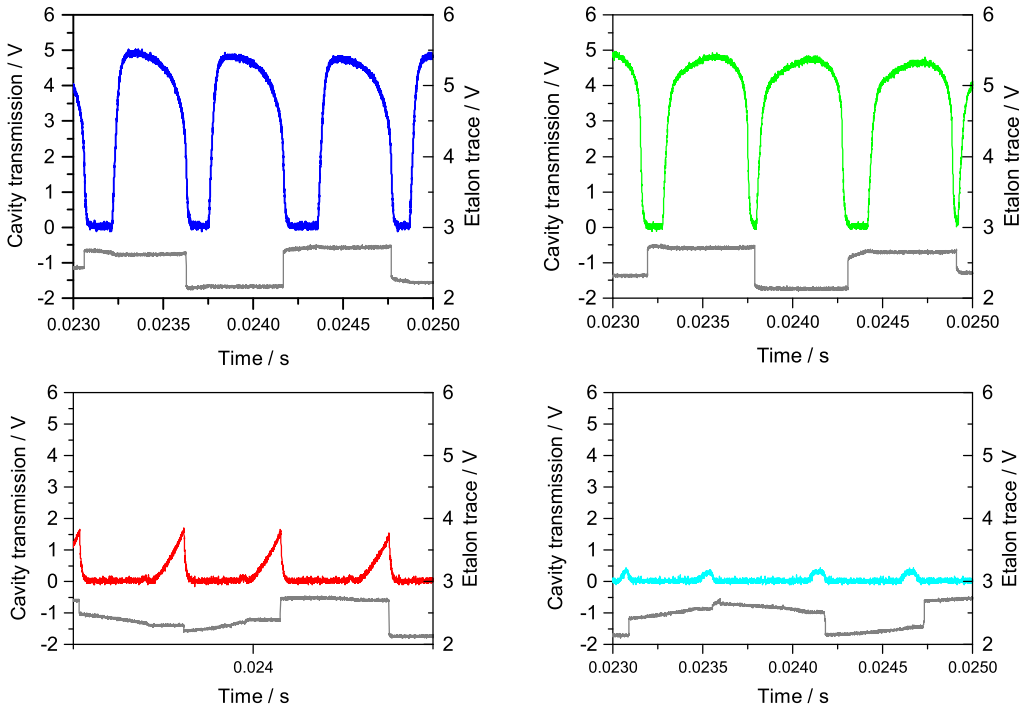

Figure 5.21: Cavity transmission (colour) for four different phase settings to match Figure 5.6. The laser output through the Ge etalon was measured simultaneously (grey) to show when the laser remained fixed to a single frequency.

system, some constraints were applied to the Voigt fits: the Gaussian linewidths were set to be at least the Doppler linewidth, the relative areas of the $^{16}O^{12}C^{16}O$ transitions were set according to HITRAN values, and the relative centre frequencies of significantly overlapped transitions were also fixed.

By comparing the cavity mode maxima with (I) and without (I_o) CO_2 present, the absorption (the term in square brackets in Equation 5.12) spectrum could be plotted. The

Table 5.1: Details from HITRAN of the main CO_2 transitions within the spectral region scanned. Integrated absorption cross-sections are given for CO_2 containing the natural isotopic abundances.[6]

Molecule	Frequency / cm^{-1}	Transition	Cross-section / cm^2 cm^{-1}
$^{16}O^{12}C^{16}O$	1887.771	1 2^2 0 2 ← 0 1^1 0 1 P(41)	3.94×10^{-25}
$^{16}O^{12}C^{17}O$	1887.787	1 1^1 0 2 ← 0 0^0 0 1 P(39)	6.19×10^{-27}
$^{16}O^{12}C^{18}O$	1887.862	1 1^1 0 2 ← 0 0^0 0 1 P(19)	6.05×10^{-26}
$^{16}O^{12}C^{16}O$	1887.889	3 0^0 0 4 ← 1 1^1 0 2 R(33)	1.79×10^{-27}
$^{16}O^{12}C^{16}O$	1887.980	1 3^3 0 2 ← 0 2^2 0 1 P(23)	4.19×10^{-26}

I_o value was determined in different ways depending on the spectra measured. The simplest method was to directly compare mode-by-mode the cavity transmission through an evacuated cavity to the transmission with the absorber. If the sample pressure is not low (> 150 Torr), it is sometimes necessary to use the transmission when a matching pressure of non-absorbing gas (*e.g.* N_2) is in the cavity to account for slight changes in mirror alignment as the bellow mounts shift with internal pressure changes.

If there are extended absorption-free regions in the sample measurement, a function representing I_o can be fit to these areas; this relies on the assumption that the baseline can be modelled with a function – which is a reasonable assumption based on Figure 5.10 – and reduces the random noise on the measurement since only one cavity transmission spectrum contributes to the absorption spectrum. This method only works when the spectral region

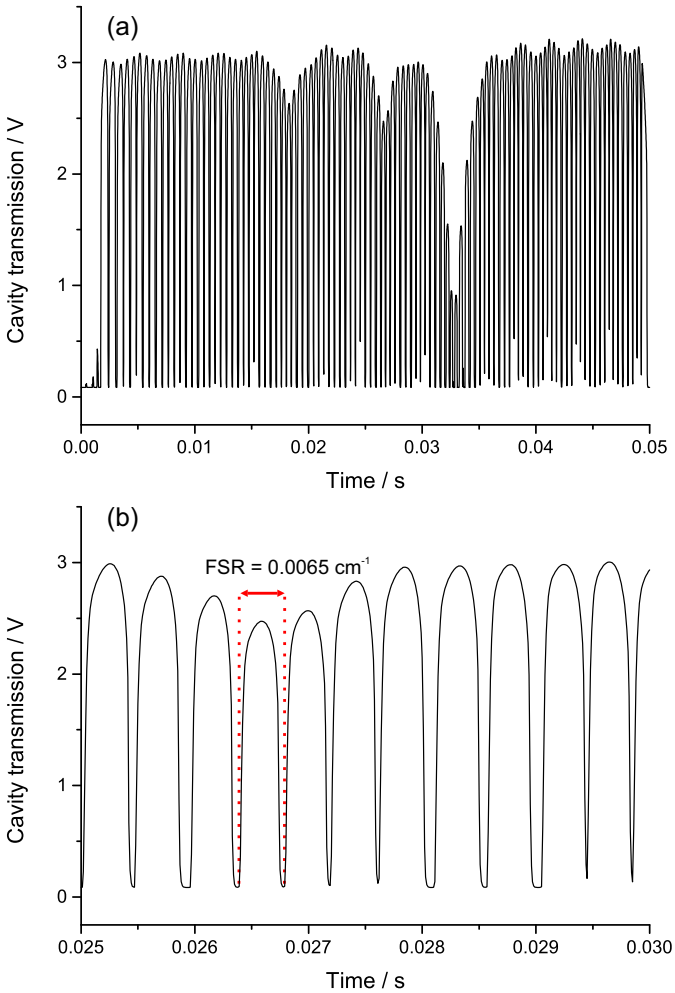

Figure 5.22: (a) Example cavity transmission from a single laser scan, with frequency decreasing from left to right, of 100 Torr 10% CO_2 in the cavity. (b) The lower panel shows a subsection in higher detail in order to highlight the symmetric cavity mode shapes and high signal-to-noise ratio. The oscillation in the signal is due to an etalon between the detector window and cavity mirror.

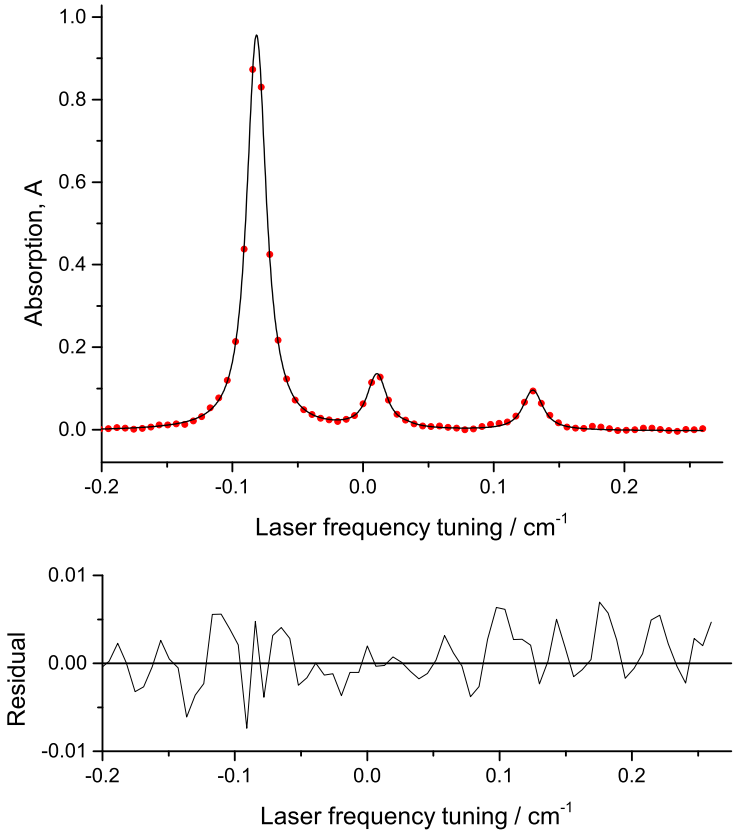

Figure 5.23: A sample plot of absorption data calculated from a single 100 ms cavity scan over a CO_2 absorption feature (red circles) with corresponding fit (black line) based on the transitions listed in Table 5.1. For this measurement, 100 Torr of a gas mixture containing 10% CO_2 was in the cavity, and the laser was scanned over the range 1887.65 – 1888.15 cm^{-1}. Below the spectrum is a plot of the residual to the fit. The 1σ standard deviation of the residual, which is an estimate of MDA, is 3.1×10^{-3}.

is not congested by many overlapping transitions from the target or interfering species. The absorption spectrum shown in Figure 5.23 was determined using the latter method for I_o, however using the cavity transmission without absorption did not give a significantly different result.

It was determined that simply measuring the decay of light when the laser frequency changed from resonance to free running as the frequency was scanned through successive modes yielded the same ring-down times as actively tuning the laser current below threshold provided no other modes were excited within the decay period. The R value is used to account for all loss mechanisms in the cavity apart from absorption by the sample gas, in-

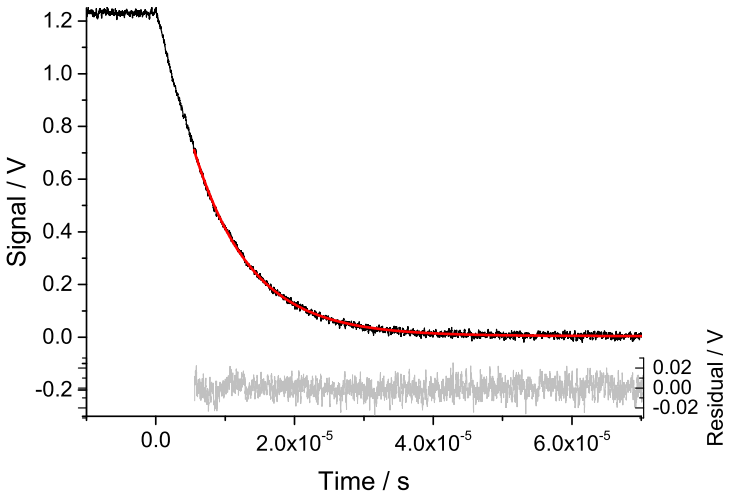

Figure 5.24: Sample single exponential ring-down fit for a TEM_{10} transverse mode selectively excited in the cavity. The ring-down was measured when the laser frequency jumped discontinuously from its coupled frequency locked on resonance to its free running frequency. In this case, $\tau_{RD} = (8.39 \pm 0.02)\ \mu$s.

cluding diffraction and absorption by cavity components. A sample ring-down measurement and fit are shown in Figure 5.24.

A second way to determine R that does not require a fast detector is to use a calibrated gas mixture with known concentration of an absorbing gas species with a defined absorption profile in the operating region of the laser. If the absorption spectra of this gas are plotted against the partial pressure, or number density, of the gas then a linear fit will provide a slope related to R. For example, Figure 5.25 shows a plot of the integrated absorption (A) of the P(41) hot band CO_2 transition (see Table 5.1) as a function of total pressure of a gas mixture (in atm) containing 10% CO_2. R can be deduced from the linear fit with slope m_p:

$$1 - R = \frac{\sigma(0.1N^o)L}{m_p} \tag{5.24}$$

where σ is the integrated cross-section of the transition and N^o is the total number density of molecules at 760 Torr (2.5×10^{19} cm^{-3}).

The area of the absorption profiles plotted against pressure yields a reflectivity of $0.999603 \pm 6{\times}10^{-6}$. Measurements were repeated for different incident powers set by the polarizer. These showed consistency in the R values returned, implying that there were no power-dependent effects *vide infra*. Ring-down measurements through an evacuated cavity yielded an R value of $0.999676 \pm 2{\times}10^{-6}$ ($\tau^o_{RD} = 7.92 \pm 0.05\ \mu$s); the small decrease in

cavity finesse when a gas sample is present has been observed previously, likely due to small changes in alignment when filling the cell with gas.[201] The derived broadening coefficients are slightly smaller than those predicted by HITRAN (for example 0.1234 cm^{-1} atm^{-1} measured compared to 0.1380 cm^{-1} atm^{-1} predicted by HITRAN for the P(41) hot band transition at 1888.77 cm^{-1} representing a difference of 10%), however the uncertainty on reference values is large.[6] The relative isotopic abundances were close to expected, with the concentrations of $^{16}O^{12}C^{16}O$, $^{16}O^{12}C^{18}O$, and $^{16}O^{12}C^{17}O$ in a ratio of 1343:4.9:1 (compared with expected ratio of 1348:5.3:1).[6]

The absorption can be converted to concentration *via* α, which requires normalizing to the optical path length of the beam through the sample accounted for by the $(1-R)/L$ term in Equation 5.12. The absorption spectrum shown (Figure 5.23) was converted to absorption coefficient (Figure 5.26) with the R value determined from the pressure series. The standard deviation of the residual – shown in the lower panel – is 1.8×10^{-8} cm^{-1} for a single 100 ms scan. This value is likely higher than the one reported earlier for the baseline fit

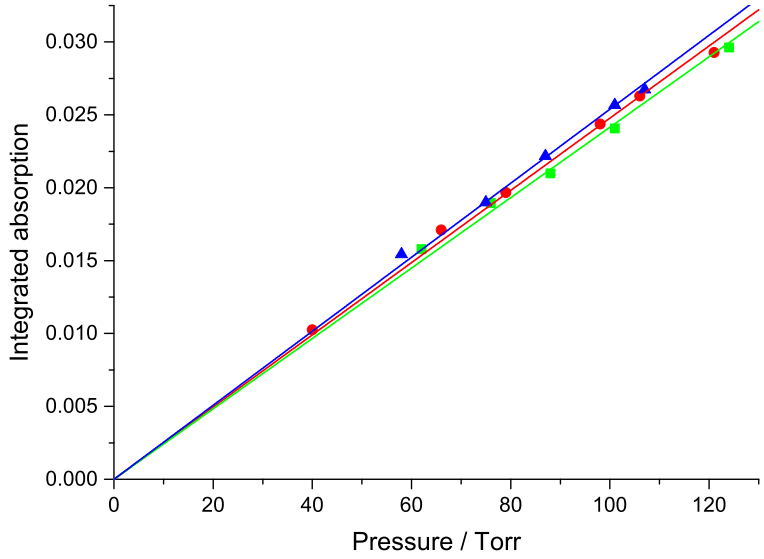

Figure 5.25: Plot of integrated absorption (with units of cm^{-1}) as a function of total sample pressure for different polarizer conditions. The polarizer was adjusted to change the incident power on the cavity and overall feedback rate. The incident power on the cavity was 30 mW (blue), 49 mW (red), and 70 mW (green). Linear fits are shown, and the values of the slopes indicated no significant difference in effective reflectivity (and hence in absorption) for the three different cases.

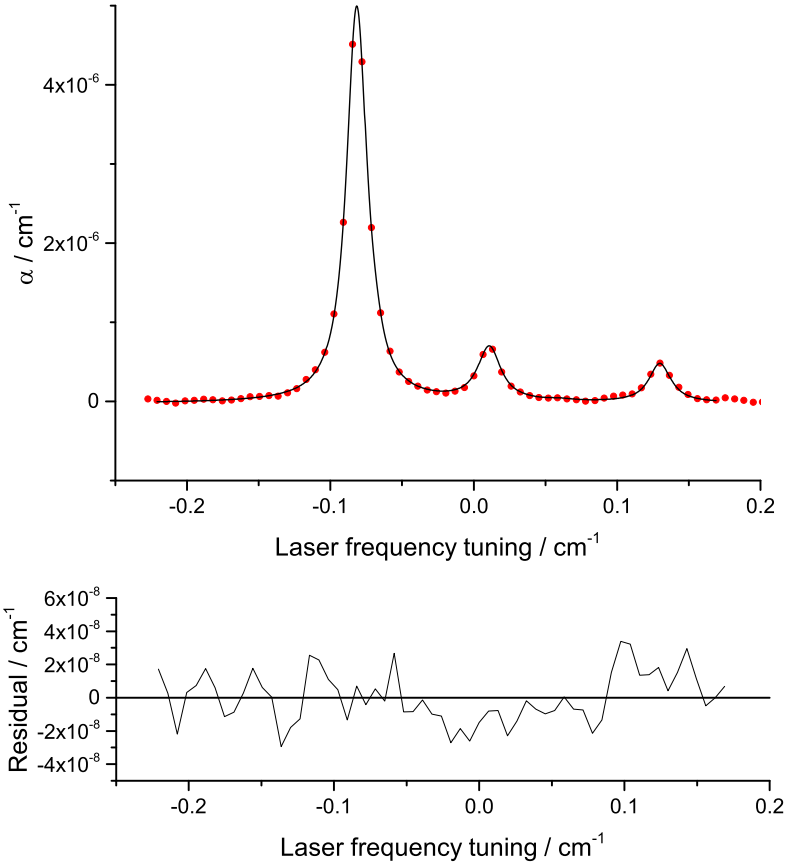

Figure 5.26: Absorption coefficient spectrum corresponding to data presented in Figure 5.22. The standard deviation of residual gives $\alpha_{min} = 1.8 \times 10^{-8}$ cm^{-1} for the single 100 ms scan.

($\alpha_{min} = 5 \times 10^{-9}$ cm^{-1}) due to etalon fringes affecting the Voigt model agreement. Another method for determining absorption coefficient based on a single ring-down time during the measurement was not used due to insufficient time between successive modes.[179,204]

Since the etalon structure in the baseline limits how well the model absorption profile fits the data, it is useful to alternatively assess the consistency of repeated measurements. After independently analysing consecutive measurements of 121 Torr 10% CO_2 in the cell, an Allan-Werle variance analysis was performed to predict the potential improvement in sensitivity with averaging. The result, converted into both α_{min} and the volume fraction of CO_2, is shown in Figure 5.27. Averaging ten spectra (1 s) results in $\alpha_{min} = 4 \times 10^{-9}$ cm^{-1} Hz$^{-1/2}$

In terms more pragmatic for gas detection applications, the α_{min} value can be reported

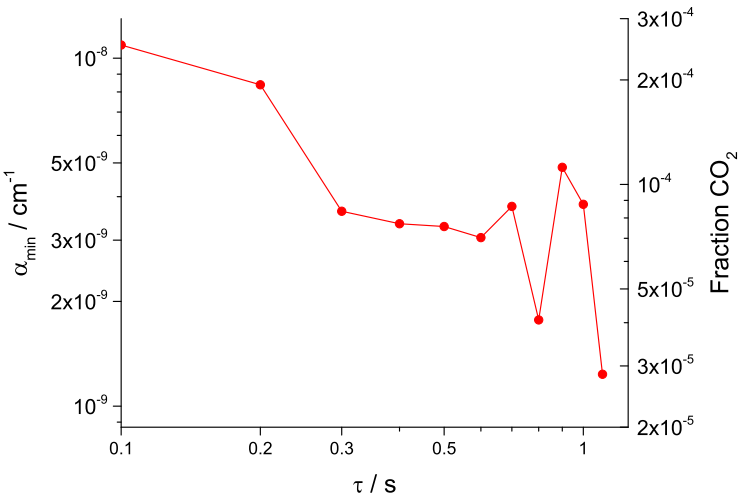

Figure 5.27: Plot of α_{min} and the corresponding minimum detectable fraction of CO_2 as a function of averaging for a measurement of 121 Torr 10% CO_2 in air. The absorption of individual spectra were fit independently, and an Allan-Werle variance analysis performed on the integrated absorption of the P(41) 1887.77 cm^{-1} CO_2 transition.

as a minimum detectable concentration. For the strongest CO_2 line probed in this region, this single scan measurement results in a minimum detectable number density of 1.4×10^{15} cm^{-3}, or 425 ppm at 100 Torr. With 1 s averaging, this drops down to about 90 ppm (see Figure 5.27). The CO_2 lines accessible with this laser are generally quite weak, relative to others nearby. For example, a laser emitting around 2060 cm^{-1}, where absorption within the $\nu_1 + \nu_2$ combination band occurs, with mirrors of the same reflectivity should be able to achieve at least a factor of ten improvement in the minimum detectable concentration using the same method.

The residual to the fit (see Figure 5.26) exhibits a scatter indicative of white noise, showing that a poor model does not limit the sensitivity. The analogue-to-digital conversion is performed either with an 8-bit oscilloscope or 16-bit DAQ, both of which have sufficiently high fixed point SNR to negligibly contribute to noise. Using the noise equivalent absorption sensitivity (NEAS) estimation, the acquisition bandwidth-normalized α_{min} is 5.7×10^{-9} cm^{-1} Hz$^{-1/2}$, or 18 ppm Hz$^{-1/2}$ CO_2, based on a 10 Hz acquisition rate of successive scans.[52] The shot noise limit has been given by Morville *et al.* as:[179]

$$\delta\alpha_{min}^{SN} = \frac{\pi}{\mathcal{F}L}\sqrt{\frac{e\Delta f}{\eta P_{\text{det}}}} \tag{5.25}$$

where variables include bandwidth of the detector (Δf), responsivity of detector (η), electron charge (e), and optical power on the detector (P_{det}). In this case, the high bandwidth

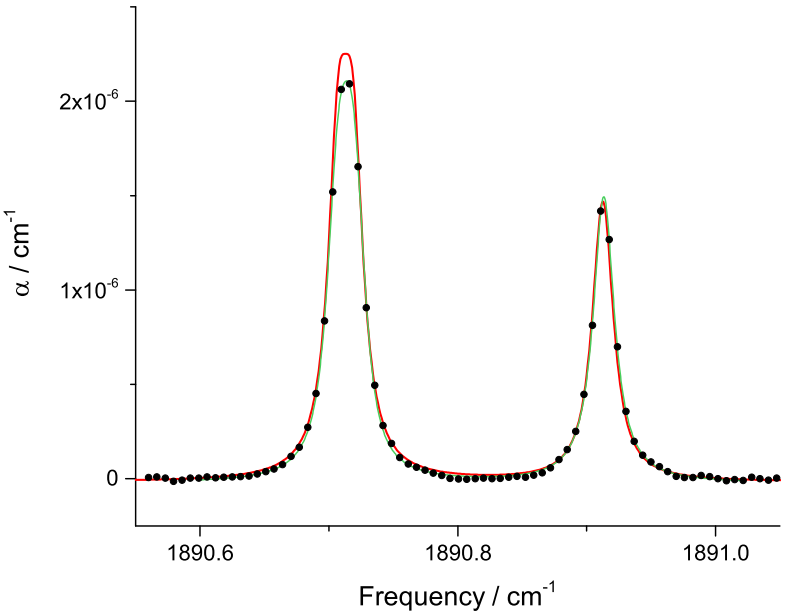

Figure 5.28: Absorption coefficient spectrum of 250 ppm NO buffered to 115 Torr measured with linear OF-CEAS (black circles) with Voigt fit (green line). The Voigt fit uses a combination of two Voigt profiles to model the lower wavenumber transition where Λ doublet splitting is evident and a single Voigt profile for the higher wavenumber feature. The red line shows the corresponding HITRAN simulation.[6]

photovoltaic detector (20 MHz), the finesse ($\mathcal{F}$) is 7900, the power on detector $\sim$ 3 mW, and the responsivity $\sim$ 0.1 A W^{-1} giving $\delta\alpha_{min}^{SN} \approx 5.4 \times 10^{-10}$ cm^{-1} Hz$^{-1/2}$. The measured sensitivity from the baseline fit is therefore about tenfold higher than the shot-noise limit, so improvements to the sensitivity are possible by, for example, using a detector without an immersion lens, or completely isolating the system from nearby electronics and pumps that may cause mechanical disturbances.

The 5.3 μm wavelength region is useful for exploiting large absorption cross-sections of NO ro-vibrational transitions to make sensitive measurements. A linear OF-CEAS spectrum collected on a sample of 250 ppm NO diluted in N_2 and dehumidified air at a total pressure of 115 Torr is shown in Figure 5.28. Features are visible at 1890.72 and 1890.91 cm^{-1} corresponding to R(3.5) $^2\Pi_{1/2}$ and $^2\Pi_{3/2}$ transitions respectively; each contains contributions from five Λ doublet-resolved rotational transitions.[6] The overlapping contributions make the absorption spectrum fitting non-trivial, however it could be fairly well modelled using

a sum of two Voigt profiles for the lower wavenumber feature and single Voigt at higher wavenumber, as shown by the green line. The residual of the fit yields an α_{min} of 1.3×10^{-8} cm^{-1} for a single 100 ms scan. A comparison to a HITRAN simulation (red line) reveals a discrepancy between the measured and reference data near the centre of the $^2\Pi_{1/2}$ feature at 1890.72 cm^{-1}. The measurement underestimates the actual value and indicates that feedback enhancement effects (see Section 4.4) may be affecting the recovered absorption profile at these high α values. Under the same feedback and cavity finesse conditions, a coupled QCL will have a narrower linewidth compared to an ICL due to its smaller Henry coefficient ($\alpha_H \approx 0$), which means that changes to the cavity–laser spectral overlap (ϵ^2) arising from absorption will be more significant.

5.3.4 Power saturation study

Given the high intracavity power, care must be taken to ensure that saturation of the ro-vibrational transition does not occur. Here, *saturation* refers to the condition where a large fraction of absorbing molecules have been excited to the upper energy state and the rate of relaxation becomes nearly equal to the rate of absorption. The sample then becomes transparent – the number of photons being lost by absorption is matched by the number emitted by the molecules relaxing back to the lower energy state. In this case, the assumptions applied to Equation 1.8, which form the basis for linear absorption spectroscopy, fall apart; calculations based on Equation 5.12 may therefore result in an underestimation of the concentration of the gas species in the cavity. Saturation of H_2O ro-vibrational transitions was explored with linear OF-CEAS and is discussed here.

Cavity transmission signals measured with two different resonant modes excited in the cavity are shown in Figure 5.29(a) with data offset for clarity. The laser was scanned over 110 – 180 modes corresponding to ranges of 0.73 – 1.2 cm^{-1} with 90 – 115 Torr of laboratory air in the cavity. It is evident from Figure 5.29 that the attenuation due to absorption appears to be more significant with the TEM_{21} mode excited. This observation cannot be accounted for with different ring-down times since the higher order modes exhibit shorter ring-down times and therefore would be expected to show diminished absorption

due to the shorter effective path lengths. It was therefore hypothesized that saturation effects were responsible for the difference.

Figure 5.30(a) shows the calculated absorption coefficient with Voigt fits for the H_2O (8,4,4)←(8,1,7) fundamental ν_2 bend transition at 1888.80 cm^{-1} for different laser powers.[6] The laser power could be increased by lowering the Peltier temperature while increasing the applied current to maintain the same centre frequency and selected transverse mode. The measured integrated absorption coefficient is significantly larger when less laser power is incident upon the cavity. This effect is even more evident for weaker transitions, as shown in Figure 5.30(b) for the (7,3,4)←(6,2,5) ν_2 H_2O hot band (2←1) transition at 1891.55 cm^{-1} and the (12,7,5)←(12,6,6) ν_2 fundamental at 1891.99 cm^{-1}.[6] The integrated absorption coefficient of two transitions are plotted against laser power incident on the cavity in Figure 5.31.

To verify that these are indeed saturation effects, the intensity of the beam in the cavity is compared with the theoretical prediction of the saturation intensity. The power

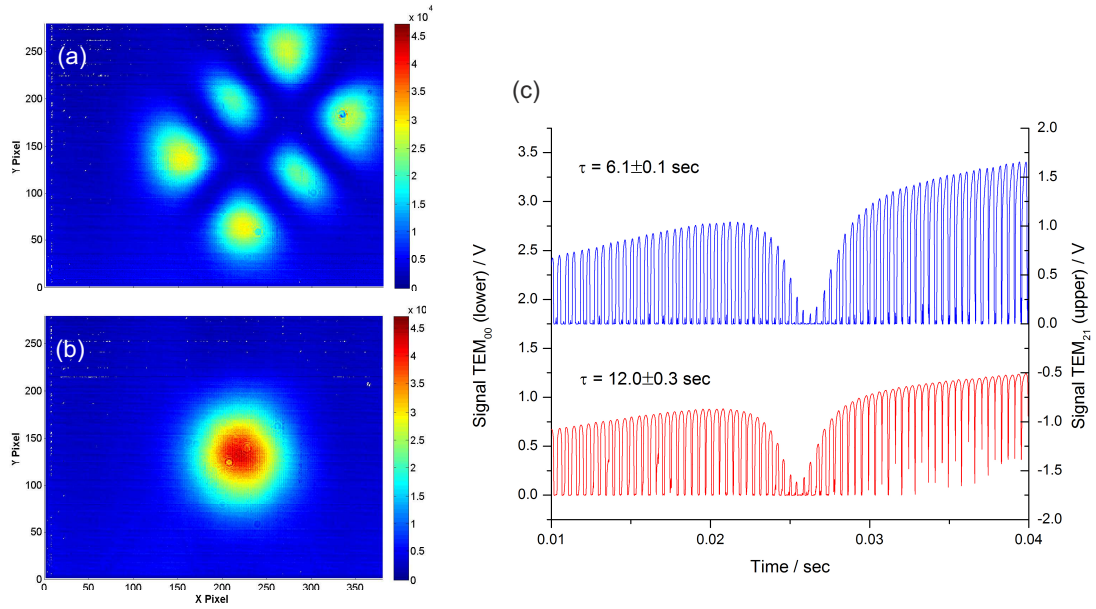

Figure 5.29: (a) Infrared camera profiles of TEM_{00} (lower) and TEM_{21} (upper) transverse modes excited in the cavity. (b) Corresponding cavity transmission signals for TEM_{00} (red) and TEM_{21} (blue) transverse modes. Note that the ring-down time, and hence the effective reflectivity, is smaller for more spatially dispersed, higher order modes. Data collected for the H_2O transition at 1888.8 cm^{-1} in laboratory air.

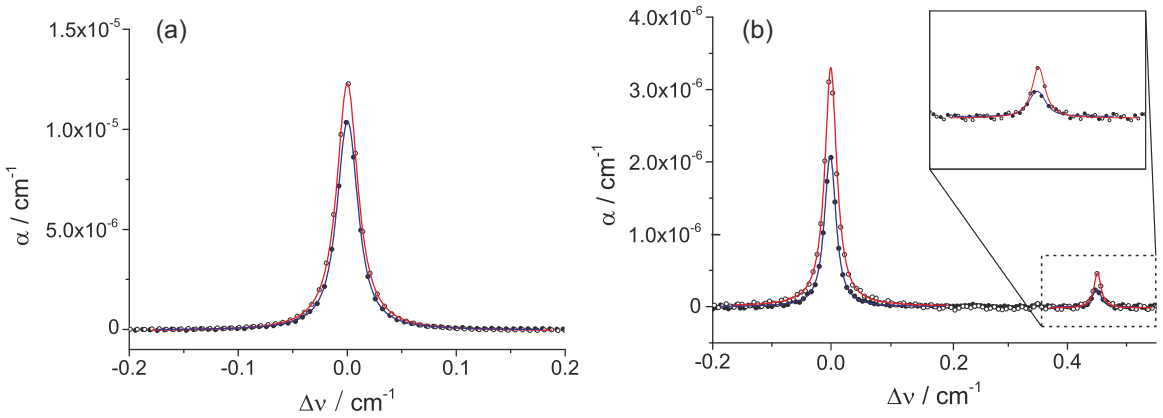

Figure 5.30: (a) α measurements for fundamental ν_2 bend transition of water vapour at 1888.8 cm^{-1} for 155 mW (filled circles) and 108 mW (open circles) incident power on the cavity. (b) α measurements for ν_2 hot band transition (2←1) of H_2O at 1891.6 cm^{-1} and fundamental transition at 1892.0 cm^{-1} (magnified in inset) for 98 mW (solid circles) and 35 mW (open circles) incident power on cavity. In all plots, the higher power Voigt fits are indicated in blue and the lower power in red.

circulating in an optical cavity (P_{circ}) can be estimated using:[35]

$$P_{\text{circ}} = P_{\text{inc}} \frac{(1-R)}{(1-R^2)^2}. \tag{5.26}$$

This formula is based solely on the incident power (P_{inc}) and effective reflectivity of the cavity mirrors, and does not take into account enhanced coupling efficiency. The highest intensity of light in the cavity will be at the beam waist (w_o) along the central axis:[35]

$$I_{\text{max}} = \frac{2P_{circ}}{\pi w_o^2}. \tag{5.27}$$

Power builds up rapidly and is maintained for several hundred microseconds with the linewidth of the laser narrowed below the cavity bandwidth (20 kHz). Based on the set-up used, the maximum intensity in the cavity was calculated to be 1.8×10^8 W m^{-2} for TEM_{00} modes. The power density of higher order modes is much more diffuse, and therefore when these modes are selected the intracavity intensity will be lower than this maximum value. For example, the cross-section of the beam (defined by the radius at which the power drops off to $1/e^2$) for the TEM_{11} mode is over twice that of the TEM_{00} mode, albeit with a different intensity profile.

The saturation intensity (I_{sat}) of an inhomogeneously broadened sample can be calculated based on the transition dipole moment (μ) and rate of relaxation from the upper state (γ):[8,234]

$$I_{\text{sat}} = \frac{c\gamma^2\hbar^2}{4\pi\mu^2}. \tag{5.28}$$

I_{sat} defines the intensity of light required for the measured absorption coefficient to equal half of its true value. The two main relaxation mechanisms to consider are vibrational and rotational collisional relaxations. Based on work by Keeton and Bass, the rotational relaxation rate of water vapour in air is dominated by collisions with O_2 and N_2, and is estimated to be 1.56×10^6 s^{-1} under these experimental conditions.[235] Vibrational relaxations are dominated by collisions with other water molecules. For the fundamental ν_2 mode, the relaxation rate is 1.31×10^6 s^{-1} at 295 K and a partial pressure of 0.74 Torr.[236,237] Under the same conditions, the vibrational relaxation rate for the 1891.6 cm^{-1} transition which involves the first and second excited states is approximately 2.92×10^6 s^{-1}.[236,237] Since the rotational and vibrational relaxation occurs upon the same timescale, γ was taken as the average of the two for calculations of I_{sat}.

The theoretical saturation intensities for the three transitions studied here are given in Table 5.2. These are all significantly lower than the maximum intracavity intensity, and so more significant saturation effects might be expected. The gas sample is, however, not purely inhomogeneously broadened as the absorption profile can be fit well to a Voigt profile. Under

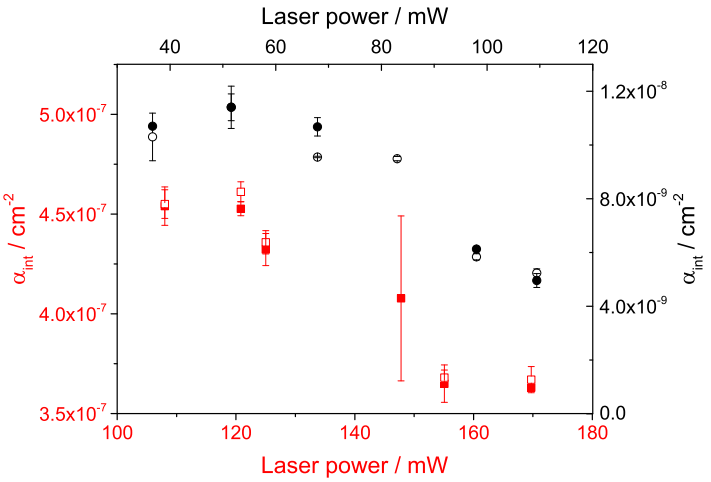

Figure 5.31: Integrated absorption coefficient ($\alpha_{\text{int}} = \int \alpha \mathrm{d}\nu$) as a function of laser power incident on cavity for two fundamental ν_2 transitions: (12,7,5) ← (12,6,6) at 1892.0 cm^{-1} (black) and (8,4,4) ← (8,1,7) at 1888.8 cm^{-1} (red). Error bars show standard deviation of several measurements. Open/filled points indicate two separate data sets measured with frequency increasing or decreasing.

Table 5.2: Calculated saturation intensities for water vapour transitions.

Frequency (cm^{-1})	$\mathbf{I}_{sat}$ (W m^{-2})
1888.8	4.93×10^6
1891.6	3.12×10^5
1892.0	2.52×10^5

typical experimental conditions for OF-CEAS experiments, the Doppler and Lorentzian components both contribute significantly to the lineshape – at room temperature and for transitions around 5 μm the Doppler linewidth is around 100 MHz while the Lorentzian linewidth is in the range 150 – 750 MHz for sample pressures between 20 – 200 Torr. The saturation intensity for a homogeneously broadened gas is much larger ($\sim 10^{10}$ W m^{-2}), therefore the true I_{sat} values under these experimental conditions are likely to be somewhat higher than those given in the table, and saturation effects not as pronounced.[238] This linear OF-CEAS system, with a FSR of 195 MHz, cannot resolve purely inhomogeneously broadened spectral lines.

Measurements of the absorption coefficient as a function of laser intensity were used to determine the amount of water vapour in laboratory air based on a simple two-level system according to the treatment by Steinfeld:[8]

$$\frac{1}{\alpha} = \frac{1}{\alpha^o} + \frac{I}{\alpha^o I_{sat}}. \tag{5.29}$$

Based on this equation, the true absorption coefficient (α^o) was found by taking the intercept of a plot of $1/\alpha$ for the ν_2 fundamental bend of H_2O as a function of I/I_{sat}. Based on this value, the partial pressure of water vapour in the cavity was determined to be 0.695 ± 0.225 Torr, corresponding to a relative humidity of $28.3 \pm 9.1\%$ in laboratory air. This agrees well with a nearby hygrometer (Testo), which reported a relative humidity of 31%.

5.4 Conclusions

In this chapter, a variant of OF-CEAS utilizing a simple linear cavity was explored. The theory developed for V-shaped systems was extended to this new approach to quantitatively

explain its functionality. Despite the presence of non-resonant feedback to the laser in this geometry, it is possible to spatially filter this sufficiently to allow stable locking to the high finesse resonant cavity feedback. This was accomplished by mode-mismatching the laser to the cavity field such that the spot size of the non-resonant feedback was much larger than the laser facet aperture, while at the same time the resonant feedback had a small spot size allowing effective coupling for injection seeding. This theoretical basis was supported by complementary experimental results using a high power 5.3 μm DFB-QCL, and the observed laser frequency and phase behaviour matched the predicted behaviour. Fits to baseline measurements indicate that the limit to sensitivity is approximately 5×10^{-9} cm^{-1} for 100 ms, though a sensitivity of $\alpha_{min} = 1.6 \times 10^{-8}$ cm^{-1} for a single 100 ms scan was demonstrated for measurements of CO_2 and NO. With 1 s averaging, α_{min} values of 4×10^{-9} cm^{-1} are achievable. This is on par with the best values reported in the literature with V-shaped OF-CEAS systems using QCLs.[199–201] In addition, high intracavity power allowed for identification of resonant transverse mode profile, and was shown to saturate ro-vibrational excitations of H_2O even at pressures of $\sim$ 100 Torr.

Chapter 6

General conclusions and future directions

6.1 Overview and conclusions

The mid-infrared is well-known as the fingerprint region of the electromagnetic spectrum since many important gases can be selectively identified by the strongly absorbing, well-separated ro-vibrational transitions. The main aim of this thesis has been the demonstration of a range of spectroscopic techniques for trace gas detection using new continuous wave mid-infrared laser sources.

The first results chapter (Chapter 2) introduces two methods by which frequency modulation of a semiconductor laser can improve spectroscopic measurements. First, an 8 μm DFB-QCL was frequency-stabilized to the third derivative of a ro-vibrational transition of CH_4 using an automated LabVIEW program. With the optical frequency stabilized to within a range of 3 MHz over two minutes, wavelength modulation spectroscopy (WMS) could be performed with the potential for long-term averaging. Then, frequency modulation spectroscopy was performed using a 5 μm DFB-QCL on NO to demonstrate that high frequency modulation of QCL current enhances the performance, though improvement for this system was limited by parasitic filtering of high frequency modulation in the bias tee junction and residual amplitude modulation.

Off-axis cavity-enhanced absorption spectroscopy (CEAS), presented in Chapter 3, is a robust, precise method for measuring trace gas concentrations in a limited spatial volume with long optical path lengths. While off-axis alignment of the laser beam (with respect to

the central axis of the two-mirror cavity) enhances sensitivity, residual mode structure often limits the instrument performance. However, measurements of CO_2 using a 5 μm DFB-QCL demonstrated a tenfold improvement in sensitivity simply by adding a broadband RF perturbation to the laser current. The linewidth broadening effects of the added white noise allowed adjustments to the effective linewidth of the QCL, a potentially useful feature for experiments requiring linewidths broader than the intrinsically narrow linewidth of the laser.

In Chapter 4, optical-feedback cavity-enhanced absorption spectroscopy (OF-CEAS) was extended to new laser sources. The technique was originally demonstrated with diode lasers, followed by DFB-QCLs, with V-shaped optical cavities. In this thesis, DFB-ICLs emitting within the important 3 μm spectral region were used as OF-CEAS for the first time for measurements of VOCs and N_2O. The sensitivity achieved, 2.5×10^{-8} cm^{-1} in 100 ms is similar to past studies using DFB-QCLs. A 5 μm EC-QCL was also used for OF-CEAS studies but, despite achieving comparable sensitivity, exhibited mode-hops that caused irregular frequency tuning of the laser and prevented averaging.

Lastly, Chapter 5 presented a variation of OF-CEAS with a simpler linear geometry of the optical cavity. Surprisingly, the resonant feedback field could dominate over unavoidable non-resonant back-reflections, and quantitative models of the coupled laser field and beam propagation clearly showed that the laser can lock to a linear cavity given certain conditions are met. In order to ensure stable locking to successive modes, focussing optics were used to mode-mismatch the beam with the intracavity field. While this reduced the coupling efficiency into the cavity modes, stable injection seeding of the DFB-QCL by the resonant feedback field was demonstrated for measurements of CO_2. In addition to the fundamentally simpler design, the linear cavity is advantageous because reflectivity does not vary for even and odd harmonics, the sample volume can be quite small, and other cavity-based experiments – such as CRDS or CEAS – can be readily converted for OF-CEAS without additional cavity optics or specialized sample cells. The best sensitivity ($\alpha_{min} = 5 \times 10^{-9}$ cm^{-1} in 100 ms) was determined by fitting a baseline, absorption-free measurement; a fit of an absorption spectrum of a sample containing CO_2 returned a sensitivity of 4×10^{-9}

cm^{-1} with one second averaging similar to some of the best V-shaped systems described in the literature.

6.2 Future work

As the general purpose of this thesis was to present proof-of-principle, laboratory-based experiments of new or improved spectroscopic techniques, the next stage is to apply the techniques in field or clinic settings. As mentioned earlier, many of the target molecules are important for atmospheric and medical studies. One area of growing interest where laser absorption spectroscopy – particularly in the mid-infrared – may prove extremely useful is for detection of VOCs emitted by plants. Plants emit VOCs when stressed, with many studies demonstrating that particular cocktails of volatile gases correspond to different stressors.[239–241] For example, methyl salicylate is a well-known product of tobacco plants under attack from the tobacco mosaic virus.[242] Developing a better understanding of these emissions is important for a number of reasons. Firstly, some VOCs have been shown to elicit a predator resistance as some herbivores are warned away by specific airborne chemicals.[243] Plants are one of the key atmospheric sources of these reactive species, and may be important for understanding O_3 budgets and chemistry in the troposphere.[244] Finally, plant scientists propose using specific, well-studied species as sentinel plants; by monitoring the emissions from these plants, it may be possible to see signs of drought or disease before severe damage occurs to neighbouring crops.[245] Deploying mid-infrared laser absorption spectrometers for field and laboratory studies may provide the sensitivity and selectivity of VOC components required to establish an effective warning system.

Preliminary studies indicate that ICL-based OF-CEAS may be a powerful technique for measuring these important VOCs exhibiting strong fingerprints in the 3 μm region. The V-shaped OF-CEAS experiment discussed in Section 4.6 was used to take measurements of geraniol (trans-3,7-dimethyl-2,6-octadien-1-ol), a common monoterpene species notable as one of the main components of rose oil.[246] This large molecule has a broad, featureless absorption in the 3040 cm^{-1} region with α approximately constant over ~ 0.8 cm^{-1}. The sample was introduced to the cavity by heating a vial containing liquid geraniol that was

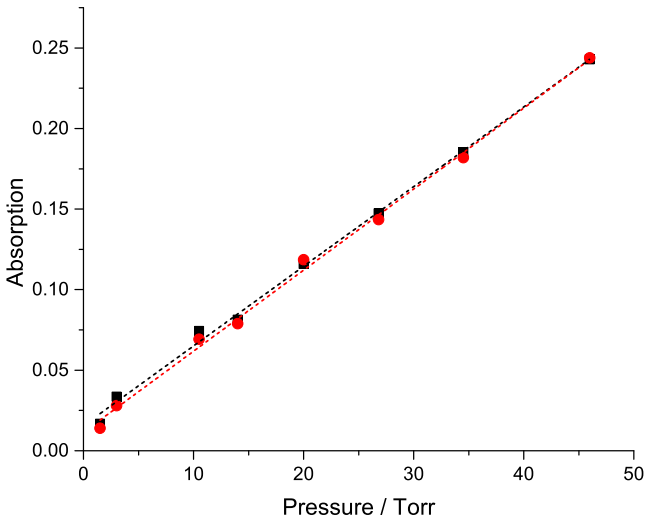

Figure 6.1: Plot of average absorption as a function of pressure of geraniol vapour measured using the 3.29 μm DFB-ICL with V-shaped OF-CEAS system. Red and black data represent even and odd modes with dotted lines showing linear fit.

connected to the evacuated sample box. While there is good linearity between the measured absorption and pressure of geraniol (see Figure 6.1), there was evidence that condensation of the geraniol vapour onto the surface of the mirrors diminished the reflectivity. Therefore, while preliminary results indicate that OF-CEAS can be used to measure this VOC, further experiments are necessary to develop a robust calibration method to account for changes in mirror reflectivity and reduce the degree of condensation.

The effect of modulation, particularly high frequency, broadband noise perturbation, of QCLs and ICLs warrants further research. While the frequency response of DFB-QCLs was limited to below 50 MHz in the experiments presented here by parasitic impedance effects of the bias tee, other experiments have demonstrated modulation in the GHz. Higher modulation frequencies are beneficial for probing molecular transitions with a single sideband separated from the carrier frequency by more than the linewidth of the ro-vibrational transition. However, unlike diode lasers, QCLs do exhibit a decreased frequency response at high frequencies that may be useful for studies requiring quasi-single sideband generation.[247] It was hypothesized in the paper by Hanguaer *et al.* that this unique feature arises from the negligible linewidth enhancement of QCLs, so it is unclear whether ICLs would exhibit similar behaviour. Indeed, there is evidence of unique frequency response for ICLs subject to modulation in the hundreds of kHz region.[248] In addition to considering frequency response, it would also be useful to study the relationship between noise perturbation and effective

laser linewidth for both QCLs and ICLs. As well as the benefits of linewidth broadening for CEAS described in Chapter 3, recent studies indicate that broadened QCL linewidths enhance population transfer efficiency in both bulk and molecular beam environments.[249] Recent work also indicates that QCL frequency combs can be generated by four-wave mixing in the laser medium for very sensitive spectroscopic measurements.[250]

EC-QCLs have the great advantage of being widely tunable over many ro-vibrational transitions, making selectivity more straightforward and allowing greater flexibility. Further pursuits of sensitive OF-CEAS studies with newer, mode-hop free EC-QCLs is a promising avenue. The effect of feedback on EC-QCLs should also be studied in greater detail, as the effect of the injection seeding on the carrier density of the laser, as well as the temperature of both the chip and grating, should impact the feedback response of these lasers differently to DFB systems. Feedback effects on ICLs also demand further attention. Although this work demonstrates the ability of ICLs to lock to optical feedback, a more comprehensive study of feedback regimes to describe these lasers is necessary. It is unclear, for example, whether ICLs will exhibit coherence collapse at high feedback rates like diode lasers, or whether they will remain stable due to small linewidth enhancement factors compared to diode lasers.

The capability to remain locked to a single frequency and build-up intracavity power over seconds (see Figure 6.2) is attractive for a range of different experiments. High intracavity power could be used, for example, for Raman scattering, polarization, or fluorescence experiments. Performing coherent anti-Stokes Raman spectroscopy (CARS) in an optical cavity enhanced the sensitivity by over three orders of magnitude, and combining this with optical feedback may allow an even greater enhancement for trace measurements of Raman-active molecules (with the caveat that a smaller Raman signals would be expected in the infrared compared to the visible).[251] Polarization and laser-induced fluorescence measurements, which could benefit from the high intracavity power of OF-CEAS, are particularly useful for measurements of radicals and simple hydrocarbons in the atmosphere and combustion processes.[252–256] Again, however, these techniques are generally better suited to shorter wavelengths.

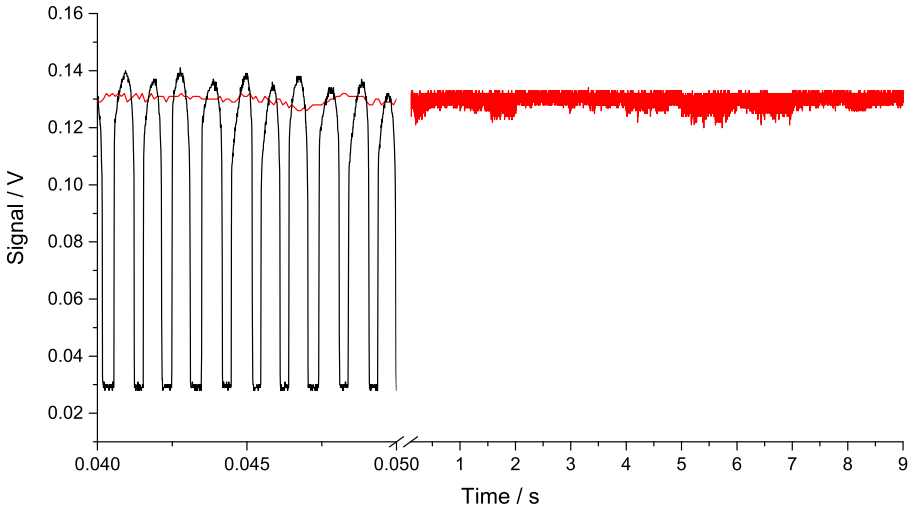

Figure 6.2: Sample measurement of cavity transmission as laser continuously remains locked to a single cavity mode (red). The black line shows a typical OF-CEAS measurement under the same conditions. For the single frequency measurement, no active phase-matching was enabled and the standard deviation of the signal is 1% of the mean. Data collected using 3.29 μm DFB-ICL and an empty cavity with $\mathcal{F} \approx 3000$. The intracavity power in this case is about 3 W.[35]

Sustained intracavity power also opens up possibilities of measuring a gas subject to an external modulating field. Recent experiments on our group demonstrate that applying an oscillating field using a solenoid surrounding a linear optical cavity allows for intracavity Faraday modulation spectroscopy (INFAMOS). Faraday modulation spectroscopy (FAMOS) is a powerful technique for selectively measuring paramagnetic species, most notably NO.[65] Combining OF-CEAS and FAMOS exploits the long optical path lengths, high intracavity power, and narrow linewidth of OF-CEAS with the selectivity of the modulated magnetic field. Preliminary results of INFAMOS for NO detection (see Figure 6.3) are promising, however optimization and limit of detection measurements are ongoing.

Continuing progress in laser technology will inevitably pave the way for more sophisticated and sensitive experiments utilizing these semiconductor sources. For example, the first dual wavelength QCL was recently demonstrated for near-simultaneous measurements of NO and NO_2.[257] There has also been progress in developing QCLs that have a constant power output over a range of frequencies, though thus far this has only been accomplished with pulsed THz QCLs.[140] As ICLs and QCLs become established laser sources, commer-

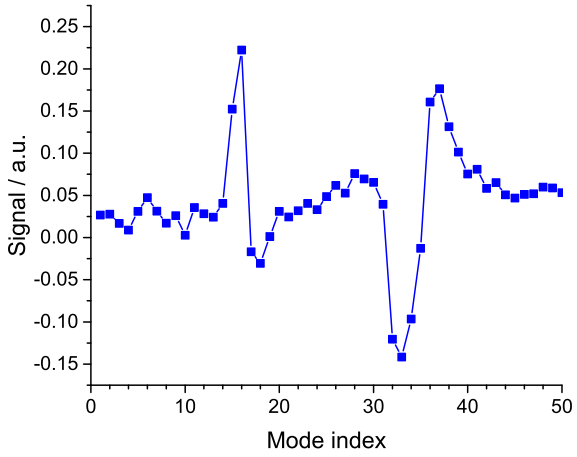

Figure 6.3: Faraday modulation signal collected by modulating the magnetic field surrounding a high finesse linear cavity locked to a 5.3 μm DFB-QCL. The signal arises from $^2\Pi_{3/2}$ and $^2\Pi_{1/2}$ R(4.5) transitions of NO with each point representing excitation of a resonant longitudinal mode of the cavity.

cial availability will rise, costs will decrease, and the power and robustness will continue to improve.

Appendix

Coupled laser frequency derivation

Lang and Kobayashi developed an equation for the laser field (E) subject to optical feedback:[173]

$$\frac{d}{dt}E(t)\exp(i2\pi\nu t) = E(t)\exp(i2\pi\nu t)\left[\frac{i\pi c}{n_o\ell} + \frac{1}{2}\left(G(N) - \Gamma_o\right)\right] + \kappa E(t-\tau)\exp(i2\pi\nu(t-\tau)) \tag{A.1}$$

where variables include the carrier density (N) dependent gain factor (G), laser cavity loss (Γ_o), refractive index of gain medium (n_o), laser cavity length (ℓ), laser frequency (ν), and feedback term (κ). The cavity loss term is a combination of waveguide losses (Γ_{wg}) and the amount of light retained in the cavity after reflection off the facets:

$$\Gamma = \Gamma_{wg} - \frac{c}{n_o\ell}\ln\left(\sqrt{R_1R_2}\right). \tag{A.2}$$

If there is feedback, the effective reflectivity of this surface ($R_{(2)}$) is adjusted to account for light re-entering the laser cavity:

$$\sqrt{R_{(2)}} = \sqrt{R_2}\left(1 - \sqrt{\beta}\frac{1-R_2}{\sqrt{R_2}}h_{fb}(\nu)\exp\left(\frac{-i4\pi\nu L}{c}\right)\right) \tag{A.3}$$

where h_{fb} is the frequency-dependent complex transfer function, which represents the ratio between the emitted and feedback fields, and depends on the optics that the beam passes through. Since Equation A.1 must be constant regardless of the presence of feedback, a

generalized loss term (Γ) can be defined such that:

$$\Gamma = \Gamma_o - 2\kappa, \tag{A.4}$$

which, when used with Equations A.2 and A.3 (under the assumption that the term on the right-hand side of Equation A.3 is $\ll 1$) yields:

$$\kappa = \frac{c}{2n_o\ell}\left(-\sqrt{\beta}\frac{1-R_2}{\sqrt{R_2}}h_{fb}(\nu)\exp\left(\frac{-i4\pi\nu L}{c}\right)\right). \tag{A.5}$$

The steady state of the circulating laser field means the imaginary components of Equation A.1 (assuming constant E) can be set equal with and without feedback at resonant longitudinal laser frequencies of ν_o and ν_{fb} respectively:

$$\nu_o = \nu_{fb} + \mathrm{Im}(\kappa). \tag{A.6}$$

Combining with Equation A.5 gives:

$$\nu_o = \nu_{fb} + \frac{\sqrt{\beta}(1-R_2)c}{2\ell n_o\sqrt{R_2}}\left[\mathrm{Re}(h_{fb})\sin\left(\frac{4\pi\nu_{fb}L'}{c}\right) - \mathrm{Im}(h_{fb})\cos\left(\frac{4\pi\nu_{fb}L'}{c}\right)\right]. \tag{A.7}$$

The expression cannot be solved explicitly for ν_{fb}, however a MATLAB program was written to plot ν_{fb} as a function of ν_o for a given range of ν_{fb} values. Typical values applied in the model are: $n_o = \eta = 3.35$; $\ell = 0.0015$ m; $R_2 = 0.3$.[258,259] Note that in the text, R_2 is labelled as R_o.

Gaussian ray trace analysis

Gaussian ray trace matrix analysis was used to model the beam propagation.[35] These matrices can be applied to the Gaussian beam factor (q) according to Equation 5.22 to account for changes in spot size and phase front curvature due to, for example, focussing or propagation through a medium.

We will use the approximation of a thin lens to describe both the mode-matching lens and cavity mirror with the convention that $R > 0$ for converging optics where R_i is radius

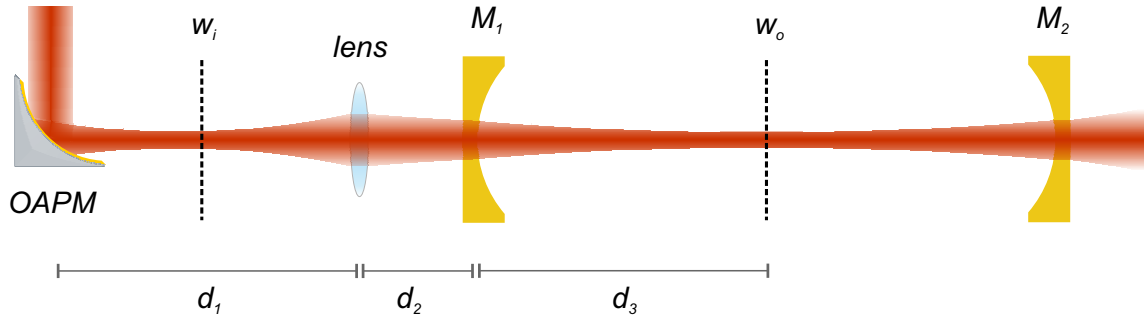

Figure A.1: Basic diagram of mode-matching portion of linear OF-CEAS set-up with variables indicated.

of curvature of the optic i, d_i is distance (see Figure A.1), and f_l is focal length ($f = R/2$). The total matrix representing the propagation from the collimated beam incident on the OAPM to the intracavity beam waist is:

$$\mathbf{M} = \begin{pmatrix} 1 & d_3 \\ 0 & 1 \end{pmatrix} \times \begin{pmatrix} 1 & 0 \\ -\frac{2}{R_1} & 1 \end{pmatrix} \times \begin{pmatrix} 1 & d_2 \\ 0 & 1 \end{pmatrix} \times \begin{pmatrix} 1 & 0 \\ -\frac{1}{f_l} & 1 \end{pmatrix} \times \begin{pmatrix} 1 & d_1 \\ 0 & 1 \end{pmatrix} \times \begin{pmatrix} 1 & 0 \\ -1/f_{\mathrm{OAPM}} & 1 \end{pmatrix} \tag{A.8}$$

where matrices are multiplied from right-to-left. The example values used are listed below, with all values given in metres given in Table A.1. Using these values, we find that matrix $\mathbf{M}$ is:

$$\mathbf{M} = \begin{pmatrix} 0.111 & -0.3193 \\ 3.557 & -1.221 \end{pmatrix} \tag{A.9}$$

Table A.1: Values used for sample beam propagation model.

f_l	f_{OAPM}	R_1	d_1	d_2	d_3
0.15	0.125	0.50	0.25	0.167	0.375

Linear cavity transfer function

Here the equation for absorption in a linear OF-CEAS cavity is derived. The field transmitted through the cavity independent upon the reflectivity coefficients (r) and transmission

coefficients (t) of the first and second cavity mirrors:

$$E = E_i t_1 t_2 \exp(-ikL)\left(1 + r_1 r_2 \exp(-2ikL) + \dots\right) \approx \frac{E_i t_1 t_2 \exp(-ikL)}{1 - r_1 r_2 \exp(-2ikL)}. \tag{A.10}$$

The transfer function of a lossless cavity assuming that the mirrors are identical is:

$$H_o = \frac{I_o}{I_i} = \frac{t^4}{\left(1 - r^2 \exp(-2ikL)\right)\left(1 + r^2 \exp(2ikL)\right)} = \frac{T^2}{1 + R^2 - 2R\cos(2kL)}. \tag{A.11}$$

For a cavity with an absorbing medium, the transfer function is:

$$H = \frac{I_\alpha}{I_i} = \frac{T^2 \exp(-\alpha L)}{1 + R^2 \exp(-2\alpha L) - 2R\exp(-\alpha L)\cos(2kL)}. \tag{A.12}$$

On resonance (*i.e.* $2kL = 2n\pi$) and assuming $1 - R = T$, this yields:

$$\frac{I_o}{I_\alpha} = \frac{H_o}{H} = \frac{\left(1 - R\exp(-\alpha L)\right)^2}{(1-R)^2 \exp(-\alpha L)} \tag{A.13}$$

Take $\exp(-\alpha L) \approx 1$ in the denominator and using the approximation that $\ln(1 - x) \approx -x - \frac{x^2}{2} - \dots$ when $|x| < 1$:

$$\alpha = -\frac{1}{L}\left[\ln\left(1 - (1-R)\sqrt{\frac{I_o}{I}}\right) - \ln(R)\right] = \frac{(1-R)}{L}\left(\sqrt{\frac{I_o}{I}} - 1\right) \tag{A.14}$$

Coupled cavity analysis

It is also possible to consider the linear cavity system as a series of coupled optical resonators, as shown in Figure A.2. The arrows indicate fields heading toward and away from the laser facet (laser cavity in blue), and each of the cavity mirrors (yellow). Neglecting the relative spatial distribution of the components, the fields can be defined as:

$$E_1 = it_L E_L - r_L E_8 \tag{A.15}$$

$$E_2 = E_1 \exp(i\phi_1) \tag{A.16}$$

$$E_3 = t_1 E_2 - r_1 E_6 \tag{A.17}$$

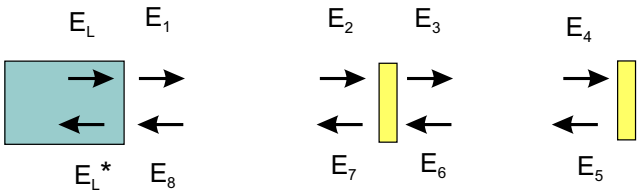

Figure A.2: Coupled cavity scheme.

and so on with:

$$E_L^* \quad = \quad -r_L E_L + i t_L E_8. \tag{A.18}$$

The i term in Equations A.15 and A.18 refers to the phase shift at the laser facet. Reflection (r) and transmission (t) coefficients are labelled according to laser facet, mirror 1, or mirror 2. The ϕ term represents phase shift of the field through the cavity, with ϕ_1 describing the laser–cavity resonator and ϕ_2 the high finesse optical resonator formed between the two mirrors. After some algebra, E_8 can be described in terms of E_L and E_1 as:

$$E_8 = \exp(2i\phi_1)\left(it_L E_L - r_L E_8\right)\left[-\frac{r_2 t_1^2 \exp(2i\phi_2)}{1 - r_1 r_2 \exp(2i\phi_2)} - r_1\right]. \tag{A.19}$$

E_L^* can then be written as a function of the two phase conditions:

$$E_L^* = -r_L E_L - \frac{t_L^2 E_L \exp(2i\phi_1)\left[-\frac{r_2 t_1^2 \exp(2i\phi_2)}{1 - r_1 r_2 \exp(2i\phi_2)} - r_1\right]}{1 + r_L \exp(2i\phi_1)\left[-\frac{r_2 t_1^2 \exp(2i\phi_2)}{1 - r_1 r_2 \exp(2i\phi_2)} - r_1\right]}. \tag{A.20}$$

It would be interesting in the future to consider this equation, alongside an understanding of the specific laser physics of QCLs, to investigate whether locking can be preferred in some situations with the feedback field slightly out-of-phase with the laser cavity field. However, it is important to note that Equation A.19 is very similar to the transfer function (Equation 5.5) derived in the previous section.

MATLAB Codes

Frequency tuning model

```
clear all
figure
grey=[0.6,0.6,0.6];
hold on
b=1e-4; %feedback attenuation
c1=0.3; %reflection amplitude
c2=1; %resonant feedback amplitude
R2=0.3; %laser facet reflectivity
R=0.999; %cavity mirror reflectivity
N=3.51; %refractive index laser gain material
c=3e8; %speed of light
L=0.77; %cavity length
L1=0.77; %laser cavity distance
l=0.0015; % laser cavity size
syms w
phi=0;
w=(5.66451E13:.05e5:5.66458E13);
w1=w/(3E10);
for ind=1:length(w);
   % G(ind)=3e8/w(ind)/4;
    G(ind)=0;
    h(ind)=c1.*sqrt(R)+c2.*(1-R)*sqrt(R)*exp(-2i*2*pi*w(ind).*(L+G(ind))/c)/(1-(R^2).*exp(-2i.*2*pi*(
    P(ind)=real(h(ind));
    Q(ind)=imag(h(ind));
    wo(ind)=((w(ind))+sqrt(b).*(1-R2).*c./(2*N.*l.*sqrt(R2)).*(P(ind).*sin(2.*(L1.*(2*pi*w(ind))./c+pl
    wo1(ind)=wo(ind)/(3E10);
       [m, in] = max(wo(1:ind));
        woo(ind)=wo(in);
    woo1(ind)=woo(ind)/(3E10);
    ht1(ind)=c2.*(1-R)*exp(-2*pi*w(ind).*(L+G(ind)).*1i./c)*exp(-1i*(L1.*2*pi*w(ind)/c+phi))/(1-R.*exp
end
I1=ht1.*conj(ht1);
%subplot(2,1,1)
plot(wo1,w1off,'b','Linewidth',1.);
hold on
plot(woo1,w1,'b','Linewidth',2);
%subplot(2,1,2)
%hold on
%plot(woo1,I1,'b','Linewidth',1);
```

Beam size model

```
%ABCD analysis of resonant and nonresonant beam
%refractive indices
```

```
%ylabel('Intensity / au')
%xlabel('Beam radius / m')
figure
L=0.77;
lambda=5.26e-6;
f_coll=0.004;
n_air=1.00027266; %at 15C (Penndorf, 1957)
n_ZnSe=2.4278; %CVD ZnSe at 20C (NIST, Li, 1984)
n_BD=2.616; %Black Diamond, ThorLabs
n_CaF2=1.3952; %Crystran
l_BD=0.0025; %thickness black diamond collimating lens
l_M=0.003; %thickness of cavity mirrors (based on normal window thickness)
l_CaF2=0.0033; %thickness of CaF2 lens (Thorlabs)
x_LasPM=0.21; %distance laser to OAPM
x_PMwind=0.; %distance parabolic mirror to window
l_wind=0.000; %thickness window
x_cav=0.77; %cavity length
f_lens=0.15;
f_lensrev=0.15;
f_OAPM=0.125;
f_M=.5;
g=.29;
wo=0.0015; %beam spot size (radius) at collimating lens
woo=sqrt(lambda*L/(pi*2)*sqrt(2*1/L-1));
qoo=(-1i*lambda/(pi()*woo^2))^(-1);
qo=(-1i*lambda/(pi()*wo^2))^(-1);
k=1.8855e5;
x_meas=-0.004;%must be between 0.208 and 0.348 (x_LasPM to x_LasPM+x_PMwind)
A2=1; %amplitude resonant
R3=(abs(n_air-n_ZnSe)/(n_air+n_ZnSe))^2;
A1=0.71; %amplitude reflection
f0=0.32;
f1=0.45;%focal points on return (can get from model2 plot or plotting wa(xx))
f2=0.37;
f3=0.02;
x_lensCav=0.105;
x_PMlens=0.77-x_LasPM-x_lensCav-l_M-l_wind;
%first pass
x1=(-0.0040:0.0001:0.0);
for ind = 1:length(x1);
if (x1(ind)<0)
    M1a=[1 -x1(ind);0 1]; M1b=[1 0;(-1/f_coll) 1];
    M2=[1 0;0 1];
    M3=[1 0;0 1]; M4=[1 0;0 1]; M4e=[1 0;0 1]; M4c=[1 0;0 1]; M4d=[1 0;0 1];
    M5=[1 0;0 1]; M7z=[1 0;0 1]; M8=[1 0;0 1]; M9=[1 0;0 1];M10=[1 0;0 1];
    M=M1a*M1b;
elseif (x1(ind)>=0)&&(x1(ind) < x_LasPM)
    M1a=[1 0;0 1]; M1b=[1 0;0 1];
    M2=[1 x1(ind);0 1];
    M3=[1 0;0 1]; M4=[1 0;0 1]; M4e=[1 0;0 1]; M4c=[1 0;0 1]; M4d=[1 0;0 1];
M5=[1 0;0 1]; M7z=[1 0;0 1]; M8=[1 0;0 1]; M9=[1 0;0 1];M10=[1 0;0 1];
    M=M10*M9*M8*M7z*M5*M4d*M4c*M4e*M4*M3*M2;
elseif (x_LasPM <= x1(ind)) && (x1(ind) < (x_LasPM + x_PMwind))
    M1a=[1 0;0 1]; M1b=[1 0;0 1];
```

```
    M2=[1 x_LasPM;0 1];
    M3=[1 0;(-1/f_OAPM) 1];
    M4=[1 (x1(ind)-x_LasPM);0 1];
    M4e=[1 0;0 1]; M4c=[1 0;0 1]; M4d=[1 0;0 1]; M5=[1 0;0 1]; M7z=[1 0;0 1];
    M8=[1 0;0 1]; M9=[1 0;0 1];M10=[1 0;0 1];
    M=M10*M9*M8*M7z*M5*M4d*M4c*M4e*M4*M3*M2;
elseif ((x_LasPM+x_PMwind) <= x1(ind)) && (x1(ind) < (l_wind+x_LasPM + x_PMwind ))
    M1a=[1 0;0 1]; M1b=[1 0;0 1];
    M2=[1 x_LasPM;0 1];
    M3=[1 0;(-1/f_OAPM) 1];
    M4=[1 (x_PMwind);0 1];
    M4e=[1 0;0 n_air/n_CaF2];
    M4c=[1 (x1(ind)-x_LasPM-x_PMwind);0 1];
    M4d=[1 0;0 1]; M5=[1 0;0 1]; M7z=[1 0;0 1]; M8=[1 0;0 1]; M9=[1 0;0 1];
    M10=[1 0;0 1];
    M=M10*M9*M8*M7z*M5*M4d*M4c*M4e*M4*M3*M2;
elseif ((x_LasPM+x_PMwind) <= x1(ind)) & (x1(ind) < (l_wind+x_LasPM + x_PMlens ))
    M1a=[1 0;0 1]; M1b=[1 0;0 1];
    M2=[1 x_LasPM;0 1];
    M3=[1 0;(-1/f_OAPM) 1];
    M4=[1 (x_PMwind);0 1];
    M4e=[1 0;0 n_air/n_CaF2];
    M4c=[1 l_wind;0 1];
    M4d=[1 0;0 n_CaF2/n_air];
    M5=[1 x1(ind)-(l_wind+x_LasPM+x_PMwind);0 1];
    M7z=[1 0;0 1]; M8=[1 0;0 1]; M9=[1 0;0 1]; M10=[1 0;0 1];
    M=M10*M9*M8*M7z*M5*M4d*M4c*M4e*M4*M3*M2;
elseif ((x_LasPM+x_PMlens+l_wind) <= x1(ind))& (x1(ind) < (x_LasPM+x_PMlens
         +x_lensCav+l_wind))
    M1a=[1 0;0 1]; M1b=[1 0;0 1];
    M2=[1 x_LasPM;0 1];
    M3=[1 0;(-1/f_OAPM) 1];
    M4=[1 (x_PMwind);0 1];
    M4e=[1 0;0 n_air/n_CaF2];
    M4c=[1 l_wind;0 1];
    M4d=[1 0;0 n_CaF2/n_air];
    M5=[1 (x_PMlens-x_PMwind-l_wind);0 1];
    M7z=[1 0;-1/f_lens 1];%thin lens approximation
    M8=[1 (x1(ind)-(x_LasPM+x_PMlens+l_wind));0 1];
    M9=[1 0;0 1];M10=[1 0;0 1];
    M=M10*M9*M8*M7z*M5*M4d*M4c*M4e*M4*M3*M2;
elseif ((x_LasPM+x_PMlens+x_lensCav+l_wind)<=x1(ind))&(x1(ind) <(x_LasPM
         +x_PMlens+x_lensCav+l_M+l_wind))
    M1a=[1 0;0 1]; M1b=[1 0;0 1];
    M2=[1 x_LasPM;0 1];
    M3=[1 0;(-1/f_OAPM) 1];
    M4=[1 (x_PMwind);0 1];
    M4e=[1 0;0 n_air/n_CaF2];
    M4c=[1 l_wind;0 1];
    M4d=[1 0;0 n_CaF2/n_air];
    M5=[1 (x_PMlens-x_PMwind);0 1];
    M7z=[1 0;-1/f_lens 1];
    M8=[1 (x_lensCav);0 1];
    M9=[1 0;0 n_air/n_ZnSe];
```

```
M10=[1 x1(ind)-(x_lensCav+x_LasPM+x_PMlens+l_wind);0 1];
    M=M10*M9*M8*M7z*M5*M4d*M4c*M4e*M4*M3*M2;
else
    M1a=[1 0;0 1]; M1b=[1 0;0 1];
    M2=[1 x_LasPM;0 1];
    M3=[1 0;(-1/f_OAPM) 1];
    M4=[1 (x_PMwind);0 1];
    M4e=[1 0;0 n_air/n_CaF2];
    M4c=[1 l_wind;0 1];
    M4d=[1 0;0 n_CaF2/n_air];
    M5=[1 (x_PMlens-x_PMwind);0 1];
    M7z=[1 0;-1/f_lens 1];
    M8=[1 x_lensCav;0 1];
    M9=[1 0;0 n_air/n_ZnSe];
    M10=[1 l_M;0 1];%propagation first cavity mirror
    M=M10*M9*M8*M7z*M5*M4d*M4c*M4e*M4*M3*M2;
end
A=M(1,1);
B=M(1,2);
C=M(2,1);
D=M(2,2);
Q(ind)=1/((A*qo+B)/(C*qo+D));
Qr(ind)=real(Q(ind));
Qi(ind)=-1*imag(Q(ind));
w(ind)=sqrt(lambda/pi/Qi(ind));
R(ind)=1/Qr(ind);
if x1==f0
    Qq=1/((A*qo+B)/(C*qo+D));
    Qrq=real(Qq);
    Qiq=-1*imag(Qq);
    wq=sqrt(lambda/pi/Qiq);
    Rq=1/Qrq;
end
if x1==x_meas
    Qm=1/((A*qo+B)/(C*qo+D));
    Qrm=real(Qm);
    Qim=-1*imag(Qm);qm=1/Qm;
    wm=sqrt(lambda/pi/Qim);
    Rm=1/Qrm;
end
if x1==0.77
    Qm1=1/((A*qo+B)/(C*qo+D));
    Qm1r=real(Qm1);
    Qm1i=-1*imag(Qm1);
    qm1=1/Qm1;
    wm1=sqrt(lambda/pi/Qm1i);
    Rm1=1/Qm1r;
end
plot(x1(ind),w(ind),'g.')
hold on
end
xx=(-0.004:0.0001:0.0);
%resonant cavity beam(b)
%nonresonant from first (c) and second (a) reflection -- return pass
```

```
    for ind=1:length(xx)
%find q factor at front cavity mirror from resonant cavity properties
Rcav=0.5;
wcav=sqrt(lambda*0.5/pi/sqrt(1/.375-1));
qcav=(1/Rcav-5.3E-6*i/pi/wcav^2)^(-1);
M0b=[1 0.75/2;0 1];%propagation through half of cavity
M1b=[1 0;(n_air-n_ZnSe)/(-2*f_M*n_ZnSe) n_air/n_ZnSe];%refraction at curved surface
M2a=[1 x_LasPM;0 1];
M3a=[1 0;(-1/f_OAPM) 1];
M4a=[1 (x_PMwind);0 1];
M5a=[1 0;0 n_air/n_CaF2];
M6a=[1 l_wind;0 1];
M7a=[1 0;0 n_CaF2/n_air];
M8a=[1 (x_PMlens-x_PMwind);0 1];
M9a=[1 0;-1/f_lens 1];
M10a=[1 x_lensCav;0 1];
M11a=[1 0;0 n_air/n_ZnSe];
M11c=[1 0;0 1];
M12a=[1 l_M;0 1];
M13a=[1 0;1/f_M 1]; %reflection off surface 2
if xx(ind)>(0.77-l_M)
    M2b=[1 (0.77-xx(ind));0 1];%propagation through mirror
    M3b=[1 0;0 1]; M4b=[1 0;0 1]; M5b=[1 0;0 1]; M6b=[1 0;0 1]; M7b=[1 0;0 1];
    M8b=[1 0;0 1]; M9b=[1 0;0 1]; M10b=[1 0;0 1]; M11b=[1 0;0 1]; M12b=[1 0;0 1];
    M13b=[1 0;0 1];
elseif (xx(ind)<=(0.77-l_M))&&(xx(ind)>(0.77-l_M-x_lensCav))
    M2b=[1 l_M;0 1];
    M3b=[1 0;0 n_ZnSe/n_air];%refraction at flat surface of M1
    M4b=[1 (0.77-l_M-xx(ind));0 1];
    M5b=[1 0;0 1]; M6b=[1 0;0 1]; M7b=[1 0;0 1]; M8b=[1 0;0 1];
    M9b=[1 0;0 1]; M10b=[1 0;0 1]; M11b=[1 0;0 1]; M12b=[1 0;0 1]; M13b=[1 0;0 1];
    M14b=[1 0;0 1];
elseif (xx(ind)<=(0.77-l_M-x_lensCav))&&(xx(ind)>(0.77-l_M-x_lensCav-(x_PMlens
        -l_wind-x_PMwind)))
    M2b=[1 l_M;0 1];
    M3b=[1 0;0 n_ZnSe/n_air];
    M4b=[1 x_lensCav;0 1];
    M5b=[1 0;-1/f_lensrev 1];
    M6b=[1 (0.77-xx(ind)-l_M-x_lensCav);0 1];
    M7b=[1 0;0 1]; M8b=[1 0;0 1]; M9b=[1 0;0 1];
    M10b=[1 0;0 1]; M11b=[1 0;0 1]; M12b=[1 0;0 1]; M13b=[1 0;0 1];M14b=[1 0;0 1];
 elseif (xx(ind)<=(0.77-l_M-x_lensCav-(x_PMlens-l_wind-x_PMwind)))&&(xx(ind)>(0.77
        -l_M-x_lensCav-(x_PMlens-x_PMwind)))
    M2b=[1 l_M;0 1];
    M3b=[1 0;0 n_ZnSe/n_air];
    M4b=[1 x_lensCav;0 1];
    M5b=[1 0;-1/f_lensrev 1];
    M6b=[1 (x_PMlens-x_PMwind-l_wind);0 1];
    M7b=[1 0;0 n_air/n_CaF2];
    M8b=[1 (0.77-xx(ind)-l_M-(x_PMlens-x_PMwind-l_wind));0 1];
    M9b=[1 0;0 1]; M10b=[1 0;0 1]; M11b=[1 0;0 1]; M12b=[1 0;0 1]; M13b=[1 0;0 1];
    M14b=[1 0;0 1];
 elseif (xx(ind)<=(0.77-l_M-x_lensCav-(x_PMlens-x_PMwind)))&&(xx(ind)>(0.77-l_M
        -x_lensCav-x_PMlens))
```

```
    M2b=[1 l_M;0 1];
    M3b=[1 0;0 n_ZnSe/n_air];
    M4b=[1 x_lensCav;0 1];
    M5b=[1 0;-1/f_lensrev 1];
    M6b=[1 (x_PMlens-x_PMwind-l_wind);0 1];
    M7b=[1 0;0 n_air/n_CaF2];
    M8b=[1 l_wind;0 1];
    M9b=[1 0;0 n_CaF2/n_air];
    M10b=[1 (0.77-l_M-x_lensCav-xx(ind)-(x_PMlens-x_PMwind));0 1];
    M11b=[1 0;0 1]; M12b=[1 0;0 1]; M13b=[1 0;0 1];M14b=[1 0;0 1];
elseif (0<=xx(ind))&&(xx(ind)<=(0.77-l_M-x_lensCav-x_PMlens))
    M2b=[1 l_M;0 1];
    M3b=[1 0;0 n_ZnSe/n_air];
    M4b=[1 x_lensCav;0 1];
    M5b=[1 0;-1/f_lensrev 1];
    M6b=[1 (x_PMlens-x_PMwind-l_wind);0 1];
    M7b=[1 0;0 n_air/n_CaF2];
    M8b=[1 l_wind;0 1];
    M9b=[1 0;0 n_CaF2/n_air];
    M10b=[1 (x_PMwind);0 1];
    M11b=[1 0;-1/f_OAPM 1]; %reflection from oapm, reverse
    M12b=[1 (0.77-l_M-x_PMlens-x_lensCav-xx(ind));0 1]; M13b=[1 0;0 1];
M14b=[1 0;0 1];
elseif (xx(ind)<0)
    M2b=[1 l_M;0 1];
    M3b=[1 0;0 n_ZnSe/n_air];
    M4b=[1 x_lensCav;0 1];
    M5b=[1 0;-1/f_lensrev 1];
    M6b=[1 (x_PMlens-x_PMwind-l_wind);0 1];
    M7b=[1 0;0 n_air/n_CaF2];
    M8b=[1 l_wind;0 1];
    M9b=[1 0;0 n_CaF2/n_air];
    M10b=[1 (x_PMwind);0 1];
    M11b=[1 0;-1/f_OAPM 1]; %reflection from oapm, reverse
    M12b=[1 (0.77-l_M-x_PMlens-x_lensCav-xx(ind));0 1];
    M13b=[1 0;-1/f_coll 1];M14b=[1 -xx(ind);0 1];

end
Mb=M14b*M13b*M12b*M11b*M10b*M9b*M8b*M7b*M6b*M5b*M4b*M3b*M2b*M1b*M0b;
Ma=M14b*M13b*M12b*M11b*M10b*M9b*M8b*M7b*M6b*M5b*M4b*M3b*M2b*M13a*M12a*M11a*M10a*M9a*M8a
     *M7a*M6a*M5a*M4a*M3a*M2a;
Mc=M14b*M13b*M12b*M11b*M10b*M9b*M8b*M7b*M6b*M5b*M4b*M11c*M10a*M9a*M8a*M7a*M6a*M5a
     *M4a*M3a*M2a;
Ab=Mb(1,1); Aa=Ma(1,1); Ac=Mc(1,1);
Bb=Mb(1,2); Ba=Ma(1,2); Bc=Mc(1,2);
Cb=Mb(2,1); Ca=Ma(2,1); Cc=Mc(2,1);
Db=Mb(2,2); Da=Ma(2,2); Dc=Mc(2,2);
Qb(ind)=1/((Ab*qcav+Bb)/(Cb*qcav+Db));
Qa(ind)=1/((Aa*qo+Ba)/(Ca*qo+Da));
Qc(ind)=1/((Ac*qo+Bc)/(Cc*qo+Dc));
Qrb(ind)=real(Qb(ind)); Qra(ind)=real(Qa(ind)); Qrc(ind)=real(Qc(ind));
Qib(ind)=-1*imag(Qb(ind)); Qia(ind)=imag(Qa(ind))*-1; Qic(ind)=imag(Qc(ind))*-1;
wb(ind)=sqrt(lambda/pi/Qib(ind)); wa(ind)=sqrt(lambda/pi/Qia(ind));
wc(ind)=sqrt(lambda/pi/Qic(ind));
```

```
Rb(ind)=1/Qrb(ind); Ra(ind)=1/Qra(ind); Rc(ind)=1/Qrc(ind);
if xx==f2
   Qbb=1/((Ab*qcav+Bb)/(Cb*qcav+Db));
Qrbb=real(Qbb);
Qibb=-1*imag(Qbb);qbb=1/Qbb;
wbb=sqrt(lambda/pi/Qibb);
Rbb=1/Qrbb;
end
if xx==f1
    Qaa=1/((Aa*qo+Ba)/(Ca*qo+Da));
    Qraa=real(Qaa);
    Qiaa=-1*imag(Qaa);qaa=1/Qaa;
    waa=sqrt(lambda/pi/Qiaa);
    Raa=1/Qraa;
end
if xx==f3
    Qcc=1/((Ac*qo+Bc)/(Cc*qo+Dc));
    Qrcc=real(Qcc);
    Qicc=-1*imag(Qcc);qcc=1/Qcc;
    wcc=sqrt(lambda/pi/Qicc);
    Rcc=1/Qrcc;
end
if xx==x_meas
    Qbm=1/((Ab*qcav+Bb)/(Cb*qcav+Db));
    Qrbm=real(Qbm);
    Qibm=-1*imag(Qbm);qbm=1/Qbm;
    wbm=sqrt(lambda/pi/Qibm);
    Rbm=1/Qrbm;
    Qam=1/((Aa*qo+Ba)/(Ca*qo+Da));
    Qram=real(Qam);
    Qiam=-1*imag(Qam);qam=1/Qam;
    wam=sqrt(lambda/pi/Qiam);
    Ram=1/Qram;
    Qcm=1/((Ac*qo+Bc)/(Cc*qo+Dc));
    Qrcm=real(Qcm);
    Qicm=-1*imag(Qcm);qcm=1/Qcm;
    wcm=sqrt(lambda/pi/Qicm);
    Rcm=1/Qrcm;
end
plot(xx(ind),wa(ind),'b.',...
   xx(ind),wb(ind),'r.',...
   xx(ind),wc(ind),'k.')
hold on
    end
```

Bibliography

1. R. Boyle, "Suspicions about some Hidden Qualities in the AIR," in *Tracts*, pp. 1–51, London: printed by W.G. and are to be sold by M. Pitt, 1674–1675.
2. E. Moser and M. McCulloch, "Canine scent detction of human cancers: A review of methods and accuracy," *J. Vet. Behav.*, vol. 5, pp. 145–152, 2010.
3. J. A. Shaw, N. L. Seldomridge, D. L. Dunkle, P. W. Nugent, L. H. Spangler, J. J. Bromenshank, C. B. Henderson, J. H. Churnside, and J. J. Wilson, "Polarization lidar measurements of honey bees in flight for locating land mines," *Opt. Exp.*, vol. 13, pp. 5853–5863, 2005.
4. P. Newswire, "Gas sensors market is expected to reach USD 2.32 billion globally in 2018: Transparency Market Research," July 2013.
5. J. M. Hollas, *Modern Spectroscopy.* Hoboken, New Jersey: Wiley, 4th ed., 2004.
6. L. S. Rothman, I. E. Gordon, Y. Babikov, A. Barbe, D. Chris Benner, P. F. Bernath, M. Birk, L. Bizzocchi, V. Boudon, L. R. Brown, A. Campargue, K. Chance, E. A. Cohen, L. H. Coudert, V. M. Devi, B. J. Drouin, A. Fayt, J.-M. Flaud, R. R. Gamache, J. J. Harrison, J.-M. Hartmann, C. Hill, J. T. Hodges, D. Jacquemart, A. Jolly, J. Lamouroux, R. J. LeRoy, D. Long, O. M. Lyulin, C. J. Mackie, S. T. Massie, S. Mikhailenko, H. S. P. Müller, O. V. Naumenko, A. V. Nikitin, J. Orphal, V. Perevalov, A. Perrin, E. R. Polovtseva, and C. Richard, "The HITRAN2012 molecular spectroscopic database," *J. Quant. Spectrosc. Radiat. Transfer*, vol. 130, pp. 4–50, 2013.
7. L. Galatry, "Simultaneous effect of doppler and foreign gas broadening on spectral lines," *Phys. Rev.*, vol. 122, pp. 1218–1223, 1961.
8. J. I. Steinfeld, *Molecules and Radiation: An Introduction to Modern Molecular Spectroscopy.* Mineola, New York: Dover, 2 ed., 1985.
9. D. H. Sliney and B. C. Freasier, "Evaluation of optical radiation hazards," *Appl. Opt.*, vol. 12, pp. 1–24, 1973.
10. O. Svelto and D. Hanna *(transl.)*, *Principles of Lasers.* New York: Plenum Press, 4 ed., 1998.
11. C. C. Davis, *Lasers and Electro-optics: Fundamentals and Engineering.* Cambridge: Cambridge University Press, 2 ed., 2014.
12. M. Olson, "History of laser weapon research," *Leading Edge*, vol. 7, pp. 26–35, 2012.
13. R. N. Hall, G. E. Fenner, J. D. Kingsley, T. J. Soltys, and R. O. Carlson, "Coherent light emission from GaAs junctions," *Phys. Rev. Lett.*, vol. 9, pp. 366–368, 1962.
14. Z. Alverov, "Double heterostructure lasers: early days and future perspectives," *IEEE J. Sel. Top. Quantum Electron.*, vol. 6, pp. 832–840, 2000.
15. M. B. Panish, I. Hayashi, and S. Sumski, "Double-heterostructure injection lasers with room-temperature thresholds as low as 2300 A/cm^2," *Appl. Phys. Lett.*, vol. 16, pp. 326–328, 1970.
16. M. Tacke, "Lead-salt lasers," *Phil. Trans. R. Soc. Lond. A*, vol. 359, pp. 547–566, 2001.
17. A. S. Pine, "Doppler-limited molecular spectroscopy by differency-frequency mixing," *J. Opt. Soc. Am.*, vol. 64, pp. 1683–1690, 1974.
18. D. Richter, A. Fried, and P. Weibring, "Difference frequency generation laser based spectrometers," *Laser Photonics Rev.*, vol. 3, pp. 343–354, 2009.
19. Tran-Ba-Chu and M. Broyer, "Intracavity cw difference frequency generation by mixing three photons and using Gaussian laser beams," *J. de Physique*, vol. 46, pp. 523–533, 1985.
20. L. Ciaffoni, R. Grilli, G. Hancock, A. J. Orr-Ewing, R. Peverall, and G. A. D. Ritchie, "3.5-μm high-resolution gas sensing employing a $LiNbO_3$ QPM-DFG waveguide module," *Appl. Phys.*

B, vol. 94, pp. 517–525, 2008.
21. W. C. Eckhoff, R. S. Putnam, S. Wang, R. F. Curl, and F. K. Tittel, "A continuously tunable long-wavelength cw IR source for high-resolution spectroscopy and trace-gas detection," *Appl. Phys. B*, vol. 63, pp. 437–441, 1996.
22. P. Gross, M. Klein, K.-J. Boller, M. Auerbach, P. Wessels, and C. Fallnich, "Fiber-laser-pumped continuous-wave singly resonant optical parametric oscillator," *Opt. Lett.*, vol. 27, pp. 418–420, 2002.
23. T. Sloanes, K. McEwan, B. Lowans, and L. Michaille, "Optimisation of high average power optical parametric generation using a photonic crystal fiber," *Opt. Exp.*, vol. 16, pp. 19724–19733, 2008.
24. Y. Q. Xu, K. F. Mak, and S. G. Murdoch, "Multiwatt level output powers from a tunable fiber optical parametric oscillator," *Opt. Lett.*, vol. 36, pp. 1966–1968, 2011.
25. R. F. Kazarinov and R. A. Suris, "Possibility of the amplification of electromagnetic waves in a semiconductor with a superlattice," *Sov. Phys. – Semiconductors*, vol. 5, pp. 707–709, 1971.
26. J. Faist, F. Capasso, D. L. Sivco, C. Sirtori, L. Albert, A. Y. Cho, and Y. Cho, "Quantum cascade laser," *Science*, vol. 264, pp. 553–556, 1994.
27. J. Faist, F. Capasso, C. Sirtori, D. L. Sivco, A. L. Hutchinson, and A. Y. Cho, "Continuous wave operation of a vertical transition quantum cascade laser above T=80 K," *Appl. Phys. Lett*, vol. 67, p. 3057, 1995.
28. J. Faist, F. Capasso, C. Sirtori, D. L. Sivco, J. N. Baillargeon, A. L. Hutchinson, S.-N. G. Chu, and A. Y. Cho, "High power mid-infrared ($\lambda \sim 5\mu$m) quantum cascade lasers operating above room temperature," *Appl. Phys. Lett.*, vol. 68, p. 3680, 1996.
29. M. Beck, D. Hofstetter, T. Aellen, J. Faist, U. Oesterle, M. Ilegems, E. Gini, and H. Melchior, "Continuous wave operation of a mid-infrared semiconductor laser at room temperature," *Science*, vol. 295, pp. 301–5, 2002.
30. Y. Yao, A. J. Hoffman, and C. F. Gmachl, "Mid-infrared quantum cascade lasers," *Nat. Photonics*, vol. 6, pp. 432–439, 2012.
31. R. W. Waynant, I. K. Ilev, and I. Gannot, "Mid-infrared laser applications in medicine and biology," *Phil. Trans. Soc. Lond. A*, vol. 359, pp. 635–644, 2001.
32. J. H. Northern, A. W. J. Thompson, M. L. Hamilton, and P. Ewart, "Multi-species detection using multi-mode absorption spectroscopy (MUMAS)," *Appl. Phys. B*, vol. 111, pp. 627–637, 2013.
33. F. Capasso, C. Gmachl, R. Paiella, A. Tredicucci, A. L. Hutchinson, D. L. Sivco, J. N. Baillargeon, A. Y. Cho, and H. C. Liu, "New frontiers in quantum cascade lasers and applications," *IEEE J. Quantum Electron.*, vol. 6, pp. 931–947, 2000.
34. G. Hancock, "Applications of midinfrared quantum cascade lasers to spectroscopy," *Opt. Eng.*, vol. 49, p. 111121, 2010.
35. A. E. Siegman, *Lasers*. Sausalito, California: University Science Books, 1986.
36. R. M. Williams, J. F. Kelly, J. S. Hartman, S. W. Sharpe, M. S. Taubman, J. L. Hall, F. Capasso, C. Gmachl, D. L. Sivco, J. N. Baillargeon, and A. Y. Cho, "Kilohertz linewidth from frequency-stabilized mid-infrared quantum cascade lasers," *Opt. Lett.*, vol. 24, pp. 1844–1846, 1999.
37. M. S. Taubman, T. L. Myers, B. D. Cannon, and R. M. Williams, "Stabilization, injection and control of quantum cascade lasers, and their application to chemical sensing in the infrared," *Spectrochim. Acta A*, vol. 60, pp. 3457–68, 2004.
38. K. Krishnaswami, B. E. Bernacki, B. D. Cannon, N. Hô, and N. C. Anheier, "Emission and propagation properties of midinfrared quantum cascade lasers," *IEEE Photon. Technol. Lett.*, vol. 20, pp. 306–308, 2008.
39. A. Hugi, R. Maulini, and J. Faist, "External cavity quantum cascade laser," *Semicond. Sci. Technol.*, vol. 25, p. 083001, 2010.
40. J. Devenson, D. Barate, O. Cathabard, R. Teissier, and A. N. Baranov, "Very short wavelength ($\lambda = 3.1 - 3.3$ μm) quantum cascade lasers," *Appl. Phys. Lett.*, vol. 89, p. 191115, 2006.
41. N. Bandyopadhyay, Y. Bai, S. Tsao, S. Nida, S. Slivken, and M. Razeghi, "Room temperature continuous wave operation of $\lambda = 3 - 3.2$ μm quantum cascade lasers," *Appl. Phys. Lett.*,

vol. 101, p. 241110, 2012.
42. I. Vurgaftman, R. Weih, M. Kamp, J. R. Meyer, C. L. Canedy, C. S. Kim, M. Kim, W. W. Bewley, C. D. Merritt, J. Abell, and S. Höfling, "Interband cascade lasers," *J. Phys. D: Appl. Phys.*, vol. 48, p. 123001, 2015.
43. R. Q. Yang, "Infrared laser based on intersubband transitions in quantum wells," *Superlattices and Microstruct.*, vol. 17, pp. 77–83, 1995.
44. J. R. Meyer, I. Vurgaftman, R. Q. Yang, and L. R. Ram-Mohan, "Type-II and type-I interband cascade lasers," *Electron. Lett.*, vol. 32, pp. 45–46, 1996.
45. R. Q. Yang, C. J. Hill, and B. H. Yang, "High-temperature and low-threshold midinfrared interband cascade lasers," *Appl. Phys. Lett.*, vol. 87, p. 151109, 2005.
46. M. Kim, C. L. Canedy, W. W. Bewley, C. S. Kim, J. R. Lindle, J. Abell, I. Vurgaftman, and J. R. Meyer, "Interband cascade laser emitting at $\lambda = 3.75$ μm in continuous wave above room temperature," *Appl. Phys. Lett.*, vol. 92, p. 191110, 2008.
47. C. L. Canedy, W. W. Bewley, J. R. Lindle, C. S. Kim, M. Kim, I. Vurgaftman, and J. R. Meyer, "Investigation of mid-infrared type-II "W" diode lasers," *J. Electron. Mater.*, vol. 35, pp. 453–461, 2006.
48. I. Vurgaftman, W. W. Bewley, C. L. Canedy, C. S. Kim, M. Kim, J. Ryan Lindle, C. D. Merritt, J. Abell, and J. R. Meyer, "Mid-IR type-II interband cascade lasers," *IEEE J. Quantum Electron.*, vol. 17, pp. 1435–1444, 2011.
49. J. Piotrowski and A. Rogalski, "Uncooled long wavelength infrared photon detectors," *Infrared Phys. Technol.*, vol. 46, pp. 115–131, 2004.
50. D. Allan, "Statistics of atomic frequency standards," *P. IEEE*, vol. 54, pp. 221–230, 1966.
51. P. Werle, R. Miicke, and F. Slemr, "The limits of signal averaging in atmospheric trace-gas monitoring by tunable diode-laser absorption spectroscopy (TDLAS)," *Appl. Phys. B*, vol. 57, pp. 131–139, 1993.
52. E. J. Moyer, D. S. Sayres, G. S. Engel, J. M. St. Clair, F. N. Keutsch, N. T. Allen, J. H. Kroll, and J. G. Anderson, "Design considerations in high-sensitivity off-axis integrated cavity output spectroscopy," *Appl. Phys. B*, vol. 92, pp. 467–474, 2008.
53. J. Taylor, *An Introduction to Error Analysis: The Study of Uncertainties in Physical Measurements*. Sausalito, California: University Science Books, 2 ed., 1997.
54. C. A. Northend, R. C. Honey, and W. E. Evans, "Laser radar (LIDAR) for meteorological studies," *Rev. Sci. Instr.*, vol. 37, pp. 393–400, 1966.
55. P. Weibring, H. Edner, and S. Svanberg, "Versatile mobile lidar system for environmental monitoring," *Appl. Opt.*, vol. 42, pp. 3583–3594, 2003.
56. J. U. White, "Long optical paths of large aperture," *J. Opt. Soc. Am.*, vol. 32, pp. 285–288, 1942.
57. D. R. Herriott and H. J. Schulte, "Folded optical delay lines," *Appl. Opt.*, vol. 4, pp. 883–889, 1965.
58. J. A. Silver, "Simple dense-pattern optical multipass cells," *Appl. Opt.*, vol. 44, pp. 6545–6556, 2005.
59. J. A. Silver, "Frequency-modulation spectroscopy for trace species detection: theory and comparison among experimental methods," *Appl. Opt.*, vol. 31, p. 4927, 1992.
60. A. Rosencwaig, "Photoacoustics and Photoacoustic Spectroscopy," in *Chemical Analysis* (P. J. Elving, J. D. Winefordner, and I. M. Kolthoff, eds.), New York: John Wiley & Sons, 1980.
61. B. A. Paldus, T. G. Spence, R. N. Zare, J. Oomens, F. J. Harren, D. H. Parker, C. Gmachl, F. Cappasso, D. L. Sivco, J. N. Baillargeon, A. L. Hutchinson, and A. Y. Cho, "Photoacoustic spectroscopy using quantum-cascade lasers," *Opt. Lett.*, vol. 24, pp. 178–80, 1999.
62. D. Hofstetter, M. Beck, J. Faist, M. Nägele, and M. W. Sigrist, "Photoacoustic spectroscopy with quantum cascade distributed-feedback lasers," *Opt. Lett.*, vol. 26, pp. 887–9, 2001.
63. A. A. Kosterev, Y. A. Bakhirkin, R. F. Curl, and F. K. Tittel, "Quartz-enhanced photoacoustic spectroscopy," *Opt. Lett.*, vol. 27, pp. 1902–4, 2002.
64. N. Petra, J. Zweck, A. A. Kosterev, S. E. Minkoff, and D. Thomazy, "Theoretical analysis of a quartz-enhanced photoacoustic spectroscopy sensor," *Appl. Phys. B*, vol. 94, pp. 673–680, 2009.

65. H. Ganser, W. Urban, and J. M. Brown, "The sensitive detection of NO by Faraday modulation spectroscopy with a quantum cascade laser," *Mol. Phys.*, vol. 101, pp. 545–550, 2002.
66. J. Westberg, L. Lathdavong, C. M. Dion, J. Shao, P. Kluczynski, S. Lundqvist, and O. Axner, "Quantitative description of Faraday modulation spectrometry in terms of the integrated linestrength and 1st Fourier coefficients of the modulated lineshape function," *J. Quant. Spectrosc. Radiat.*, vol. 111, pp. 2415–2433, 2010.
67. J. Ye, L. Ma, and J. Hall, "Ultrasensitive detections in atomic and molecular physics: demonstration in molecular overtone spectroscopy," *J. Opt. Soc. Am. B*, vol. 15, pp. 6–15, 1998.
68. O. Axner, P. Ehlers, A. Foltynowicz, I. Silander, and J. Wang, "NICE-OHMS – Frequency Modulation Cavity-Enhanced Spectroscopy – Principles and Performance," in *Cavity-Enhanced Spectroscopy and Sensing* (G. Gagliardi and H.-P. Loock, eds.), vol. 179 of *Springer Series in Optical Sciences*, pp. 211–251, Springer Berlin Heidelberg, 2014.
69. R. N. Zare and P. J. Dagdigian, "Tunable laser fluorescence method for product state analysis," *Science*, vol. 185, pp. 739–747, 1974.
70. D. Creasey, P. A. Halford-Maw, D. E. Heard, M. J. Pilling, and B. J. Whitaker, "Implementation and initial deployment of a field instrument for measurement of OH and HO_2 in the troposphere by laser-induced fluorescence," *J. Chem. Soc., Faraday Trans.*, vol. 93, pp. 2907–2913, 1997.
71. R. F. Begley, A. B. Harvey, and R. L. Byer, "Coherent anti-Stokes Raman spectroscopy," *Appl. Phys. Lett.*, vol. 25, pp. 387–390, 1974.
72. J. J. Valentini, "Coherent Anti-Stokes Raman Spectroscopy," in *Spectrometric Techniques: Volume IV* (G. Vanasse, ed.), pp. 2–59, Orlando, Florida, USA: Academic Press, 1985.
73. D. Smith and P. Španěl, "Selected ion flow tube mass spectrometry (SIFT-MS) for on-line trace gas analysis," *Mass Spec. Rev.*, vol. 24, pp. 661–700, 2004.
74. R. Blake, P. Monks, and A. Ellis, "Proton-transfer reaction mass spectrometry," *Chem. Rev.*, vol. 109, pp. 861–896, 2009.
75. W. Lindinger, A. Hansel, and A. Jordan, "On-line monitoring of volatile organic compounds at pptv levels by means of proton-transfer-reaction mass spectrometry (PTR-MS) medical applications, food control and environmental research," *Int. J. Mass Spectrom. Ion Processes*, vol. 173, pp. 191–241, 1998.
76. C. N. Hewitt, S. Hayward, and A. Tani, "The application of proton transfer reaction-mass spectrometry (PTR-MS) to the monitoring and analysis of volatile organic compounds in the atmosphere," *J. Environ. Monit.*, vol. 5, pp. 1–7, 2002.
77. P. Španěl and D. Smith, "Progress in SIFT-MS: Breath analysis and other applications," *Mass Spectrom. Rev.*, vol. 30, pp. 236–267, 2010.
78. G. W. Santoni, B. H. Lee, J. P. Goodrich, R. K. Varner, P. M. Crill, J. B. McManus, D. D. Nelson, M. S. Zahniser, and S. C. Wofsy, "Mass fluxes and isofluxes of methane (CH_4) at a New Hampshire fen measured by a continuous wave quantum cascade laser spectrometer," *J. Geophys. Res.: Atmos.*, vol. 117, p. D10301, 2012.
79. E. Roth, P. Gunkel-Grillon, L. Joly, X. Thomas, T. Decarpenterie, I. Mappe-Fogaing, C. Laporte-Magoni, N. Dumelié, and G. Durry, "Impact of raw pig slurry and pig farming practices on physicochemical parameters and on atmospheric N_2O and CH_4 emissions of tropical soils, Uvéa Island (South Pacific)," *Env. Sci. Pollut. Res.*, vol. 21, pp. 10022–10035, 2014.
80. D. R. Hastie and M. D. Miller, "Balloon-borne tunable diode laser absorption spectrometer for multispecies trace gas measurements in the stratosphere," *Appl. Opt.*, vol. 24, pp. 3694–3701, 1985.
81. D. C. Scott, R. L. Herman, C. R. Webster, R. D. May, G. J. Flesch, and E. J. Moyer, "Airborne laser infrared absorption spectrometer (ALIAS-II) for *in situ* atmospheric measurements of N_2O, CH_4, CO, HCl, and NO_2 from balloon or remotely piloted aircraft platforms," *Appl. Opt.*, vol. 38, pp. 4609–4622, 1999.
82. C. R. Webster, G. J. Flesch, D. C. Scott, J. E. Swanson, R. D. May, W. S. Woodward, C. Gmachl, F. Capasso, D. L. Sivco, J. N. Baillargeon, A. L. Hutchinson, and A. Y. Cho, "Quantum-cascade laser measurements of statospheric methane and nitrous oxide," *Appl. Opt.*, vol. 40, pp. 321–326, 2001.

83. D. S. Sayres, E. J. Moyer, T. F. Hanisco, J. M. St Clair, F. N. Keutsch, A. O'Brien, N. T. Allen, L. Lapson, J. N. Deusz, M. Rivero, T. Martin, M. Greenberg, C. Tuozzolo, O. S. Engel, J. H. Kroll, J. B. Paul, and J. G. Anderson, "A new cavity based absorption instrument for detection of water isotopologues in the upper troposphere and lower stratosphere," *Rev. Sci. Instrum.*, vol. 80, p. 044102, 2009.
84. A. Khan, D. Schaefer, D. J. Tao, L. Miller, K. Sun, M. A. Zondio, W. A. Harrison, B. Roscoe, and D. J. Lary, "Low power greenhouse gas sensors for unmanned aerial vehicles," *Remote Sensing*, vol. 4, pp. 1355–1368, 2012.
85. P. D. Mudgett and J. S. Pilgrim, "Multi-Gas Monitor," tech. rep., NASA, April 2015. www.nasa.gov/mission_pages/station/research/experiments/1187.html.
86. M. W. Todd, R. A. Provencal, T. G. Owano, B. A. Paldus, A. Kachanov, K. L. Vodopyanov, M. Hunter, S. L. Coy, J. I. Steinfeld, and J. T. Arnold, "Application of mid-infrared cavity-ringdown spectroscopy to trace explosives vapor detection using a broadly tunable (6–8 μm) optical parametric oscillator," *Appl. Phys. B*, vol. 75, pp. 367–376, 2002.
87. H. Dahnke, D. Kleine, P. Hering, and M. Mürtz, "Real-time monitoring of ethane in human breath using mid-infrared cavity leak-out spectroscopy," *Appl. Phys. B*, vol. 72, pp. 971–975, 2001.
88. C. Roller, A. A. Kosterev, F. K. Tittel, K. Uehara, C. Gmachl, and D. L. Sivco, "Carbonyl sulfide detection with a thermoelectrically cooled midinfrared quantum cascade laser," *Opt. Lett.*, vol. 28, pp. 2052–2054, 2003.
89. Y. A. Bakhirkin, A. A. Kosterev, C. Roller, R. F. Curl, and F. K. Tittel, "Mid-infrared quantum cascade laser based off-axis integrated cavity output spectroscopy for biogenic nitric oxide detection," *Appl. Opt.*, vol. 43, pp. 2257–66, 2004.
90. I. Ventrillard-Courtillot, T. Gonthiez, C. Clerici, and D. Romanini, "Multispecies breath analysis faster than a single respiratory cycle by optical-feedback cavity-enhanced absorption spectroscopy," *J. Biomed. Opt.*, vol. 14, p. 064026, 2009.
91. L. Ciaffoni, G. Hancock, J. J. Harrison, J.-P. H. van Helden, C. E. Langley, R. Peverall, G. A. D. Ritchie, and S. Wood, "Demonstration of a mid-infrared cavity enhanced absorption spectrometer for breath acetone detection," *Anal. Chem.*, vol. 85, pp. 846–50, 2013.
92. K. Worle, F. Seichter, A. Wilk, C. Armacost, T. Day, M. Godejohann, U. Wachter, J. Vogt, P. Radermacher, and B. Mizaikoff, "Breath analysis with broadly tunable quantum cascade lasers," *Anal. Chem.*, vol. 85, pp. 2697–2702, 2013.
93. N. Lang, J. Röpcke, S. Wege, and A. Steinbach, "In situ diagnostic of etch plasmas for process control using quantum cascade laser absorption spectroscopy," *Eur. Phys. J. Appl. Phys.*, vol. 49, p. 13110, 2010.
94. C. Wang and P. Sahay, "Breath analysis using laser spectroscopic techniques: breath biomarkers, spectral fingerprints, and detection limits," *Sensors*, vol. 9, pp. 8230–8262, 2009.
95. T. H. Risby and F. K. Tittel, "Current status of midinfrared quantum and interband cascade lasers for clinical breath analysis," *Opt. Eng.*, vol. 49, p. 111123, 2010.
96. G. E. De Benedetto, R. Laviano, L. Sabbatini, and P. G. Zambonin, "Infrared spectroscopy in the mineralogical characterization of ancient pottery," *J. Cultural Heritage*, vol. 3, pp. 177–186, 2002.
97. D. Richter, M. Erdelyi, R. Curl, F. K. Tittel, C. Oppenheimer, H. J. Duffell, and M. Burton, "Field measurements of volcanic gases using tunable diode laser based mid-infrared and Fourier transform infrared spectrometers," *Opt. Laser Eng.*, vol. 37, pp. 171–186, 2002.
98. A. Kher, S. Stewart, and M. Mulholland, "Forensic classification of paper with infrared spectroscopy and principal components analysis," *J. Near Infrared Spectr.*, vol. 13, pp. 225–229, 2005.
99. A. Kher, M. Mulholland, E. Green, and B. Reedy, "Forensic classification of ballpoint inks using high performance liquid chromatography and infrared spectroscopy with principal components analysis and linear discriminant analysis," *Vibrational Spectr.*, vol. 40, pp. 270–277, 2006.
100. N. J. Crane, E. G. Bartick, R. Schwartz Perlman, and S. Huffman, "Infrared spectroscopic imaging for noninvasive detection of latent fingerprints," *J. Forensic Sci.*, vol. 52, pp. 48–53, 2007.

101. R. Karoui, G. Downey, and C. Blecher, "Mid-infrared spectroscopy coupled with chemometrics: a tool for the analysis of intact food systems and exploration of their molecular structure-quality relationships – a review," *Chem. Rev.*, vol. 110, pp. 6144–6165, 2010.
102. D. Cozzolino, E. Corbella, and H. E. Smyth, "Quality control of honey using infrared spectroscoyp – a review," *Appl. Spectr. Rev.*, vol. 46, pp. 523–538, 2011.
103. T. Stocker, D. Qin, G.-K. Plattner, L. Alexander, S. Allen, N. Bindoff, F.-M. Bréon, J. Church, U. Cubasch, S. Emori, P. Forster, P. Friedlingstein, N. Gillett, J. Gregory, D. Hartmann, E. Jansen, B. Kirtman, R. Knutti, K. Krishna Kumar, P. Lemke, J. Marotzke, V. Masson-Delmotte, G. Meehl, I. Mokhov, S. Piao, V. Ramaswamy, D. Randall, M. Rhein, M. Rojas, C. Sabine, D. Shindell, L. Talley, D. Vaughan, and S.-P. Xie, "Technical Summary," in *Climate Change 2013: The Physical Science Basis. Contribution of Working Group I to the Fifth Assessment Report of the Intergovernmental Panel on Climate Change* (T. Stocker, D. Qin, G.-K. Plattner, M. Tignor, S. Allen, J. Boschung, A. Nauels, Y. Xia, V. Bex, and P. Midgley, eds.), Cambridge, UK and New York, NY, USA: Cambridge University Press, 2013.
104. D. S. Bomse, A. C. Stanton, and J. A. Silver, "Frequency modulation and wavelength modulation spectroscopies: comparison of experimental methods using a lead-salt diode laser," *Appl. Opt.*, vol. 31, p. 718, 1992.
105. A. Hida, Y. Mera, and K. Maeda, "Electric field modulation spectroscopy by scanning tunneling microscopy with a nanometer-scale resolution," *Appl. Phys. Lett.*, vol. 78, p. 3029, 2001.
106. P. M. Selzer and W. M. Yen, "High-speed light chopper wheel for modulation spectroscopy," *Rev. Sci. Instrum.*, vol. 47, p. 749, 1976.
107. G. Bonfiglioli and P. Brovetto, "Principles of self-modulating derivative optical spectroscopy," *Appl. Opt.*, vol. 3, pp. 1417–1425, 1964.
108. G. Bjorklund, "Frequency-modulation spectroscopy: a new method for measuring weak absorptions and dispersions," *Opt. Lett.*, vol. 5, pp. 15–17, 1980.
109. G. C. Bjorklund, M. D. Levenson, W. Lenth, and C. Ortiz, "Frequency modulation (FM) spectroscopy," *Appl. Phys. B*, vol. 32, pp. 145–152, 1983.
110. J. M. Supplee, E. A. Whittaker, and W. Lenth, "Theoretical description of frequency modulation and wavelength modulation spectroscopy," *Appl. Opt.*, vol. 33, pp. 6294–6302, 1994.
111. W. Lenth, "Optical heterodyne spectroscopy with frequency- and amplitude-modulated semiconductor lasers," *Opt. Lett.*, vol. 8, pp. 575–577, 1983.
112. W. Lenth, "High frequency heterodyne spectroscopy with current-modulated diode lasers," *IEEE J. Quantum Electron.*, vol. QE-20, pp. 1045–1050, 1984.
113. W. Lenth and M. Gehrtz, "Sensitive detection of NO_2 using high-frequency heterodyne spectroscopy with a GaAlAs diode laser," *Appl. Phys. Lett.*, vol. 47, pp. 1263–1266, 1985.
114. M. Gehrtz, A. T. Young, H. S. Johnston, and W. Lenth, "High-frequency-modulation spectroscopy with a lead-salt diode laser," *Opt. Lett.*, vol. 11, pp. 132–134, 1986.
115. C. B. Carlisle, D. E. Cooper, and H. Preier, "Quantum noise-limited FM spectroscopy with a lead-salt diode laser," *Appl. Opt.*, vol. 28, pp. 2567–2575, 1989.
116. J. A. C. Weideman, "Computing the Hilbert Transform on the Real Line," *Mathematics of Computation*, vol. 64, pp. 745–762, 1995.
117. D. E. Cooper and R. E. Warren, "Frequency modulation spectroscopy with lead-salt diode lasers: a comparison of single-tone and two-tone techniques," *Appl. Opt.*, vol. 26, pp. 3726–3732, 1987.
118. J. Reid and D. Labrie, "Second-harmonic detection with tunable diode lasers – comparison of experiment and theory," *Appl. Phys. B*, vol. 26, pp. 204–210, 1981.
119. E. I. Moses and C. L. Tang, "High-sensitivity laser wavelength-modulation spectroscopy," *Opt. Lett.*, vol. 1, pp. 115–117, 1977.
120. Stanford Research Systems, Inc., Sunnyvale, CA, USA, *Model SR810 DSP Lock-in Amplifier*, 1.8 ed., 2005.
121. T. Yanagawa, S. Saito, and Y. Yamamoto, "Frequency stabilization of 1.5 μm InGaAsP distributed feedback laser to NH_3 absorption lines," *Appl. Phys. Lett.*, vol. 45, p. 826, 1984.
122. H. Richter, S. G. Pavlov, A. D. Semenov, L. Mahler, A. Tredicucci, H. E. Beere, D. A. Ritchie, and H. W. Hubers, "Submegahertz frequency stabilization of a terahertz quantum cascade laser

to a molecular absorption line," *Appl. Phys. Lett.*, vol. 96, p. 3, 2010.
123. A. G. V. Bergin, *Applications of Optical-Feedback Cavity-Enhanced Absorption Spectroscopy.* PhD thesis, University of Oxford, 2013.
124. K. Pierściński, D. Pierścińska, M. Iwińska, K. Kosiel, A. Szerling, P. Karbownik, and M. Bugajski, "Investigation of thermal properties of mid-infrared AlGaAs/GaAs quantum cascade lasers," *J. Appl. Phys.*, vol. 112, p. 043112, 2012.
125. F. M. O'Connor, O. Boucher, N. Gedney, C. D. Jones, G. A. Folberth, R. Coppell, P. Friedlingstein, W. J. Collins, J. Chappellaz, J. Ridley, and C. E. Johnson, "Possible role of wetlands, permafrost, and methane hydrates in the methane cycle under future climate change: A review," *Rev. Geophys.*, vol. 48, p. RG4005, 2010.
126. L. F. McKay, M. A. Eastwood, and W. G. Brydon, "Methane excretion in man – a study of breath, flatus, and faeces," *Gut*, vol. 26, pp. 69–74, 1985.
127. H. A. Jahn, "A new Coriolis perturbation in the methane spectrum. I. Vibrational-rotational Hamiltonian and wave functions," *Proc. R. Soc. London, Ser. A*, vol. 168, pp. 469–495, 1938.
128. W. H. J. Childs and H. A. Jahn, "A new Coriolis perturbation in the methane spectrum. III. Intensities and optical spectrum," *Proc. R. Soc. London, Ser. A*, vol. 169, pp. 451–463, 1939.
129. E. K. Plyler, E. D. Tidwell, and L. R. Blaine, "Infrared absorption spectrum of methane from 2470 to 3200 cm^{-1}," *J. Res. Natl. Bur. Stand., Sect. A*, vol. 64A, pp. 201–212, 1960.
130. R. W. P. Drever, J. L. Hall, and F. V. Kowalski, "Laser phase and frequency stabilization using an optical resonator," *Appl. Phys. B*, vol. 105, pp. 97–105, 1983.
131. J. Manne, A. Lim, W. Jäger, and J. Tulip, "Wavelength modulation spectroscopy with a pulsed quantum cascade laser for the sensitive detection of acrylonitrile," *Appl. Opt.*, vol. 50, pp. E112–E118, 2011.
132. L. Tao, K. Sun, M. A. Khan, D. J. Miller, and M. A. Zondlo, "Compact and portable open-path sensor for simultaneous measurements of atmospheric N_2O and CO using a quantum cascade laser," *Opt. Exp.*, vol. 20, pp. 28106–28118, 2012.
133. G. Gagliardi, S. Borri, F. Tamassia, F. Capasso, C. Gmachl, D. Sivco, J. Baillargeon, A. Hutchinson, and A. Cho, "A frequency-modulated quantum-cascade laser for spectroscopy of CH_4 and N_2O isotopes," *Isot. Environ. Health Stud.*, vol. 41, pp. 313–321, 2005.
134. S. Borri, S. Bartalini, P. De Natale, M. Inguscio, C. Gmachl, F. Capasso, D. L. Sivco, and A. Y. Cho, "Frequency modulation spectroscopy by means of quantum-cascade lasers," *Appl. Phys. B*, vol. 85, pp. 223–229, 2006.
135. R. Eichholz, H. Richter, M. Wienold, L. Schrottke, R. Hey, H. T. Grahn, and H.-W. Hübers, "Frequency modulation spectroscopy with a THz quantum-cascade laser," *Opt. Exp.*, vol. 21, pp. 32199–32206, 2013.
136. J. H. Seinfeld and S. N. Pandis, *Atmospheric chemistry and physics: From air pollution to climate change.* Hoboken, New Jersey: Wiley, 2006.
137. Neonatal Inhaled Nitric Oxide Study Group, "Inhaled nitric oxide in full-term and nearly full-term infants with respiratory failure," *N. Engl. J. Med.*, vol. 336, pp. 597–604, 1997.
138. C. D. R. Borland and T. W. Higenbottam, "A simultaneous single breath measurement of pulmonary diffusing capacity with nitric oxide and carbon monoxide," *Eur. Respir. J.*, vol. 2, pp. 56–63, 1989.
139. A. Hutchinson, *Diode Laser Studies of Trace Species and their Reactions.* PhD thesis, University of Oxford, 2006.
140. D. Turčinková, M. I. Amanti, G. Scalari, M. Beck, and J. Faist, "Electrically tunable terahertz quantum cascade lasers based on a two-sections interdigitated distributed feedback cavity," *Appl. Phys. Lett.*, vol. 106, p. 131107, 2015.
141. Z. B. Alfassi and C. M. Wai, *Preconcentration Techniques for Trace Elements.* Boca Raton, Florida: CRC Press, 1992.
142. J. H. van Helden, R. Peverall, and G. A. D. Ritchie, "Cavity enhanced techniques using continuous wave lasers," in *Cavity Ring-Down Spectroscopy: Techniques and Applications* (G. Berden and R. Engeln, eds.), pp. 27–55, Chichester: Wiley, 5th ed., 2009.
143. A. OKeefe and D. A. G. Deacon, "Cavity ring-down optical spectrometer for absorption measurements using pulsed laser sources," *Rev. Sci. Instrum.*, vol. 59, p. 2544, 1988.

144. R. Engeln, G. Berden, R. Peeters, and G. Meijer, "Cavity enhanced absorption and cavity enhanced magnetic rotation spectroscopy," *Rev. Sci. Instrum.*, vol. 69, p. 3763, 1998.
145. A. O'Keefe, "Integrated cavity output analysis of ultra-weak absorption," *Chem. Phys. Lett.*, vol. 293, pp. 331–336, 1998.
146. A. O'Keefe, J. J. Scherer, and J. B. Paul, "cw integrated cavity output spectroscopy," *Chem. Phys. Lett.*, vol. 307, pp. 343–349, 1999.
147. K. K. Lehmann, G. Berden, and R. Engeln, "An introduction to cavity ring-down spectroscopy," in *Cavity Ring-Down Spectroscopy: Techniques and Applications* (G. Berden and R. Engeln, eds.), pp. 1–26, Chichester: Wiley, 5th ed., 2009.
148. K. J. Schulz and W. R. Simpson, "Frequency-matched cavity ring-down spectroscopy," *Chem. Phys. Lett.*, vol. 297, pp. 523–529, 1998.
149. G. Berden, R. Peeters, and G. Meijer, "Cavity ring-down spectroscopy: Experimental schemes and applications," *Int. Rev. Phys. Chem.*, vol. 19, 2000.
150. M. Mazurenka, A. J. Orr-Ewing, R. Peverall, and G. A. D. Ritchie, "Cavity ring-down and cavity enhanced spectroscopy using diode lasers," *Annu. Rep. Prog. Chem.*, vol. 101, pp. 100–142, 2005.
151. D. Herriott, H. Kogelnik, and R. Kompfner, "Off-axis paths in spherical mirror interferometers," *Appl. Opt.*, vol. 3, pp. 523–526, 1964.
152. J. B. Paul, L. Lapson, and J. G. Anderson, "Ultrasensitive absorption spectroscopy with a high-finesse optical cavity and off-axis alignment," *Appl. Opt.*, vol. 40, pp. 4904–4910, 2001.
153. D. S. Baer, J. B. Paul, M. Gupta, and A. O'Keefe, "Sensitive absorption measurements in the near-infrared region using off-axis integrated-cavity-output spectroscopy," *Appl. Phys. B*, vol. 75, pp. 261–265, 2002.
154. G. S. Engel, W. S. Drisdell, F. N. Keutsch, E. J. Moyer, and J. G. Anderson, "Ultrasensitive near-infrared integrated cavity output spectroscopy technique for detection of CO at 1.57 μm: new sensitivity limits for absorption measurements in passive optical cavities," *Appl. Opt.*, vol. 45, pp. 9221–9229, 2006.
155. L. R. Brown, D. Chris Benner, J. P. Champion, V. M. Devi, L. Fejard, R. R. Gamache, T. Gabard, J. C. Hilico, B. Lavorel, M. Loete, G. Mellau, A. Nikitin, A. S. Pine, A. Predoi-Cross, C. P. Rinsland, O. Robert, R. L. Sams, M. A. H. Smith, S. A. Tashkun, and V. Tyuterev, "Methane line parameters in HITRAN," *J. Quant. Spectrosc. Radiat.*, vol. 82, pp. 219–238, 2003.
156. Y. A. Bakhirkin, A. A. Kosterev, R. F. Curl, F. K. Tittel, D. A. Yarekha, L. Hvozdara, M. Giovannini, and J. Faist, "Sub-ppbv nitric oxide concentration measurements using cw thermoelectrically cooled quantum cascade laser-based integrated cavity output spectroscopy," *Appl. Phys. B*, vol. 82, pp. 149–154, 2006.
157. D. Marchenko, J. Mandon, S. M. Cristescu, P. J. F. M. Merkus, and F. J. M. Harren, "Quantum cascade laser-based sensor for detection of exhaled and biogenic nitric oxide," *Appl. Phys. B*, vol. 111, pp. 359–365, 2013.
158. X. Liu, Y. Xu, Z. Su, W. S. Tam, and I. Leonov, "Jet-cooled infrared spectra of molecules and complexes with a cw mode-hop-free external-cavity QCL and a distributed-feedback QCL," *Appl. Phys. B*, vol. 102, pp. 629–639, 2011.
159. V. L. Kasyutich, C. E. Canosa-Mas, C. Pfrang, S. Vaughan, and R. P. Wayne, "Off-axis continuous-wave cavity-enhanced absorption spectroscopy of narrow-band and broadband absorbers using red diode lasers," *Appl. Phys. B*, vol. 75, pp. 755–761, 2002.
160. P. Malara, M. F. Witinski, F. Capasso, J. G. Anderson, and P. De Natale, "Sensitivity enhancement of off-axis ICOS using wavelength modulation," *Appl. Phys. B*, vol. 108, pp. 353–359, 2012.
161. L. Ciaffoni, J. Couper, G. Hancock, R. Peverall, P. A. Robbins, and G. A. D. Ritchie, "RF noise induced laser perturbation for improving the performance of non-resonant cavity enhanced absorption spectroscopy," *Opt. Exp.*, vol. 22, p. 17030, 2014.
162. K. M. Manfred, J. M. R. Kirkbride, L. Ciaffoni, R. Peverall, and G. A. D. Ritchie, "Enhancing the sensitivity of mid-IR quantum cascade laser-based cavity-enhanced absorption spectroscopy using RF current perturbation," *Opt. Lett.*, vol. 39, pp. 6811–6814, 2014.

163. E. Dlugokencky and P. Tans, "Trends in Atmospheric Carbon Dioxide," April 2015. www.esrl.noaa.gov/gmd/ccgg/trends/.
164. T. Boutton, "Stable Carbon Isotope Ratios of Natural Materials: 2. Atmospheric, Terrestrial, Marine, and Freshwater Environments," in *Carbon Isotope Techniques* (D. C. Coleman and B. Fry, eds.), pp. 173–186, San Diego: Academic Press, 1991.
165. A. Krough and J. Lindhard, "The regulation of respiration and circulation during the initial stages of muscular work," *J. Physiol.*, vol. 47, pp. 112–136, 1913.
166. L. S. Rothman and W. S. Benedict, "Infrared energy levels and intensities of carbon dioxde," *Appl. Opt.*, vol. 17, pp. 2605–2611, 1978.
167. L. S. Rothman, D. Jacquemart, A. Barbe, D. Chris Benner, M. Birk, L. R. Brown, M. R. Carleer, C. Chackerian, K. Chance, L. H. Coudert, V. Dana, V. M. Devi, J.-M. Flaud, R. R. Gamache, A. Goldman, J.-M. Hartmann, K. W. Jucks, A. G. Maki, J.-Y. Mandin, S. T. Massie, J. Orphal, A. Perrin, C. P. Rinsland, M. A. H. Smith, J. Tennyson, R. N. Tolchenov, R. A. Toth, J. Vander Auwera, P. Varanasi, and G. Wagner, "The HITRAN 2004 molecular spectroscopic database," *J. Quant. Spectrosc. Radiat. Transfer*, vol. 96, pp. 139–204, 2005.
168. R. J. Walker, J. Kirkbride, J. H. van Helden, D. Weidmann, and G. A. D. Ritchie, "Sub-Doppler spectroscopy with an external cavity quantum cascade laser," *Appl. Phys. B*, vol. 112, pp. 159–167, 2013.
169. J. H. van Helden, N. Lang, U. Macherius, H. Zimmermann, and J. Roöpcke, "Sensitive trace gas detection with cavity enhanced absorption spectroscopy using a continuous wave external-cavity quantum cascade laser," *Appl. Phys. Lett.*, vol. 103, p. 131114, 2013.
170. D. S. Elliott, R. Roy, and S. J. Smith, "Extracavity laser band-shape and bandwidth modification," *Phys. Rev. A1*, vol. 26, pp. 12–18, 1982.
171. C. H. Henry, "Theory of the linewidth of semiconductor lasers," *IEEE J. Quantum Electron.*, vol. QE-18, pp. 259–265, 1982.
172. A. P. Bogatov, P. G. Eliseev, L. P. Ivanov, A. S. Logginov, and A. Manko, "Study of the single-mode injection laser," *IEEE J. Quantum Electron.*, vol. 9, pp. 392–394, 1973.
173. R. Lang and K. Kobayashi, "External optical feedback effects on semiconductor injection laser properties," *IEEE J. Quantum Electron.*, vol. 16, pp. 347–355, 1980.
174. K. Petermann, "External optical feedback phenomena in semiconductor lasers," *IEEE J. Quantum Electron.*, vol. 1, pp. 480–489, 1995.
175. J. Osmundsen and N. Gade, "Influence of optical feedback on laser frequency spectrum and threshold conditions," *IEEE J. Quantum Electron.*, vol. 19, pp. 465–469, 1983.
176. J. Morville, S. Kassi, M. Chenevier, and D. Romanini, "Fast, low-noise, mode-by-mode, cavity-enhanced absorption spectroscopy by diode-laser self-locking," *Appl. Phys. B*, vol. 80, pp. 1027–1038, 2005.
177. G. Agrawal, "Line narrowing in a single-mode injection laser due to external optical feedback," *IEEE J. Quantum Electron.*, vol. 20, pp. 468–471, 1984.
178. S. G. Baran, G. Hancock, R. Peverall, G. A. D. Ritchie, and N. J. van Leeuwen, "Optical feedback cavity enhanced absorption spectroscopy with diode lasers," *Analyst*, vol. 134, pp. 243–9, 2009.
179. J. Morville, D. Romanini, and E. Kerstel, "Cavity Enhanced Absorption Spectroscopy with Optical Feedback," in *Cavity-Enhanced Spectroscopy and Sensing* (G. Gagliardi and H.-P. Loock, eds.), vol. 179 of *Springer Series in Optical Sciences*, pp. 163–209, Springer Berlin Heidelberg, 2014.
180. P. Spencer, P. Rees, and I. Pierce, "Theoretical analysis," in *Unlocking Dynamical Diversity: Optical Feedback Effects on Semiconductor Lasers* (D. M. Kane and K. A. Shore, eds.), pp. 23–53, Chichester: Wiley, 2005.
181. F. Träger, ed., *Springer Handbook of Lasers and Optics*. Berlin: Springer, 2nd ed., 2012.
182. J. Landsberg, D. Romanini, and E. Kerstel, "Very high finesse optical-feedback cavity-enhanced absorption spectrometer for low concentration water vapor isotope analyses," *Opt. Lett.*, vol. 39, pp. 1795–8, 2014.
183. V. L. Kasyutich and M. W. Sigrist, "Characterisation of the potential of frequency modulation and optical feedback locking for cavity-enhanced absorption spectroscopy," *Appl. Phys. B*,

vol. 111, pp. 341–349, 2013.
184. R. H. Rhodes, X. Faïn, C. Stowasser, J. Blunier, T.and Chappellaz, J. R. McConnell, D. Romanini, L. E. Mitchell, and E. J. Brook, "Continuous methane measurements from a late Holocene Greenland ice core: Atmospheric and in situ signals," *Earth Planet. Sci. Lett.*, vol. 368, pp. 9–19, 2013.
185. X. Faïn, J. Chappellaz, R. H. Rhodes, C. Stowasser, T. Blunier, J. R. McConnell, E. J. Brook, S. Preunkert, M. Legrand, T. Debois, and D. Romanini, "High resolution measurements of carbon monoxide along a late Holocene Greenland ice core: Evidence for in situ production," *Clim. Past*, vol. 10, pp. 987–1000, 2014.
186. R. Grilli, N. Marrocco, T. Desbois, C. Guillerm, J. Triest, E. Kerstel, and D. Romanini, "SUBGLACIOR: An optical analyzer embedded in an Antarctic ice probe for exploring the past climate," *Rev. Sci. Instrum.*, vol. 85, p. 111301, 2014.
187. E. R. T. Kerstel, R. Q. Iannone, M. Chenevier, S. Kassi, H.-J. Jost, and D. Romanini, "A water isotope (^{2}H, ^{17}O, and ^{18}O) spectrometer based on optical feedback cavity-enhanced absorption for in situ airborne applications," *Appl. Phys. B*, vol. 85, pp. 397–406, 2006.
188. D. Romanini, M. Chenevier, S. Kassi, M. Schmidt, C. Valant, M. Ramonet, J. Lopez, and H.-J. Jost, "Optical-feedback cavity-enhanced absorption: a compact spectrometer for realtime measurement of atmospheric methane," *Appl. Phys. B*, vol. 83, pp. 659–667, 2006.
189. I. Courtillot, J. Morville, V. Motto-Ros, and D. Romanini, "Sub-ppb NO_2 detection by optical feedback cavity-enhanced absorption spectroscopy with a blue diode laser," *Appl. Phys. B*, vol. 85, pp. 407–412, 2006.
190. P. Cermak, M. Triki, A. Garnache, L. Cerutti, and D. Romanini, "Optical-feedback cavity-enhanced absorption spectroscopy using a short-cavity vertical-external- cavity surface-emitting laser," *IEEE Photonics Technol. Lett.*, vol. 22, pp. 1607–1609, 2010.
191. T. Desbois, I. Ventrillard, and D. Romanini, "Simultaneous cavity-enhanced and cavity ring-down absorption spectroscopy using optical feedback," *Appl. Phys. B*, vol. 116, pp. 195–201, 2013.
192. R. W. Tkach and A. R. Chraplyvy, "Regimes of feedback effects in 1.5 μm distributed feedback lasers," *J. Lightwave Tech.*, vol. 4, pp. 1655–1661, 1986.
193. N. Schunk and K. Petermann, "Numerical analysis of the feedback regimes for a single-mode semiconductor laser with external feedback," *IEEE J. Quantum Electron.*, vol. 24, pp. 1242–1247, 1988.
194. D. Lenstra, B. H. Verbeek, and A. J. Den Boef, "Coherence collapse in single-mode semiconductor lasers due to optical feedback," *IEEE J. Quantum. Electron.*, vol. QE-21, pp. 674–679, 1985.
195. J. Helms and K. Petermann, "A simple analytic expression for the stable operation range of laser diodes with optical feedback," *IEEE J. Quantum Electron.*, vol. 26, pp. 833–836, 1990.
196. J. Mørk, B. Tromborg, and J. Mark, "Chaos in semiconductor lasers with optical feedback: theory and experiment," *IEEE J. Quantum Electron.*, vol. 28, pp. 93–108, 1992.
197. F. P. Mezzapesa, L. L. Columbo, M. Brambilla, M. Dabbicco, S. Borri, M. S. Vitiello, H. E. Beere, D. A. Ritchie, and G. Scamarcio, "Intrinsic stability of quantum cascade lasers against optical feedback," *Opt. Express*, vol. 21, p. 13748, 2013.
198. M. Lerttamrab, S. L. Chuang, R. Q. Yang, and C. J. Hill, "Linewidth enhancement factor of a type-II interband-cascade laser," *J. Appl. Phys.*, vol. 96, p. 3568, 2004.
199. D. J. Hamilton, M. G. D. Nix, S. G. Baran, G. Hancock, and A. J. Orr-Ewing, "Optical feedback cavity-enhanced absorption spectroscopy (OF-CEAS) in a ring cavity," *Appl. Phys. B*, vol. 100, pp. 233–242, 2010.
200. G. Maisons, P. Gorrotxategi-Carbajo, M. Carras, and D. Romanini, "Optical-feedback cavity-enhanced absorption spectroscopy with a quantum cascade laser," *Opt. Lett.*, vol. 35, pp. 3607–9, 2010.
201. P. Gorrotxategi-Carbajo, E. Fasci, I. Ventrillard, M. Carras, G. Maisons, and D. Romanini, "Optical-feedback cavity-enhanced absorption spectroscopy with a quantum-cascade laser yields the lowest formaldehyde detection limit," *Appl. Phys. B*, vol. 110, pp. 309–314, 2013.
202. P. Laurent, A. Clairon, and C. Breant, "Frequency noise analysis of optically self-locked diode

lasers," *IEEE J. Quantum Electron.*, vol. 25, pp. 1131–1142, 1989.
203. K. M. Manfred, G. A. D. Ritchie, N. Lang, J. Röpcke, and J. H. van Helden, "Optical feedback cavity-enhanced absorption spectroscopy with a 3.24 μm interband cascade laser," *Appl. Phys. Lett.*, vol. 106, p. 221106, 2015.
204. D. J. Hamilton and A. J. Orr-Ewing, "A quantum cascade laser-based optical feedback cavity-enhanced absorption spectrometer for the simultaneous measurement of CH_4 and N_2O in air," *Appl. Phys. B*, vol. 102, pp. 879–890, 2011.
205. A. G. V. Bergin, G. Hancock, G. A. D. Ritchie, and D. Weidmann, "Linear cavity optical-feedback cavity-enhanced absorption spectroscopy with a quantum cascade laser," *Opt. Lett.*, vol. 38, p. 2475, 2013.
206. R. Wayne, *Chemistry of the Atmospheres*. Oxford: Oxford University Press, 2 ed., 1991.
207. E. A. Davidson, "The contribution of manure and fertilizer nitrogen to atmospheric nitrous oxide since 1860," *Nature Geosci.*, vol. 2, pp. 659–662, 2009.
208. M. A. Rosen, "Nitrous oxide for relief of labor pain: A systematic review," *Am. J. Obstet. Gynecol.*, vol. 186, pp. S110–S126, 2002.
209. L. Clifton, D. A. Clifton, C. E. W. Hahn, and A. D. Farmery, "Assessment of lung function using a non-invasive oscillating gas-forcing technique," *Respir. Physiol. Neurobiol.*, vol. 189, pp. 174–182, 2013.
210. S. Ohshima and H. Schnatz, "Optimization of injection current and feedback phase of an optically self-locked laser diode," *J. Appl. Phys.*, vol. 71, pp. 3114–3117, 1992.
211. I. H. Malitson, "Interspeciman comparison of the refractive index of fused silica," *J. Opt. Soc. Am.*, vol. 55, pp. 1205–1209, 1965.
212. H. H. Li, "Refractive index of ZnS, ZnSe, and ZnTe and its wavelength and temperature derivatives," *J. Phys. Chem. Ref. Data*, vol. 13, pp. 103–150, 1984.
213. A. J. Alpert, "Hydrophilic-interaction chromatography for the separation of peptides, nucleic acids and other polar compounds," *J. Chromatogr.*, vol. 499, pp. 177–196, 1990.
214. P. Hambleton, "Support materials and solvents," in *High Performance Liquid Chromatography: Fundamental Principles and Practice* (W. J. Lough and I. W. Wainter, eds.), pp. 91–96, Glasgow: Blackie Academic, 1996.
215. T. Shimanouchi, "Tables of molecular vibrational frequencies: consolidated volume I," Tech. Rep. NSRDS-NBS 39, National Bureau of Standards, Washington, D.C., June 1972.
216. N. J. Livesey, M. D. Fromm, J. W. Waters, G. L. Manney, M. L. Santee, and W. G. Read, "Enhancements in lower stratospheric CH_3CN observed by the Upper Atmosphere Research Satellite Microwave Limb Sounder following boreal forest fires," *J. Geophys. Res.*, vol. 109, p. D06308, 2004.
217. E. Sanhueza, R. Holzinger, B. Kleiss, L. Donoso, and P. J. Crutzen, "New insights in the global cycle of acetonitrile: release from the ocean and dry deposition in the tropical savanna of Venezuela," *Atmos. Chem. Phys.*, vol. 4, pp. 275–280, 2004.
218. A. Jordan, A. Hansel, R. Holzinger, and W. Lindinger, "Acetonitrile and benzene in the breath of smokers and non-smokers investigated by proton transfer mass spectrometry (PTR-MS)," *Int. J. Mass Spectrom. Ion Processes*, vol. 148, pp. L1–L3, 1995.
219. M. Gianella and G. A. D. Ritchie, "Cavity-enhanced near-infrared laser absorption spectrometer for the measurement of acetonitrile in breath," *Anal. Chem.*, vol. 87, pp. 6881–6889, 2015.
220. G. Wysocki, R. Lewicki, R. F. Curl, F. K. Tittel, L. Diehl, F. Capasso, M. Troccoli, G. Hofler, D. Bour, S. Corzine, R. Maulini, M. Giovannini, and J. Faist, "Widely tunable mode-hop free external cavity quantum cascade lasers for high resolution spectroscopy and chemical sensing," *Appl. Phys. B*, vol. 92, pp. 305–311, 2008.
221. V. Motto-Ros, M. Durand, and J. Morville, "Extensive characterization of the optical feedbak cavity enhanced absorption spectroscopy (OF-CEAS) technique: ringdown-time calibration of the absorption scale," *Appl. Phys. B*, vol. 91, pp. 203–211, 2008.
222. B. Dahmani, L. Hollberg, and R. Drullinger, "Frequency stabilization of semiconductor lasers by resonant optical feedback," *Opt. Lett.*, vol. 12, pp. 876–878, 1987.
223. J. Morville and D. Romanini, "Sensitive birefringence measurement in a high-finesse resonator using diode laser optical self-locking," *Appl. Phys. B*, vol. 74, pp. 495–501, 2002.

224. R. Salter, J. Chu, and M. Hippler, "Cavity-enhanced Raman spectroscopy with optical feedback cw diode lasers for gas phase analysis and spectroscopy," *Analyst*, vol. 137, pp. 4669–76, 2012.
225. M. Hippler, "Cavity-enhanced Raman spectroscopy of natural gas with optical feedback cw-diode lasers," *Anal. Chem.*, vol. 87, pp. 7803–7809, 2015.
226. K. Manfred, L. Ciaffoni, and G. A. Ritchie, "Optical-feedback cavity-enhanced absorption spectroscopy in a linear cavity: model and experiments," *Appl. Phys. B*, vol. 120, pp. 329–339, 2015.
227. C. C. Davis, *Lasers and Electro-optics: Fundamentals and Engineering*. Cambridge: Cambridge University Press, 1996.
228. M. W. Pan, B. P. Shi, and G. R. Gray, "Semiconductor laser dynamics subject to strong optical feedback," *Opt. Lett.*, vol. 22, p. 166, 1997.
229. K. K. Lehmann and D. Romanini, "The superposition principle and cavity ring-down spectroscopy," *J. Chem. Phys.*, vol. 105, p. 10263, 1996.
230. J. C. Habig, J. Nadolny, J. Meinen, H. Saathoff, and T. Leisner, "Optical feedback cavity enhanced absorption spectroscopy: effective adjustment of the feedback-phase," *Appl. Phys. B*, vol. 106, pp. 491–499, 2011.
231. G. Brooker, *Modern Classical Optics*. Oxford: Oxford University Press, 2002.
232. S. Feng and H. G. Winful, "Physical origin of the Gouy phase shift," *Opt. Lett.*, vol. 26, pp. 485–487, 2001.
233. D. A. King and R. J. Pittaro, "Simple diode pumping of a power-buildup cavity," *Opt. Lett.*, vol. 23, pp. 774–6, 1998.
234. N. Djeu and G. J. Wolga, "Optical Saturation of a Single VibrationRotation Transition in the ν_3 Fundamental of SF_6," *J. Chem. Phys.*, vol. 54, p. 774, 1971.
235. R. G. Keeton and H. E. Bass, "Vibrational and rotational relaxation of water vapor by water vapor, nitrogen, and argon at 500 K," *J. Acoust. Soc. Am.*, vol. 60, pp. 78–82, 1976.
236. J. Finzi, F. E. Hovis, V. N. Panfilov, P. Hess, and C. B. Moore, "Vibrational relaxation of water vapor," *J. Chem. Phys.*, vol. 67, p. 4053, 1977.
237. P. F. Zittel and D. E. Masturzo, "Vibrational relaxation of H_2O from 295 to 1020 K," *J. Chem. Phys.*, vol. 90, p. 977, 1989.
238. T. G. M. Freegarde and G. Hancock, "A guide to laser-induced fluorescence diagnostics in plasmas," *J. Phys. IV France*, vol. 7, pp. 15–29, 1997.
239. N. Dudareva, F. Negre, D. A. Nagegowda, and I. Orlova, "Plant voltailes: recent advances and future perspectives," *Crit. Rev. Plant Sci.*, vol. 25, pp. 417–440, 2006.
240. R. M. C. Jansen, J. W. Hofstee, J. Wildt, F. W. A. Verstappen, H. J. Bouwmeester, and E. J. van Henten, "Induced plant volatiles allow sensitive monitoring of plant health status in greenhouses," *Plant Signaling Behav.*, vol. 4, pp. 824–829, 2009.
241. R. M. C. Jansen, J. Wildt, I. F. Kappers, H. J. Bouwmeester, J. W. Hofstee, and E. J. van Henten, "Detection of diseased plants by analysis of volatile organic compound emission," *Annu. Rev. Phytopathol.*, vol. 49, pp. 157–174, 2011.
242. V. Shulaev, P. Silverman, and I. Raskin, "Airborne signalling by methyl salicylate in plant pathogen resistance," *Nature*, vol. 385, pp. 718–721, 1997.
243. I. Åhman, R. Glinwood, and V. Ninkovic, "The potential for modifying plant voltaile composition to enhance resistance to arthropod pests," in *Plant Sciences Reviews 2010* (D. Hemming, ed.), Wallingford, UK: CABI, 2011.
244. D. M. Pinto, J. D. Blande, S. R. Souza, A.-M. Nerg, and J. K. Holopainen, "Plant volatile organic compounds (VOCs) in ozone (O_3) polluted atmosphere: the ecological effects," *J. Chem. Ecol.*, vol. 36, pp. 22–34, 2010.
245. K. O. Britton, P. White, A. Kramer, and G. Hudler, "A new approach to stopping the spread of invasive insects and pathogens: early detection and rapid response via a global network of sentinel plantings," *N. Z. J. For. Sci.*, vol. 40, pp. 109–114, 2010.
246. K. Bauer, D. Garbe, and H. Surburg, *Common Fragrance and Flavor Materials: Preparation, Properties, and Uses*. Weinheim: Wiley-VCH, 3 ed., 1997.
247. A. Hangauer, G. Spinner, M. Nikodem, and G. Wysocki, "High frequency modulation capabilities and quasi single-sideband emission from a quantum cascade laser," *Opt. Exp.*, vol. 22,

pp. 23439–23455, 2014.
248. J. Li, Z. Du, and Y. An, "Frequency modulation characteristics for interband cascade lasers emitting at 3 μm," *Appl. Phys. B*, vol. 121, pp. 7–17, 2015.
249. H. S. Billingham, *Quantum Cascade Lasers: Non-linear Optics and Population Transfer*. PhD thesis, University of Oxford, 2015.
250. F. Cappelli, G. Villares, S. Riede, and J. Faist, "Intrinsic linewidth of quantum cascade laser frequency combs," *Optica*, vol. 2, pp. 836–840, 2015.
251. S. Zaitsu and T. Imasaka, "Intracavity phase-matched coherent anti-stokes Raman spectroscopy for trace gas detection," *Anal. Sci.*, vol. 30, pp. 75–80, 2014.
252. B. J. Kirby and R. K. Hanson, "CO_2 imaging with saturated planar laser-induced vibrational fluorescence," *Appl. Opt.*, vol. 40, p. 6136, 2001.
253. Z. S. Li, M. Rupinski, J. Zetterberg, Z. T. Alwahabi, and M. Aldén, "Detection of methane with mid-infrared polarization spectroscopy," *Appl. Phys. B*, vol. 79, pp. 135–138, 2004.
254. Z. S. Li, M. Rupinski, J. Zetterberg, and M. Aldén, "Mid-infrared PS and LIF detection of CH_4 and C_2H_6 in cold flows and flames at atmospheric pressure," *Proc. Combust. Inst.*, vol. 30, pp. 1629–1636, 2005.
255. Z. W. Sun, Z. S. Li, B. Li, Z. T. Alwahabi, and M. Aldén, "Quantitative C_2H_2 measurements in sooty flames using mid-infrared polarization spectroscopy," *Appl. Phys. B*, vol. 101, pp. 423–423, 2010.
256. C. S. Goldenstein, V. A. Miller, and R. K. Hanson, "Infrared planar laser-induced fluorescence with a cw quantum-cascade laser for spatially resolved CO_2 and gas properties," *Appl. Phys. B*, vol. 120, pp. 185–199, 2015.
257. J. Jágerská, P. Jouy, B. Tuzson, H. Looser, M. Mangold, P. Soltic, A. Hugi, R. Brönnimann, J. Faist, and L. Emmenegger, "Simultaneous measurement of NO and NO_2 by dual-wavelength quantum cascade laser spectroscopy," *Opt. Exp.*, vol. 23, pp. 1512–1522, 2015.
258. R. Maulini, A. Lyakh, A. Tsekoun, R. Go, C. Pflgl, L. Diehl, F. Capasso, and C. K. N. Patel, "High power thermoelectrically cooled and uncooled quantum cascade lasers with optimized reflectivity facet coatings," *Appl. Phys. Lett.*, vol. 95, p. 151112, 2009.
259. Q. Yang, M. Kinzer, R. Aidam, R. Driad, W. Bronner, S. Hugger, R. Ostendorf, F. Fuchs, and J. Wagner, "Dispersion of effective refractive indices of mid-infrared quantum cascade lasers," *J. Appl. Phys.*, vol. 112, 2012.